UNIVERSITÉ DU QUÉBEC À TROIS-RIVIÈRES

DÉVELOPPEMENT D'UN JUMEAU NUMÉRIQUE INTÉGRÉ POUR LA SURVEILLANCE ET L'OPTIMISATION EN FABRICATION ADDITIVE

THÈSE PRÉSENTÉE

COMME EXIGENCE PARTIELLE DU DOCTORAT EN INGÉNIERIE (CONC. GÉNIE MÉCANIQUE)

PAR

ABDELHAMID ZIADIA

NOVEMBRE 2025

DOCTORAT (PH.D.)

Direction de recherche

Prof. Mohamed Habibi
Prénom Nom — Directeur de recherche

Prof. Sousso Kelouwani
Prénom Nom — Codirecteur de recherche

Jury d'évaluation

Prof. Luc Laperrière, UQTR
Prénom Nom, Nom établissement — Président

Prof. Jihed Zghal, UPN
Prénom Nom, Nom établissement — Évaluateur externe

Prof. Fethi Abbassi, AUM
Prénom Nom, Nom établissement — Évaluateur externe

Prof. Mohamed Habibi, UQTR
Prénom Nom, Nom établissement — Directeur de recherche

Prof. Sousso Kelouwani, UQTR
Prénom Nom, Nom établissement — Codirecteur de recherche

REMERCIEMENTS

À l'issue de cette thèse, je souhaite d'abord remercier du fond du cœur ma famille, véritable pilier de mon cheminement. À mes parents, pour leur amour inconditionnel, leur patience et leur confiance, qui m'ont portée dans les moments d'effort comme dans les instants de doute. À mes deux sœurs, pour leur soutien constant, leurs encouragements et leur présence rassurante. Votre écoute et votre énergie m'ont aidée à persévérer. À ma nièce Israa, dont la joie et la spontanéité illuminent chacun de nos instants partagés, et à la petite princesse à venir, dont la simple attente représente déjà une source de bonheur et d'inspiration.

J'exprime ma profonde gratitude à mon directeur, le Professeur Mohamed Habibi, pour sa vision, sa rigueur scientifique et sa bienveillance, ainsi qu'à mon codirecteur, le Professeur Sousso Kelouwani, pour son accompagnement et ses conseils précis. Je remercie également les membres du jury pour le temps consacré, leurs remarques éclairantes et leurs sugges-tions constructives.

Ma reconnaissance va à mes collègues et amis de laboratoire pour les échanges scientifiques stimulants, l'entraide au quotidien et la camaraderie qui ont rendu ce parcours plus humain.

À mes amis, proches ou lointains, merci pour votre écoute, vos messages et vos encouragements, surtout dans les périodes intenses.

À vous toutes et tous, merci pour votre confiance et votre présence. Cette réussite est aussi la vôtre.

RÉSUMÉ

Dans un contexte où la qualité et l'autonomie des procédés additifs deviennent des enjeux majeurs, cette thèse propose une approche intégrée alliant modélisation hors ligne, reconstruction 3D et jumeaux numériques afin d'optimiser, puis de piloter en temps réel l'impression 3D par Dépôt de fil fondu. L'objectif est de relier de façon opérationnelle le triptyque procédé-structure-propriétés pour améliorer la rugosité de surface, la précision dimensionnelle, les performances mécaniques et l'état interne de la matière.

Nous avons d'abord structuré un socle hors ligne robuste, en établissant sur PLA et PLA-CF des modèles d'apprentissage capables de prédire UTS, E et ε à partir des paramètres d'impression, puis en qualifiant la porosité par micro-tomographie avec un plan Taguchi L9, une ANCOVA pondérée et un calcul du rapport signal-bruit. Cet ensemble aboutit à des réglages et à un planning d'ajustements couche par couche qui réduisent significativement les vides tout en restant économes en essais.

Dans un second temps, la thèse passe du hors ligne au temps réel en s'appuyant sur un jumeau numérique nourri par des acquisitions couche-par-couche et par des prédicteurs rapides ou spatio-temporels. Deux stratégies d'optimisation en ligne sont déployées de manière complémentaire : une boucle dédiée à la réduction de la rugosité de surface à chaque couche et une optimisation multicritère coordonnant simultanément la rugosité (Ra), la précision dimensionnelle et les propriétés mécaniques (UTS, E), avec un tranchage adaptatif qui ajuste dynamiquement l'épaisseur de couche dans la fenêtre décisionnelle. Le dispositif s'accompagne d'interfaces de suivi qui affichent, pour chaque couche imprimée, le nuage de points et ses caractéristiques associées et visualisent en temps réel l'évolution des paramètres d'impression et des consignes appliquées. L'ensemble ferme la boucle capter-comprendre-agir et démontre un pilotage multicritère réellement opérationnel.

Aussi, l'une des contributions marquantes réside dans l'articulation commande-observation. Au-delà de la surface, un cGAN 3D reconstruit l'état interne à partir des données de procédé et des nuages de points, réduisant la dépendance à l'imagerie lourde. En fournissant une lecture interne prédictive, les cartes volumiques servent à garantir la qualité, à planifier le post-traitement et à définir les réglages de la couche suivante, au-delà des seules mesures externes.

En conclusion, cette thèse met en place une chaîne complète, reproductible et scalable pour voir, prédire et agir en FDM, avec des modèles hors ligne qui produisent des consignes robustes, une boucle fermée multicritère en temps réel orchestrée par un jumeau numérique, et une reconstruction 3D prédictive qui renseigne la santé interne de la pièce. L'ensemble ouvre

la voie à des procédés additifs plus intelligents, traçables et autonomes, et se transpose aisément à d'autres matériaux, géométries et plateformes industrielles.

Mots-clés : FDM, Fabrication Additive, Apprentissage Automatique, Optimisation Multicritère, Tranchage Adaptatif, Reconstruction 3D.

TABLE DES MATIÈRES

LISTE DES TABLEAUX

LISTE DES FIGURES

LISTE DES ABRÉVIATIONS

ABS: Acrylonitrile Butadiene Styrene

AE: Acoustic Emission

AETCN: AE Deep Time Convolutional Neural Network

AI: Artificial Intelligence

AM: Additive Manufacturing

AM: Additive Manufacturing

ANCOVA: Analysis of Covariance

ANN: Artificial Neural Network

ANN-GA: Artificial Neural Network - Genetic Algorithm

ANOVA: Analysis of Variance

AR: Augmented Reality

BBD: Box–Behnken Design

BJT: Binder Jetting Technology

BPNN: Back-Propagation Neural Network

BSE: Backscattered Electron

BT: Bed Temperature

CA: Cellular Automata

CAD: Computer-Aided Design

CAM: Computer-Aided Manufacturing

CFRPs: Carbon Fiber Reinforced Polymers

CF/PLA: PLA reinforced with Carbon fiber

CFD: Computational Fluid Dynamics

CFS: Correlation-based Feature Selection

cGAN: conditional Generative Adversarial Network

CM 247 LC: Cobalt-based Superalloy

CNN: Convolutional Neural Networks

CNN–LSTM: Convolutional Neural Network–Long Short-Term Memory

CP: Crystal Plasticity

CPS: Cyber-Physical System

CPU: Central Processing Unit

CSAM: Cold Spray Additive Manufacturing

CT: Computed Tomography

DED: Directed Energy Deposition

DEM: Discrete Element Method

DIC: Digital Image Correlation

DL: Deep Learning

DLP: Digital Light Processing

DOE: Design of Experiments

DT: Decision Tree

DT: Digital Twin

EBSD: Electron Backscatter Diffraction

FDM: Fused Deposition Modeling

FEA: Finite Element Analysis

FiLM : Feature-wise Linear Modulation

FEM: Finite Element Method

FFF: Fused Filament fabrication

GA: Genetic Algorithm

GAM: Generalized Additive Model

GPR: Gaussian Process Regression

GPU: Graphics Processing Unit

H: Hausdorff distance

hDIC: height Digital Image Correlation

HPD: Heterogeneous Pore Design

ICP: Iterative Closest Point

iCT: industrial Computed Tomography

IQR: Interquartile-range

IR: Infrared

KNN: K-Nearest Neighbors

L-DED: Laser-Directed Energy Deposition

LARM: Laser Additive Manufacturing
Lasso: Least absolute shrinkage and selection operator
LCD: Liquid Crystal Display
LCNN: Lightweight Convolutional Neural Network
LDA: Linear Discriminant Analysis
LED: Light-Emitting Diode
LFAM: Large Format Additive Manufacturing
LMD: Laser Metal Deposition
LN: Layer Number
LPBF: Laser Powder Bed Fusion
LS-SVM: Least Squares Support Vector Machine
LSTM: Long Short-Term Memory
LT: , Layer Thickness
L_1: Mean Absolute Error
MARS: Multi-variate Adaptive Regression Splines
MDACNN: Multi-fidelity Defect reconstruction strategy using A Convolutional Neural Network
ME: Material extrusion
ML: Machine Learning
ML-EM: Maximum Likelihood Expectation Maximization
MPAV: Meltpool Area Volume
MPC: Model Predictive Control
MPIV: Meltpool Intensity Volume
MSE: Mean Squared Error
MTS: Material Testing System
NN: Neural Networks
NSGA-III: Non-dominated Sorting Genetic Algorithm III
OICP: Offset Iterative Closest Point
PADL: Physics-Aware Deep Learning
PC-ABS: Polycarbonate and Acrylonitrile Butadiene Styrene
PCA: Principal Component Analysis
PETG: Polyethylene Terephthalate Glycol
PF: Phase Field
PID: Proportional-Integral-Derivative
PLA: Polylactic Acid
PLA-CF: PLA with Carbon Fiber
PS: Printing Speed
PSO: Particle Swarm Optimization
PSP: Process-Structure-Properties
PT: Printing Temperature
Ra: Average Surface Roughness
RBF: Radial Basis Function
ReLU: Rectified Linear Unit
RF: Random Forest
RL: Reinforcement Learning
RMSE: Root Mean Square Error
RNN: Recurrent Neural Network
RPA: Reinforced Polyamide
RSM: Response Surface Methodology
SEM: Scanning Electron Microscope
SiL: Simulation-in-the-Loop
SL: Structured Light
SLM: Selective Laser Melting
SOR: Statistical Outlier Removal
SOS: Symbiotic Organism Search Method
SVD: Singular Value Decomposition
SVM: Support Vector Machine

SVR: Support Vector Regression
TA-ID: Textural analysis-based image diagnosis
TED: Thermal Emission Distribution
TEP: Thermal Energy Profile
TLBM: Thermal Lattice Boltzmann Modeling
U-Net: U-shaped Neural Network
ULTEM 9085: Polyetherimide
UTS: Ultimate Tensile Strength
VAM: Volumetric Additive Manufacturing
VR: Virtual Reality
WAAM: Wire Arc Additive Manufacturing
XCT: X-ray Computed Tomography
XGB: XGBoost
YOLOv3: You Only Look Once, version 3

Chapitre 1: Introduction

1.1 Contexte général

L'Industrie 4.0 a transformé la production en reliant étroitement la conception, l'atelier et les données, grâce aux systèmes cyber-physiques, à l'Internet des objets, au cloud, à l'edge computing et à l'intelligence artificielle. Historiquement, l'industrie s'appuyait surtout sur des procédés traditionnels tels que l'usinage soustractif, le formage, le moulage et l'assemblage. Ces filières sont performantes pour les grandes séries, mais exigent des outillages coûteux, offrent une flexibilité limitée pour les géométries complexes et génèrent beaucoup de déchets. L'usinage enlève de la matière et produit des copeaux et des rebuts, la mise au point d'outillages crée des chutes et des pièces d'essai, et des chaînes logistiques longues entraînent des stocks tampons et du gaspillage. La demande actuelle va dans l'autre sens, avec personnalisation, délais courts et sobriété en matière et en énergie.

La fabrication additive s'est imposée comme une réponse cohérente à ces objectifs. Le principe d'empilement couche par couche fabrique au plus près de la forme finale et limite les pertes de matière. Les pièces allégées et les structures lattices deviennent fabricables sans usinage lourd, l'inventaire bascule vers un stock numérique et les itérations entre conception et pièce finie sont raccourcies. La fabrication additive n'est pas exempte de déchets, comme les supports ou certaines opérations de finition, mais, globalement, elle inverse le paradigme en rapprochant la matière utilisée de la matière utile. En contrepartie, la qualité reste sensible aux paramètres et aux états thermiques, ce qui introduit une variabilité sur la rugosité, la précision géométrique, la porosité et les performances mécaniques. D'où le besoin de données in situ, de reconstructions 3D et de modèles prédictifs pour relier processus, structure et propriétés, et sécuriser la répétabilité.

- **Fabrication par dépôt de filament fondu (FDM)**

Le dépôt de filament fondu est le procédé le plus diffusé, grâce à son coût modéré, à la simplicité d'intégration de capteurs et à un écosystème ouvert. Le filament est fondu puis déposé, trajectoire par trajectoire. Les leviers principaux sont la température de buse, la température de plateau, l'épaisseur de couche, la vitesse d'impression et le débit. Ces paramètres pilotent l'adhésion intercouches, l'étalement visqueux, la contraction thermique et la cristallinité, avec des effets directs sur la rugosité, la précision dimensionnelle, l'anisotropie et la porosité. FDM constitue ainsi un banc idéal pour établir des relations processus–structure–propriétés, instrumenter des acquisitions in situ et exploiter des données couche par couche dans une logique observer comprendre agir.

- **Jumeau numérique**

Le jumeau numérique est une représentation virtuelle d'un objet, d'un procédé ou d'un système, qui capture ses caractéristiques et son comportement tout au long de son cycle de vie. En fabrication additive, il sert de passerelle entre le monde physique et le monde numérique, en reflétant la conception, la production et le post-traitement des pièces. Il relie l'entité physique, le modèle virtuel et le lien de données qui assure la synchronisation. Selon le besoin, le jumeau s'alimente de flux hétérogènes, qu'il s'agisse de mesures machine, de signaux thermiques, d'images ou de nuages de points, d'indicateurs de qualité ou de modèles prédictifs, et il peut fonctionner en ligne pour suivre et corriger, ou hors ligne pour analyser et planifier. Le cœur du jumeau numérique est d'installer une boucle observer comprendre agir, fiable et reproductible, pour réduire la variabilité, améliorer la qualité et préparer la commande en boucle fermée dans les conditions du procédé réel.

1.2 Problématique

La production par fabrication additive progresse mais la variabilité reste difficile à maîtriser en pratique. En FDM, de petites dérives de procédé se propagent couche après couche et finissent par affecter la rugosité, la précision géométrique, la porosité et les propriétés mécaniques. Le caractère séquentiel du dépôt, la sensibilité thermique et l'anisotropie rendent la stabilisation de la qualité délicate, surtout lorsque l'on vise des pièces fonctionnelles et répétables sur des machines standards. Le moindre ajustement de paramètre modifie l'équilibre temps coût énergie et peut alourdir la durée d'impression et la dépense de matière.

- **Point paramètres nombreux et interdépendants**

Le réglage combine température de buse, température de plateau, épaisseur de couche, vitesse d'impression et débit, avec des fenêtres de procédé étroites. Ces paramètres interagissent fortement. La température modifie la viscosité et la diffusion inter couches. La vitesse change le temps de résidence et l'apport thermique. L'épaisseur de couche affecte à la fois le lissage de surface et la rigidité. Le débit ajuste l'aire de recouvrement et l'étanchéité. Les effets varient selon la géométrie, l'orientation, la trajectoire et le rang de couche, et dépendent aussi de la machine, du filament et de l'environnement. Une optimisation paramètre par paramètre ignore ces couplages. Les plans d'expériences complets deviennent rapidement coûteux dès que l'on croise plusieurs facteurs et plusieurs réponses. L'optimum n'est pas unique et peut se déplacer d'une zone de la pièce à l'autre.

- **Défauts fréquents et mécanismes**

Les défauts rencontrés le plus souvent dans la FDM sont bien connus. Rugosité élevée liée au stair-stepping, aux stries d'outil et aux ondulations de cordon, aggravées par sous-extrusion ou sur-extrusion et par un recouvrement latéral insuffisant. Précision dimensionnelle instable avec dérives géométriques, gauchissement et retrait dus aux gradients thermiques et à l'étalement visqueux. Porosité et vides inter-couches et intra-couche lorsque l'adhésion inter-couches est faible, que la diffusion de matière est insuffisante ou que la vitesse est trop élevée pour la température donnée. Délaminations et anisotropie mécanique quand la fusion entre passages n'est pas assurée ou que la température chute entre couches. Défauts locaux aux changements de trajectoire, avec surépaisseurs aux arrêts et reprises et sous-remplissages dans les zones rapides. Humidité du filament et variations d'environnement qui dégradent la stabilité. Chaque couche hérite de la topographie et de l'état thermique de la précédente, ce qui favorise la propagation des écarts si l'on n'intervient pas au fil de l'impression.

- **Limites des méthodes actuelles**

Pour répondre aux défis décrits, trois familles d'approches dominent mais restent incomplètes. Le choix des paramètres de procédé s'appuie encore sur l'essai erreur et sur des plans d'expériences, coûteux en temps, en matière et parfois en imagerie, et il saisit mal les relations non linéaires, les interactions entre facteurs et la dépendance couche par couche. La surveillance en ligne collecte de grandes quantités de données pendant l'impression, mais elle se limite souvent à la détection de défauts externes, exige fréquemment l'intervention de l'opérateur, reste onéreuse et n'aboutit pas systématiquement à une action corrective. La reconstruction 3D fournit une vision fine, y compris à l'intérieur des pièces, mais sa robustesse est encore perfectible, l'alignement géométrique est sensible et la détection des défauts internes demeure partielle selon la modalité et les conditions. Au final, aucune de ces approches, prise isolément, ne garantit un contrôle qualité complet, fiable et compatible avec les contraintes de temps d'un procédé FDM standard.

- **Besoin de nouvelles approches**

Face aux limites mises en évidence dans les sections précédentes, les méthodes actuelles restent fragmentées, manquent de robustesse, coûtent cher en temps et en matière, et ne détectent pas toujours les défauts vraiment critiques. Il devient nécessaire de passer à une démarche intégrée et intelligente qui relie observation prédiction et décision, prenne en compte la dynamique couche par couche, et prépare un contrôle en boucle fermée sur des machines FDM standards.

Donc comment concevoir une chaîne complète observer comprendre agir qui combine optimisation multi-objectifs des paramètres, mesures in situ et reconstructions, modèles prédictifs rapides et interprétables, afin de réduire la variabilité de surface, d'améliorer la précision géométrique et les performances mécaniques, et de rapprocher l'atelier d'un jumeau numérique opérationnel.

1.3 Objectifs de la thèse

L'objectif général de cette thèse est de concevoir et valider une chaîne intégrée mesures-modélisation-pilotage appliquée au FDM, afin d'améliorer simultanément la rugosité de surface, la précision géométrique, les vides et les performances mécaniques des pièces imprimées. Cette démarche vise à doter le procédé d'une capacité accrue de compréhension, de prédiction et d'adaptation, en articulant de manière cohérente la connaissance hors ligne et l'exploitation en ligne des données issues de l'impression.

Deux objectifs spécifiques distincts mais interdépendants émergent de cette poursuite déterminée de notre objectif global, tel que présenté ci-dessous.

- **Développer un cadre prédictif hors ligne pour l'amélioration de la qualité en FDM**
  Ce premier objectif vise à établir un cadre prédictif permettant de comprendre en profondeur comment les paramètres d'impression influencent la microstructure, la porosité et les propriétés mécaniques des pièces FDM. L'enjeu est d'identifier les relations dominantes et les interactions qui structurent le comportement du procédé, d'en dégager des tendances robustes malgré la variabilité inhérente à la fabrication additive, et de définir des zones opératoires favorisant simultanément la fabricabilité et la performance mécanique. Ce cadre hors ligne constitue la base scientifique indispensable à la préparation du pilotage en ligne.
- **Développer un jumeau numérique pour le pilotage en ligne et l'observabilité 3D**
  Le second objectif vise à transposer cette compréhension hors ligne dans un environnement décisionnel actif au cours de l'impression. Il s'agit de doter le procédé d'une représentation numérique capable de suivre en continu l'évolution de la qualité à partir des mesures couche par couche, d'anticiper les dérives géométriques ou mécaniques à partir des paramètres courants et de l'historique du dépôt, et de soutenir une adaptation dynamique des réglages dans une logique mono-objectif ou multi-objectif. Cet objectif inclut également l'intégration d'une lecture volumique prédictive permettant d'appréhender l'état interne de la pièce sans recourir à une imagerie lourde, ouvrant la

voie à une vision tridimensionnelle cohérente de la qualité. L'ensemble prépare les fondements d'un pilotage intelligent, prédictif et en boucle fermée du procédé FDM.

1.4 Contributions

Les contributions principales de cette thèse sont les suivantes :

- Établissement d'un cadre prédictif hors ligne reliant de manière quantitative les paramètres d'impression, la porosité et les propriétés mécaniques, soutenu par des modèles d'apprentissage supervisé, des analyses statistiques rigoureuses et d'algorithmes d'optimisation avancés.

- Développement d'un jumeau numérique opérationnel pour le procédé FDM, structuré selon la logique "capter–comprendre–agir" et intégrant des stratégies de pilotage couche par couche, qu'elles soient mono-objectif ou multi-objectif. Ce jumeau exploite simultanément les paramètres manipulables, les mesures in situ et des modèles prédictifs pour décider en temps réel, coordonner plusieurs critères de qualité, mettre à jour automatiquement le G-code et assurer un contrôle multicritère en quasi-boucle fermée. L'ensemble est soutenu par des interfaces dédiées, permettant le suivi des paramètres et des nuages de points, la reproduction de la trajectoire du G-code, ainsi que la visualisation de la reconstruction 3D, offrant une supervision complète et traçable du procédé.

- Développement et validation d'un prédicteur volumique 3D, fondé sur un modèle génératif conditionnel, permettant d'estimer la structure interne d'une pièce FDM sans recourir à l'imagerie lourde. Cette reconstruction 3D prédictive constitue un outil inédit pour anticiper la santé interne des pièces et orienter les prochains réglages du procédé.

Ces contributions constituent une avancée significative vers une fabrication additive FDM plus autonome, prédictive et traçable, en intégrant pour la première fois modélisation hors ligne, pilotage en ligne multicritère et reconstruction 3D prédictive au sein d'un jumeau numérique opérationnel.

1.5 Structure de la thèse

Cette thèse est structurée en deux parties principales, chacune répond à un des deux objectifs spécifiques ci-dessus,

- La première partie est consacrée à la modélisation et l'optimisation hors ligne en FDM. Elle installe le cadre scientifique du procédé FDM et clarifie les leviers qui gouvernent la qualité. Elle explore comment les paramètres d'impression façonnent les propriétés des pièces imprimées. L'axe central est de relier procédé, structure et propriétés à l'aide d'approches d'apprentissage qui transforment des données expérimentales en modèles

prédictifs rapides. Ces modèles soutiennent des choix de paramètres plus rationnels, dégagent des surfaces de réponse lisibles et alimentent des optimisations multi-objectifs capables de proposer des réglages robustes. La partie se prolonge par une lecture interne de la matière via la micro-CT, qui apporte un regard complémentaire sur les vides et la consolidation inter-couches.

- La deuxième partie se concentre le pilotage en ligne et jumeau numérique du procédé FDM. Elle transpose le socle hors ligne dans une boucle capter, comprendre, agir au plus près de l'impression. Elle met en place une métrologie de surface couche par couche et des modèles capables de prédire rapidement des indicateurs de qualité à partir des paramètres d'impression et de l'historique des couches. Ces prédictions alimentent une décision en ligne soit en mode mono-objectif dédié à la réduction de la rugosité ou en mode multicritère, pour améliorer les propriétés mécaniques, les rugosités des surfaces et les précision dimensionnelles simultanément, qui ajuste les paramètres dans la fenêtre disponible entre deux couches, avec une coordination des consignes et un découpage adaptatif intégré à la décision. Une interface opérateur rend visibles paramètres, nuages de points et métriques de chaque couche imprimée pour un usage fiable et traçable. Enfin, la partie ajoute une observabilité volumique prédictive de la pièce entière par apprentissage génératif, afin d'estimer la santé interne à partir des données accessibles en production.

Le lien entre les deux parties s'établit de manière progressive et complémentaire. La première partie se consacre à la compréhension et à la modélisation du procédé FDM, en structurant les liens procédé–structure–propriétés et en posant des bases méthodologiques et prédictives pour guider les choix hors ligne. La deuxième partie transpose ces acquis vers l'action, au plus près de l'impression, en déployant un jumeau numérique qui observe la surface couche par couche, décide en ligne en mode ciblé sur la rugosité ou en mode multicritère, et prépare une observabilité volumique prédictive de la pièce entière. Cette articulation transforme un corpus de connaissances en un pilotage effectif, où le socle hors ligne sécurise la décision et où le pilotage en ligne, en retour, enrichit la compréhension, jusqu'à converger vers un contrôle de plus en plus autonome de la qualité en FDM.

Ainsi, ce travail couvre la pré-production en structurant la connaissance et en formant des modèles et recettes hors ligne, l'en production en opérant une boucle d'observation et de décision sur machine via le jumeau numérique, et la post-production en qualifiant les pièces par mesures finales et reconstruction 3D prédictive afin d'orienter contrôles et améliorations ultérieures.

Partie I : Modélisation et optimisation hors ligne en FDM

Chapitre 2: Revue de littérature sur l'utilisation de l'apprentissage automatique dans la fabrication par dépôt de fil fondue

Ce chapitre a fait l'objet d'une publication :
Machine learning study of the effect of process parameters on tensile strength of FFF PLA and PLA-CF. ZIADIA Abdelhamid, HABIBI Mohamed, and KELOUWANI Sousso. Journal of the Brazilian Society of Mechanical Sciences and Engineering, 46(2), p.70.
Il peut être consulté en ligne à l'adresse suivante :
https://doi.org/10.1007/s40430-023-04637-5

L'étude propose une revue d'état de l'art sur l'usage de l'apprentissage automatique pour modéliser les relations processus-structure-propriétés (PSP) en fabrication additive par dépôt de fil fondu (FDM/FFF). Elle montre qu'aucune revue récente ne traite exclusivement ce sujet en articulant clairement les liens PSP et le suivi in situ. Les travaux antérieurs se concentrent soit sur le monitoring sans recours au ML, soit sur la fabrication additive en général sans approfondir le couple FDM et PSP, ce qui constitue une lacune que l'étude vise à combler. Les objectifs sont d'analyser l'effet des paramètres de procédé sur la qualité des pièces en termes de propriétés mécaniques, de précision dimensionnelle, de rugosité et de temps de fabrication, et de cartographier les apports du ML pour la détection et la décision en temps réel ainsi que pour la prédiction et l'optimisation des relations PSP en FDM.
La première partie dresse un état des connaissances sur l'influence des paramètres. La qualité en FDM dépend surtout de l'épaisseur de couche, du taux de remplissage, des températures d'extrusion et de plateau, de l'orientation d'impression, de la vitesse et du débit. Des couches fines améliorent l'adhésion inter-couches et la rugosité mais allongent le temps d'impression. Un remplissage élevé réduit les vides et augmente rigidité et résistance au prix d'un poids et d'une durée accrus. Une température d'extrusion trop basse limite le mouillage alors qu'une trop élevée dégrade la matière, avec une zone optimale propre au matériau. La température de plateau stabilise l'adhésion initiale et diminue le warping. L'orientation et l'angle de trame gouvernent l'anisotropie mécanique, tandis que vitesse et débit règlent l'énergie déposée et la stabilité géométrique. Au final, les réglages se jouent en compromis entre résistance, précision, rugosité, temps de fabrication et énergie, d'où l'intérêt de plans d'expériences et d'optimisation.

La seconde partie synthétise les apports de l'apprentissage automatique. Sur le fond, cette partie est organisée en deux grands axes. Le premier concerne le monitoring in situ, où des traitements d'images issus de caméras ou de la thermographie sont associés à des CNN ou à YOLO pour détecter porosités, manques de matière et défauts de surface, tandis que des mesures multi-capteurs comme la vibration, l'acoustique ou le thermique sont exploitées par des architectures séquentielles de type RNN ou LSTM pour suivre l'état du dépôt et anticiper les anomalies de procédé. Le second axe porte sur la modélisation et l'optimisation des relations PSP, avec des approches de régression et de classification telles que les réseaux de neurones, les SVM, les Random Forest ou le Gradient Boosting, qui permettent de relier variables de procédé et réponses comme la résistance à la traction, le module de Young, la rugosité, la dérive dimensionnelle ou la productivité, d'identifier les paramètres dominants et de réduire l'effort expérimental. Dans les deux axes, le ML est présenté comme complémentaire aux plans d'expériences tels que Taguchi ou Box-Behnken et aux approches méta-heuristiques, afin d'affiner les fenêtres de procédé et d'arbitrer les compromis entre qualité, temps et coût.

L'étude conclut que le ML appliqué à la FDM constitue déjà un levier efficace pour le contrôle qualité et la prédiction des relations PSP. Sa maturité industrielle dépend cependant de la mise en place de bases de données standardisées et partageables face à l'hétérogénéité des matériaux, des machines et des jeux de données, du développement de chaînes de traitement reproductibles et de la fusion multi-capteurs pour renforcer la robustesse, de l'intégration dans des boucles temps réel reliant monitoring, diagnostic et action, et du couplage avec des jumeaux numériques pour relier simulation et expérience et soutenir l'optimisation multi-objectif en termes de qualité, productivité et énergie. La feuille de route proposée insiste sur la nécessité de normaliser les jeux de données, de documenter rigoureusement les protocoles et de rapprocher ML, plans d'expériences et contrôle avancé afin de favoriser l'émergence de plateformes FDM auto-adaptatives, fiables et transférables à l'échelle industrielle.

The use of Machine learning in process-structure-property modeling for Material Extrusion: A Comprehensive review

Ziadia Abdelhamid[1], Habibi Mohamed[1*] and Sousso Kelouwani[1]

[1*]*Department of mechanical engineering, University of Quebec in Trois-Rivieres, 3351 Bd des Forges, Trois-Rivieres, G8Z 4M3, Quebec, Canada.*

**Corresponding author(s). E-mail(s): Mohamed.Habibi@uqtr.ca;*

Contributing authors: Abdelhamid.Ziadia@uqtr.ca; Sousso.Kelouwani@uqtr.ca;

2.1 Abstract

Since its first appearance in the 1980s, additive manufacturing has become increasingly popular. Complex parts can be produced with high quality, minimal waste, and a variety of materials. However, selecting the appropriate process parameters for printing remains a challenge. In this context, researchers have studied the effects of process parameters on the properties of 3D-printed parts. With the rise of machine learning, researchers have adopted this technology to optimize the relationships between process, structure, and properties and monitor the printing process in real time. Therefore, this review article introduces the influence of the parameters of the material extrusion process on the properties of the printed parts. Then, the potential of machine learning in optimizing 3D printing for the material extrusion process is highlighted. Several technologies and methods have been identified. Most of the research on in-situ monitoring focused on visual data, identifying print defects, with Convolutional Neural Network being the most commonly used algorithm, or other sensor data, with acoustic emission sensors being the most commonly used and that to monitor the state of the polymer and the extruder where time series algorithms were predominantly used. To determine the relationships between process-structure-property relationships, the strategies used focused on predicting part properties, determining optimal printing parameters, or estimating process parameters based on part properties. However, there are still research gaps. Future research should consider the computational cost of machine learning prediction, careful choice of sensors, and data sharing to obtain a larger data set, as researchers often use different new materials and methods and can benefit from each other.

Keywords*:* Additive Manufacturing, Material Extrusion, Machine learning, 3D printing, Process optimization

2.2 Introduction

While subtractive methods are mostly used in traditional manufacturing [1–7], challenges with present-day industrial production have forced the development of other approaches. A fundamental shift occurred with the introduction of additive manufacturing (AM) in the 1980s, which provided a response to the rising need for highly customized, high-quality items at competitive prices [8–10,12–15]. Contrary to their subtractive predecessors, additive manufacturing methods construct products layer by layer from a geometric 3D model, considerably reducing material waste [11, 22–26].

The quick adoption of AM across a variety of industries, from aerospace to medical, is evidence of its revolutionary potential [37–43]. In contrast with traditional methods, it allows for the flexible production of complicated parts using a variety of materials [16–21, 45–48]. Additionally, 3D printing is computerized, which decreases human involvement, reduces errors, and allows for remote manufacturing [31–36].

However, each innovation has its own unique set of problems. Despite the revolutionary potential of AM, choosing the best process parameters, particularly for material extrusion, is still a difficult task [49, 51]. Machine Learning (ML) comes into play in this situation. AM's problems can be overcome by ML's capacity to evaluate large databases and produce useful insights.

Machine learning, a branch of artificial intelligence (AI), uses models and algorithms to give machines the ability to carry out tasks on their own without being explicitly instructed [172]. It thrives on analyzing data, recognizing patterns, and taking decisions according to that analysis [173]. ML can be utilized in a variety of ways in the context of additive manufacturing [174–176].

It can be useful for in-situ monitoring by fault detection and prevention where Anomalies or defects in the printing process can be detected in real-time [177, 178]. For instance, methods like acoustic emission monitoring can reveal information about the flow state, and vibration signals can be utilized to monitor the condition of extruders [179]. Consistent print quality is ensured by immediate correction actions. In-situ monitoring also serves to give feedback by evaluating data from sensors and cameras where corrective actions can be quickly proposed in response to any deviations or faults that are noticed [180, 181]. ML also serves to model Complex Process-Structure-Properties (PSP) relationships. In fact, it can optimize and predict process parameters and printed parts' properties [182, 183]. By using machine learning, researchers can quickly discover the most optimal values for variables like layer thickness,

print speed, and temperature, removing the need for manual guesswork and cutting down on waste [184]. Additionally, ML models that have been trained on a large amount of data may forecast how particular parameters will affect the structural characteristics of printed parts, such as predicting tensile or flexural strengths [185, 186]. Manually setting the parameters for the AM procedure can be ineffective. When trained on data sets, ML models can forecast the optimum values for variables like layer thickness, print speed, and temperature [187, 188]. This promotes waste minimization and guarantees a high-quality final product. The combination of ML and AM not only provides manufacturing effectiveness and dependability but also generates quick innovation, lower production costs, and better final products. Despite these advances, ML models have limitations, such as computational intensity, especially for large datasets, and dependence on the quality of data provided by sensors, which must be carefully selected to withstand the printing environment and detect the desired features.

Although the use of ML in material extrusion is becoming increasingly popular, there is no recent review article that deals exclusively with this topic, especially with determining the relationships between process, structure, and properties and in-situ monitoring. Most previous review articles addressed in-situ monitoring in material extrusion without focusing on the use of ML [167,168] or focused on the use of ML in additive manufacturing in general [50, 169–171], without discussing in depth the use of ML for determining process–structure–property relationships and in-situ monitoring.

In this context, the primary purpose of this article is to investigate the impact of material extrusion process parameters on the qualities of 3D printed components and to explore the application of machine learning in process-structure-property for the 3D printing process material extrusion.

Consequently, the rest of this article will be divided as follows: The second section will present the methodology used in this comprehensive review. The third section will outline additive manufacturing techniques and the most essential material extrusion process parameters. The impact of the material extrusion process parameter on the mechanical qualities, dimensional accuracy, build time, and surface roughness of 3D printed items will be presented in the third section. The application of Machine Learning in the material extrusion process, more specifically, in-situ monitoring, which is the real-time evaluation of the material extrusion process and the optimization of the process-structure-properties connection, will be addressed in the fourth part. The article will emphasize the many topics discussed as well as the predicted future possibilities in the fifth section. In the last section the paper will end with a conclusion.

2.3 Search methodology and Results

The focus of this research is the application of machine learning in the Material Extrusion (ME) additive manufacturing process. The emphasis is on in-situ monitoring and identifying relationships between process-structure-properties (PSP), using a systematic review methodology.

The task included doing a thorough literature search using a logical and repeatable strategy to locate numerous papers relevant to the issue (Figure 1). The search was conducted using the keywords "("material" AND "extrusion") OR "fdm" OR "fff" OR ("fused" AND "filament" AND "fabrication") OR ("fused" AND "deposition" AND "modeling") OR ("fused" AND "deposition" AND "modelling")) AND ("machine" AND "learning")".

To ensure the relevance and recentness of the studies included, the study was done in the year 2022 with an emphasis on literature published between 2018 and 2022. The search turned up 8155 results where duplicates were removed using Zotero, a literature management tool, to refine the dataset.

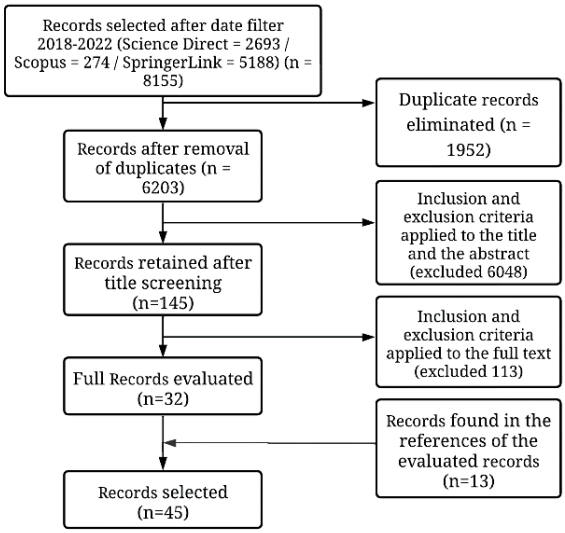

Figure 1. Systematic search process description

The dataset was extensively analyzed based on preset inclusion and exclusion criteria to identify the most pertinent sources.

Inclusion criteria:

- Studies addressing the Material Extrusion process.
- Primary focus on identifying process-structure-property connections or in-situ monitoring using visual or sensor-generated data.
- Original research.

The exclusion criteria:

- Process-structure-property was not the focus of the research.

- Studies with no experimental activity.
- Studies not written in English.

This analysis resulted in 32. In the references of the evaluated articles 13 records were found and added to give us a total of 45 records selected.

Following a rigorous systematic review, the research shows a visible trend toward the incorporation of ML in material extrusion additive manufacturing. As shown in Figure 2 from 2018 to 2022, this trend, supported by a substantial amount of academic literature, highlights the growing importance of ML in improving real-time monitoring and comprehending the complex process-structure-properties (PSP) relationships in Material Extrusion (ME). The research focus reflects a larger industry trend in which merging Machine Learning (ML) additive manufacturing with Material Extrusion (ME) additive manufacturing is producing smarter manufacturing methods. This results in more efficient manufacturing processes and reduced unexpected breakdowns of machinery.

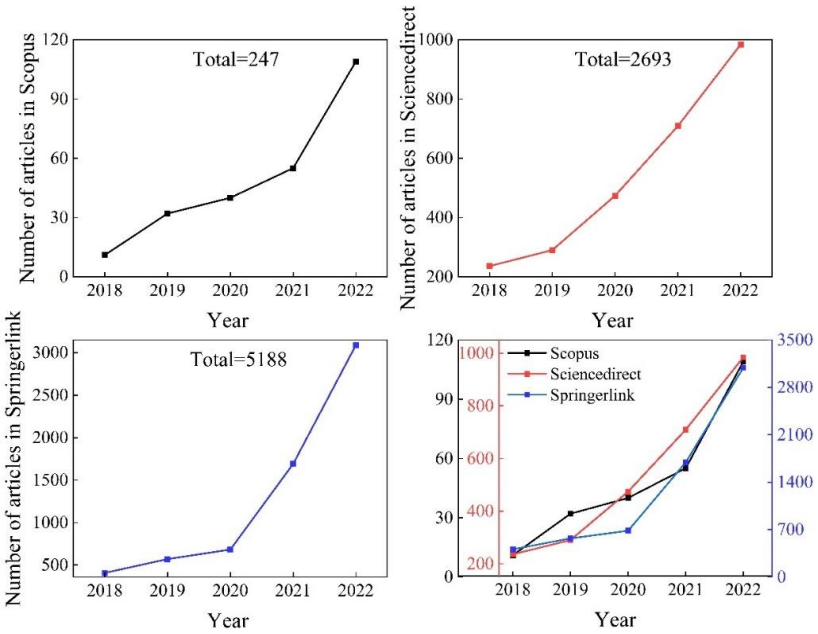

Figure 2. Number of articles related to Material extrusion and Machine Learning per year.

2.4 Additive Manufacturing

The term Additive manufacturing appeared for the first time in the 1980s and as stated before, it has been a rapidly advancing and increasingly popular manufacturing technology. ISO/ASTM 52900:2015 [44] stated that seven process categories exist: binder jetting, direct energy deposition, material extrusion, material jetting, powder bed fusion, sheet lamination, and vat photopolymerization. Material extrusion is a 3D printing technique that is commonly used in research.

Material extrusion and Material jetting can print various materials like Polymers, Composites, Ceramics, Hybrids, Metals, and Biologicals, which is considered a huge advantage compared to other processes like Vat photopolymerization and Directed energy deposition [85–88]. Moreover, Binder Jetting, Powder bed fusion and Material extrusion are the processes with the largest build volumes, allowing the possibility of building different parts [85–88]. Furthermore, Material extrusion's low cost [52–54], wide market availability[52–54], ability to construct complex parts[55], and safety and cleanliness[55] make it extremely popular among researchers. Consequently, this paper will focus on the Additive Manufacturing process, Material Extrusion, its parameters, the structural properties of its printed parts, and their relationship.

2.4.1 Material extrusion process description

The term Material extrusion first appeared in 1989 [23, 56]. It was invented and patented by the co-founder of Stratasys, Scott Crump [57–60]. This company introduced material extrusion to the market as Fused Deposition Modelling (FDM) and popularized its use across a wide range of industries. Fused Filament Fabrication (FFF) was another name for this technology. This term became popular after the Stratasys FDM patent expired [56, 61–63]. This process is able to 3D print multiple types of materials [64–67]. It can be either Plastic/Polymers like acrylonitrile butadiene styrene (ABS) and Polylactic acid (PLA), Metals like Bronze and Silver [68, 69], Ceramics [70, 71], Composites [72–74], Biological [65, 75–77], or others like papers and wood [78–80]. Parts are created for this process by melting a material filament and extruding it through a nozzle. Then, melted material is deposited layer by layer. The first layer is deposited on the build platform, and the new layer is poured right on top of the preceding layer until the part is entirely produced [81–83] (Figure 3).

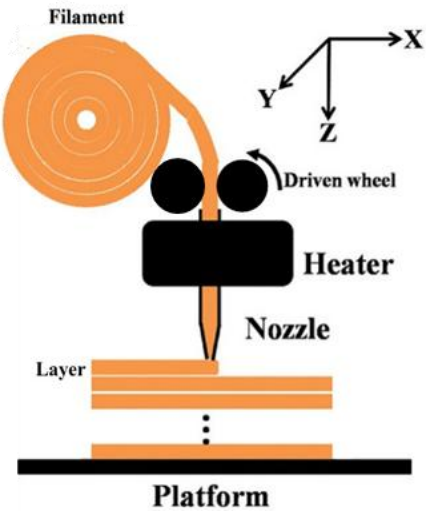

Figure 3. Fused deposition modelling process [84] (Reproduced with permission)

The most fundamental FDM process parameters [89] will be covered in this section. There are quality parameters, such as layer thickness, which indicates the thickness of each layer in the printing process in millimeters. There are parameters related to the contours/walls of the part, such as contour thickness, which represents the horizontal thickness of the walls, contours number, which represents the number of contours surrounding the part being printed, and contour width, which is the wall thickness divided by the number of contours and represents the width of the path of the contour that surrounds the part. Similarly, there are parameters connected to the material temperature, such as the printing temperature and the build plate temperature used to heat the printing platform. There are further infill parameters, such as infill density, which is the proportion of material used on the interior of the print, infill pattern, which describes the form or structure of the material within the component [90], and raster angle which is the angle between 0 and 180 degrees at which the nozzle deposits the material line by line for each layer [91]. There are also speed-related parameters such as printing speed, which is represented in mm/s. Lastly, the build orientation parameter [92] which indicates the orientation of the printed part on the build platform in relation to the x, y, and z axes. Table 1 summarizes these discussed parameters.

Table 1. Fused deposition modeling process parameters

Parameter name	Unity	Role
Layer thickness	mm	The thickness of each layer in the printing part
Contour thickness	mm	The horizontal thickness of the contours
Contour width	mm	The width of the path of the contour tool that surrounds the part
Number of contours		The number of contours surrounding the part
Printing speed	mm/s	The speed at which printing runs
Infill density	%	The amount of material used in the inside of the print
Infill pattern		The form or structure of the material within the component
Extruding temperature	°C	The temperature at which material is extruded
Bed temperature	°C	Used to heat the build platform
Build orientation	Degree	The orientation of the printed part on the build platform
Raster angle	Degree	The angle at which the nozzle deposits the material line

2.5 Influence of FDM process parameters on parts properties

3D-printed FDM parts are being considered to replace traditionally manufactured parts made from traditional materials [93, 94]. So, to improve printing performance and quality, it is necessary to understand the properties of 3D printed parts and their relationship with FDM process parameters. As a result, researchers all over the world have been studying this topic.

The effect of FDM process parameters on mechanical behavior (tensile strength, compressive strength, flexural strength...), surface roughness, dimensional accuracy (bridging, overhanging...), and build time has been the focus of active research.

2.5.1 Influence of FDM process parameters on the mechanical behavior of the part

Understanding the mechanical behavior of FDM 3D printed items is essential for using them in an industrial setting [95–97]. Research has shown that the mechanical properties of these items are significantly influenced by the FDM process parameters.

Gebisa et al. [98] highlighted the importance of the raster angle in determining the tensile strength of ULTEM 9085. Numerous research on materials like Polyethylene terephthalate glycol (PETG), PLA, and ABS have discovered that while increasing layer thickness decreased tensile strength, raising infill density improved it [99–101]. Furthermore, with Reinforced Polyamide (RPA), it was discovered that printing temperature and layer thickness had a greater impact on tensile strength than printing speed did [102].

According to numerous research [104, 106–107], the influence of parameters such layer thickness, infill pattern, and number of curves were significant on flexural strength. When it comes to compressive strength, infill density has emerged as the most significant factor for parts with materials like PETG and PLA [108, 100].

The findings highlight the complex relationship between the FDM process parameters and the mechanical properties of the final products. Table 2 summarizes the influence of FDM process parameters on mechanical properties.

2.5.2 Influence of FDM process parameters on surface roughness of the part

In the 3D printing sector, surface quality is a crucial issue for early consumer acceptance because it immediately influences aesthetic value and, as a result, the product's marketability [109–114].

Various study approaches have been used to understand how process parameters affect surface roughness. Layer thickness, infill percentage, and build orientation have consistently been found to be the most important variables [106, 115–118]. Surface roughness improves with increasing infill density, according to studies utilizing materials like PLA and PTEG, with infill density, pattern, and layer thickness being the main factors [99, 115]. The significant impact of layer thickness on surface roughness was highlighted in other studies, including those on ABS and PLA reinforced with Carbon fiber (CF/PLA) [117, 118]. Research on polycarbonate and acrylonitrile butadiene styrene (PC-ABS) has shown that the build orientation and layer thickness also play a significant influence [106]. Table 3 provides a thorough description of the effects of these parameters in various research.

Table 2. Comparison of fractures and surfaces appearance, and mechanical and thermal properties of molded and 3D printed parts.

Ref	Material	Conclusion	Ref	Material	Conclusion
[98]	ULTEM 9085	Raster angle has significant influence on tensile strength.	[123]	ABS	Layer thickness and raster width have significant influence on viscoelastic properties
[99]	PETG	Tensile strength decreases when layer thickness increases and increases when infill density increases	[124]	rPET	The strength of the specimens is improved the printing temperature is increased from 230°C to 260 °C and with a horizontal raster angle
[101]	ABS, PLA	The tensile strength increases when the infill density increases	[103]	PLA	The printing temperature has a significant influence on tensile strength. When it increases from 200°C to 220°C the tensile force increases significantly
[102]	RPA	Printing temperature and layer thickness had a greater impact on tensile strength than print speed.	[125]	PC/ABS Blends	When Layer thickness increases dynamic flexural modulus improves
[104]	PLA	Infill pattern and contours number have a significant effect on tensile strength Layer thickness and contours number have a significant effect on flexural strength	[100]	PLA	Infill density has a significant influence on the mechanical properties Mechanical properties improve when the infill density and layer thickness increase
[106]	(PC)-ABS	Infill density has the highest influence on flexural strength followed by the layer thickness Horizontal build orientation, low layer thickness and high infill density will generate high flexural strength	[107]	ULTEM 9085	Raster angle and raster width have the highest influence on flexural properties followed by the contour number and contour width
[105]	PLA	Infill density has the most influence on tensile strength followed by contour thickness and then layer thickness	[108]	PLA & PETG	Infill density has a significant influence on compressive strength.

Table 3. Influence of FDM process parameters on Surface Roughness

Ref	Material	Parameters used	Conclusion
[99]	PETG	Layer thickness Infill density Infill pattern Build orientation	The surface roughness decreases when the infill density increases.
[115]	PLA	Infill pattern Infill density Printing speed Layer thickness	Infill density has the most influence in FDM performance. Infill pattern and layer thickness have an important influence on FDM performance. Printing speed has the least influence on FDM performance.
[116]	ABS	Infill density Layer thickness Bed temperature	The surface roughness is mainly influenced by the bed temperature and layer thickness relationship.
[117]	ABS	Layer thickness Raster angle	The surface roughness is mainly influenced by layer thickness.
[118]	CF/PLA	Infill pattern Infill density Layer thickness	The layer thickness and the infill density highly influence surface roughness.
[106]	(PC)-ABS	Layer thickness Build orientation Infill density	Build orientation and layer thickness have significant influence on surface roughness. Horizontal build orientation, low layer thickness, and high infill density will generate low surface roughness.

2.5.3 Influence of FDM process parameters on build time

The quality of FDM 3D printed items, which influences their appearance, lifetime, functionality, and cost, is crucial to their commercial success. Minimizing printing time without sacrificing these qualitative characteristics is crucial [119–122]. The study focuses on the duration printers take to manufacture parts. According to research by Venkatraman et al. [116], among variables like layer thickness, infill density, and bed temperature, only the latter does not significantly affect printing time. By using Polycarbonate/ABS Blends, Othman et al. [100] highlighted the important effects of layer thickness, air gap, build orientation, and the number

of contours on the printing time. Using PLA, Patil et al. [115] found that infill density has the greatest impact on printing time, followed by infill patterns and layer thickness. Layer thickness and print speed were found to be important factors of energy consumption and printing time by Enemuoh et al. [105]. Table 4 summarizes the results of numerous studies.

Table 4. Influence of FDM process parameters on build time

Ref	Material	Parameters used	Conclusion
[115]	PLA	Infill pattern Infill density Printing speed Layer thickness	Infill density have the most influence in FDM performance. Infill pattern and layer thickness have an important influence on FDM performance. Printing speed has the least influence on FDM performance.
[116]	ABS	Infill density Layer thickness Bed temperature	The main contribution percentage for printing time is layer thickness and infill percentage.
[125]	(PC)-ABS	Layer thickness Air gap Build orientation Number of contours Layer thickness Raster angle Raster width	Layer thickness, air gap, build orientation and number of contours have the most influence on Printing Time. Raster angle and raster width have the least influence on Printing time and feedstock material consumption.
[105]	PLA	Layer thickness Printing speed Infill density Infill pattern Contour thickness	Layer thickness has the most influence on energy consumption and production time followed by print speed. Infill density, infill pattern and contour thickness have a less influence on energy consumption, part weight, and production time.

2.5.4 Influence of FDM process parameters on dimensional accuracy

Dimensional accuracy in 3D printing evaluates how well an output object matches the nominal values of the original model [126, 127]. For a printer to be trusted to accurately reproduce objects as intended, this accuracy is essential [128, 129]. Due to the complex procedures and modifications that must be made during the production phase, it is difficult to achieve this degree of precision in FDM parts [131, 132]. There is no one-size-fits-all technique for improving this precision because of the process's complexity and the variety of materials. For instance, Agarwal et al. [133] found in a study using ABS as the printing material that layer

thickness and print speed have a significant impact on dimensional accuracy, whereas bed temperature had a negligible effect. Enemuoh et al. [105] investigated the effects of several PLA part parameters and discovered that the contour thickness and layer thickness have the greatest impact on dimensional accuracy. Hanon et al. [134] further underlined the crucial function of layer thickness in obtaining dimensional accuracy, emphasizing the little influence of other parameters such as build orientation. In an alternative study, Galetto et al. [130] found that for PLA parts, lower values of infill density, printing speed, and layer thickness produce higher dimensional accuracy for overhanging structures, whereas the opposite is true for guaranteeing the quality of bridging structures. Table 5 summarizes all these discoveries.

2.6 Machine Learning in Additive Manufacturing

Artificial Intelligence application in Additive Manufacturing is in constant growth. AI can cover a variety of significant factors that directly influence the resulting 3D printed part quality. This section will discuss the use of AI in in-situ monitoring and in process–structure–properties relationships.

2.6.1 Machine Learning in in-situ monitoring

Conventionally, the quality of 3D-printed parts is evaluated after they have been printed. But, while parameter optimization can help improve quality, it cannot completely eliminate anomalies. Print failures account for a significant portion of the cost of 3D-printed parts [91]. With in-situ monitoring, the printing process is evaluated in real-time. Detecting a possible defect can save material and time and offer the possibility to take corrective actions to the printing parameters [52][135]. Different Machine Learning algorithms have been used and they were based on either Visual data or sensor-generated data. Figure 4 resumes the strategies used for in-situ monitoring.

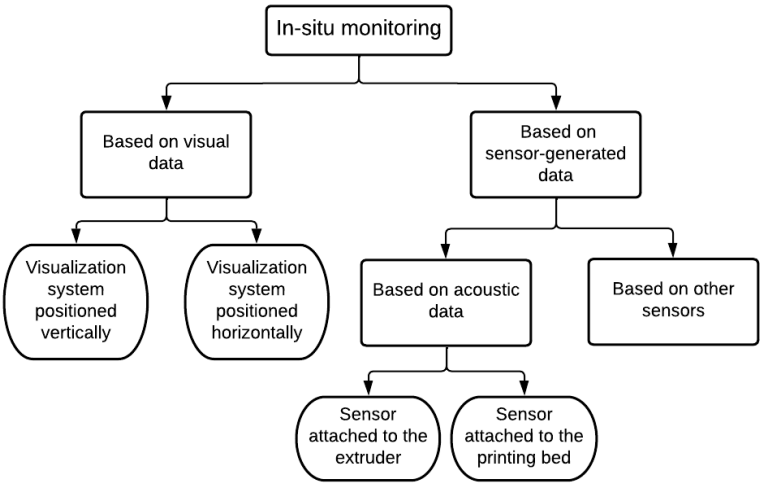

Figure 4: Strategies used for in-situ monitoring using ML.

Table 5. Influence of FDM process parameters on Dimensional accuracy

Ref	Material	Parameters used	Conclusion
[130]	PLA	Layer thickness Infill density Printing temperature Build orientation Number of contours Printing speed Retraction speed	Low values of infill density, printing speed, and layer thickness ensure better dimensional accuracy of overhang. High values of infill density, printing speed, and layer thickness ensure better dimensional accuracy of bridging quality.
[133]	ABS	Contour thickness Infill density Bed temperature Printing speed Layer thickness Printing temperature	Layer thickness and printing speed have the most influence on dimensional accuracy. Contour thickness and infill density have an important influence on dimensional accuracy. Printing temperature has almost no influence on dimensional accuracy. Bed temperature has no influence on dimensional accuracy.
[134]	PLA	Build orientation Raster angle Layer thickness	Layer thickness has a significant influence on dimensional accuracy. Build orientation has a small influence on dimensional accuracy. Raster angle has no influence on dimensional accuracy.
[105]	PLA	Layer thickness Printing speed Infill density Infill pattern Contour thickness	Contour thickness has the most influence on dimensional changes of the part, followed by layer thickness.

2.6.2 Algorithms based on Visual Data.

With the advances in Central Processing Unit (CPU) and Graphics Processing Unit (GPU) performance in recent years [136], advanced image processing and computer vision [137] have been used for in-situ defect detection of 3D printed parts. Researchers have adopted different strategies.

Saluja et al [54] developed a system for warp detection. They used a closed-loop architecture with a Prusa i3 MK2S 3D printer, a Sony A5100 camera placed on the same plane as the platform, a computer running Windows 10 64-bit with Intel® Core™ i5- 6300U CPU @ 2.40 GHz and 8 GB memory, and a Raspberry Pi. To take clear images of the corners of the part, the G-code was adjusted to pause printing at the end of each layer and resume after 2 seconds.

The original dataset contains 6000×4000 pixel images evenly divided into two classes. The object constructed to collect un-warped corners was a 70 mm×15 mm×5 mm printed rectangular cuboid. The warped corners were peeled off the build platform during the printing process with an average value of distortion of 4° (Figure 5).

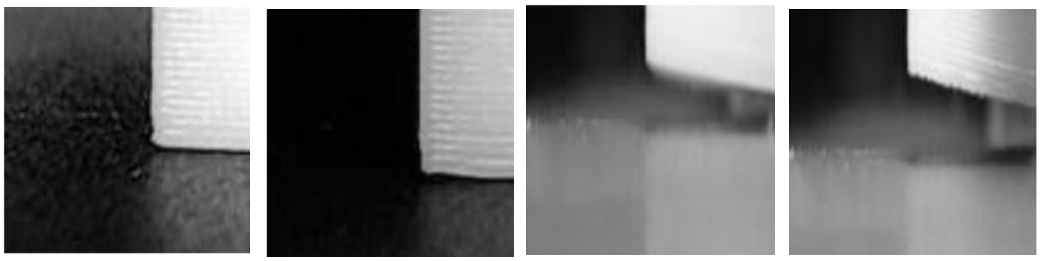

(a) (b) (c) (d)

Figure 5. Samples from the training set: (a), (b) unwarped; and (c), (d) warped [54] (reproduced with permission).

After processing the data, they reduced the images to 100×100 pixels using nearest neighbour interpolation to decrease the number of nodes that could be trained. They also converted the processed images to grayscale to reduce computational costs (Figure 6). Then, the dataset was shuffled and randomly divided into training (416) and validation (104) sets. Then, a Convolutional Neural Networks (CNN) model was used. After creating a test set with additional geometries (rectangular cuboids, triangular prism, cylinder), this method yielded an accuracy of 99.3% (153/154).

In the same context, Brion et al [138] used ABS to detect and correct deformations in FDM. They presented an automated image acquisition and storage system that allowed the creation of the first labeled dataset with 1414 labeled images and 1976 warping cases for a variety of part geometries and starting material colors. YOLOv3 (You Only Look Once, version 3) models were then used, which achieved high accuracy in detecting warps, with the best model having an average precision of 88.72%. Then, a trained deep convolutional neural network provided bounding box detection where new metrics were developed to predict warping severity. To help calibrate the metric, data were collected for several stages of faulting by varying the print bed temperature. Several statistical methods were used to test the effectiveness of the developed metrics in determining the degree of deformation. The metrics were then used in conjunction with the trained model to not only detect warping during a print but also to take action to slow the progression of faulting and limit its severity. In-situ correction cannot save all prints because warp faults are irreversible and temporally separated from their cause (Figure 6). Therefore, a separate feedback pipeline was created to analyze a

warped print and update the necessary slicing and printing settings for future attempts to reduce or eliminate the warp.

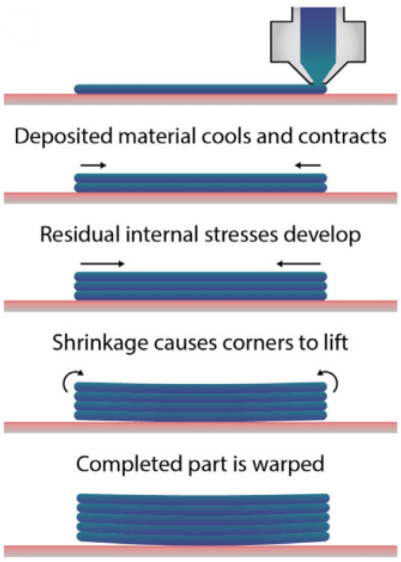

Figure 6. Graphic showing the formation of warping in the extrusion 3D printing process [138] (Reproduced with permission)

In another work, Jin et al [53] predicted irregularities between layers. Their approach is based on the fact that delamination is caused by the wrong height of the nozzle with respect to the print and its calibration. They used a mounted camera to assess the position of the nozzle (Figure 7). They categorized the nozzle positions as Good, High, High+, and Low (Figure 8) and used CNN, which achieved 97.8% on the test data and 91% on the validation data.

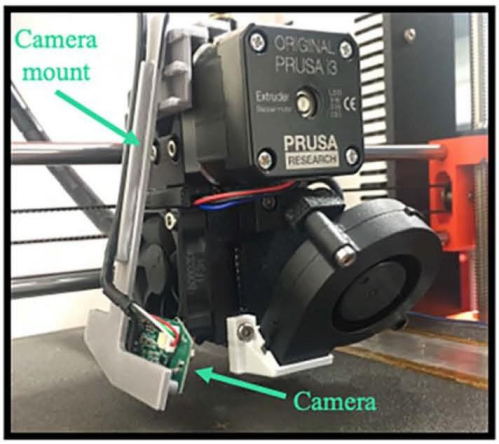

Figure 7. Monitoring system where a camera is attached to the mount in-house designed and 3D printed [53] (reproduced with permission).

For in-process monitoring of the layer topography of FDM, Rossi et al [139] used PLA as the printing material. They chose a cube and a cylinder as test geometries to collect data. They produced two cubes with 100 layers each and two cylinders with 50 layers each. One image was taken of each layer, resulting in 200 raw images. After visually inspecting the raw images,

150 were selected, converted to grayscale, and side cropped. The data were manually labeled, with anomalies considered as missing or incomplete binding between adjacent strands (Figure 9). The three families of architectures used ML represent common approaches to image classification by machine learning: support vector machine (SVM), CNN, and convolutional autoencoders. The results show that CNN has the best performance, confirming the popularity of the method for image classification.

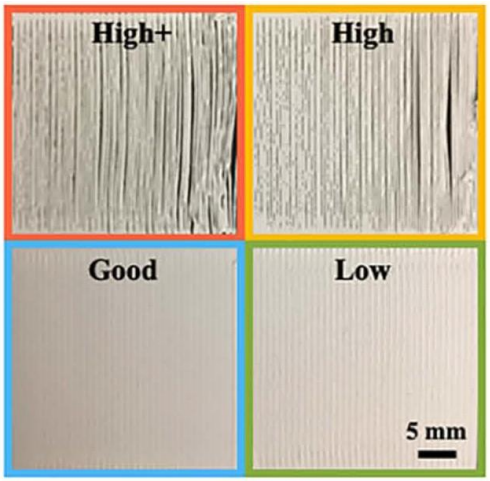

Figure 8. Images for four cases which represent the four conditions of nozzle height [53] (reproduced with permission).

Delli and Chang [135] used a Lulzbot Mini FDM printer to print parts from PLA and ABS. The printing process was monitored with a camera equipped with LED light to ensure constant illumination, which captured a top view of the object (Figure 10). Their strategy is to determine appropriate control points for the 3D printed part according to its geometry. Then, a Python script ensures that the camera captures images of the semi-finished part at each control point. Then, the captured image is fed to a support vector machine (SVM) model that identifies the quality of each part, i.e., whether it is ’good’ or ’defective.'

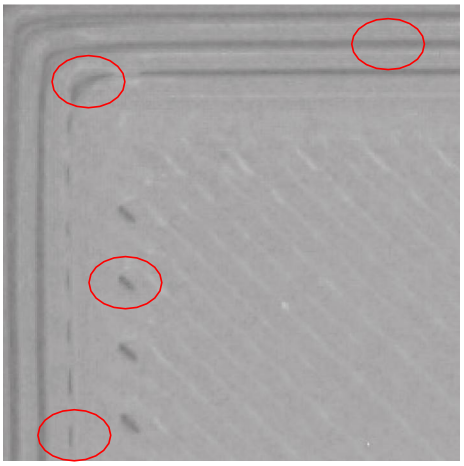

Figure 9. Examples of local defects due to incomplete bonding between adjacent strands. [139] (reproduced with permission).

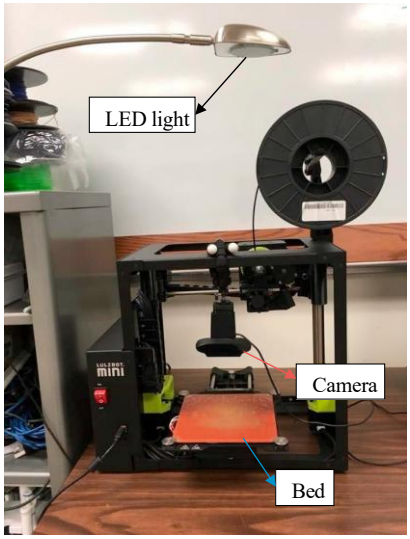

Figure 10. Experimental setup for top view defect detection system [135] (reproduced with permission)

This method is used for in-situ monitoring of a 3D printing process and can detect defects at completion or geometric or structural defects mid-process. However, the main problem with this method is that the printing process must be stopped in order for the camera to capture images of the unfinished part. In addition, the camera only takes pictures from above, so defects in the vertical plane cannot be detected.

In another study, Banadaki et al [140] used PLA as a printing material to monitor the performance of an FDM machine in real time. They captured images of each layer of the printed part using an image acquisition system. After normalizing the image intensity, 5000 images were selected for training and 100 images from the 5000 images were randomly selected as test data for each class. The sample images are acquired at a resolution of 600x600 pixels to ensure that they are large enough to detect small errors in the AM process. Then the training data is used to train a deep convolutional neural network model. The model is used to monitor surface and internal defects resulting from either overfilling or underfilling of the material (Figure 11) and classify the FDM process into five quality levels. It achieved an average accuracy of 94% and a specificity of 96%.

Hu et al [141] investigated FDM printing defects caused by the temperature field (Figure 12). They used a Makerbot Creator printer with ABS as the material, a VarioCAM®hr- HS thermal imaging system, and three test shapes: Cylinder, Cuboid and Drum with seven different test designs that have different sizes, and the printing temperature gradually decreased from 220°C to 180°C while printing these parts.

In their work, after pre-processing the input data, they used a multi-class classification model SVM in the first phase of the printing process to predict whether the part would be printed

normally. In the second phase, they used three binary SVM classifiers, each of which is used to distinguish between two of three abnormal states of 3D printing. The final result is determined by the max-min voting strategy. When testing the accuracy of the algorithms, the results showed that the model used in the first stage has an accuracy of 96.25%. The accuracy of the models used in the second stage was 87.50%, outperforming the other popular classification algorithms such as the K-Nearest Neighbors (KNN) algorithm (68.75%), the Bagging-based ensemble learning algorithm (76.25%), and the RUSBoost-based ensemble learning algorithm (48.75%).

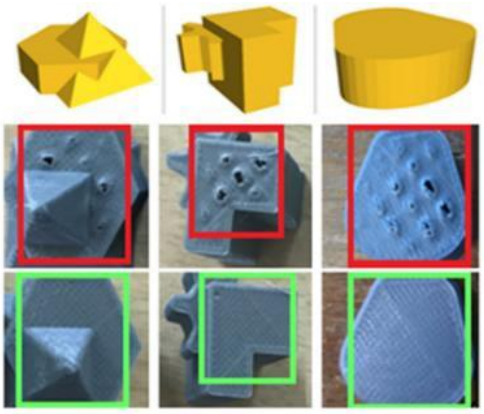

Figure 11. Examples of defects in the printed objects. [140] (reproduced with permission)

(a) (b) (c)

Figure 12. Examples of FDM defects: (a) Warping, (b) Insufficient filling, (c) Serious fault [141]

Wang et al [163] used a moving camera that uses an acquisition position planning algorithm to acquire prints at different angles. The main objective of this study is to use CNN to classify print defects such as blob, voids, thick line, crack, misalignment, or normal print condition. After pre-processing the acquired images, a dataset of 4900 images was used, which was divided into a test set and a validation set. The CNN model yielded an accuracy of 91.05% and a processing time per image of 0.487 seconds.

Wu et al [160] used a camera to capture images of the top view of each printed layer. They simulated a printing defect by designing 5 different infill defects. The data acquisition resulted in 156 images, which were divided into a training set and a test set. In this study, two ML

models were compared, Naïve Bayes with an accuracy of 85.26% and decision trees with an accuracy of 95.51%.

Jin et al [161] used a camera mounted on top of the extruder cap of a PRUSA i3 MK3 FDM printer to capture images of the printed part in plan view. They wanted to find out if the print quality was good, too little or too much extruded. For this purpose, 120000 images were collected for each category, 70% of which were randomly selected as training data and the rest as validation or test data. A CNN model was trained to classify the printing condition, which achieved 98% accuracy. Corrections could be made during printing by changing the flow rate of the filament.

Using two digital microscopes, Liu et al [162] investigated overfill and underfill defects. The microscopes were attached to the extrusion head and allowed continuous analysis of the film surface. A texture analysis method describing the layer surface with a gray-level coincidence matrix was used for feature extraction. Then, an algorithm called Textural analysis-based image diagnosis (TA-ID) was proposed to classify the layer surface into five categories. This algorithm achieved an accuracy of 85%. The material flow rate and the fan speed were adjusted using a proportional-integral-derivative (PID) controller based on the classification, with the aim of improving layer quality.

Narayanan et al [164] developed an automatic method to detect geometry defects. By examining the images of the geometry of the part printed by the FFF process, this method was able to classify good and defective polymer. Two different ML algorithms are used to detect geometry defects. First, principal component analysis (PCA) is used to reduce the dimensions of the images. Then, an SVM algorithm is used to categorize the product into good or poor, resulting in an overall accuracy of 98.2%. Next, a deep learning method based on CNN is investigated. This approach has a classification accuracy of 99.5%. In another study, a CNN algorithm was also used to detect incomplete printing failures with an average accuracy of 70% [165]. Table 6 summarizes the different approaches studied in this section.

2.6.3 Algorithms based on Sensor-generated data.

Various approaches to in-situ monitoring have been used. Printer failures can occur without warning, affecting the printing quality of the parts. So, Acoustic emission sensors have been used to monitor the state of the FDM printer. Some researchers chose to attach the sensor on top of the printing bed (Figure 13) and others to attach it to the extruder (Figure 14) of the 3D printer.

Table 6. In-situ monitoring using Visual Data

Ref	Strategy	ML technique	Accuracy
[135]	Completion failure & Geometrical defects	SVM	-
[54]	Warping	CNN	99.3%
[53]	Nozzle position	CNN	91%
[139]	Layer topography	CNN	-
[138]	Warping	YOLOv3	-
[140]	Printing defects	CNN	94%
[141]	Printing defects	SVM	87.5%
[160]	Printing defects	Decision trees	95.51%
[161]	Extrusion quality	CNN	98%
[162]	Overfill and underfill	TA-ID	85%
[163]	Printing defects	CNN	91.05%
[164]	Printing defects	CNN	99.5%
[165]	Incomplete printing failure	CNN	70%

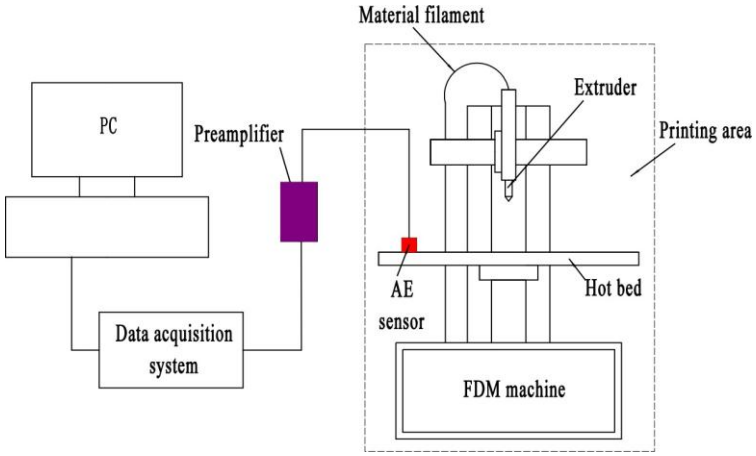

Figure 13. Experimental setup of the monitoring system with AE sensor attached to the printing platform [142]

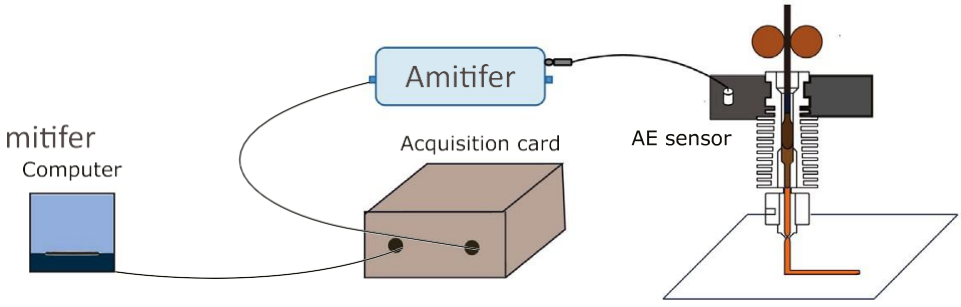

Figure 14. Experimental setup of the monitoring system with AE sensor attached to the extruder [144] (reproduced with permission).

In this context, Wu et al [142] wanted to detect failures in AM. It consists of three parts: an acoustic emission sensor (AE), a preamplifier, and a data acquisition system. They used the

HYREL3D Model E5 FDM printing machine and ABS as the printing material. They processed the AE signal, which was stored as a series of AE hits. Then, two features were selected for a K-Means cluster model: peak frequency, i.e., maximum magnitude, and amplitude, i.e., peak voltage of the signal in an acoustic sensor hit. As a result, four categories were identified.

In the same context, Liu et al [143] also used a sensor-based fault diagnosis system. They used Hyrel3d E5 engine with a MK -1 extruder, a desktop computer, and a AE sensor, a preamplifier, and a data acquisition card to detect the vibration signal from the extruder. They intentionally created different states of the extruder, namely normal (230°), semi- blocked (180°), blocked (130°), as well as the state of material, loading/unloading material, and running out of material. After collecting the data and extracting the features, the dimensions of the frequency and time domain features are reduced using the linear discriminant analysis (LDA) method to reduce the computational cost. After comparing the different dimensions of the feature space and combining normal extrusion and semi-blocking, the model gave 98% accuracy for normal extrusion and semi-blocking, 88% for blocking, 98% for lack of material, 98% for loading/unloading, and 96% accuracy for all states.

Li et al [144] used acoustic emissions to monitor the flow state of the polymer melt in the nozzle. Using PLA, three different types of products with different grades were printed in three different flow states: stable, unstable, and overspeed. An acoustic emission sensor placed near the nozzle was used to collect data on the flow state. Then, a AE Deep Time Convolutional Neural Network (AETCN) is introduced for AE signal processing. This method provides superior pattern recognition performance while significantly reducing pre-processing and computational costs, with an accuracy rate of 98%. The other methods used are Long Short-Term Memory (LSTM) and K-means, which did not achieve great accuracy rates of 86.73% and 69.50%, respectively.

Westphal et al. [145] used PLA+ as a material to distinguish between normal printing and five different defective printing conditions (old filament, new nozzle, higher temperature, higher speed, blocked nozzle). For this purpose, an environmental sensor was used to record humidity, temperature, air pressure and gas particles. The obtained recordings are sequenced and pre-classified for training the machine learning algorithms. The XceptionTime Deep Learning architecture achieved the best performance with 96.9% accuracy and 0.895 F1 score, followed by the Recurrent Neural Network (RNN) LSTM architecture. Table 7 summarizes the use of AE sensors for in-situ monitoring of the FDM process.

Table 7. Acoustic emission sensors used for in-situ monitoring of Material extrusion process

Ref	Sensor	Utility	Method	Frequency	Temperature
[144]	Softland Times rs-54a broadband	Monitor flow state of the polymer in the nozzle	Attached to the nozzle through vacuum grease	100-900 kHz	-20-130 °C
[146]	Mistragroup Model MD	Identification of normal and abnormal states of the machine	Attached to the side of the extruder with vacuum grease	100-900 kHz	-65-177 °C
[147]	Physical Acoustic Corp Model WSa	Identification of filament breakage	Attached to the housing (Back of the extruder)	100-1000 kHz	-65-175 °C
[142]	Mistagroup Model MD	Detecting 4 categories of AM failures	Attached on the upper surface of the print bed with vacuum grease	100-900 kHz	-
[143]	MISTRAS differential AE sensor	Predict the state of the extruder	Attached to the extruder with vacuum grease	100-900 kHz	-

Other researchers did not rely on AE sensors. Li et al [166] used vibration sensors and data-driven ML models to monitor the printing process of FDM. To detect the state of the filament in the FDM machine, the least squares support vector machine (LS-SVM) model was used, which achieved more than 90% accuracy. To ensure product quality during the FFF process, the back-propagation neural network (BPNN) algorithm was used to monitor and diagnose quality defects, warpage, and material stacking, which achieved more than 95% accuracy.

Miao et al. [177] used thermocouples, thermistors, and a IR sensor to study the effect of temperature on the printing process. They printed the same parts with different settings and measured the distortion in each case. They used a linear regression model to predict the distortion which outperformed the ANN and SVM models. Then they developed a cyber-physical system (CPS) to automatically adjust the temperature of the nuzzle.

Chhetri et al. [188] wanted to create a digital twin for an FDM system. To do this, they used numerous sensors (low-end acoustic, accelerometer, magnetic, and current). A clustering approach is used to create a fingerprint library based on the received signals, which effectively

represents the physical state or physical twin of the system. The digital twin is used to identify and locate anomalous physical emissions that may cause variations in quality. Using the random forest approach, the digital twin achieved an average accuracy of 83.09% in locating the fault.

2.6.4 Machine learning in finding process–structure–properties relationships.

Manual optimization of FDM process parameters costs time and money. These methods require the creation of numerous patterns and consume a significant amount of time and materials [148]. With the advent of machine learning, researchers have introduced its use to optimize process parameters.

Saad et al [149] wanted to minimize the surface roughness of an FDM printed part. For this purpose, they studied the layer thickness, printing speed, printing temperature, and outer shell speed as process parameters and the Tarantula Prusa 13 as printer. They used Response Surface Methodology (RSM) as the experimental design and selected 5 levels for each parameter, resulting in 46 samples. Then, an integrated artificial neural network (ANN) and the symbiotic organism search method (SOS) were used, resulting in a coefficient of determination R^2 of 0.96.

Hooda et al [150] chose to predict the build orientation (deposition angle) based on process time, material weight, length of material wire, and how the sample is built (Edge, upright, or flat). In the data collection phase, different sample specimens were used: Cube, Rectangle, Pyramid, Sphere, Cone and Wheel. Printing was done with seven different angles of deposition and three building orientations. Then, the data was cleaned, and features were selected using correlation-based feature selection (CFS). Seven different models were created. However, when the models were tested using the K-fold cross-validation technique, the Random Forest machine learning model had the best accuracy (94.57), correlation (0.88), R^2 (0.77), and Root Mean Square Error (RMSE) (0.45). The resulting model efficiently predicts the best deposition angle for each geometry.

Jiang et al [151] aimed to optimize the relationship between printing speed, film thickness, filament extrusion speed, and air gap to obtain the best possible connection between lines. A total of 400 experiments were conducted with an FDM 3D printer using PLA as the material. Based on the status of the connection between the printed lines, the data were divided into five groups (Figure 15). Then, the data were divided into a training set (280) and a test set (120), and a machine learning model consisting of six layers was used to predict the status of the link between the printed lines. This model yielded an accuracy of 83.33% in the test set.

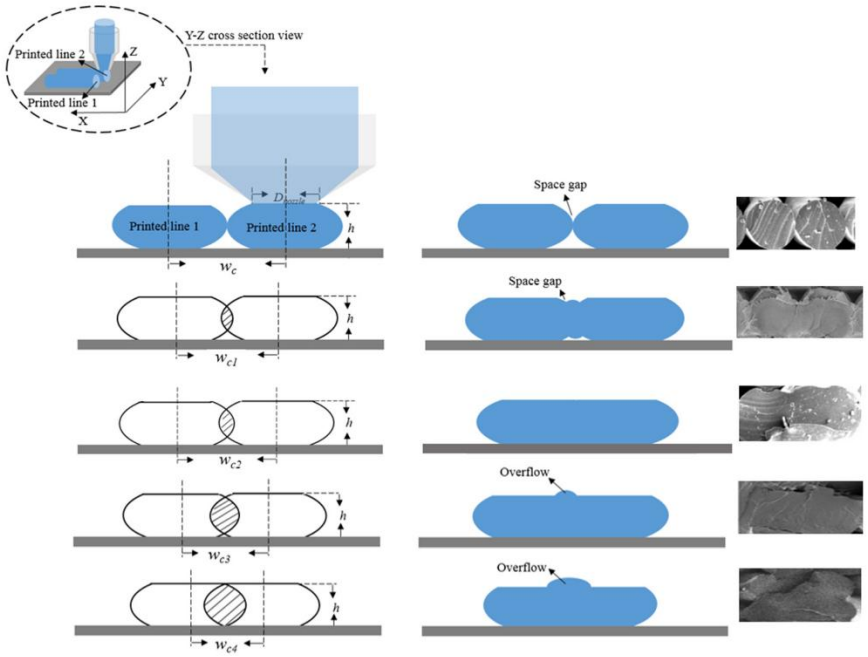

Figure 15. Illustration of connection status between paths [151]

Moradi et al [152] aimed to improve the 3D printing producibility of PLA. They investigated the thickness, toughness, and production time of dog bone samples. The parameters used are printing temperature, the infill density, and layer thickness. They used ANN and Artificial Neural Network - Genetic Algorithm (ANN-GA) to predict the studied properties. Compared with ANN, ANN-GA can improve the accuracy by 11.5%, 7.5% and 4.5% %, respectively, for part thickness, toughness and production cost. This article concluded that it is possible to reduce the production cost while maintaining the desired properties. It was also found that the most important parameter affecting the thickness of the printed part is the interaction between the layer thickness and the infill density.

In another study, Cai et al [153] investigated the dynamic strength of additively manufactured polypropylene-based composites. They used different materials, different layer thicknesses, and different printing temperatures. Split Hopkinson compression bars were used to investigate the dynamic strength (Figure 16).

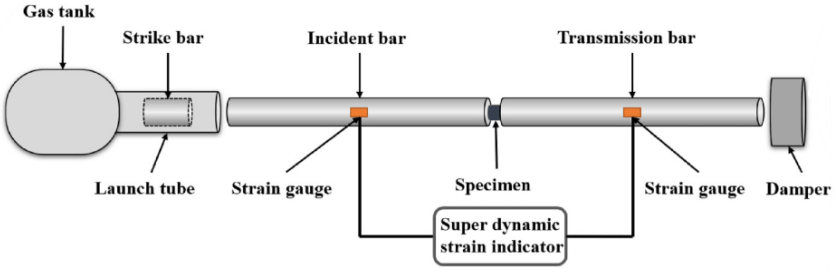

Figure 16. Setup of split Hopkinson pressure bars [153] (reproduced with permission).

They applied six machine learning techniques to understand the relationship between dynamic strength, material, and the printing parameters. These models took as input parameters the material, layer thickness, and the printing temperature, and as output the dynamic compressive strength. The evaluation of these models showed that the decision tree (DT) showed overfitting. KNN, on the other hand, showed underfitting. Therefore, these two algorithms are not recommended. ANN showed very high accuracy but very low computational efficiency. On the other hand, Support Vector Regression (SVR) showed fast prediction speed and high accuracy. However, it cannot interpret well how the prediction is made. XGBoost (XGB) and Random Forest (RF), on the other hand, can be interpreted and give meaning to the inputs. So, in summary, ANN was recommended when high prediction accuracy was a priority in practical applications. When high computational efficiency was required, SVR was recommended. When the importance of each input was required, the choice could be made between RF and XGB.

Zhang et al [154] took a different approach. They took into account the printing process. Namely, they used a IR sensor to measure the layer-by-layer thermal activity and an accelerometer to measure the vibration of the sample during printing (Figure 17).

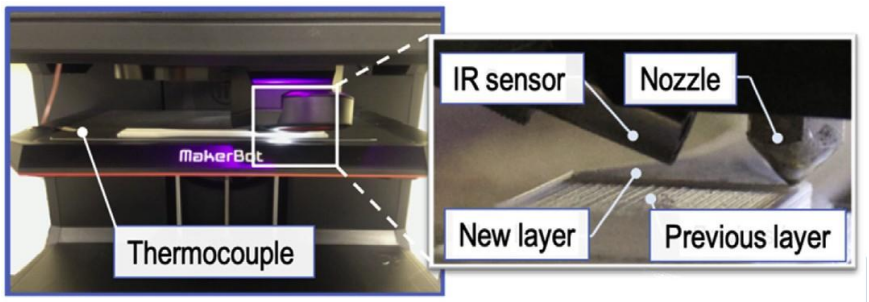

Figure 17. Setup of the accelerometer and the IR sensor [154] (reproduced with permission)

Sensor data are processed in LSTM cells and fused with process parameters and material properties to predict the tensile strength of manufactured parts. The study concludes that in-process sensing can significantly improve the prediction of tensile strength of parts in the FDM process. It reduces the RMSE of the prediction by 44% and improves the variation prediction by 22.6% (which is reflected in the R^2 value) compared to the model using only process parameters and material properties as network input. In addition, IR sensors and accelerometers were shown to provide the most important information for improving the prediction of tensile strength. The study also showed that the pressure temperature, pressure speed and layer thickness play an important role in predicting the tensile strength.

Charalampous et al [155] investigated the best printing conditions for tensile strength. They used layer thickness, printing speed, and printing temperature as process parameters. They

collected and preprocessed the data obtained after performing tensile tests on the printed parts. Then they developed and tested ML regression algorithms such as RF, SVR and KNN. Finally, they created an optimization tool to determine the best printing parameters to achieve the highest tensile strength. Their research showed that a medium printing speed, temperature, and low film thickness improved the tensile strength.

Zhang et al [156] introduced a new data-driven predictive modeling approach to understand the structure-property relationship of FDM-manufactured carbon fiber reinforced polymers (CCFRPs). The ensemble learning-based predictive modeling approach estimated the flexural modulus of CCFRP specimens with various design factors such as the number of layers, contours, and the infill pattern. The ensemble learning algorithm combined eight base learners: multiple linear regression, least absolute shrinkage and selection operator (Lasso), Multi-variate Adaptive Regression Splines (MARS), Generalized Additive Model (GAM), KNN, SVM, extra trees, and XGBoost. Their study found that the prediction model created can accurately predict the flexural strength of CCFRP specimens. The minimum RMSE was 9.87%, the minimum RE was 7.75%, and the maximum R^2 was 96.99%.

Li et al [159]. investigated the effects of printing parameters on surface roughness and used extruder temperature, layer thickness and the ratio between printing speed and extrusion rate as input data. Following feature extraction, a random forest method is used to predict surface roughness after comparing it with six other machine learning methods.

Charalampous et al [157] predicted the deviation between CAD and the actual printed parts using regression-based machine learning algorithms: KNN, SVR, and RF. During the process, they studied the parameters of layer thickness, printing speed, and printing temperature. The model used was a 25 mm x 25 mm x 25 mm cube printed with PLA. The printed parts were measured with a digital caliper and compared with the CAD model. The data set was then created (Figure 18). The test results showed that the KNN regressor performed best in the X and Y directions, while the RF regressor performed best in the Z direction. The study also revealed strategies to adjust the dimensions of the 3D model to improve the accuracy of the printing process and compensate for the shape deviation.

Yanamandra et al [158] investigated the reverse engineering of a high-quality fiber reinforced composite material. They proposed a reverse engineering method based on μCT scans and SEM images of the printed model using a glass fiber reinforced ABS filament as the material (Figure 19). Using RNN with LSTM architecture, they identified the fiber orientation in each layer. The model achieved good accuracy with a mean square error loss of 0.04, which

corresponds to an error of 0.5 degrees. The original models were replicated with a difference of only 0.33% in dimensional accuracy

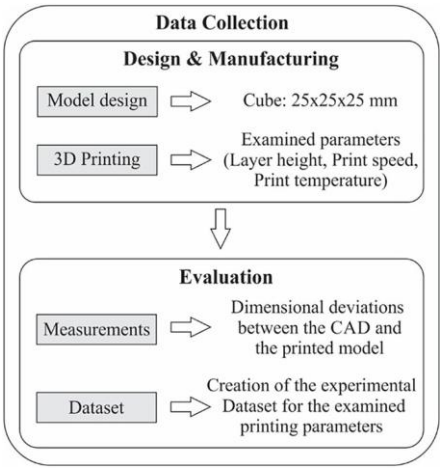

Figure 18. Data acquisition approach [157]

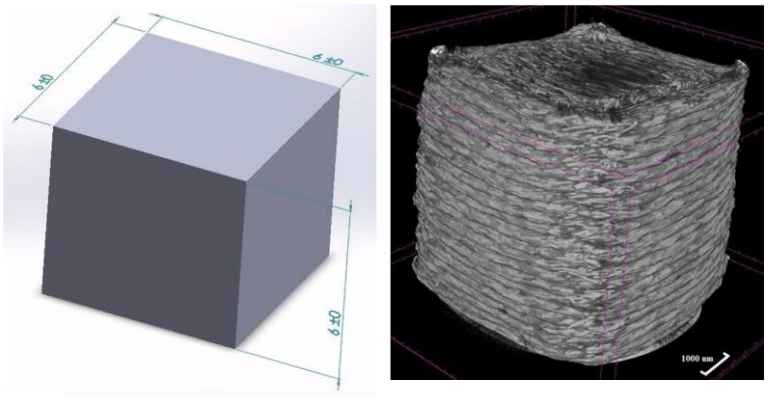

(a) (b)

Figure 19. (a) CAD model with dimensions in mm, (b) μCT scan of the 3D printed part [158] (Reproduced with permission).

2.7 Conclusion

In the industrial sector, additive manufacturing is considered a revolution. It involves manufacturing physical objects by adding material layer by layer based on a 3D model. It offers several advantages over conventional production methods. It can produce complicated components with great accuracy, in a short time and using a wide range of materials. It also significantly reduces waste and makes it easy to manufacture components, even remotely and without high levels of expertise. The comparison of 3D printing technologies has confirmed the attractiveness of material extrusion in research and industry. Namely, it has a wide range of printing materials, is economical, scalable, and has great market availability. Material extrusion offers tremendous potential for the development of new technologies. Although research in this field is progressing rapidly, the relationship between process parameters and part properties still needs to be improved. To better understand this relationship, the influence

of process parameters on printed part properties was studied. According to the study, the most influential factors on mechanical properties are layer thickness, extrusion temperature, infill density, infill pattern, build orientation and raster angle. On the other hand, infill density, infill pattern, layer thickness and printing speed are the most influential parameters on build time. Similarly, the most influential parameters for surface roughness are infill density, bed temperature, layer thickness and build orientation. Dimensional accuracy is also influenced by infill density, printing speed, layer thickness and build orientation. To optimize the relationship between process parameters and part properties, some researchers have used machine learning techniques. Researchers have used many methods to optimize the interactions between process, structure, and properties, in which the optimal parameters are determined before printing. Some projected the optimal parameters to achieve the best bond between the layers and the applied mark, while others predicted the properties of the parts, such as tensile strength and deviation, and then optimized the process parameters. Still others chose to predict process parameters based on component properties and other process factors. This was done using various machine learning methods such as ANN, LSTM, and SVM, as well as optimization strategies such as Symbiotic Organism Search. For in situ monitoring, some studies used visual data while others used other sensor-generated data. For visual data, the works used a camera or thermal imager. The camera is placed either vertically or horizontally. In the vertical direction, it takes a top view of the printed article to detect problems such as insufficient filling or deformation. Alternatively, it can be positioned horizontally to monitor print quality by checking the position of the nozzle or taking a side view of the article to detect problems such as delamination or deformation. Others have used vertical thermal imaging sensors to detect abnormal printing conditions. In these methods, researchers have used machine learning techniques such as SVM, CNN and YOLOv3 and achieved high accuracy. Other work has proposed using acoustic emission sensors to monitor machine status. The sensors were placed either on the print bed or on the back or side of the extruder using vacuum grease. Machine learning methods such as K-means clustering, density-based clustering approach CFSFDP, AETCN deep neural network framework, XceptionTime deep neural network architecture, RNN architecture, and LSTM architecture were employed by researchers using AE.

Training a machine learning model is sometimes computationally intensive and therefore requires a lot of execution time, especially when large amounts of data are involved. Moreover, in on-site monitoring, label prediction using machine learning should be almost instantaneous, so that the majority of defects can be detected, corrective actions can be taken, and the construction rate is not significantly affected. Therefore, future work should consider the

computational cost of prediction. In addition, the algorithms of ML are dependent on the data provided. Consequently, careful selection of the sensors used to collect the data is required, as they must be capable of detecting the desired features. In addition, the sensors used must be able to withstand the printing environment, such as high temperatures or vibrations. In addition, to obtain a larger data set, data sharing can be a solution, as researchers often use different new materials and methods and can benefit from each other.

2.8 Acknowledgement

The authors acknowledge the funding provided by the Natural Sciences and Engineering Research Council (NSERC) of Canada and Canada Research Chair Program.

2.9 Declarations

The authors certify that they have NO affiliations with or involvement in any organization or entity with any financial interest or non-financial interest in the subject matter or materials discussed in this manuscript.

2.10 References

[1] Prajapati H, Ravoori D, Woods RL, et al (2018) Measurement of anisotropic thermal conductivity and inter-layer thermal contact resistance in polymer fused deposition modeling (FDM). Additive Manufacturing 21(November 2017):84–90.

[2] Altıparmak SC, Yardley VA, Shi Z, et al (2021) Challenges in additive manufacturing of high-strength aluminium alloys and current developments in hybrid additive manufacturing. International Journal of Lightweight Materials and Manufacture 4(2):246–261.

[3] Abbot DW, Kallon DV, Anghel C, et al (2019) Finite element analysis of 3D printed model via compression tests. Procedia Manufacturing 35(Smpm):164–173.

[4] Abdulhameed O, Al-Ahmari A, Ameen W, et al (2019) Additive manufacturing: Challenges, trends, and applications. Advances in Mechanical Engineering 11(2):1–27.

[5] Zivanovic ST, Popovic MD, Vorkapic NM, et al (2020) An overview of rapid prototyping technologies using subtractive, additive and formative processes. FME Transactions 48(1):246–253.

[6] Fanni FA, Cherchi G, Muntoni A, et al (2018) Fabrication oriented shape decomposition using polycube mapping. Computers and Graphics (Pergamon) 77:183–193.

[7] Mercado Rivera FJ, Rojas Arciniegas AJ (2020) Additive manufacturing methods: techniques, materials, and closed-loop control applications. International Journal of Advanced Manufacturing Technology 109(1-2):17–31.

[8] De Camargo IL, Erbereli R, Taylor H, et al (2021) 3Y-TZP DLP additive manufacturing: Solvent-free slurry development and characterization. Materials Research 24(2):2–9.
[9] Jiang J, Xu X, Stringer J (2018) Support structures for additive manufacturing: A review. Journal of Manufacturing and Materials Processing 2(4).
[10] Weger D, Lowke D, Gehlen C, et al (2018) Additive manufacturing of concrete elements using selective cement paste intrusion–effect of layer orientation on strength and durability. Proceedings of RILEM 1st International Conference on Concrete and Digital Fabrication (September):3–5.
[11] Ngo TD, Kashani A, Imbalzano G, et al (2018a) Additive manufacturing (3D printing): A review of materials, methods, applications and challenges. Composites Part B: Engineering 143(December 2017):172–196.
[12] Matos F, Godina R, Jacinto C, et al (2019) Additive manufacturing: Exploring the social changes and impacts. Sustainability (Switzerland) 11(14).
[13] Matos F, Jacinto C (2019) Additive manufacturing technology: mapping social impacts. Journal of Manufacturing Technology Management 30(1):70–97.
[14] Caviggioli F, Ughetto E (2019) A bibliometric analysis of the research dealing with the impact of additive manufacturing on industry, business and society. International Journal of Production Economics 208(December 2018):254–268.
[15] Tagliaferri V, Trovalusci F, Guarino S, et al (2019) Environmental and economic analysis of FDM, SLS and MJF additive manufacturing technologies. Materials 12(24).
[16] Prakash KS, Nancharaih T, Rao VV (2018) Additive Manufacturing Techniques in Manufacturing -An Overview. Materials Today: Proceedings 5(2):3873–3882.
[17] Sinha, S., & Meisel, N. A. (2018). Influence of process interruption on mechanical properties of material extrusion parts. Rapid Prototyping Journal, 24(5), 821-827.
[18] Chacon JM, Caminero MA, Nunez PJ, et al (2019) Additive manufacturing of continuous fibre reinforced thermoplastic composites using fused deposition modelling: Effect of process parameters on mechanical properties. Composites Science and Technology 181(June):107,688.
[19] Owens, J. T., Das, A., & Bortner, M. J. (2022). Accelerating heat transfer modeling in material extrusion additive manufacturing: From desktop to big area. Additive Manufacturing, 55, 102853.
[20] Kuschmitz, S., Schirp, A., Busse, J., Watschke, H., Schirp, C., & Vietor, T. (2021). Development and processing of continuous flax and carbon fiber-reinforced thermoplastic composites by a modified material extrusion process. Materials, 14(9), 2332.

[21] Bandyopadhyay A, Heer B (2018) Additive manufacturing of multi-material structures. Materials Science and Engineering R: Reports 129(March):1–16.

[22] Alhumayani H, Gomaa M, Soebarto V, et al (2020) Environmental assessment of large-scale 3D printing in construction: A comparative study between cob and concrete. Journal of Cleaner Production 270:122,463.

[23] Khosravani MR, Reinicke T (2020) On the environmental impacts of 3D printing technology. Applied Materials Today 20:100,689.

[24] Malik A, Haq MIU, Raina A, et al (2022) 3d printing towards implementing industry 4.0: sustainability aspects, barriers and challenges. Industrial Robot: the international journal of robotics research and application.

[25] Kalender M, Kilic SE, Ersoy S, et al (2019) Additive manufacturing and 3D printer technology in aerospace industry. Proceedings of 9th International Conference on Recent Advances in Space Technologies, RAST 2019 pp 689– 695.

[26] Khosravani MR, Berto F, Ayatollahi MR, et al (2022) Characterization of 3Dprinted PLA parts with different raster orientations and printing speeds. Scientific Reports 12(1):1–9.

[27] Khorsandi D, Fahimipour A, Abasian P, et al (2021) {3D} and {4D} printing in dentistry and maxillofacial surgery: Printing techniques, materials, and applications. Acta Biomater 122:26–49.

[28] Bayraktar b, Senturk E (2022) Machinability of 3D Printed Materials. In: Innovations in Additive Manufacturing. Springer, p 297–319.

[29] Galante R, Figueiredo-Pina CG, Serro AP (2019a) Additive manufacturing of ceramics for dental applications: A review. Dental Materials 35(6):825– 846.

[30] Kessler A, Hickel R, Reymus M (2020) {3D} printing in dentistry-state of the art. Oper Dent 45(1):30–40.

[31] Luo H, Zhou X, Guo R, et al (2020) 3D printing of anisotropic polymer nanocomposites with aligned BaTiO 3 nanowires for enhanced energy density. Materials Advances 1(1):14–19.

[32] Bhayana M, Singh J, Singh J, et al (2021) Analysis of performance enhancement of composite specimen of wood and PLA prepared through the computer controlled FDM technique. In: 2021 3rd International Conference on Advances in Computing, Communication Control and Networking (ICAC3N). IEEE.

[33] Wang Z, Gao W, Zhang Q, et al (2018) 3D-printed graphene/polydimethylsiloxane composites for stretchable and strain-insensitive temperature sensors. ACS applied materials & interfaces 11(1):1344–1352.

[34] Elbadawi M, McCoubrey LE, Gavins FK, et al (2021) Harnessing artificial intelligence for the next generation of 3d printed medicines. Advanced Drug Delivery Reviews 175:113,805.

[35] Irfan Ul Haq M, Khuroo S, Raina A, et al (2020) 3D printing for development of medical equipment amidst coronavirus (COVID-19) pandemic—review and advancements. Res Biomed Eng.

[36] Attaran M, Others (2020) 3D printing role in filling the critical gap in the medical supply chain during COVID-19 pandemic. American Journal of Industrial and Business Management 10(05):988.

[37] Mooraj S, Qi Z, Zhu C, et al (2021) 3D printing of metal-based materials for renewable energy applications. Nano Research 14(7):2105–2132.

[38] Ramazani H, Kami A (2022) Metal FDM, a new extrusion-based additive manufacturing technology for manufacturing of metallic parts: a review. Progress in Additive Manufacturing pp 1–18.

[39] Najmon JC, Raeisi S, Tovar A (2019) Review of additive manufacturing technologies and applications in the aerospace industry. Additive manufacturing for the aerospace industry pp 7–31.

[40] Mohd Yusuf S, Cutler S, Gao N (2019) The impact of metal additive manufacturing on the aerospace industry. Metals 9(12):1286.

[41] Altiparmak SC, Xiao B (2021) A market assessment of additive manufacturing potential for the aerospace industry. Journal of Manufacturing Processes 68:728–738.

[42] Guzzi EA, Tibbitt MW (2020) Additive manufacturing of precision biomaterials. Adv Mater 32(13):e1901,994.

[43] Veeman D, Sai MS, Sureshkumar P, et al (2021) Additive manufacturing of biopolymers for tissue engineering and regenerative medicine: An overview, potential applications, advancements, and trends. Int J Polym Sci 2021:1–20.

[44] ISO/ASTM 52900:2021(E) (2021) Additive manufacturing — General principles — Fundamentals and vocabulary. Standard, International Organization for Standardization.

[45] Zocca A, Colombo P, Gomes CM, et al (2015) Additive manufacturing of ceramics: Issues, potentialities, and opportunities. J Am Ceram Soc 98(7):1983–2001.

[46] Yuan S, Shen F, Chua CK, et al (2019) Polymeric composites for powder-based additive manufacturing: Materials and applications. Progress in Polymer Science 91:141–168.

[47] Bourell D, Kruth JP, Leu M, et al (2017) Materials for additive manufacturing. CIRP annals 66(2):659–681.

[48] Aboulkhair NT, Simonelli M, Parry L, et al (2019) 3D printing of Aluminium alloys: Additive Manufacturing of Aluminium alloys using selective laser melting. Progress in materials science 106:100,578.

[49] Pinomaa T, Yashchuk I, Lindroos M, et al (2019) Process-structure-properties performance modeling for selective laser melting. Metals 9(11):1138.

[50] Goh GD, Sing SL, Yeong WY (2021) A review on machine learning in 3D printing: applications, potential, and challenges. Artificial Intelligence Review 54(1):63–94.

[51] Kantaros A, Piromalis D (2021) Employing a low-cost desktop 3D printer: Challenges, and how to overcome them by tuning key process parameters. International Journal of Mechanics and Applications 10(1):11–19.

[52] Liu, C., Tong, J., Ma, J., Wang, D., Xu, F., Liu, Y., ... & Lao, C. (2019). Low-temperature deposition manufacturing: a versatile material extrusion-based 3D printing technology for fabricating hierarchically porous materials. Journal of Nanomaterials, 2019.

[53] Jin Z, Zhang Z, Gu GX (2020) Automated real-time detection and prediction of interlayer imperfections in additive manufacturing processes using artificial intelligence. Advanced Intelligent Systems 2(1):1900,13.

[54] Saluja A, Xie J, Fayazbakhsh K (2020) A closed-loop in-process warping detection system for fused filament fabrication using convolutional neural networks. Journal of Manufacturing Processes 58:407–415.

[55] Mohamed OA, Masood SH, Bhowmik JL (2015) Optimization of fused deposition modeling process parameters: a review of current research and future prospects. Advances in manufacturing 3(1):42–53.

[56] Shaqour B, Abuabiah M, Abdel-Fattah S, et al (2021) Gaining a better understanding of the extrusion process in fused filament fabrication 3D printing: a review. International Journal of Advanced Manufacturing Technology 114(5-6):1279–1291.

[57] Calignano F, Galati M, Iuliano L, et al (2019) Design of additively manufactured structures for biomedical applications: A review of the additive manufacturing processes applied to the biomedical sector. J Healthc Eng 2019:9748,212.

[58] Radadiya VA, Gandhi AH (2022) A Study of Tensile Characteristics for Glass and Carbon Fiber Along with Sandwiched Reinforced ABS Composites, Journal of The Institution of Engineers (India): Series C 103: 1049–1057.

[59] Rust B, Tsaponina O, Maniruzzaman M (2019) Recent innovations in additive manufacturing across industries: 3D printed products and FDA's perspectives. 3D and 4D

Printing in Biomedical Applications: Process Engineering and Additive Manufacturing pp 443–462.

[60] Choi NY, Advanced Materials Engineering, Dong-Eui University, Shin BC, et al (2020) A comparative study of the linear-elastic and hyperelastic models for degradation of PLA prepared using fused filament fabrication. J Korean Soc Manuf Process Eng 19(3):1–7.

[61] Taufik M, Others (2021) Fused filament fabrication (FFF) based 3D printer and its design: a review. Advanced Manufacturing Systems and Innovative Product Design pp 497–505.

[62] Sieminski P (2021) Introduction to fused deposition modeling. In: Additive Manufacturing. Elsevier, p 217–275.

[63] Buj-Corral I, Tejo-Otero A, Fenollosa-Art´es F (2022) Evolution of additive manufacturing processes: From the background to hybrid printers. In: Materials Forming, Machining and Tribology. Springer International Publishing, Cham, p 95–110.

[64] Liu Z, Lei Q, Xing S (2019) Mechanical characteristics of wood, ceramic, metal and carbon fiber-based PLA composites fabricated by FDM. Journal of Materials Research and Technology 8(5):3741–3751.

[65] Liu F, Vyas C, Poologasundarampillai G, et al (2018a) Structural evolution of PCL during melt extrusion 3D printing. Macromolecular Materials and Engineering 303(2):1700,494.

[66] Fitzharris ER, Watt I, Rosen DW, et al (2018) Interlayer bonding improvement of material extrusion parts with polyphenylene sulfide using the Taguchi method. Additive Manufacturing 24(October):287–297.

[67] Zhou Z, Salaoru I, Morris P, et al (2018) Additive manufacturing of heatsensitive polymer melt using a pellet-fed material extrusion. Additive Manufacturing 24:552–559.

[68] Nielsen AV, Beauchamp MJ, Nordin GP, et al (2020) 3d printed microfluidics. Annual review of analytical chemistry (Palo Alto, Calif) 13(1):45.

[69] Gonzalez-Gutierrez J, Arbeiter F, Schlauf T, et al (2019) Tensile properties of sintered 17-4ph stainless steel fabricated by material extrusion additive manufacturing. Materials Letters 248:165–168.

[70] Rane K, Strano M (2019) A comprehensive review of extrusion-based additive manufacturing processes for rapid production of metallic and ceramic parts. Advances in Manufacturing 7(2):155–173.

[71] Gonzalez-Gutierrez J, Cano S, Schuschnigg S, et al (2018) Additive manufacturing of metallic and ceramic components by the material extrusion of highly-filled polymers: A review and future perspectives. Materials (Basel) 11(5).

[72] Hmeidat NS, Pack RC, Talley SJ, et al (2020) Mechanical anisotropy in polymer composites produced by material extrusion additive manufacturing. Addit Manuf 34(101385):101,385.

[73] Somireddy M, Czekanski A (2020) Anisotropic material behavior of 3D printed composite structures – Material extrusion additive manufacturing. Materials and Design 195:108,953.

[74] Zhang X, Chen L, Kowalski C, et al (2019c) Nozzle flow behavior of aluminum/polycarbonate composites in the material extrusion printing process. J Appl Polym Sci 136(12):47,252.

[75] Jiang T, Munguia-Lopez JG, Flores-Torres S, et al (2019) Extrusion bioprinting of soft materials: An emerging technique for biological model fabrication Appl Phys Rev 6(1):11,310.

[76] Ren L, Song Z, Liu H, et al (2018) 3D printing of materials with spatially non-linearly varying properties. Materials & Design 156:470–479.

[77] Ramesh S, Harrysson OLA, Rao PK, et al (2021) Extrusion bioprinting: Recent progress, challenges, and future opportunities. Bioprinting 21:e00,116.

[78] Yang TC, Yeh CH (2020) Morphology and mechanical properties of 3D printed wood fiber/polylactic acid composite parts using fused deposition modeling (FDM): the effects of printing speed. Polymers 12(6):1334.

[79] Kananathan J, Samykano M, Kadirgama K, et al (2022) Comprehensive investigation and prediction model for mechanical properties of coconut wood–polylactic acid composites filaments for FDM 3D printing. European Journal of Wood and Wood Products 80(1):75–100.

[80] Lamm ME, Wang L, Kishore V, et al (2020) Material extrusion additive manufacturing of wood and lignocellulosic filled composites. Polymers 12(9):2115.

[81] Elkaseer A, Schneider S, Scholz SG (2020) Experiment-based process modeling and optimization for high-quality and resource-efficient FFF 3D printing. Applied Sciences 10(8):2899.

[82] Mackay ME (2018) The importance of rheological behavior in the additive manufacturing technique material extrusion. Journal of Rheology 62(6):1549–1561.

[83] Hsiang Loh G, Pei E, Gonzalez-Gutierrez J, et al (2020) An overview of material extrusion troubleshooting. Applied Sciences 10(14):4776.

[84] Zhang X, Fan W, Liu T (2020a) Fused deposition modeling 3D printing of polyamide-based composites and its applications. Composites Communications 21:100,413.

[85] Tofail SA, Koumoulos EP, Bandyopadhyay A, et al (2018a) Additive manufacturing: scientific and technological challenges, market uptake and opportunities. Materials Today 21(1):22–37.

[86] Daminabo SC, Goel S, Grammatikos SA, et al (2020) Fused deposition modeling-based additive manufacturing (3D printing): techniques for polymer material systems. Materials today chemistry 16:100,248.
[87] Palmara G, Frascella F, Roppolo I, et al (2021) Functional {3D} printing: Approaches and bioapplications. Biosens Bioelectron 175(112849):112,849.
[88] Saleh Alghamdi S, John S, Roy Choudhury N, et al (2021) Additive manufacturing of polymer materials: Progress, promise and challenges. Polymers 13(5):753.
[89] Sheoran AJ, Kumar H (2020) Fused Deposition modeling process parameters optimization and effect on mechanical properties and part quality: Review and reflection on present research. Materials Today: Proceedings 21:1659– 1672.
[90] Yadav P, Sahai A, Sharma RS (2021) Strength and surface characteristics of FDM-based 3D printed PLA parts for multiple infill design patterns. Journal of The Institution of Engineers (India): Series C 102(1):197–207.
[91] Goh GD, Yap YL, Tan HKJ, et al (2020) Process–structure–properties in polymer additive manufacturing via material extrusion: A review. Critical Reviews in Solid State and Materials Sciences 45(2):113–133.
[92] Lalegani Dezaki M, Mohd Ariffin MKA (2020) The effects of combined infill patterns on mechanical properties in fdm process. Polymers 12(12):2792.
[93] Al Khawaja H, Alabdouli H, Alqaydi H, et al (2020) Investigating the mechanical properties of 3D printed components. In: 2020 Advances in Science and Engineering Technology International Conferences (ASET), IEEE, pp 1–7.
[94] Dizon JRC, Espera Jr AH, Chen Q, et al (2018) Mechanical characterization of 3D-printed polymers. Additive manufacturing 20:44–67.
[95] Cwik la G, Grabowik C, Kalinowski K, et al (2017) The influence of printing parameters on selected mechanical properties of FDM/FFF 3D-printed parts. In: IOP conference series: materials science and engineering, IOP Publishing, p 12033.
[96] Galeja M, Hejna A, Kosmela P, et al (2020) Static and dynamic mechanical properties of 3D printed ABS as a function of raster angle. Materials 13(2):297.
[97] Wang S, Ma Y, Deng Z, et al (2020) Effects of fused deposition modeling process parameters on tensile, dynamic mechanical properties of 3D printed polylactic acid materials. Polymer testing 86:106,483.
[98] Gebisa AW, Lemu HG (2019) Influence of 3D printing FDM process parameters on tensile property of ULTEM 9085. Procedia Manufacturing 30:331–338.

[99] Srinivasan R, Prathap P, Raj A, et al (2020) Influence of fused deposition modeling process parameters on the mechanical properties of PETG parts. Materials Today: Proceedings 27:1877–1883.

[100] Othman FM, Abbas T, Ali HB (2018) Influence of process parameters on mechanical properties and printing time of FDM PLA printed parts using design of experiment. J Eng Res pp 2248–9622.

[101] Rodriguez-Panes A, Claver J, Camacho AM (2018) The influence of manufacturing parameters on the mechanical behaviour of PLA and ABS pieces manufactured by FDM: A comparative analysis. Materials 11(8):1333.

[102] Ouballouch A, Ettaqi S, Bouayad A, et al (2019) Evaluation of dimensional accuracy and mechanical behavior of 3D printed reinforced polyamide parts. Procedia Structural Integrity 19:433–441.

[103] Huynh LPT, Nguyen HA, Nguyen HQ, et al (2019) Effect of process parameters on mechanical strength of fabricated parts using the fused deposition modelling method.

[104] Chokshi H, Shah DB, Patel KM, et al (2022) Experimental investigations of process parameters on mechanical properties for PLA during processing in FDM. Advances in Materials and Processing Technologies 8(sup2):696–709.

[105] Enemuoh EU, Duginski S, Feyen C, Menta VG (2021) Effect of process parameters on energy consumption, physical, and mechanical properties of fused deposition modeling, Polymers 13: 2406.

[106] Pawar S, Dolas D (2022) Effect of process parameters on flexural strength and surface roughness in fused deposition modeling of PC-ABS material. Journal of Micromanufacturing 5(2):164–170.

[107] Gebisa AW, Lemu HG (2018) Investigating effects of fused-deposition modeling (FDM) processing parameters on flexural properties of ULTEM 9085 using designed experiment. Materials 11(4):500.

[108] Boesch E, Siadat A, Rivette M, et al (2019) Impact of fused deposition modeling (FDM) process parameters on strength of built parts using Taguchi's design of experiments. The international journal of Advanced Manufacturing technology 101(5):1215–1226.

[109] Saad MS, Nor AM, Baharudin ME, et al (2019) Optimization of surface roughness in FDM 3D printer using response surface methodology, particle swarm optimization, and symbiotic organism search algorithms. The International Journal of Advanced Manufacturing Technology 105(12):5121–5137.

[110] Alsoufi MS, Elsayed AE, Others (2018) Surface roughness quality and dimensional accuracy—a comprehensive analysis of 100% infill printed parts fabricated by a personal/desktop cost-effective FDM 3D printer. Materials Sciences and Applications 9(01):11.

[111] Manziuc MM, Gasparik C, Burde AV, et al (2019) Effect of glazing on translucency, color, and surface roughness of monolithic zirconia materials. Journal of Esthetic and Restorative Dentistry 31(5):478–485.

[112] Akhouri D, Banerjee D, Mishra SB (2020) A review report on the plating process of fused deposition modelling (FDM) built parts. Materials Today: Proceedings 26:2140–2142.

[113] Kozior T, Mamun A, Trabelsi M, et al (2020) Quality of the Surface Texture and Mechanical Properties of FDM Printed Samples after Thermal and Chemical Treatment. Strojniski Vestnik/Journal of Mechanical Engineering 66(2).

[114] Colpani A, Fiorentino A, Ceretti E (2019) Characterization of chemical surface finishing with cold acetone vapours on ABS parts fabricated by FDM. Production Engineering 13(3):437–447.

[115] Patil P, Singh D, Raykar SJ, et al (2021) Multi-objective optimization of process parameters of Fused Deposition Modeling (FDM) for printing Polylactic Acid (PLA) polymer components. Materials Today: Proceedings 45:4880–4885.

[116] Venkatraman R, Raghuraman S, Others (2021) Experimental analysis on density, micro-hardness, surface roughness and processing time of Acrylonitrile Butadiene Styrene (ABS) through Fused Deposition Modeling (FDM) using Box Behnken Design (BBD). Materials Today Communications 27:102,353.

[117] Tura AD, Mamo HB, Gemechu WF (2021) Mathematical modeling and parametric optimization of surface roughness for evaluating the effects of fused deposition modeling process parameters on ABS material. International Journal of Advanced Engineering Research and Science 8(5):49–57.

[118] Vinoth Babu N, Venkateshwaran N, Rajini N, et al (2022) Influence of slicing parameters on surface quality and mechanical properties of 3D-printed CF/PLA composites fabricated by FDM technique. Materials Technology 37(9):1008–1025.

[119] Yang L, Li S, Li Y, et al (2019) Experimental investigations for optimizing the extrusion parameters on FDM PLA printed parts. Journal of Materials Engineering and Performance 28(1):169–182.

[120] Sai T, Pathak VK, Srivastava AK (2020) Modeling and optimization of fused deposition modeling (FDM) process through printing PLA implants using adaptive neuro-fuzzy inference

system (ANFIS) model and whale optimization algorithm. Journal of the Brazilian Society of Mechanical Sciences and Engineering 42(12):1–19.

[121] Le L, Rabsatt MA, Eisazadeh H, et al (2022) Reducing print time while minimizing loss in mechanical properties in consumer FDM parts. International Journal of Lightweight Materials and Manufacture 5(2):197–212.

[122] Camposeco-Negrete C (2020) Optimization of FDM parameters for improving part quality, productivity and sustainability of the process using Taguchi methodology and desirability approach. Progress in Additive Manufacturing 5(1):59–65.

[123] Dakshinamurthy D, Gupta S (2018) A study on the influence of process parameters on the viscoelastic properties of ABS components manufactured by FDM process. Journal of The Institution of Engineers (India): Series C 99(2):133–138.

[124] Bakir AA, Atik R, Ozerinc S (2021) Effect of fused deposition modeling ¨ process parameters on the mechanical properties of recycled polyethylene terephthalate parts. Journal of Applied Polymer Science 138(3):49,709.

[125] Mohamed OA, Masood SH, Bhowmik JL (2016) Mathematical modeling and FDM process parameters optimization using response surface methodology based on Q-optimal design. Applied Mathematical Modelling 40(23- 24):10,052–10,073.

[126] Aslani KE, Kitsakis K, Kechagias JD, et al (2020) On the application of grey Taguchi method for benchmarking the dimensional accuracy of the PLA fused filament fabrication process. SN Applied Sciences 2(6):1–11.

[127] Minetola P, Galati M (2018) A challenge for enhancing the dimensional accuracy of a low-cost 3D printer by means of self-replicated parts. Additive Manufacturing 22:256–264.

[128] Kechagias J, Chaidas D, Vidakis N, et al (2022) Key parameters controlling surface quality and dimensional accuracy: A critical review of FFF process. Materials and Manufacturing Processes pp 1–22.

[129] Mukhtarkhanov M, Perveen A, Talamona D (2020) Application of stereolithography based 3D printing technology in investment casting. Micromachines 11(10):946.

[130] Galetto M, Verna E, Genta G (2021) Effect of process parameters on parts quality and process efficiency of fused deposition modeling. Computers & Industrial Engineering 156:107,238.

[131] Milovanovic A, Milosevic M, Mladenovic G, et al (2018) Experimental dimensional accuracy analysis of reformer prototype model produced by FDM and SLA 3D printing technology. In: Experimental and numerical investigations in materials science and engineering. Springer, p 84–95.

[132] Gendviliene I, Simoliunas E, Rekstyte S, et al (2020) Assessment of the morphology and dimensional accuracy of 3D printed PLA and PLA/HAp scaffolds. Journal of the mechanical behavior of biomedical materials 104:103,616.

[133] Agarwal KM, Shubham P, Bhatia D, et al (2022) Analyzing the impact of print parameters on dimensional variation of ABS specimens printed using fused deposition modelling (FDM). Sensors International 3:100,149.

[134] Hanon MM, Zsidai L, Ma Q (2021) Accuracy investigation of 3D printed PLA with various process parameters and different colors. Materials Today: Proceedings 42:3089–3096.

[135] Delli U, Chang S (2018) Automated process monitoring in 3D printing using supervised machine learning. Procedia Manufacturing 26:865–870.

[136] Leliaert J, Dvornik M, Mulkers J, et al (2018) Fast micromagnetic simulations on gpu—recent advances made with. Journal of Physics D: Applied Physics 51(12):123,002.

[137] Zhang Q, Zhang M, Chen T, et al (2019b) Recent advances in convolutional neural network acceleration. Neurocomputing 323:37–51.

[138] Brion DAJ, Shen M, Pattinson SW (2022) Automated recognition and correction of warp deformation in extrusion additive manufacturing. Additive Manufacturing 56:102,838.

[139] Rossi A, Moretti M, Senin N (2021) Layer inspection via digital imaging and machine learning for in-process monitoring of fused filament fabrication. Journal of Manufacturing Processes 70:438–451.

[140] Banadaki Y, Razaviarab N, Fekrmandi H, et al (2021) Automated Quality and Process Control for Additive Manufacturing using Deep Convolutional Neural Networks. Recent Progress in Materials 4(1).

[141] Hu H, He K, Zhong T, et al (2019) Fault diagnosis of FDM process based on support vector machine (SVM). Rapid Prototyping Journal.

[142] Wu H, Yu Z, Wang Y (2016b) A new approach for online monitoring of additive manufacturing based on acoustic emission. In: International Manufacturing Science and Engineering Conference, American Society of Mechanical Engineers, p V003T08A013.

[143] Liu J, Hu Y, Wu B, et al (2018b) An improved fault diagnosis approach for FDM process with acoustic emission. Journal of Manufacturing Processes 35:570–579.

[144] Li H, Yu Z, Li F, et al (2022) Real-time polymer flow state monitoring during fused filament fabrication based on acoustic emission. Journal of Manufacturing Systems 62:628–635.

[145] Westphal E, Seitz H (2022) Machine learning for the intelligent analysis of 3D printing conditions using environmental sensor data to support quality assurance. Additive Manufacturing 50:102,535.

[146] Wu H, Wang Y, Yu Z (2016a) In situ monitoring of FDM machine condition via acoustic emission. The International Journal of Advanced Manufacturing Technology 84(5):1483–1495.

[147] Yang Z, Jin L, Yan Y, et al (2018) Filament breakage monitoring in fused deposition modeling using acoustic emission technique. Sensors 18(3):749.

[148] S. T. Z˘ivanovi´c, M. D. Popovi´c, N. M. Vorkapi´c, M. D. Pjevi´c, N. R. Slavkovi´c, An overview of rapid prototyping

[149] technologies using subtractive, additive and formative processes, FME Transactions 48 (2020) 246–253.

[150] Saad MS, Mohd Nor A, Abd Rahim I, et al (2022) Optimization of FDM process parameters to minimize surface roughness with integrated artificial neural network model and symbiotic organism search. Neural Computing and Applications pp 1–17.

[151] Hooda N, Chohan JS, Gupta R, et al (2021) Deposition angle prediction of Fused Deposition Modeling process using ensemble machine learning. ISA transactions 116:121–128.

[152] Jiang J, Yu C, Xu X, et al (2020) Achieving better connections between deposited lines in additive manufacturing via machine learning. Math Biosci Eng 17(4):3382–3394.

[153] Moradi M, Meiabadi MS, Moghadam MK, et al (2020) Enhancing 3D Printing Producibility in Polylactic Acid Using Fused Deposition Modelling and Machine Learning.

[154] Cai R, Wang K, Wen W, et al (2022) Application of machine learning methods on dynamic strength analysis for additive manufactured polypropylenebased composites. Polymer Testing 110:107,580.

[155] Zhang J, Wang P, Gao RX (2019a) Deep learning-based tensile strength prediction in fused deposition modeling. Computers in industry 107:11–21.

[156] Charalampous P, Kladovasilakis N, Kostavelis I, et al (2022) Machine Learning-Based Mechanical Behavior Optimization of 3D Print Constructs Manufactured Via the FFF Process. Journal of Materials Engineering and Performance 31(6):4697–4706.

[157] Zhang Z, Shi J, Yu T, et al (2020b) Predicting flexural strength of additively manufactured continuous carbon fiber-reinforced polymer composites using machine learning. Journal of Computing and Information Science in Engineering 20(6).

[158] Charalampous P, Kostavelis I, Kontodina T, et al (2021) Learning-based error modeling in FDM 3D printing process. Rapid Prototyping Journal.

[159] Yanamandra K, Chen GL, Xu X, et al (2020) Reverse engineering of additive manufactured composite part by toolpath reconstruction using imaging and machine learning. Composites Science and Technology 198:108,318.

[160] Zhixiong Li, Ziyang Zhang, Junchuan Shi, Dazhong Wu, Prediction of surface roughness in extrusion-based additive manufacturing with machine learning, Robot. Comput.-Integr. Manuf. 57 (2019) 488–495.

[161] Wu M, Phoha VV, Moon YB et al (2016) Detecting malicious defects in 3D printing process using machine learning and image classifcation. Proc ASME 2016 Int Mech Eng Congre Expo.

[162] Jin Z, Zhang Z, Gu GX (2019) Autonomous in-situ correction of fused deposition modeling printers using computer vision and deep learning. Manuf Lett 22:11–15.

[163] Liu C, Law ACC, Roberson D et al (2019) Image analysis-based closed loop quality control for additive manufacturing with fused flament fabrication. J Manuf Syst 51:75–86

[164] Wang Y, Huang J, Wang Y et al (2020) A CNN-based Adaptive Surface Monitoring System for Fused Deposition Modeling. IEEE ASME Trans Mechatron.

[165] Barath Narayanan, Kelly Beigh, Gregory Loughnane, Nilesh U. Powar, Support vector machine and convolutional neural network based approaches for defect detection in fused filament fabrication, in: Michael E. Zelinski, Tarek M. Taha, Jonathan Howe, Abdul A. Awwal, Khan M. Iftekharuddin (Eds.), Applications of Machine Learning, SPIE, 2019.

[166] Zhang, Z., Fidan, I., & Allen, M. (2020). Detection of material extrusion in-process failures via deep learning. Inventions, 5(3), 25.

[167] Li Y, Zhao W, Li Q et al (2019) In-situ monitoring and diagnosing for fused flament fabrication process based on vibration sensors. Sensors.

[168] Oleff, A., Küster, B., Stonis, M., & Overmeyer, L. (2021). Process monitoring for material extrusion additive manufacturing: a state-of-the-art review. Progress in Additive Manufacturing, 6(4), 705-730.

[169] Fu, Y., Downey, A., Yuan, L., Pratt, A., & Balogun, Y. (2021). In situ monitoring for fused filament fabrication process: A review. Additive Manufacturing, 38, 101749.

[170] Parsazadeh, M., Sharma, S., & Dahotre, N. (2023). Towards the next generation of machine learning models in additive manufacturing: A review of process dependent material evolution. Progress in Materials Science, 101102.

[171] Wang, C., Tan, X. P., Tor, S. B., & Lim, C. S. (2020). Machine learning in additive manufacturing: State-of-the-art and perspectives. Additive Manufacturing, 36, 101538.

[172] Qin, J., Hu, F., Liu, Y., Witherell, P., Wang, C. C., Rosen, D. W., ... & Tang, Q. (2022). Research and application of machine learning for additive manufacturing. Additive Manufacturing, 52, 102691.

[173] Sarker, I. H., Kayes, A., Badsha, S., Alqahtani, H., Watters, P., & Ng, A. (2020). Cybersecurity data science: an overview from machine learning perspective. Journal of Big data, 7, 1-29.

[174] Razvi, S. S., Feng, S., Narayanan, A., Lee, Y.-T. T., & Witherell, P. (2019). A review of machine learning applications in additive manufacturing. International design engineering technical conferences and computers and information in engineering conference,

[175] Baumgartl, H., Tomas, J., Buettner, R., & Merkel, M. (2020). A deep learning-based model for defect detection in laser-powder bed fusion using in-situ thermographic monitoring. Progress in Additive Manufacturing, 5(3), 277-285.

[176] Zhang, B., Liu, S., & Shin, Y. C. (2019). In-Process monitoring of porosity during laser additive manufacturing process. Additive Manufacturing, 28, 497-505.

[177] Khan, M. F., Alam, A., Siddiqui, M. A., Alam, M. S., Rafat, Y., Salik, N., & Al-Saidan, I. (2021). Real-time defect detection in 3D printing using machine learning. Materials Today: Proceedings, 42, 521-528.

[178] Xu, K., Lyu, J., & Manoochehri, S. (2022). In situ process monitoring using acoustic emission and laser scanning techniques based on machine learning models. Journal of Manufacturing Processes, 84, 357-374.

[179] McCann, R., Obeidi, M. A., Hughes, C., McCarthy, É., Egan, D. S., Vijayaraghavan, R. K., Joshi, A. M., Garzon, V. A., Dowling, D. P., & McNally, P. J. (2021). In-situ sensing, process monitoring and machine control in Laser Powder Bed Fusion: A review. Additive Manufacturing, 45, 102058.

[180] Cunha, F. G., Santos, T. G., & Xavier, J. (2021). In situ monitoring of additive manufacturing using digital image correlation: a review. Materials, 14(6), 1511.

[181] Nasiri, S., & Khosravani, M. R. (2021). Machine learning in predicting mechanical behavior of additively manufactured parts. Journal of materials research and technology, 14, 1137-1153.

[182] Tayebati, S., & Cho, K. T. (2023). A hybrid machine learning framework for clad characteristics prediction in metal additive manufacturing. arXiv preprint arXiv:2307.01872.

[183] Fu, Z., Angeline, V., & Sun, W. (2021). Evaluation of printing parameters on 3D extrusion printing of pluronic hydrogels and machine learning guided parameter recommendation. International journal of bioprinting, 7(4).

[184] Jatti, V. S., Sapre, M. S., Jatti, A. V., Khedkar, N. K., & Jatti, V. S. (2022). Mechanical Properties of 3D-Printed Components Using Fused Deposition Modeling: Optimization Using the Desirability Approach and Machine Learning Regressor. Applied System Innovation, 5(6), 112.

[185] Peloquin, J., Kirillova, A., Rudin, C., Brinson, L., & Gall, K. (2023). Prediction of tensile performance for 3D printed photopolymer gyroid lattices using structural porosity, base material properties, and machine learning. Materials & Design, 232, 112126.

[186] Sarkon, G. K., Safaei, B., Kenevisi, M. S., Arman, S., & Zeeshan, Q. (2022). State-of-the-art review of machine learning applications in additive manufacturing; from design to manufacturing and property control. Archives of Computational Methods in Engineering, 29(7), 5663-5721.

[187] Xames, M. D., Torsha, F. K., & Sarwar, F. (2023). A systematic literature review on recent trends of machine learning applications in additive manufacturing. Journal of Intelligent Manufacturing, 34(6), 2529-2555.

[188] Miao, G., Hsieh, S. J., Segura, J. A., & Wang, J. C. (2019). Cyber-physical system for thermal stress prevention in 3D printing process. The International Journal of Advanced Manufacturing Technology, 100, 553-567.

[189] Chhetri, S. R., Faezi, S., Canedo, A., & Faruque, M. A. A. (2019, April). QUILT: Quality inference from living digital twins in IoT-enabled manufacturing systems. In Proceedings of the International Conference on Internet of Things Design and Implementation (pp. 237-248).

Chapitre 3: Étude par apprentissage automatique de l'effet des paramètres de procédé sur la résistance à la traction du PLA et du PLA-CF en fabrication par dépôt de fil fondu FFF

Ce chapitre a fait l'objet d'une publication :

A Machine Learning study of the Effect of Process Parameters on Tensile Strength of FFF PLA and PLA-CF. Abdelhamid ZIADIA, Mohamed HABIBI, Sousso KELOUWANI. Eng, 4(4), pp.2741-2763.

Il peut être consulté en ligne à l'adresse suivante :

https://doi.org/10.3390/eng4040156

Dans la continuité du chapitre précédent, qui a montré le potentiel du machine learning pour relier procédé, structure et propriétés et pour assurer un suivi en temps réel en extrusion de matière, ce chapitre met en pratique une chaîne complète allant de l'expérience au calcul. Il cible le PLA et le PLA renforcé par fibres de carbone et vise des réglages d'impression directement exploitables.

Le protocole expérimental s'appuie sur des éprouvettes ASTM D638-14 Type I imprimées sur une Ultimaker S5 avec Cura 5.4.0. Les essais de traction sont réalisés à 2 millimètres par minute. Les facteurs étudiés sont la température d'extrusion, l'épaisseur de couche, la vitesse d'impression et le choix de matériau entre PLA et PLA-CF.

Les données obtenues alimentent un modèle d'ensemble blending. Il combine Random Forest, XGBoost, Gradient Boosting, arbre de décision, régressions linéaire, lasso et ridge. Une régression linéaire méta-apprenante agrège les prédictions. La base est divisée en 70 pour cent pour l'entraînement, 20 pour cent pour la validation et 10 pour cent pour le test.

Les performances prédictives sont élevées. Le coefficient de détermination atteint 91,75 % pour la résistance ultime à la traction, 94,08 % pour le module d'Young et 88,54 % pour l'allongement à la rupture. Les erreurs quadratiques moyennes sont faibles, ce qui autorise une optimisation multi-objectif fiable.

L'optimisation repose sur un algorithme génétique dans des bornes réalistes. La température varie de 200 à 230 °C. L'épaisseur de couche s'étend de 0,25 à 0,45 mm. La vitesse couvre 40 à 60 mm par seconde. Le matériau peut être PLA ou PLA-CF. Le critère à maximiser est une somme pondérée et normalisée des propriétés, avec des poids fixés par l'utilisateur. L'arrêt est défini à 250 générations.

Les optima identifiés sont directement actionnables. Pour la résistance ultime, le point optimal est de 41,129 MG avec PLA-CF à environ 222,28 °C, 0,261 mm et 40,30 mm par seconde. Pour le module, l'optimum est de 4423,63 MP avec PLA-CF à environ 200,01 °C, 0,388 mm et 40,38 mm par seconde. Pour l'allongement, l'optimum est de 2,249 % avec PLA à environ 200,34 °C, 0,390 mm et 45,30 mm par seconde.

Ces résultats confirment le rôle déterminant de la température, de l'épaisseur de couche et de la vitesse. Ils valident l'avantage structurel de l'ajout de fibres de carbone pour la résistance et la rigidité. Ils traduisent enfin les tendances issues de la revue en consignes d'impression prêtes à l'emploi.

L'apport du chapitre est double. D'un côté, il fournit des modèles précis intégrés à une optimisation multi-objectif pilotable par des poids pour améliorer les propriétés mécaniques. De l'autre, il prépare un couplage naturel avec le monitoring in situ et les jumeaux numériques afin de fermer la boucle vers un contrôle en temps réel.

A Machine Learning study of the Effect of Process Parameters on Tensile Strength of FFF PLA and PLA-CF

Ziadia Abdelhamid[1], Habibi Mohamed[1*] and Sousso Kelouwani[1]

[1*]*Department of mechanical engineering, University of Quebec in Trois-Rivieres, 3351 Bd des Forges, Trois-Rivieres, G8Z 4M3, Quebec, Canada.*

**Corresponding author(s). E-mail(s): Mohamed.Habibi@uqtr.ca;*

Contributing authors: Abdelhamid.Ziadia@uqtr.ca; Sousso.Kelouwani@uqtr.ca;

3.1 Abstract

Material Extrusion is a popular additive manufacturing technology due to its low cost, wide market availability, ability to construct complex parts, safety, and cleanliness. However, optimizing the process parameters to obtain the best possible mechanical properties has not been extensively studied. This paper aims to develop ensemble learning-based models to predict the ultimate tensile strength, Young's modulus, and strain at break of PLA and PLA-CF 3D-printed parts, using printing temperature, printing speed, and layer thickness as process parameters. Additionally, the study investigates the impact of process parameters and material selection on the mechanical properties of the printed parts and uses Genetic Algorithms for multi-objective optimization according to user specifications. The results indicate that process parameters and material selection significantly influence the mechanical properties of the printed parts. The ensemble learning predictive models yielded an R^2 value of 91.75% for Ultimate Tensile Strength, 94.08% for Young's Modulus, and 88.54% for Strain at Break. The Genetic Algorithm successfully identifies optimal parameter values for the desired mechanical properties. For optimal Ultimate Tensile Strength, PLA-CF was used at 222.28°C, 0.261mm layer, 40.30mm/s speed, yielding 41.129MPa. For Young's Modulus: 4423.63MPa, PLA-CF, 200.01°C, 0.388mm layer, 40.38mm/s. For strain at break: 2.249%, PLA, 200.34°C, 0.390mm layer, 45.30mm/s. Moreover, this work is the first to model Process-Structure-Properties relationships for an additive manufacturing process and to use a multi-objective optimization approach for multiple mechanical properties, utilizing ensemble learning-based algorithms and Genetic Algorithms.

Keywords*:* Additive Manufacturing; Material Extrusion; Machine learning; Genetic Algorithm; Process optimization.

3.2 Introduction

Additive manufacturing, also known as 3D printing, is revolutionizing the manufacturing and prototyping industries by providing a simpler and more cost-effective product development process than traditional manufacturing techniques. Among various 3D printing technologies, material extrusion, or fused filament fabrication (FFF), is the most widely used and rapidly growing technique [1,2]. Material extrusion was first introduced in 1989 and patented by Scott Crump, the cofounder of Stratasys [3], who also introduced it to the market as fused deposition modeling (FDM). Initially, this technology was also referred to as fused filament fabrication (FFF), which gained popularity after the expiration of the Stratasys FDM patent [1].

The popularity of material extrusion can be attributed to its capability to print with a wide range of materials, making it possible to build new technologies with various characteristics. Additionally, its low cost, scalability, and wide market availability make it an attractive option for researchers and industry professionals alike [4].

However, research has shown that parts produced using traditional manufacturing methods exhibit superior mechanical properties compared to those fabricated with material extrusion. This is because the parts are printed layer by layer, creating voids that generate internal stress when subjected to mechanical tests. To overcome this obstacle, researchers worldwide are pursuing different strategies to optimize the mechanical properties of 3D-printed parts by selecting the appropriate process parameters [5,6]. In summary, material extrusion has significantly improved the product development process with its versatility and cost-effectiveness. Despite its limitations in terms of mechanical properties, ongoing research aims to overcome these challenges and further enhance the capabilities of this innovative technology [4,5].

Several researchers have employed different approaches to investigate the optimization of process–structure properties of 3D-printed polymers. Gebisa et al. [5] employed a full factorial design experiment to study the effect of FFF process parameters on the tensile properties of ULTEM 9085. They investigated five variables, including the contours number, contour width, raster width, raster angle, and air gap, and found that raster angle had the greatest influence on mechanical properties. Claver et al. [6] studied the effect of layer height, infill density, and layer orientation on the tensile strength of polylactic acid (PLA) and acrylonitrile butadiene styrene (ABS). They found that infill density significantly impacted tensile strength, while layer height had little effect. Chokshi et al. [7] investigated the effect of layer thickness, infill pattern, and contours number using PLA as the printing material. Their study showed that layer thickness and contours number significantly impact flexural strength. Othman et al. [8] studied

the influence of layer thickness, infill pattern, and contours number on the mechanical properties and showed that all three process parameters studied have close contribution values on mechanical strengths. Infill density has the highest influence on mechanical properties, followed by layer thickness.

To enhance the mechanical properties of polymers, researchers have developed composites that combine polymers with reinforcing materials such as fibers, particles, or fillers. Introducing these reinforcing materials allows the resulting composite material to exhibit improved properties such as increased strength, stiffness, toughness, and wear resistance compared to pure polymers. Several researchers have studied and compared the mechanical performance of polymers and composites using various materials and techniques. Ning et al. [9] evaluated the effects of carbon fibers on the mechanical properties of FFF-fabricated parts made of ABS. They found that carbon fibers enhanced tensile strength and Young's modulus but reduced toughness, yield strength, and ductility. Love et al. [10] observed that combining carbon fibers and polymers increased strength, stiffness, thermal conductivity, and reduced distortion in FFF-fabricated parts. Perez et al. [11] investigated the effects of reinforcing materials such as fibers and TiO2 on the mechanical properties of 3D-printed ABS matrix composites. They found that ABS reinforced with TiO2 at a 5% weight ratio showed the highest ultimate tensile strength. Aissa et al. [12] experimented with reinforced polyamide (RPA) as the printing material and used printing speed, extrusion temperature, and layer thickness as FFF process parameters. They found that extrusion temperature and layer thickness had a more significant impact on tensile strength than printing speed. Mushtaq et al. [13] used ABS as a printing material and focused on part properties like flexural strength, tensile strength, surface roughness, print time, and energy consumption. The process parameters were layer thickness, printing speed, and infill density. Using a full central composite design, twenty specimens were tested. Layer thickness was shown to be critical for achieving the optimum surface roughness and print time, while infill density was critical for mechanical qualities. Zhang et al. [14] developed a data-driven predictive modeling approach to understand the structure–property relationship of FFF-fabricated continuous carbon fiber reinforced polymers (CCFRP). The ensemble learning algorithm combined eight base learners: multiple linear regression, least absolute shrinkage and selection operator (lasso), multivariate adaptive regression splines (MARS), generalized additive model (GAM), K-nearest neighbors (KNN), support vector machine (SVM), extra-trees, and extreme gradient boosting (XGBoost). Their study concluded that the predictive model accurately predicted the flexural strength of CCFRP specimens, with a minimum RMSE of 9.87%, a minimum RE of 7.75%, and a maximum R2 of 96.99%.

The analyses of the previous investigations, summarized in Table 8, provide a presentation of an important study direction in the field of FFF, particularly with materials like PLA and PLA-CF. As previously stated, numerous researchers have conducted studies to better understand the impact of various process factors on the mechanical properties of printed parts. Several of these studies used the design of experiments, empirical methodologies, or direct experimentation to identify these relationships. Although these methodologies have produced useful insights, there appears to be a clear gap in these studies: a lack of advanced prediction and optimization strategies. While traditional methods are rigorous, they may fail to capture the complex interplay of several elements. Furthermore, it appears that the current literature lacks an integrated approach that not only predicts results but also optimizes parameters for ideal results. This identified gap emphasizes the potential need for more integrated and advanced techniques in future research initiatives.

In this context, we present a novel way to model the Process-Structure-Properties interactions for the FFF process. The primary focus of this study is to use ensemble learning algorithms to predict the mechanical properties of FFF-printed parts using PLA and PLA with Carbon Fiber (PLA-CF) as printing materials. Additionally, the study aims to understand the impact of process parameters on the mechanical properties of the parts and perform a multi-objective optimization of process parameters to achieve the desired mechanical properties. As shown in Figure 20, this novel method aims to provide a complete method that fills gaps in previous studies. The rest of this article will be organized as follows: Section 2 will define the machine learning algorithms and performance metrics used in this study. Section 3 will provide details on the experimental and computational methods adopted, and the results obtained will be discussed. Finally, in section 4, the article will be concluded with a summary and future research perspectives.

3.3 Machine Learning

The four main categories of machine learning techniques are supervised, unsupervised, semi-supervised, and reinforcement. However, in this paper, the focus is on supervised learning, which is a formalization of the concept of learning from examples. The supervised learning approach involves providing the learner with a training set and a test set of labeled data, which it uses to learn from the labeled data to identify the unlabeled data as accurately as possible [15]. This paper focuses explicitly on regression-supervised models since the variables to predict are discrete.

Table 8. Summary of the literature review

Ref	Material	Parameters studied	Major findings
[5]	ULTEM 9085	Contours number Raster parameters Air gap	Raster angle had the greatest influence on mechanical properties
[6]	PLA, ABS	Layer height Infill density Layer orientation	Infill density highly impacted tensile strength, layer thickness had smaller effect
[7]	PLA	Layer thickness Infill pattern Contours number	Layer thickness and contours number impact flexural strength
[8]	PLA	Layer thickness Infill pattern Contours number	Infill density, followed by layer thickness, have the highest influence on mechanical properties
[9]	ABS with carbon fibers	-	Carbon fibers enhanced tensile strength and Young's modulus but reduced toughness and yield strength
[10]	Polymers with carbon fibers	-	Carbon fibers increased strength, stiffness, thermal conductivity, and reduced distortion in FDM parts
[11]	ABS with fibers and Tio2	-	ABS reinforced with TiO2 at 5% weight ratio showed highest ultimate tensile strength
[12]	RPA	Printing speed Extrusion temperature Layer thickness	Extrusion temperature and layer thickness influenced tensile strength more than printing speed
[13]	ABS	Layer thickness Printing speed Infill density	Layer thickness has a critical influence for achieving the optimum surface roughness and print time, infill density was critical for mechanical qualities.
[14]	CCFRP	-	Predictive model accurately determined flexural strength of CCFRP specimens

3.3.1 Machine Learning regression models

This section provides an in-depth explanation of the various machine-learning regression models employed in this study.

3.3.1.1 Multiple Linear Regression

Multiple linear regression is a statistical method that enables the prediction of a target variable based on the values of two or more explanatory variables [16]. This technique builds upon linear regression and is sometimes referred to as multiple regression. In this context, the variable to be predicted is designated as the dependent variable, while the variables employed for

prediction are called independent variables. The primary objective of this algorithm is to establish a linear association between the independent variables (x) and the dependent variable (y), as illustrated in Equation 1.

$$y = \beta_0 + \beta_1 x_1 + \cdots + \beta_p x_p \quad (1)$$

where β_0 is the value of y when the independent variables are equal to zero, and $\{\beta_1, ..., \beta_p\}$ are the estimated regression coefficients.

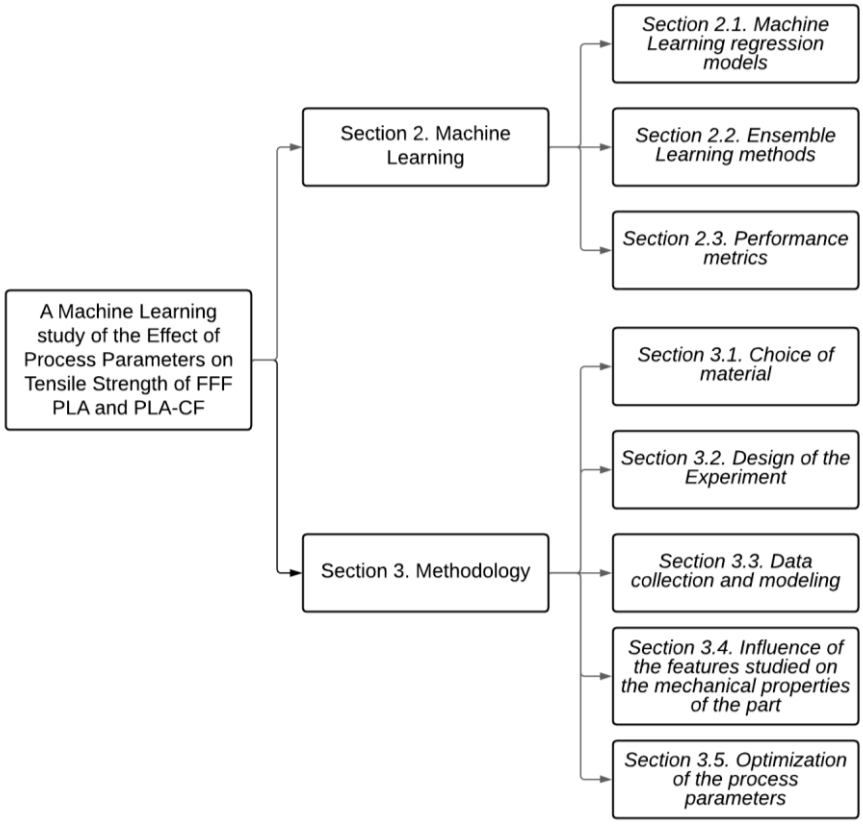

Figure 20. Schematic diagram of article content structure.

3.3.1.2 Decision Tree Regression

A decision tree is a method that employs a tree-like framework for constructing regression models [17, 18]. This approach progressively develops a corresponding decision tree by dividing a dataset into increasingly smaller subsets. The decision tree consists of three types of nodes. The root node serves as the starting point and represents the entire data sample. Interior nodes symbolize the features of the dataset, with their branches denoting the respective decisions. Lastly, leaf nodes signify the outcomes derived from the model.

3.3.1.3 Least Absolute Shrinkage and Selection Operator (lasso)

Lasso, a shrinkage method, applies constraints on the coefficients of the least squares estimates [14]. The objective function for the lasso technique is illustrated in Equation 2:

$$J = \sum_{i=1}^{N} \left(y_i - \beta_0 - \sum_{j=1}^{p} \beta_j x_{ij}\right)^2 + \lambda \sum_{j=1}^{p} \beta_j \quad (2)$$

here β_0 and β_j represent the coefficients for the least squares estimates, and λ denotes the tuning parameter that regulates the penalty effect on the estimation of coefficients. The lasso offers an advantage over traditional least squares approaches as the penalty term facilitates managing the trade-off between variance and bias.

3.3.1.4 Ridge Regression

Ridge Regression, a linear regression variation, contains a regularization method to avoid overfitting and deal with multicollinearity among predictor variables. It predicts the dependent variable y based on the independent variables x1, x2, x3, …, xp via the linear relationship:

$$y = \beta_0 + \beta_1 x_1 + \beta_2 x_2 + \cdots + \beta_p x_p + \lambda \sum_{i=1}^{p} \beta_i^2 \quad (3)$$

where, $\beta_0, \beta_1, \beta_2 \ldots, \beta_p$ are the coefficients estimated to minimize the residual sum of squares plus the penalty term. The presence of the penalty term $\lambda \sum_{i=1}^{p} \beta_i^2$ distinguishes Ridge Regression from ordinary linear regression; it penalizes large coefficients with a tuning parameter λ.

Ridge Regression behaves exactly like normal linear regression when (λ = 0). As λ increases, the model's coefficients approach zero, simplifying the model. To assist the model predict effectively on new data, the best value for λ is commonly chosen through cross-validation. Ridge Regression performs better when the predictors are correlated, leading to more stable predictions and preventing calculation issues.

3.3.2 Ensemble Learning methods

Ensemble learning is a technique that combines multiple base learners to enhance the final prediction [18]. Individual base models might exhibit suboptimal performance due to high variance or bias. However, when these base learners are connected, they form a more robust learner, as their combination effectively reduces bias or variance, leading to improved model performance. In this study, four distinct types of ensemble learning techniques have been employed.

3.3.2.1 Bagging and Boosting

The key distinction between bagging and boosting lies in their training methodologies. In bagging, the base models are trained concurrently, whereas boosting necessitates sequential training of the base models [19].

The underlying principle of bagging ensemble learning is straightforward; it depends on samples generated using the bootstrap statistical method, which is based on an original dataset [18]. Given N bootstrap samples, each with a size of S (as shown in Equation 4), bagging proceeds accordingly:

$$\{(r_1^1, r_2^1, \ldots, r_S^1), (r_1^2, r_2^2, \ldots, r_S^2), \ldots, (r_1^N, r_2^N, \ldots, r_S^N)\} \quad (4)$$

These samples are subsequently utilized to train multiple base models, as demonstrated in Equation 5:

$$\{m_1, m_2, \dots, m_N\} \quad (5)$$

In a regression scenario, as is the case in this study, the average of the predictions from the base models is computed to generate a final prediction with reduced variance, as depicted in Equation 6:

$$fm_i(x) = \frac{1}{N}\Sigma_{i=1}^{N} m_i(x) \quad (6)$$

In this study, the bagging method employed is Random Forest (RF), which utilizes deep decision trees as weak learners, fitted to bootstrap samples derived from an initial dataset [20]. In RF, feature sampling also occurs, ensuring that each decision tree trains on a random subset of features. Boosting shares similarities with bagging, as both techniques use multiple base models to achieve a better-performing model [18].

The primary difference between the two is that boosting trains base models sequentially, with each model focusing on the data poorly addressed by its predecessor. Upon completing the process, a learner with reduced bias is obtained. The boosting methods utilized in this study include Gradient Boosting and Extreme Gradient Boosting (XGB).

Gradient Boosting is an approach wherein the ensemble model is constructed as the sum of weighted weak learners, as illustrated in Equation 7:

$$fm_N(.) = \Sigma_{i=1}^{N} c_i \times m_i(.) \quad (7)$$

This algorithm transforms the problem into a Gradient Descent-based one. During each sequential iteration, a weak learner is fitted to the negative of the current fitting error in relation to the existing ensemble model [19], as demonstrated in Equation 8:

$$fm_i(.) = fm_{i-1}(.) - c_i \times \nabla_{fm_{i-1}} L(fm_{i-1})(.) \quad (8)$$

Where L(.) represents the fitting error of the model, ci is the step size, and $-\nabla_{fm_{i-1}} L(fm_{i-1})(.)$ denotes the opposite of the current fitting error relative to the existing model.

Extreme Gradient Boosting (XGB) is constructed similarly as a sum of weighted weak learners (refer to Equation 6), where the first weak learner is trained on the entire input data. Subsequent models are trained on the residuals to address the limitations of the previous training, continuing until the stopping criterion is achieved [21].

XGB strives to prevent overfitting while optimizing computational resources [22, 23]. To accomplish this, an objective function (shown in Equation 9) that assesses both loss and regularization should be minimized:

$$Obj^{(t)} = \sum_{k=1}^{n} l(y_i, \hat{y}_i) + \sum_{k=1}^{t} \Omega(f_i) \quad (9)$$

In this case, n is the number of values, l denotes the loss function, y_i and $\hat{y}_i$ are the actual label and the predicted label, respectively, f_i is the week learner, and **Ω** is the regulation term (Equation 10) which is defined as:

$$\Omega(f_i) = \gamma T + \frac{1}{2}\lambda \parallel w \parallel^2 \quad (10)$$

Where γ represents the minimum loss necessary to further partition the leaf node, T denotes the number of leaves in the tree, λ is the regularization parameter, and w refers to the weight assigned to each leaf.

3.3.2.2 Stacking

Unlike bagging and boosting methods, which rely on basic models utilizing the same algorithm, stacking models employ a hierarchical ensemble framework. The stacking model enhances modeling accuracy by combining different classifiers or regressors [24-26]. The simplest stacking model typically comprises two levels: level 0, which includes basic models, and level 1, which features the meta-learner. The basic models (level-0) utilize various algorithms to learn from the original dataset, generating the meta-feature dataset, while the meta-learner (level-1) processes the meta-feature dataset to produce the final results. K-fold cross-validation is commonly employed during the training process of a single basic model to prevent overfitting and ensure that all original datasets contribute to training for generating new meta-feature datasets.

3.3.2.3 Blending

The primary distinction between blending and stacking lies in the manner in which basic models generate the meta-feature dataset. Instead of using the K-fold cross-validation method, blending reserves a portion of the training dataset (typically 10% or 20%) as the validation set [26]. Figure 21 provides a summary of the ensemble learning blending method.

3.3.3 Performance metrics

A critical aspect of developing a robust machine learning model is assessing its performance. Various metrics are employed to evaluate the quality of the model. These performance indicators facilitate the measurement of the model's effectiveness based on the available data. By fine-tuning the hyperparameters, it is possible to improve the model's performance.

3.3.3.1 Root Mean Squared Error (RMSE)

Root Mean Square Error (RMSE) represents the standard deviation of the prediction errors, indicating how closely the data is clustered around the best-fit line [27, 28]. The formula to calculate the RMSE is shown in Equation 11:

$$RMSE = \sqrt{\frac{1}{n}\Sigma_{i=1}^{n}(y_i - \hat{y}_i)^2} \quad (11)$$

In this equation, y represents the actual value, ŷ is the predicted value, n denotes the number of values, and i refers to the index of each value.

3.3.3.2 Coefficient of determination (R^2)

R^2, also known as the coefficient of determination, represents the difference between 1 and the ratio of the sum of residual squares to the total sum of squares [28], as shown in Equation 12:

$$R^2 = 1 - \frac{\sum_{i=1}^{n}(y_i - \hat{y}_i)^2}{\sum_{i=1}^{n}(y_i - \bar{y})^2} \quad (12)$$

In this equation, y denotes the actual value, ŷ is the predicted value, ȳ represents the mean value, n refers to the number of values, and i indicates the index of each value.

An R^2 score of 1.0 signifies a perfect fit of the model to the data, while an R^2 value of 0.0 suggests that the predicted values are constant and equal to the mean value of the training data. A negative R^2 score implies that the model's performance is exceptionally poor.

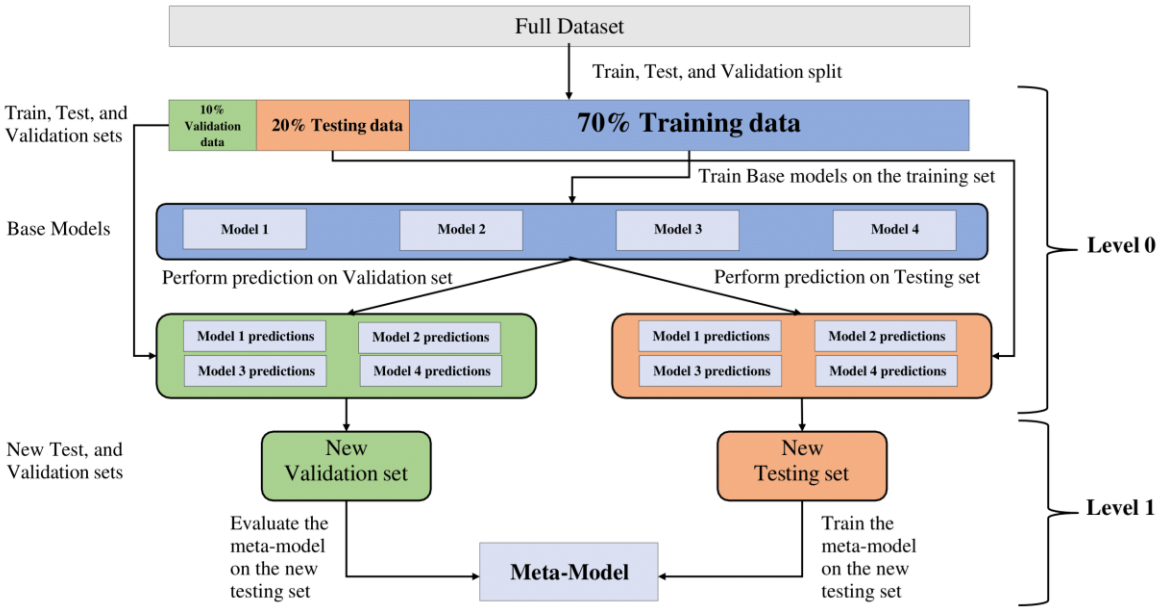

Figure 21. Blending method.

3.4 Methodology

The CAD models of the test specimens are designed using SolidWorks and saved as STL files. These files are then processed using Ultimaker Cura software, which slices them and generates the G-code for printing the models with the Material Extrusion printer, Ultimaker S5. The test specimens are prepared for tensile strength testing in accordance with the ASTM D638-14 Type I [29] standard method. This test method aims to determine the tensile properties of un-reinforced and reinforced plastics in the form of standard dumbbell-shaped test specimens when tested under specified conditions. The test specimens have an overall width of 19mm and an overall length of 165mm (Figure 22).

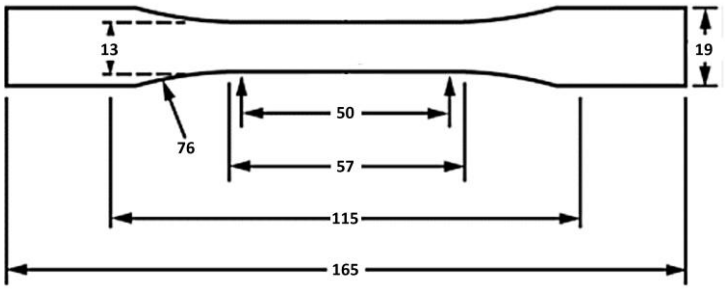

Figure 22. Tensile specimen shape and dimensions.

3.4.1 Choice of material

PLA, or polylactic acid, is a biodegradable and bioactive polyester that is derived from renewable resources, such as cornstarch, sugarcane, or cassava roots. It has become a popular material for 3D printing due to its environmental friendliness, ease of printing, and low toxicity. However, its mechanical properties are not as strong as some other materials, such as ABS.

To improve the properties of PLA, researchers have turned to composite materials, such as PLA-CF. Carbon fiber is a strong and lightweight material that can be used to reinforce plastic materials. PLA-CF is a composite material made by adding carbon fiber to PLA. It has improved mechanical properties, such as strength and stiffness, compared to pure PLA.

The use of bioplastics, such as PLA, is becoming increasingly important as concerns about the environment and sustainability grow. Petroleum-based plastics, such as ABS, are non-renewable and contribute to pollution and waste. The availability of these materials is also decreasing, making it necessary to find alternative materials that are more sustainable. By using PLA and PLA-CF, this study contributes to the development of more environmentally friendly 3D-printing materials.

3.4.2 Design of the Experiment

The optimization of process-structure-properties of materials is a crucial aspect of 3D printing. In this study, three key parameters were considered for optimizing the 3D printing process of PLA and PLA-CF: Printing Temperature, Layer Thickness, and Printing Speed.

Printing Temperature refers to the temperature at which the material is extruded from the printer nozzle. It is a critical parameter that can significantly impact the final mechanical properties of the printed part. If the temperature is too low, the material may not bond well between layers, leading to a weak and brittle part. On the other hand, if the temperature is too high, the material may burn or degrade, affecting its structural integrity [30]. *Layer Thickness* refers to the thickness of each layer of material that is deposited on top of the previous layer. This parameter affects the resolution and quality of the final printed part. A thinner layer thickness results in higher resolution and smoother surface finish, but it also increases printing time. A

thicker layer thickness results in faster printing but may compromise the quality and mechanical properties of the final part [31]. *Printing Speed* refers to the speed at which the printer moves the nozzle across the printing bed. This parameter affects the overall printing time and the quality of the final part. A slower printing speed allows for better adhesion between layers, resulting in a stronger part with a better surface finish. However, it also increases printing time. A faster printing speed reduces printing time but may result in weaker parts with lower quality surface finish [32].

Other parameters, such as infill density and pattern, and bed temperature, can also affect the final properties of the printed part. However, for this study, these parameters were set as indicated in Table 9 and were not considered in the optimization process.

Table 9. Fixed FFF process parameters and their description

Factors	Description	Value
Bed Temperature (°C)	Used to heat the build platform	60
Infill density %	The amount of material used in the inside of the print	100
Infill pattern	The form or structure of the material within the component	Lines
Number of contours	The number of contours surrounding the part	1
Number of contours	The number of contours surrounding the part	1

Full Factorial design of the experiment involves testing all possible combinations of the chosen parameter levels to determine their effect on the final properties of the printed part. As depicted in Table 10, three levels were selected for each parameter: Printing Temperature, Layer Thickness, and Printing Speed.

Table 10. Selected factors and their levels

Factors	Level 1	Level 2	Level 3
Printing Temperature (°C)	200	215	230
Layer Thickness (mm)	0.25	0.35	0.45
Printing Speed (mm/s)	40	50	60

For Printing Temperature, the levels chosen were 200, 215, and 230°C. These temperatures were selected based on the melting point of the PLA and PLA-CF materials and their recomended printing temperature range.

For Layer Thickness, the levels chosen were 0.25, 0.35, and 0.45 mm. This parameter affects the resolution and quality of the final printed part, as well as printing time.

Finally, for Printing Speed, the levels chosen were 40, 50, and 60 mm/s. This parameter affects printing time and the overall quality of the printed part, as well as its mechanical properties.

By applying a Full Factorial design of the experiment, this study can determine the effect of each parameter and their interactions on the final properties of the printed parts. This approach allows for the optimization of the printing process and the production of high-quality parts with the desired mechanical properties.

The full factorial design of the experiment yielded 27 specimens for each material, resulting in a total of 54 specimens for the study. Of these, 27 specimens were printed using pure PLA, and the remaining 27 specimens were printed using PLA-CF. Each specimen represents a unique combination of the chosen parameter levels, allowing for the determination of how each parameter affects the final mechanical properties of the printed part. By testing multiple specimens for each material and parameter combination, the study can determine the consistency and repeatability of the printing process and ensure that the results are statistically significant. Overall, the use of a full factorial design of the experiment and multiple specimens allows for a comprehensive analysis of the 3D printing process and the properties of the printed parts. This approach can help to optimize the printing process, improve the quality of the final parts, and contribute to the development of more sustainable and environmentally friendly 3D-printing materials.

3.4.3 Data collection and modeling

Tensile tests are a standard method for determining the mechanical properties of materials, including their strength, stiffness, and ductility. In this study, the specimens created using the full factorial design of the experiment were used for tensile tests to evaluate the mechanical properties of PLA and PLA-CF.

The tensile tests were performed using a universal tensile material testing system MTS, which is a commonly used equipment for material testing. The crosshead speed was set to 2 mm/min, which is a typical speed for tensile tests on 3D printed parts. The experimental setup for the tensile test includes the MTS equipment, the specimen holder, and the strain gauge for measuring the deformation of the specimen. After the tensile tests were performed, the obtained data were manually preprocessed and stored in CSV files. Preprocessing involves removing any outliers or errors in the data and ensuring that the data is formatted correctly for analysis. The results of data collection and preprocessing are shown in Table A1, which includes the tensile strength, modulus of elasticity, and elongation at break for each specimen.

The tensile test results are used to evaluate the effect of the chosen parameters on the mechanical properties of the printed parts. By analyzing the data and comparing the results for different parameter combinations, the optimal printing parameters can be determined for producing parts with the desired mechanical properties.

In this study, the collected data from tensile tests were used to train ensemble learning models to predict the ultimate tensile strength, Young's modulus, and strain at the break of the printed parts. The blending ensemble learning method was used, which combines multiple weak learners to create a stronger, more accurate predictive model.

The weak learners employed were the bagging method Random Forest, the boosting methods Xgboost and Gradient Boosting, and the regression models Decision Tree Regressor, the Multiple Linear Regression, lasso, and Ridge regression. The Multiple Linear Regression was used as the meta-learner, which combines the predictions of the weak learners to create the final prediction.

To train and evaluate the ensemble learning models, the data was randomly split into training data (70%), testing data (20%), and validation data (10%). The weak learners were trained using the training data, and their predictions were combined to create the data that the meta-learner was trained on. The prediction results of the validation set of the weak learners were combined with the validation set to evaluate the model.

The results of the ensemble learning models (Table 11) showed high accuracy in predicting the mechanical properties of the printed parts. The R^2 score for the prediction of ultimate tensile strength was 91.75%, the R^2 score for Young's modulus was 94.08%, and the R^2 score for strain at break was 88.54% (Figure 23). The RMSE values were also relatively low, indicating that the models have good predictive accuracy.

These results prove that the models trained are capable of predicting with high accuracy the mechanical properties studied. Therefore, the optimization of the process parameters within the range studied became possible. Consequently, it is necessary to analyze the influence of the process parameters used on these mechanical properties.

Table 11. Prediction accuracy of the blending methods.

Property predicted	R^2 (%)	RMSE	Mean of actual values
Ultimate Tensile strength (σ) (MPa)	91.75%	1.23	33.87
Young's Modulus (E) (MPa)	94.08%	278.00	3233.74
Strain at break (ϵ) (%)	88.54%	0.09	1.91

3.4.4 Influence of the features studied on the mechanical properties of the part

Table A1 provides data on the mechanical properties of the PLA and PLA-CF specimens. There is a clear difference between the properties of the two materials, which confirms the effect of carbon fiber on PLA. The addition of carbon fiber improves the mechanical properties of PLA, including its strength, stiffness, and toughness.

Figure 24 presents the behavior of runs 1, 10, 12, and 13 of PLA and PLA-CF. These runs represent different combinations of the printing parameters and their effect on the mechanical properties of the printed parts. The plots show the stress-strain curves for each run, which provide information on the mechanical behavior of the printed parts under tensile load.

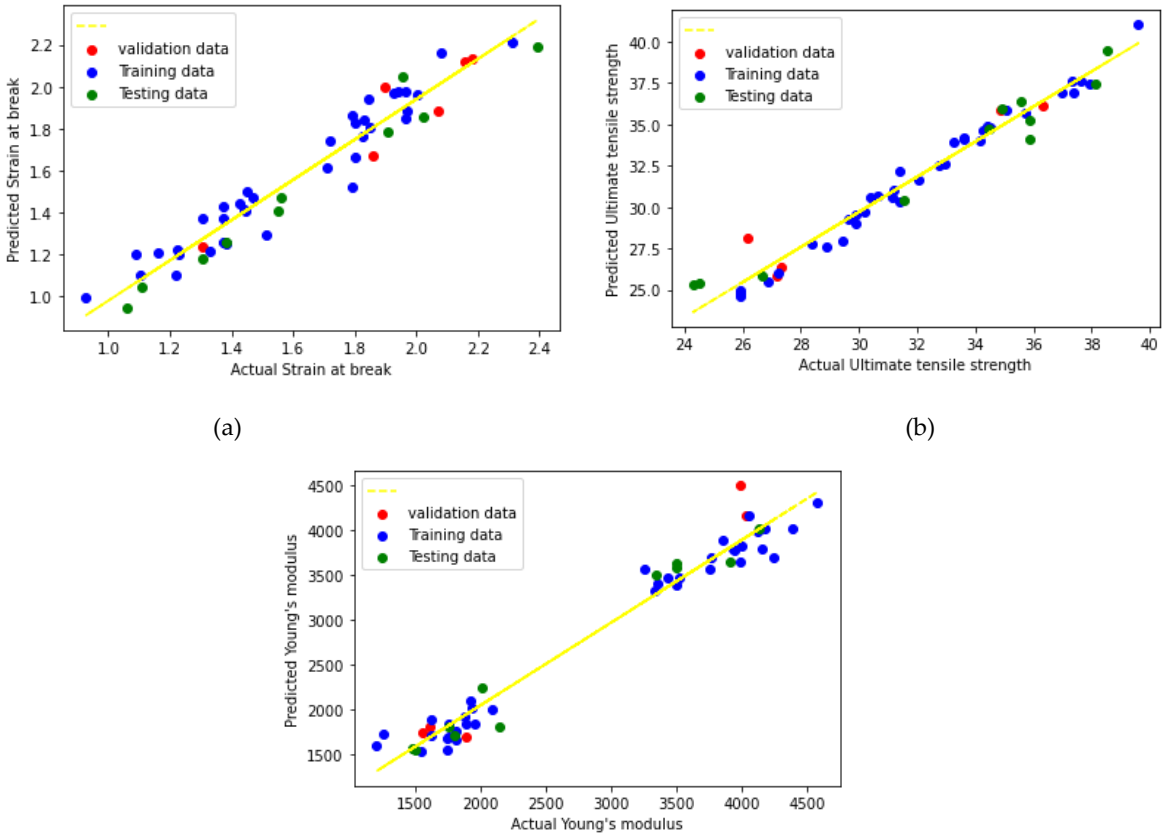

Figure 23. Observed versus predicted mechanical properties: (a) Strain at break (%), (b) Ultimate tensile strength (MPa), (c) Young's modulus (MPa)

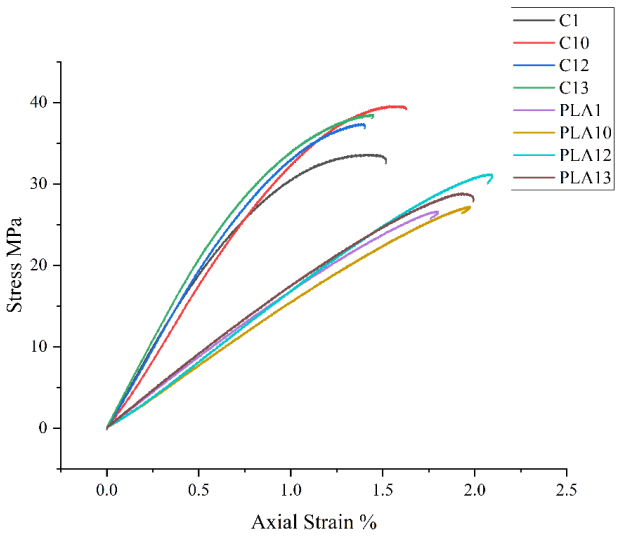

Figure 24. Tensile test behavior of PLA and PLA-CF parts

3.4.4.1 Feature importance

The Decision Tree Regressor algorithm was used to study the importance of the features, as it provides good interpretability and the ability to output the importance of the features. The importance of the features indicates the extent to which a given input feature affects the outcome, which can be used to evaluate the relative influence of the input features on the mechanical properties of the printed parts.

The results presented in Table 12 show that the material has the greatest importance on all the mechanical properties studied, which confirms the significant effect of carbon fiber on the mechanical properties of PLA which is supported by various studies. In fact, Ning et al. [9] deduced that the inclusion of carbon fibers into ABS significantly increased its tensile strength and Young's modulus, albeit with a noted reduction in toughness, yield strength, and ductility, which is consistent with our observations regarding the significant improvement in mechanical performance through the use of carbon fiber reinforcement. Similarly, Love et al. [10] confirmed that combining carbon fibers with polymers increased strength, stiffness, and heat conductivity while decreasing distortion in FFF-fabricated parts.

The study of feature importance also confirms that the printing temperature has the most significant influence on the ultimate tensile strength of the printed parts. For Young's modulus and strain at break, the layer thickness is the process parameter with the most significant influence, as shown in Figure 25 which showcases the influence of the process parameters on the mechanical properties of the printed parts. In a study conducted by Aissa et al. [12], printing temperature had a greater influence on tensile strength than other FFF process factors such as layer thickness and printing speed. Furthermore, other researchers' investigations of various Process-Structure-Properties of FFF-printed polymers, as noted in Gebisa et al. [5] and Claver et al. [6], demonstrated the importance of optimal process parameter settings, with printing temperature emerging as a critical determinant of mechanical properties. These findings highlight the major influence of printing temperature on the mechanical properties of FFF printed objects. The results of feature importance also revealed the critical function of layer thickness in affecting mechanical properties. This discovery is supported by Othman et al. [8], who emphasized the significance of layer thickness in their work, citing its strong association to mechanical strengths when paired with other parameters. Aissa et al. [12] discovered layer thickness as a key FFF process parameter impacting tensile strength, stressing its importance in 3D printing. They also stated that printing speed has a smaller impact on mechanical properties compared to layer thickness and printing temperature.

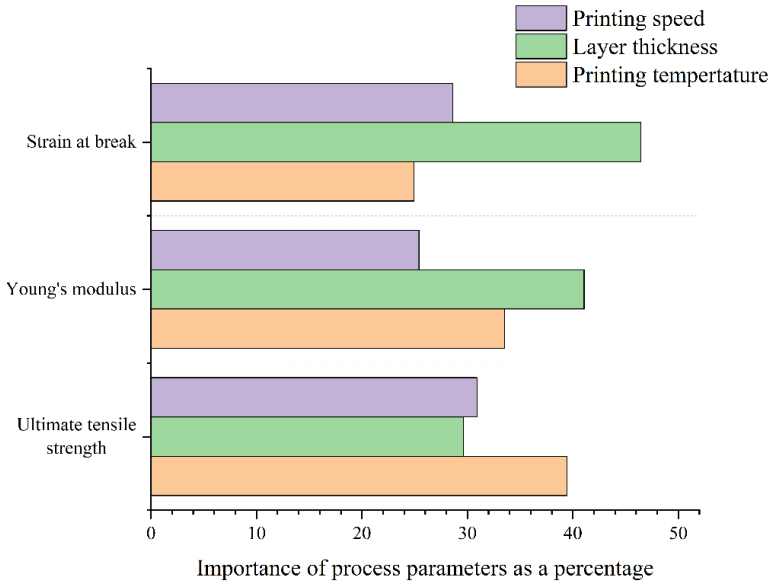

Figure 25. Importance of the process parameters on the mechanical properties

Table 12. Features importance for each mechanical property studied using decision tree

	Ultimate tensile strength	Young's Modulus	Strain at break
Material (PLA/PLA-CF)	67.30%	92.70%	71.60%
Printing Temperature	12.89%	2.44%	7.08%
Layer thickness	9.68%	2.99%	13.19%
Printing speed	10.11%	1.85%	8.12%

These findings can be used to optimize the printing process and improve the mechanical properties of the printed parts. By selecting the appropriate material and optimizing the printing temperature and layer thickness, it is possible to achieve the desired mechanical properties for 3D printed parts, contributing to the development of more sustainable and environmentally friendly materials.

Moreover, thanks to the models created to predict the mechanical properties studied, 3d plots of the response surfaces of these properties are created in Figures 72, 73, 74, 75, 76, and 77. These plots can approve the study of the feature importance.

3.4.4.2 Analysis of response surfaces

The response surfaces presented in Annexe 1 provide additional insights into the influence of the printing parameters on the mechanical properties of the PLA and PLA-CF specimens.

For PLA-CF, the response surfaces show that the ultimate tensile strength decreases with increasing layer thickness and printing speed. The printing temperature has a more complex influence on the ultimate tensile strength, with the highest values observed in a range of temperatures between 210°C and 225°C. Young's modulus increases with increasing layer

thickness at high printing speeds and low temperatures. The strain at break has its maximum values at a range of layer thicknesses between 0.375mm and 0.425mm, and increases with increasing printing temperature and decreasing printing speed.

For PLA, the response surfaces show that printing temperature has the highest influence on the ultimate tensile strength, with an increase in strength observed with increasing temperature. Layer thickness has a significant influence on Young's modulus, with an increase in modulus observed with increasing layer thickness. The increase in printing speed also produces a higher Young's modulus. The maximum values of strain at break for PLA specimens appear at a range of layer thicknesses between 0.375mm and 0.425mm, a range of printing speed between 45mm/s and 55mm/s, and at low temperatures.

These findings coincide with the studies of Othman et al. [8] who used PLA as printing material and layer thickness and other process parameters to study their influence on the mechanical properties of the printed parts and Aissa et al. [12] who used printing temperature, layer thickness and printing speed and Reinforced Polyamide as printing materials. The findings also confirm the importance of feature importance analysis, presented in the previous section, and the need for optimizing the printing parameters to achieve the desired mechanical properties.

3.4.5 Optimization of the process parameters

After the analysis presented in Section 3.4, it is concluded that the material used has the most significant influence on the mechanical properties studied. Once the appropriate material is selected, the choice of the process parameters depends on the desired mechanical properties. Therefore, to optimize these relationships and find the optimal set of printing parameters for a given material, a Genetic Algorithm was used.

3.4.5.1 Genetic algorithm

The Genetic Algorithm (GA) is a population-based stochastic optimization algorithm that was inspired by Charles Darwin's theory of evolution. The GA algorithm begins by creating an initial population of multiple solutions that represent the chromosomes of the individuals. The fitness of each individual in the population is then evaluated by calculating a fitness score [33]. Natural selection is applied by selecting the fittest individuals from the population. Crossover and mutation are then applied to produce offspring that descend from the fittest individuals.

The crossover operator takes two parents and produces two offspring by exchanging parts of their chromosomes. The mutation operator introduces small random changes to the offspring's chromosomes to promote diversity in the population. These operators are used to produce a new population, and the process of selection, crossover, and mutation is repeated until the termination criteria are achieved.

The use of GA in 3D printing optimization has become increasingly popular in recent years due to its ability to find the optimal set of printing parameters efficiently. By using GA, it is possible to search through a large parameter space and find the best set of parameters that result in the desired mechanical properties of the printed parts. Figure 26 summarizes the GA process, showing the steps involved in generating the initial population, evaluating fitness, selecting the fittest individuals, and applying crossover and mutation to produce offspring for the next generation.

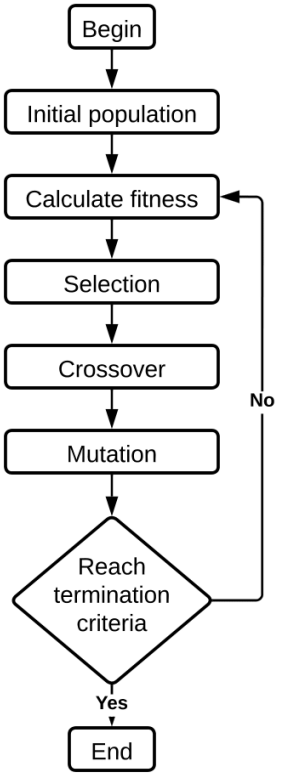

Figure 26. Flow chart of the Genetic Algorithm.

3.4.5.2 Optimization of the process parameters

The fitness function used in the genetic algorithm plays a crucial role in determining the optimal set of process parameters. In this study, the fitness function is defined as a weighted sum of the predicted mechanical properties using the process parameters. The weights of each mechanical property are determined by the user, based on the application of the printed part and the importance of each property in the design criteria.

The fitness function (Equation 13) includes the ultimate tensile strength, Young's modulus, and strain at break as predicted mechanical properties. The process parameters to optimize are the material (m) used, printing temperature (t), layer thickness (h), and printing speed (s). The

predicted mechanical properties, $\hat{\sigma}$, $\hat{E}$, and $\hat{\epsilon}$, are calculated using the ensemble learning models trained in Section 3.3.

$$f(m,t,h,s) = \alpha \times \frac{\hat{\sigma}}{\bar{\sigma}} + \frac{\beta \times \hat{E}}{\bar{E}} + \frac{\gamma \times \hat{\epsilon}}{\bar{\epsilon}} \quad (13)$$

To normalize the mechanical properties, the average values of the mechanical properties in the collected data, $\bar{\sigma}$, $\bar{E}$, and $\bar{\epsilon}$, are used in the fitness function. This normalization is important to ensure that the optimization process is not biased toward a specific mechanical property. The weights of the mechanical properties, α, β, and γ, are assigned by the user. These weights determine the importance of each mechanical property in the optimization process. The user can assign higher weights to the properties that are more critical to the application of the printed part.

By using the fitness function in the genetic algorithm, it is possible to efficiently search for the optimal set of process parameters that result in the desired mechanical properties of the printed parts. This approach can significantly reduce the time and cost required to find the optimal printing parameters for a given material and application.

Equation 14 represents the range of values for the parameters that will be optimized by the Genetic Algorithm. The optimization process aims to maximize the fitness function while keeping the printing temperature, layer thickness, printing speed, and printing material within the specified range. By setting these boundaries, the GA algorithm can efficiently search for the optimal set of parameters that result in the desired mechanical properties of the printed parts. The range of values for each parameter is based on the experimental results obtained in the previous sections and represents the feasible and optimal values for the printing parameters.

$$\begin{cases} \text{maximize } f \\ m \in \{0,1\};\ 0 \text{ attributed to PLA and } 1 \text{ attributed to PLA-CF} \\ 200°\text{C} < t < 230°\text{C} \\ 0.25\text{mm} < h < 0.45\text{mm} \\ 40\text{mm/s} < \text{s} < 60\text{mm/s} \end{cases} \quad (14)$$

During each generation, the fitness score of each individual is calculated using the weighted sum of predicted mechanical properties based on the parameters assigned by the user. The top five fittest individuals are then selected to create the next generation through crossover and mutation. This process is repeated until the termination criteria, which is set to a maximum of 250 generations, is reached.

Figure 27 shows the evolution of fitness scores over the 250 generations. As can be seen, the fitness score improves significantly from the initial population to the later generations. This indicates that the genetic algorithm is effective in finding the optimal set of parameters that maximize the desired mechanical properties. The best individual found by the algorithm

provides the optimal combination of printing parameters to achieve the desired mechanical properties for the printed parts.

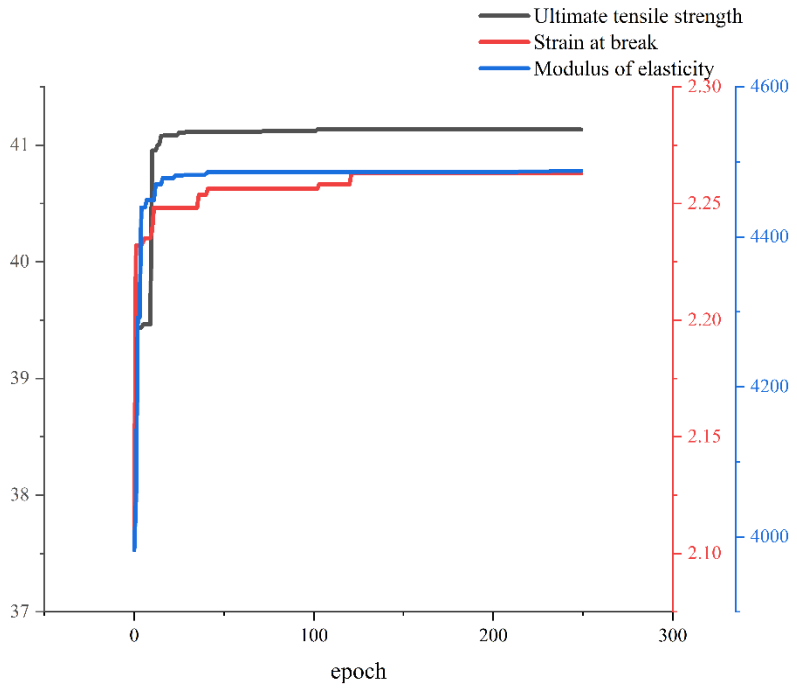

Figure 27. The optimal solution for each iteration of the optimization process for the mechanical properties.

The results summarized in Table 13 show the optimal solutions for different mechanical properties using Fused Filament Fabrication (FFF) 3D printing with PLA-CF (Polylactic Acid-Carbon Fiber) and PLA (Polylactic Acid) materials. The optimal values and parameters for each property are as follows:

1. Ultimate Tensile Strength (UTS) - The optimum solution has a value of 41.129 MPa. The optimal parameters for achieving this value are:

- Printing temperature: 222.28°C
- Layer thickness: 0.261mm
- Printing speed: 40.03mm/s
- Material: PLA-CF

2. Young's Modulus - The optimal value is 4423.63 MPa, and the optimal parameters are:

- Printing temperature: 200.01°C
- Layer thickness: 0.388mm
- Printing speed: 40.038mm/s
- Material: PLA-CF

Note: In this case, the goal was to maximize Young's modulus, which is unusual. To search for the minimum, one could change the weight attributed to Young's modulus in the fitness function by changing its value to -1, for example.

3. Strain at Break - The optimal solution has a value of 2.249%. The parameters for achieving this value are:

- Printing temperature: 200.34°C
- Layer thickness: 0.39mm
- Printing speed: 45.30mm/s
- Material: PLA

According to the literature, as layer thickness increases, Ultimate tensile strength decreases [33], which explains the low layer thickness value produced by the GA method. Furthermore, Huynh et al. [34] demonstrated that increasing the temperature from 200°C to 220°C using PLA as a printing material greatly enhances ultimate tensile strength, which explains the printing temperature of 222.28°C coming from ultimate tensile strength optimization.

These results are confirmed by the response surfaces presented in Figures 73, 74, 75, 76, 77, and 78. These figures demonstrate the relationships between the process parameters and the mechanical properties of the printed materials.

Table 13. Solutions to the optimization process.

Mechanical property	Value	Material	Printing temperature	Layer thickness	Printing speed
Ultimate tensile strength	41.129MPa	PLA-CF	222.28°C	0.261mm	40.30mm/s
Young's Modulus	4423.63MPa	PLA-CF	200.01°C	0.388mm	40.38mm/s
Strain at break	2.249%	PLA	200.34°C	0.390mm	45.30mm/s

3.5 Conclusion and prospects

This article presents a data-driven modeling approach to predict the Ultimate Tensile Strength (UTS), Young's Modulus, and Strain at Break of PLA and PLA-CF dog-bone specimens. The specimens were manufactured according to ASTM D638-14 Type I and tested using a universal tensile material testing system (MTS). The study investigated the influence of material type and process parameters such as printing temperature, printing speed, and layer thickness on the mechanical properties. A Genetic Algorithm was employed to optimize the process parameters for specific conditions. Ensemble learning algorithms, including XGBoost, Gradient Boosting Regressor, Random Forest, Decision Tree, Multiple Linear Regression, Lasso, and Ridge Regression, were used to predict the mechanical properties with high accuracy.

This study has shown that PLA-CF specimens exhibit higher Ultimate Tensile Strength (UTS) and Young's Modulus compared to PLA specimens. For PLA-CF specimens, the following trends were observed in relation to process parameters:

- UTS increases when layer thickness and printing speed decrease, with maximum values at printing temperatures between 210°C and 225°C.
- Young's Modulus increases with increasing layer thickness and printing speed and decreasing printing temperature.
- Strain at Break increases with increasing printing temperature and decreasing printing speed, with maximum values for layer thicknesses between 0.375mm and 0.425mm.

For PLA specimens, the following trends were observed:

- Both UTS and Young's Modulus increase when all studied process parameters (printing temperature, printing speed, and layer thickness) increase.
- Strain at Break increases when printing temperature decreases, with maximum values for layer thicknesses between 0.375mm and 0.425mm and printing speeds between 45mm/s and 55mm/s.

The Genetic Algorithm used in the study produced values of 41.129 MPa for UTS, 4423.63 MPa for Young's Modulus, and 2.249% for Strain at Break.

The study focused on the effect of printing materials (PLA and PLA-CF) and process parameters (printing speed, printing temperature, and layer thickness) on the mechanical properties of 3D printed parts. Future research aims to investigate the influence of additional process parameters, such as infill density and bed temperature, on the mechanical properties of 3D printed parts, as well as explore more materials to broaden the scope of the study.

3.6 Acknowledgments

The authors acknowledge the funding provided by the Natural Sciences and Engineering Research Council (NSERC) of Canada and Canada Research Chair Program.

3.7 Declarations

Conflicts of interests

The authors certify that they have NO affiliations with or involvement in any organization or entity with any financial interest or non-financial interest in the subject matter or materials discussed in this manuscript.

Author Contribution

Conceptualization, Abdelhamid Ziadia; Formal analysis, Mohamed Habibi and Abdelhamid Ziadia; Funding acquisition, Mohamed Habibi and Sousso Kelouwani; Investigation,

Abdelhamid Ziadia; Methodology, Mohamed Habibi; Software, Abdelhamid Ziadia; Supervision, Mohamed Habibi and Sousso Kelouwani; Writing – original draft, Abdelhamid Ziadia; Writing – review & editing, Mohamed Habibi.

3.8 References

[1] Khosravani, M.R., Reinicke, T.: On the environmental impacts of 3D printing technology. Applied Materials Today (2020), 20, 100689. https://doi.org/10.1016/j.apmt.2020.100689

[2] Shaqour, B., Abuabiah, M., Abdel-Fattah, S., Juaidi, A., Abdallah, R., Abuzaina, W., Qarout, M., Verleije, B., Cos, P.: Gaining a better understanding of the extrusion process in fused filament fabrication 3D printing: a review. International Journal of Advanced Manufacturing Technology (2021), 114(5-6), 1279–1291. https://doi.org/10.1007/ s00170-021-06918-6

[3] Radadiya, V.A., Gandhi, A.H.: A Study of Tensile Characteristics for Glass and Carbon Fiber Along with Sandwiched Reinforced ABS Composites. Journal of The Institution of Engineers (India): Series C (2022), 103(5), 1049–1057. https://doi.org/10.1007/s40032-022-00848-2

[4] Farhan Khan, M., Alam, A., Ateeb Siddiqui, M., Saad Alam, M., Rafat, Y., Salik, N., Al-Saidan, I.: Real-time defect detection in 3D printing using machine learning. Materials Today: Proceedings (2020), 42, 521–528. https://doi.org/10.1016/j.matpr.2020.10.482

[5] Gebisa, A.W., Lemu, H.G.: Influence of 3D printing FDM process parameters on tensile property of ultem 9085. Procedia Manufacturing (2019), 30, 331–338. https://doi.org/10.1016/j.promfg.2019.02.047

[6] Rodr´ıguez-Panes, A., Claver, J., Camacho, A.M.: The influence of manufacturing parameters on the mechanical behaviour of PLA and ABS pieces manufactured by FDM: A comparative analysis. Materials (2018), 11(8). https://doi.org/10.3390/ma11081333

[7] Ning, F., Cong, W., Qiu, J., Wei, J., Wang, S.: Additive manufacturing of carbon fiber reinforced thermoplastic composites using fused deposition modeling. Composites Part B: Engineering (2015), 80, 369–378. https://doi.org/10.1016/j.compositesb.2015.06.013

[8] H. Chokshi, D.B. Shah, K.M. Patel, S.J. Joshi.: Experimental investigations of process parameters on mechanical properties for PLA during processing in FDM, Advances in Materials and Processing Technologies (2022), 8(sup2), 696-709. https://doi.org/10.1080/2374068X.2021.1946756

[9] F.M. Othman, T. Fadhil, A.H.B. Ali, Influence of process parameters on mechanical properties and printing time of FDM PLA printed parts using design of experiment, J. Eng. Res 8 (2018) 2248-9622.

[10] Love, L.J., Kunc, V., Rios, O., Duty, C.E., Elliott, A.M., Post, B.K., Smith, R.J., Blue, C.A.: The importance of carbon fiber to polymer additive manufacturing. Journal of Materials Research (2014), 29(17), 1893–1898. https://doi.org/10.1557/jmr.2014.212

[11] Torrado Perez, A.R., Roberson, D.A., Wicker, R.B.: Fracture surface analysis of 3D-printed tensile specimens of novel ABS-based materials. Journal of Failure Analysis and Prevention (2014), 14(3), 343–353. https://doi.org/10.1007/s11668-014-9803-9

[12] Ouballouch, A., Alaiji, R.E., Ettaqi, S., Bouayad, A., Sallaou, M., Lasri, L.: Evaluation of dimensional accuracy and mechanical behavior of 3D printed reinforced polyamide parts. Procedia Structural Integrity (2019), 19, 433– 441. https://doi.org/10.1016/j.prostr.2019.12.047

[13] R.T. Mushtaq, A. Iqbal, Y. Wang, M. Rehman, M.I. Petra, Investigation and Optimization of Effects of 3D Printer Process Parameters on Performance Parameters, Materials (2023) 16(9) 3392. https://doi.org/10.3390/ma16093392

[14] Zhang, Z., Shi, J., Yu, T., Santomauro, A., Gordon, A., Gou, J., Wu, D.: Predicting flexural strength of additively manufactured continuous carbon fiber- reinforced polymer composites using machine learning. Journal of Computing and Information Science in Engineering (2020), 20(6), 1–9. https://doi.org/10.1115/1.4047477

[15] Goh GD, Yap YL, Tan HKJ, et al: Process--structure--properties in polymer additive manufacturing via material extrusion: A review. Crit Rev Solid State Mater Sci (2020), 45:113–133

[16] Maulud, D., Abdulazeez, A.M.: A Review on Linear Regression Compre- hensive in Machine Learning. Journal of Applied Science and Technology Trends (2020), 1(4), 140–147. https://doi.org/10.38094/jastt1457

[17] J.H.R. Huang, C.-Y. Wu, H.-M. Chan, J.-Y. Ciou, Printing parameters of Sugar/Pectin Jelly Candy and application by using a decision tree in a hot-extrusion 3D printing system, Sustainability 14(18) (2022) 11618. https://doi.org/10.3390/su141811618

[18] J.M. Barrios, P.E. Romero, Decision tree methods for predicting surface roughness in fused deposition modeling parts, Materials (2019), 12(16), 2574. https://doi.org/10.3390/ma12162574

[19] B. Ghojogh, M. Crowley, The theory behind overfitting, cross validation, regularization, bagging, and boosting: tutorial, arXiv preprint arXiv:1905.12787 (2019). https://doi.org/10.48550/arXiv.1905.12787

[20] Y. Ma, M.A. Schutyser, R.M. Boom, L. Zhang, Predicting the extrudability of complex food materials during 3D printing based on image analysis and gray-box data-driven modelling, Innovative Food Science & Emerging Technologies (2021), 73 102764. https://doi.org/10.1016/j.ifset.2021.102764

[21] X. Li, M. Zhang, M. Zhou, J. Wang, W. Zhu, C. Wu, X. Zhang, Qualify assessment for extrusion-based additive manufacturing with 3D scan and machine learning, Journal of Manufacturing Processes (2023), 90 274-285. https://doi.org/10.1016/j.jmapro.2023.01.025

[22] S. Lee, J. Park, N. Kim, T. Lee, L. Quagliato, Extreme Gradient Boosting-inspired process optimization algorithm for manufacturing engineering applications, Materials & Design 226 (2023) 111625. https://doi.org/10.1016/j.matdes.2023.111625

[23] R. Cai, K. Wang, W. Wen, Y. Peng, M. Baniassadi, S. Ahzi, Application of machine learning methods on dynamic strength analysis for additive manufactured polypropylene-based composites, Polymer Testing (2022), 110 107580. https://doi.org/10.1016/j.polymertesting.2022.107580

[24] Wu, T., Zhang, W., Jiao, X., Guo, W., Alhaj Hamoud, Y.: Evaluation of stacking and blending ensemble learning methods for estimating daily reference evapotranspiration. Computers and Electronics in Agriculture (2021) (October 2020), 184 106039. https://doi.org/10.1016/j.compag.2021.106039

[25] Cui, S., Yin, Y., Wang, D., Li, Z., Wang, Y.: A stacking-based ensemble learning method for earthquake casualty prediction. Applied Soft Computing (2021), 101, 107038. https://doi.org/10.1016/j.asoc.2020.107038

[26] Sun, W., Trevor, B.: A stacking ensemble learning framework for annual river ice breakup dates. Journal of Hydrology (2018), 561, 636–650. https://doi.org/10.1016/j.jhydrol.2018.04.008

[27] A.K. Gupta, M. Taufik, Investigation of dimensional accuracy of material extrusion build parts using mathematical modelling and artificial neural network, International Journal on Interactive Design and Manufacturing (IJIDeM) (2023), 17(2) 869-885. https://doi.org/10.1007/s12008-022-01186-4

[28] Chicco, D., Warrens, M.J., Jurman, G.: The coefficient of determination R-squared is more informative than SMAPE, MAE, MAPE, MSE and RMSE in regression analysis evaluation. PeerJ Computer Science (2021), 7, 1–24. https://doi.org/10.7717/PEERJ-CS.623

[29] Materials, P., Materials, E.I.: Standard Test Method for Tensile Properties of Plastics (2015), 1, 1–17. https://doi.org/10.1520/D0638-14.1

[30] J. Butt, R. Bhaskar, V. Mohaghegh, Investigating the effects of extrusion temperatures and material extrusion rates on FFF-printed thermoplastics, The International Journal of Advanced Manufacturing Technology (2021), 117(9-10) 2679-2699. https://doi.org/10.1007/s00170-021-07850-5

[31] P. Wang, B. Zou, H. Xiao, S. Ding, C. Huang, Effects of printing parameters of fused deposition modeling on mechanical properties, surface quality, and microstructure of PEEK, Journal of Materials Processing Technology (2019), 271 62-74. https://doi.org/10.1016/j.jmatprotec.2019.03.016

[32] M. Spoerk, C. Holzer, J. Gonzalez-Gutierrez, Material extrusion-based additive manufacturing of polypropylene: A review on how to improve dimensional inaccuracy and warpage, Journal of Applied Polymer Science (2020) 137(12) 48545. https://doi.org/10.1002/app.48545

[33] R. Feng, J. Jiang, Z. Sun, A. Thakur, X. Wei, A hybrid of genetic algorithm and particle swarm optimization for reducing material waste in extrusion-based additive manufacturing, Rapid Prototyping Journal (2021) 27(10) 1872-1885. https://doi.org/10.1108/RPJ-11-2020-0292

[34] Srinivasan R, Prathap P, Raj A, et al Influence of fused deposition modeling process parameters on the mechanical properties of PETG parts. Materials Today: Proceedings (2020) 27:1877–1883 https://doi.org/10.1016/j.matpr.2020.03.809

[35] Huynh LPT, Nguyen HA, Nguyen HQ, et al Effect of process parameters on mechanical strength of fabricated parts using the fused deposition modelling method (2019). http://doi.org/10.7736/KSPE.2019.36.8.705

Chapitre 4: Optimisation Taguchi pilotée par micro-CT pour réduire les vides en FDM

CT-Driven Taguchi Optimization for Void Reduction in FDM 3D Printing. Abdelhamid ZIADIA, Mohamed HABIBI, Sousso KELOUWANI, Sheena YAN & Yasmine ABDIN.

Dans le prolongement direct du chapitre 3, qui a fourni des modèles prédictifs robustes et un cadre d'optimisation multi-objectif reliant paramètres de procédé et performances mécaniques, ce chapitre transpose la même boîte à outils vers la qualité interne de la matière. La porosité est prise comme critère central et la micro-CT comme référence métrologique. L'objectif est de proposer des réglages globaux robustes et un schéma d'ajustements couche par couche pour réduire la surface moyenne des vides tout en maîtrisant la charge expérimentale.

Le chapitre met en place un dispositif dédié à la porosité mesurée par micro-CT. Les éprouvettes sont imprimées sur une Prusa MK3S+ avec une buse de 0,40 mm et un filament PLA. La géométrie est un coupon de 10 × 10 × 2 mm, construit à plat avec une densité de remplissage de 100% et un seul périmètre. Les paramètres non étudiés restent constants pour isoler les effets. Les acquisitions micro-CT sont réalisées à résolution isotrope de 15 µm avec un objectif 0,4×, une tension de 60 kV et une puissance de 5 W. Les piles d'images TIFF exportées du reconstructeur servent d'entrée au pipeline d'analyse.

Le plan d'expérience adopte une matrice Taguchi L9 sur quatre facteurs à trois niveaux chacun. La température d'extrusion prend les niveaux 200, 215 et 230 °C. La température du lit prend 50, 60 et 70 °C. L'épaisseur de couche prend 0,20, 0,30 et 0,40 mm. Le débit prend 95, 100 et 105 %. Ce choix remplace 81 essais par 9, ce qui réduit fortement le coût d'acquisition CT tout en permettant de lire clairement les effets principaux.

Le traitement d'images aligne d'abord les volumes sur l'axe de dépôt et normalise l'intensité. La segmentation sépare l'air et le polymère par seuillage global, suivie d'un nettoyage morphologique avec fermeture, suppression des petites régions isolées et filtrage médian puis gaussien. Les composantes sont étiquetées et un filtre robuste basé sur l'intervalle interquartile élimine les artefacts rares. Chaque vide est associé à un numéro de couche en fonction de sa position dans l'empilement. Pour chaque couche d'un spécimen, les aires des vides sont agrégées et résumées par la moyenne, l'écart type et l'effectif, ce qui constitue la table d'analyse.

L'analyse statistique s'appuie sur une ANCOVA en moindres carrés pondérés par le nombre de vides par couche. Le modèle inclut les quatre facteurs, un terme linéaire de numéro de

couche pour capter l'évolution avec la hauteur et un blocage par spécimen. La robustesse est évaluée en parallèle via le rapport signal-bruit de type plus petit est le mieux de Taguchi, calculé sur les résumés couche par couche et agrégé par niveau de facteur, puis décliné par couche pour dériver un planning vertical.

Les résultats montrent un ajustement de bonne qualité avec un coefficient de détermination de 84.9% et des résidus acceptables. Après ajustement sur le numéro de couche, toutes les variables de procédé sont significatives. La hiérarchie d'influence indiquée par les η^2 partiels place la température de lit en tête, suivie du débit, puis de l'épaisseur de couche et de la température d'extrusion. Le numéro de couche est lui-même significatif, ce qui confirme une dépendance à la hauteur et motive un réglage adaptatif.

Le rapport signal-bruit identifie une recette globale facile à appliquer. La combinaison température d'extrusion à 230 °C, température de lit à 50 °C, épaisseur de couche à 0,20 mm et débit à 105% abaisse la moyenne prédite des aires de vides à environ 16,78 pixels contre 63,68 en condition témoin milieu de gamme. Cela correspond à une réduction d'environ 73.7% par rapport au témoin et d'environ 60.1% par rapport à la moyenne du jeu de données. Ces directions concordent avec les effets moyens ajustés et le classement des facteurs.

Au-delà de la recette globale, un planning couche par couche dérivé des courbes signal-bruit permet d'améliorer encore la performance. Les couches basses bénéficient d'une extrusion plus chaude à 230 °C pour favoriser la fusion sur un socle relativement froid, le lit restant majoritairement à 50 °C. L'épaisseur de couche de 0,20 mm et un débit élevé à 105 % réduisent les lacunes inter-routes et améliorent la coalescence. Lorsque la pièce gagne en masse thermique, la température d'extrusion peut par moments redescendre vers 200 °C pour limiter l'étalement visqueux et les micro-déformations. Le lit peut localement être porté à 60 °C sur une plage étroite afin de stabiliser la géométrie. Une épaisseur de 0,30mm peut être momentanément préférée si elle réduit la variance à une hauteur donnée. Le débit peut, en fin de pièce, revenir vers 95 % lorsque le recouvrement est déjà important. Ce planning surpasse la recette témoin à chaque couche considérée, avec des gains plus marqués en début d'empilement.

L'apport du chapitre est double. D'abord, il décrit une méthode guidée par la micro-CT, reproductible et économe en essais, qui va de l'imagerie complète de la pièce à l'ANCOVA pondérée et à l'analyse Taguchi couche par couche. Ensuite, il fournit des consignes d'impression immédiatement déployables et un planning par hauteur compact, en cohérence avec la consolidation inter-couches et l'accumulation thermique observées, sans modélisation thermique explicite. Enfin, il ouvre la voie à un contrôle en boucle fermée en préparant l'intégration d'un contrôleur à ajustements graduels et encadrés sur la température d'extrusion, la température de

lit, l'épaisseur de couche et le débit, afin de viser une réduction active des vides pendant l'impression.

CT-Driven Taguchi Optimization for Void Reduction in FDM 3D Printing

Abdelhamid Ziadia[1], Mohamed Habibi[1, *], Sousso Kelouwani[1], Sheena Yan[2] & Yasmine Abdin[2]

Affiliation 1; University of Quebec in Trois-Rivieres, (Department of Mechanical Engineering), Trois-Rivieres, (Quebec), Canada

Affiliation 2; University of British Columbia, (Department of Materials Engineering), Vancouver, BC, Canada

*Correspondence: erima@uqtr.ca

4.1 Abstract

FDM 3D printed parts often suffer from inter-layer voids that degrade strength and reliability. This work introduces a CT-driven, statistically grounded workflow that uses whole-part CT scans with void statistics mapped to layer numbers to suppress voiding. PLA coupons were printed under a Taguchi L9 design varying Printing Temperature, Bed Temperature, Layer Thickness, and Flow Rate. Micro-CT images were segmented to compute layer-level void metrics, which were analyzed via weighted least-squares ANCOVA with adjustment for layer number and specimen blocking. All four factors significantly influenced mean void area, with an effect hierarchy led by Bed and Flow, followed by LT and PT. The model showed strong fit with a R^2 of 84.9%. A Smaller-the-Better signal-to-noise analysis yielded a single robust global recipe with Printing Temperature of 230 °C, a Bed Temperature of 50 °C, a Layer Thickness of 0.20 mm, and a Flow Rate of 105%, predicting a 73.7% reduction versus a mid-level baseline and 60.1% versus the dataset average. A compact, layer-adaptive schedule delivered an additional void-weighted reduction of 69%, with the largest gains in early layers and smaller gains where scheduled levels briefly converge toward baseline. The workflow provides immediately deployable settings and height-aware tuning and establishes a reproducible benchmark for future studies extending to additional process parameters, infill patterns, more complex geometries, and in-situ control.

Keywords: Additive manufacturing, Fused Deposition Modeling, Process optimization, Micro-computed tomography, Porosity.

4.2 Introduction

Fused Deposition Modeling (FDM) is a 3D printing process that builds parts layer by layer from melted plastic. A solid filament is pushed into a heated nozzle, the plastic softens, and the printer lays down a thin bead along planned paths. When one layer is finished, the build plate or the print head moves by the set layer thickness, and the next layer is placed on top. Layers bond by heat and contact, turning a digital model into a physical part [1, 2].

FDM is widely used because it is low-cost, fast, and flexible. It produces complex geometries without molds or tooling, supports on-demand customization, and shortens lead times from design to part. A broad range of thermoplastics is available, from general-purpose to engineering grades, so properties can be matched to use [3-5]. These advantages make FDM increasingly attractive for industrial use, where it enables rapid iteration, small-batch production, and ready availability of functional parts, fixtures, and spares with reduced inventory and time-to-market [6-8].

However, FDM still has limitations, particularly in choosing the best parameters that critically influence production quality and efficiency [8-11]. One of these limitations, and the focus of this study, is the presence of microscopic voids within and between deposited roads. Voids arise from insufficient overlap or flow, poor wetting, or unfavorable cooling, and they often change with layer height as the thermal environment evolves. These defects act as stress concentrators and increase scatter in strength and fatigue [12-14].

To address this issue, researchers have followed three main routes. Before printing, voids are prevented by changing the paths and widths of deposited material, using lower layer height with tuned track width, planning medial-axis toolpaths, and adaptive bead width so corners and tight regions don’t under- or over-fill [15-19]. Another pre-deposition lever is parameter optimization. In fact, many studies show that thinner layers and adequate nozzle temperature reduce inter-filament voids by lowering height and improving flow, with the usual trade-off of longer print time or tighter dimensional control [20-32].

During printing, added heat whether via a warmed platform, a head-mounted heat block, or localized laser reheating, improves wetting and neck growth and has been shown to close voids and raise bond strength. In some cases ultrasonic vibration is used for similar gains [33-41].

After printing or post-processing, thermal, chemical, or mechanical treatments can fuse or fill remaining pores, though benefits depend on polymer and exposure and may introduce time or dimensional-accuracy costs [21, 40-46].

Most studies that try to reduce voids in FDM do one of three things: change paths and optimize parameters before printing, add heat or ultrasonics during printing, or apply post-processing after printing. However, two practical gaps remain. First, results are usually reported at the specimen level, even when CT is used, so the way voiding changes with layer height is not modeled explicitly. Second, Taguchi analysis is commonly used to pick robust settings, but it is typically applied to whole-part averages, not to layer-resolved data that could guide settings through the build.

To respond to these gaps, this study measures layer-wise voids by CT scanning and summarizes them layer by layer. A weighted least-squares ANCOVA tests the effect of Printing Temperature, Bed Temperature, Layer Thickness, and Flow Rate on the mean void area while accounting for layer number and specimen-to-specimen differences. In parallel, Taguchi Smaller-the-Better S/N is computed from the same layer summaries to target robustness. S/N is applied specimen-wide to recommend a single, general-use recipe and per-layer to propose a layer-adaptive schedule for printers that allow level changes across height. The outcome is actionable guidance, ranked factor importance, a specimen-wide robust combination, a compact per-layer schedule, and baseline-referenced improvements, complementing the pre-, in-, and post-process strategies surveyed in the literature.

The remainder of this paper is organized as follows:

- Section 2 describes the methodology, including the printing setup and Taguchi L9 factors and levels, CT acquisition, layer mapping, and the analysis workflow.
- Section 3 presents the results which includes the significance and effect hierarchy, baseline-referenced gains for the schedule versus the mid-level baseline.
- Section 4 concludes the paper by reviewing major contributions and identifying possible paths for future additive manufacturing research.

4.3 Methodology

4.3.1 Design of experiment

A Taguchi L9 orthogonal array was used to screen four FDM parameters at three levels each across nine specimens (Table 14): Printing Temperature (200, 215, 230 °C), Bed Temperature (50, 60, 70 °C), Layer Thickness (0.20, 0.30, 0.40 mm), and Flow Rate (95, 100, 105 %). These factors and ranges were selected based on the literature, which repeatedly identifies them as primary levers for void formation and consolidation in material-extrusion printing [21, 47-49]. In brief, printing temperature is the temperature at which the material is extruded from the printer nozzle, bed temperature is the temperature set on the build plate that the first layers are printed onto , layer thickness is the height of each deposited layer in the print, and flow rate is the extrusion multiplier that sets how much material is pushed through the nozzle. The chosen levels span a common, practical window for PLA on a desktop FDM system.

Specimens were printed on a Prusa MK3S+ using PLA 1.75 mm filament and a 0.40 mm nozzle. PLA was chosen because it is bio-sourced, biodegradable, and among the most widely used materials in FDM, making the results broadly applicable [50-54]. The printed geometry was a 10 mm × 10 mm × 2 mm coupon, built flat on the bed with 100 % infill, one perimeter,

and a print speed of 40 mm/s. Aside from the four study factors, all other settings were held constant to isolate factor effects.

Table 14. Taguchi l9 orthogonal array

Run	Printing Temperature (°C)	Bed Temperature (°C)	Layer Thickness (mm)	Flow Rate (%)
1	200	50	0.2	95
2	200	60	0.3	100
3	200	70	0.4	105
4	215	50	0.3	105
5	215	60	0.4	95
6	215	70	0.2	100
7	230	50	0.4	100
8	230	60	0.2	105
9	230	70	0.3	95

The Taguchi L9 was chosen to estimate main effects efficiently with minimal experimental burden, and the small coupon geometry was selected to enable high-resolution CT with shorter scan times. Together, these choices limit the number of parts and the total CT workload, providing a cost- and time-effective methodology while preserving the ability to detect practically important factor effects.

4.3.2 CT imaging, data processing, and data preparation

Each specimen was scanned under identical micro-CT conditions (0.4× objective, 15 μm isotropic voxels). The X-ray tube was set to 60 kV and 5 W with exposure time of 0.7 s per projection. Reconstruction on the scanner produced volumetric data exported as stacked TIFF images, which constitute the input to the analysis.

Image stacks were first cropped to the specimen region and aligned so that the build direction corresponds to the CT z-axis. Void detection was carried out from the stacked TIFFs using a Python workflow. For every slice, polymer and air were separated by a global threshold of 0.5. Morphological closing operations were then applied, followed by the removal of isolated regions and median and Gaussian filtering to attenuate high-frequency noise. For slice, the script extracted 2-D features containing area in voxels, bounding-box limits, solidity, and centroid and recorded the slice index for each void. Components outside the part region of interest or touching the exterior boundary were excluded. The attribution of the layer number for each void was manually based on the position of the it. A minimum-area rule removed tiny detections attributable to noise. Each void was also saved as a fixed-size (128×128) binary image patch, centered within a square canvas to standardize downstream processing. Per-layer

statistics (mean, standard deviation, and count of void areas) were then computed by grouping detections by specimen and layer number. To guard against rare segmentation defects, a robust tail filter (IQR-based) was applied to eliminate extreme outliers for each layer. For every specimen-LN pair, individual void areas within that layer were aggregated to form the analysis table used throughout the study. The table records the mean void area, the standard deviation, and the count of voids, alongside the four print settings.

4.3.2.1 Response, aggregation, weighting, and S/N computation

The primary response is the area of voids. For each layer of specimen printed, the mean area of voids ($\bar{y}_i$), standard deviation (s_i), and count (n_i) are calculated. Robustness metrics require a sum of squares, the layer-wise total of squared void areas is reconstructed from summaries via

$$\sum_{j=1}^{n_i} y_{ij}^2 = (n_i - 1)s_i^2 + n_i\bar{y}_i^2 \qquad (15)$$

All analyses use the cleaned data with variables, specimen number, layer number, mean area of voids, standard deviation of voids, number of voids, printing temperature, bed temperature, layer thickness, and flow rate.

Effects of the print parameters on mean void area are estimated using weighted least squares (WLS) ANCOVA applied to the layer summaries:

$$\bar{y}_i = \mu + \tau_{\mathrm{PT}}(\mathrm{PT}_i) + \tau_{\mathrm{Bed}}(\mathrm{Bed}_i) + \tau_{\mathrm{LT}}(\mathrm{LT}_i) + \tau_{\mathrm{Flow}}(\mathrm{Flow}_i) + \beta\mathrm{LN}_i + \gamma_{\text{specimen }(i)} + \varepsilon_i \qquad (16)$$

Here, μ is the intercept; each $\tau_{\cdot}(\cdot)$ denotes the setting effect function for that parameter across its three preset settings (per example PT = 200, 215, 230), β captures the linear trend with height (layer number), and $\gamma_{\text{specimen }(i)}$ is a fixed blocking term that absorbs between-specimen baselines. Estimation uses weights $\omega_i = n_i$ (number of voids in layer i), reflecting $\mathrm{Var}(\bar{y}_i) \approx \sigma^2/n_i$ to stabilize heteroscedasticity and give greater influence to better-estimated layer means. Inference relies on Type-II ANOVA for the fitted WLS model, reporting F-statistics and p-values (significance at $p < 0.05$). Effect magnitude is summarized by η^2,

$$\eta^2_{\text{partial}} = \frac{SS_{\text{effect}}}{SS_{\text{effect}} + SS_{\text{error}}}. \qquad (17)$$

Here, SS_{effect} is the variability attributed to a specific term (a print parameter or layer number) after accounting for the other terms, and SS_{error} is the unexplained variability of the full model. Model adequacy is summarized by R^2.

Robustness is evaluated with the Smaller-The-Better signal-to-noise ratio:

$$S/N_{STB} = -10\log_{10}\left(\frac{\sum_i \sum_{j=1}^{n_i} y_{ij}^2}{\sum_i n_i}\right) \quad (18)$$

using Equation 4 above, S/N is computed overall (across all LNs) for each setting of each parameter to identify a single global combination, and per LN to obtain a height-resolved best-setting-versus-LN profile. Larger (less negative) S/N indicates lower mean void area and greater within-setting consistency.

By using this methodology, the study will generate a clear finding on which print parameters significantly affect void area and their relative influence, a specimen-wide optimal combination of parameters with the expected improvement, and a layer-by-layer optimal schedule across the build height.

4.4 Results

4.4.1 Data overview

All CT-derived planar measurements are expressed in physical units using a calibration of 15 µm per pixel, which corresponds to a per-pixel area of 225 µm². Reported void areas are therefore obtained by multiplying the segmented pixel counts by 2.25×10^{-4} mm², ensuring that all layer and specimen summaries are directly comparable in metric units.

The specimen-level distribution of mean void area shows clear dispersion (Figure 28(a)), with most specimens clustered at low and moderate values and a minority exhibiting larger means. This spread indicates that internal quality varies meaningfully with process parameters and build volume, motivating a layer-aware analysis.

The position of the voids analysis further verifies positional consistency and low noise in the detections. Plotting voids z position versus layer of ct scan (Figure 28(b)) yields continuous horizontal bands that persist across the full stack, demonstrating that voids are distributed between layers. This cross-layer persistence, together with area thresholding and cleanup, indicates that noise has been effectively suppressed, and that retained data correspond to true void geometry suitable for subsequent statistical modeling.

4.4.2 Parameter significance and influence

The WLS-ANCOVA showed good fit with R^2=84.9% (Figure 29) and residuals exhibited no discernible trend or variance funnel, supporting model assumptions.

Table 15 indicates that all four print parameters are statistically significant contributors to the mean void area (Prob>F < 0.05 for each), after adjusting for layer number (LN). The accompanying partial η^2 values provide a clear influence hierarchy among the controllable factors:

— Bed Temperature shows the largest effect (partial $\eta 2 \approx 0.75$, $F \approx 68.7$, $p < 10^{-13}$), identifying it as the primary lever for reducing void area.

— Flow Rate exhibits a substantial effect (partial $\eta 2 \approx 0.53$, $F \approx 26.0$, $p < 10^{-7}$), ranking second in influence.

— Layer Thickness has a moderate-to-large effect (partial $\eta 2 \approx 0.34$, $F \approx 12.3$, $p < 0.001$), indicating meaningful but smaller impact than Bed and Flow.

— Printing Temperature also has a moderate effect (partial $\eta 2 \approx 0.33$, $F \approx 11.3$, $p < 0.001$), providing additional tuning capacity.

— The layer number is itself significant (partial $\eta 2 \approx 0.15$, $F \approx 8.27$, $p \approx 0.006$), evidencing a height-dependent trend in void area. This supports complementing the specimen-wide optimization with a layer-resolved analysis, where recommended settings may vary across the build height.

In summary, the ANOVA establishes that all parameters materially affect the response, with Bed Temperature and Flow Rate providing the strongest leverage, Layer Thickness and Printing Temperature offering secondary adjustments, and a significant LN trend motivating the per-layer optimization and confirming the sequential aspect of FDM.

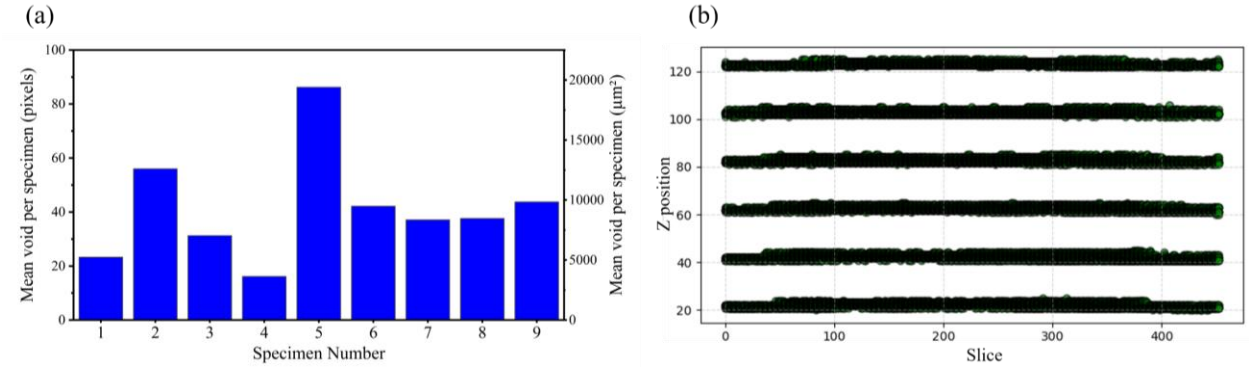

Figure 28. Mean void statistics and positional consistency: (a) Mean void area per specimen, (b) Example of the position of voids.

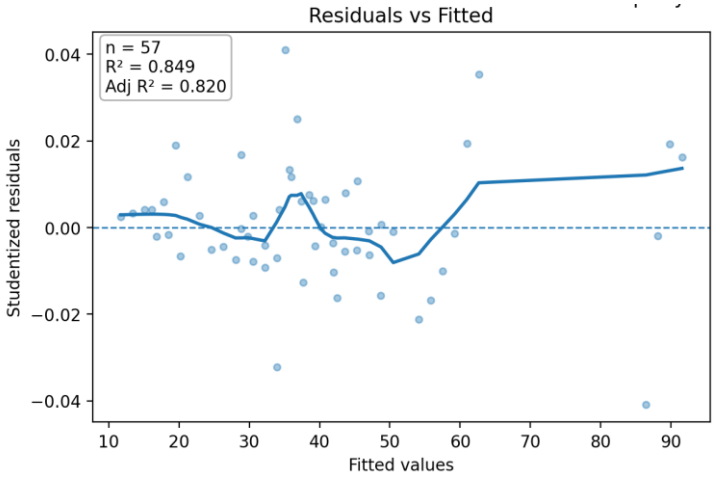

Figure 29. WLS-ANCOVA diagnostics: residuals vs fitted.

Table 15. Type-II ANOVA for the layer-wise model.

Source	df	SS	F	Prob>F	partial η^2	significant_($p<0.05$)
Bed Temperature	2	53582157	68.668	1.13E-14	0.74503	TRUE
Flow Rate	2	20290969	26.004	2.49E-08	0.52529	TRUE
Layer Thickness	2	9618202	12.326	4.97E-05	0.34406	TRUE
Printing Temperature	2	8854545	11.348	9.53E-05	0.32563	TRUE
Layer number	1	3226151	8.2690	0.006043	0.14961	TRUE

4.4.3 Global optimal combination via S/N

Robustness was assessed using the Taguchi Smaller-the-Better signal-to-noise ratio (S/N, dB). S/N was computed from the layer-wise summaries (mean, standard deviation, and count of void areas) and aggregated by factor level, with counts used as weights; larger S/N indicates smaller and more stable void area. This metric provides a single, scale-free score that penalizes both high means and high variability, making it suitable for selecting process settings that generalize across layers and specimens.

Figure 30 summarizes robustness trends across the printing parameters. Flow Rate exhibits a monotonic improvement in robustness, with S/N increasing from 95% to 105% (Figure 30(b)), indicating that higher flow reduces and stabilizes void area. In fact, with more material in each path, the deposited bead is wider, the overlap between adjacent roads increases, and inter-filament gaps close. This lowers the voids area and makes deposition more repeatable [48, 55]. Layer Thickness shows the opposite behavior. In fact, S/N decreases from 0.20 to 0.40 mm (Figure 30(c)), identifying thinner layers as the robust choice. Thicker layers reduce the contact area and local pressure between adjacent/underlying roads, limiting neck growth and interlayer diffusion.. Thinner layers produce wider, more squashed beads with better overlap and more effective thermal bonding, reducing both the mean and the scatter of void area [47, 56, 57]. Bed Temperature and Printing Temperature both present pronounced V-shaped responses (Figure 30(a) and Figure 30(d)): for Bed, the best robustness occurs at 50 °C. For Printing Temperature, 230 °C is best.

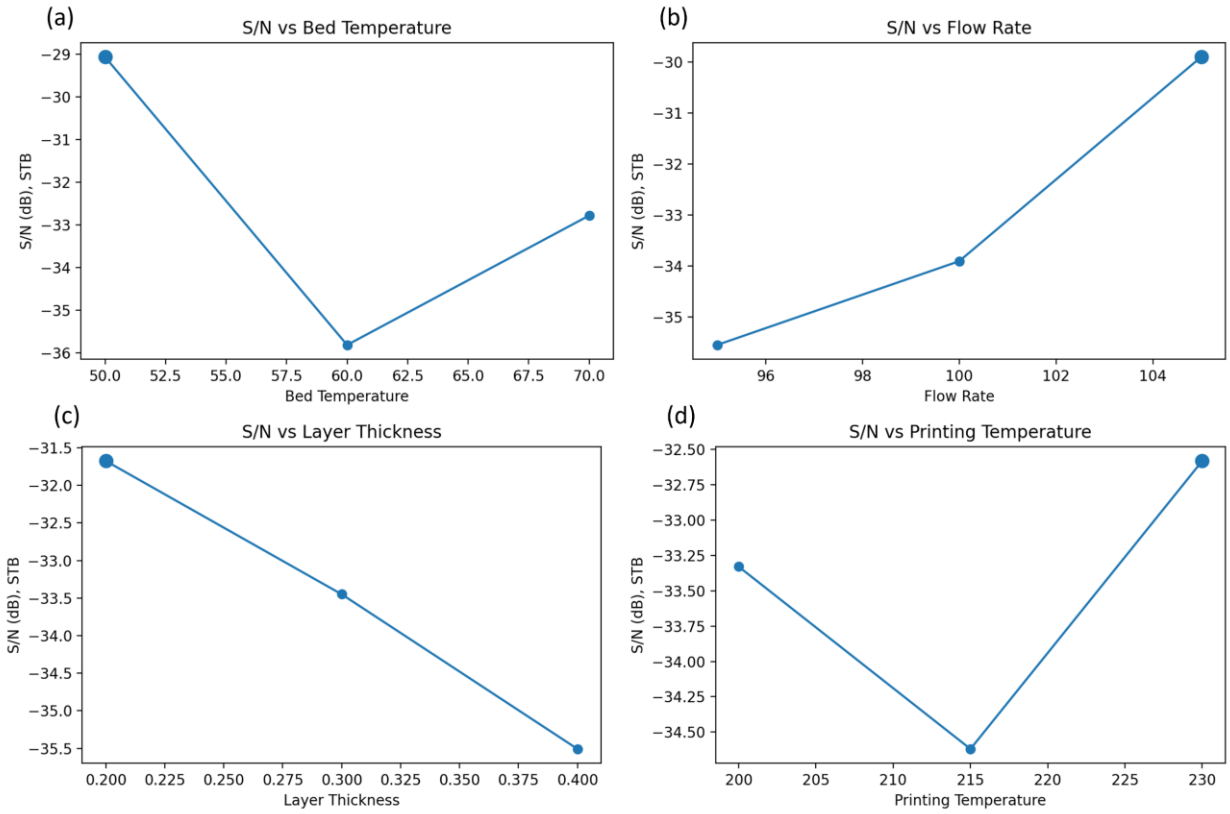

Figure 30. Taguchi Smaller-the-Better signal-to-noise ratio versus factor setting: (a) Bed Temperature, (b) Flow Rate, (c) Layer Thickness, and (d) Printing Temperature.

Taken together, the S/N analysis recommends the specimen-wide robust recipe: Printing Temperature = 230 °C, Bed Temperature = 50 °C, Layer Thickness = 0.20 mm, and Flow Rate = 105%. These directions are consistent with the adjusted-mean main-effect plots and with the ANOVA ranking (largest effects for Bed Temperature and Flow Rate), reinforcing the recommendation.

In summary. Using these results, the S/N-optimal recipe delivers a predicted mean void area of 16.78 pixels (vs. 63.68 at the mid-level baseline), a 73.7% reduction relative to baseline and 60.1% lower than the dataset's overall average. This single, robust setting set simultaneously reduces the average void area and its variability across layers and specimens, aligning with the ANOVA significance and the adjusted-mean trends, and providing an immediately deployable process recipe for void suppression.

4.4.4 Layer adaptative recommendations

The S/N selection at each layer reflects how the local thermal environment evolves with height. Early layers rest on a rigid heated bed, so consolidation is driven by first-layer squish, bead overlap, and rapid freeze. Later layers sit on already-printed material that retains heat longer, shifting the balance between wetting, interdiffusion, and geometric stability. Within this context, higher Flow Rate consistently improves robustness by closing inter-road gaps, a Layer

Thickness of 0.20 mm is generally better because thinner layers increase contact area and re-heating of the previous layer. A Bed Temperature of 50 °C dominates except where a warmer bed locally stabilizes geometry. Printing Temperature toggles between 230 °C for better wetting and 200 °C for reduced overheating depending on local heat accumulation. These per-Layer Number S/N (Annexe 2) curves therefore justify each recommended level and explain departures from the specimen-wide recipe where the height-dependent thermal history changes the optimum.

Figure 31 summarizes the best level (highest S/N) versus LN for all four parameters. For the first nine layers (LN 1-9) this schedule shows:

- Printing Temperature: Early layers benefit from hotter extrusion (230 °C) to promote interfacial fusion on the relatively cool foundation. As the build thickens and retains heat, a lower setpoint (200 °C) can reduce viscosity-driven bead spread and micro-slump, improving repeatability (Figure 31(a)).
- Bed Temperature: A low bed temperature accelerates freeze-in and limits void coalescence for most of the stack. The localized switch to 60 °C suggests a narrow height band where slightly slower solidification improves adherence or mitigates transient warpage, after which conditions revert to favoring 50 °C (Figure 31(b)).
- Layer Thickness: Thinner layers usually enhance overlap and thermal bonding. The momentary preference for 0.30 mm indicates a local variance trade-off at that height, the thicker pass likely stabilizes bead geometry against a transient cooling, raising S/N despite a higher mean (Figure 31(c)).
- Flow Rate: Increasing flow closes pores until a point where overfill begins to add variability. The late-build reduction to 95% is consistent with a modest overfill penalty once the part's thermal mass is larger and path overlap is already high. These step changes indicate modest height-dependent adjustments to the global recipe where local consolidation and cooling conditions shift (Figure 31(d)).

The schedule outperforms the mid-level baseline at every LN considered, with larger gains in early layers and smaller gains where the schedule briefly converges toward baseline settings, like the example at layer number 7 where the bed temperature has a value of 60 °C, or where improvements are dominated by variance reduction rather than mean shift (Figure 32). The void-weighted overall reduction (69%) indicates that, beyond the specimen-wide recipe, per-layer tuning captures additional improvements concentrated at height bands.

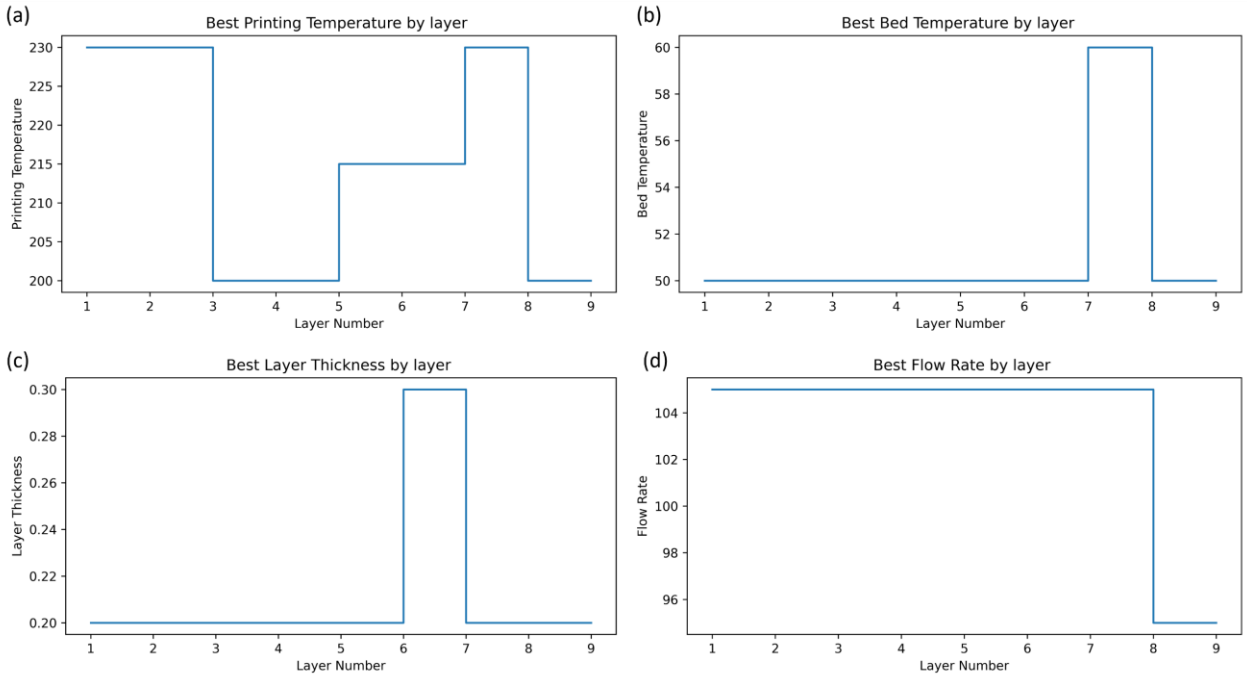

Figure 31. Layer-adaptive schedule from S/N analysis: (a) Printing Temperature, (b) Bed Temperature, (c) Layer Thickness, and (d) Flow Rate

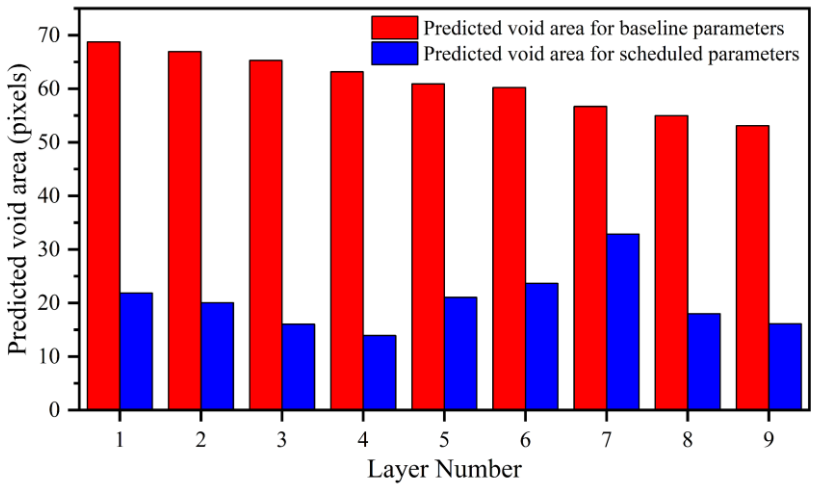

Figure 32. Predicted void area by layer: baseline versus layer-adaptive schedule

By using these recommendations, beginning with the first layer printed at standard parameters, the schedule can then be applied from the second layer onward to minimize interlayer voids. Once a stable base is established, raising flow, selecting the thinner layer, and using the cooler bed with the hotter nozzle increases road overlap and wetting while improving reheating of the previous layer, which closes gaps at the road to road and layer to layer interfaces. In practice, this approach is easy to implement on most slicers, preserves reliable adhesion where it matters most, and then systematically suppresses void formation between subsequent layers where the gains are largest.

4.5 Conclusion and Perspectives

This work establishes a CT-driven, statistically grounded pathway to suppress voiding in FDM printing by coupling imaging with WLS-ANCOVA and Taguchi robustness analysis. After adjusting for build height, all four controllable parameters (bed temperature, flow rate, layer thickness, and printing temperature) emerge as significant drivers of mean void area, with bed temperature and flow rate exerting the largest effects. A precise WLS-ANCOVA model with R^2=84.9% supports inference and effect sizing, while Smaller-the-Better S/N analysis yields a single robust global recipe (PT = 230 °C, Bed = 50 °C, LT = 0.20 mm, Flow = 105 %) that predicts a 73.7% reduction in mean void area versus a mid-level baseline and a 60.1% versus the overall dataset average. A compact layer-adaptive schedule further improves performance across the stack, with the largest gains in early layers and an overall void-weighted reduction of 69% relative to baseline. In practice, the first layer should be printed with standard parameters to secure adhesion and dimensional anchoring. From layer 2 onward, applying the height-aware schedule minimizes inter-layer voids while maintaining stability. Collectively, these results provide immediately deployable guidelines and height-aware refinements that align with known consolidation mechanisms yet keep experimental burden low.

Looking ahead, priority directions include testing beyond PLA and simple coupons by applying the workflow to additional materials and more complex geometries, enabling routine use on production printers by relying on lightweight in-situ signals, like thermal imaging, optical scanning, or acoustics, periodically calibrated against CT to detect and mitigate void risk during printing, closing the loop by embedding the per-layer schedule in a controller that adjusts printing temperature, bed temperature, flow, and layer thickness on the fly within machine limits, and optimizing more than one objective by balancing void reduction with surface finish, dimensional accuracy, mechanical properties, and print time via multi-objective methods. Taken together, these directions position the study as a benchmark for extending CT-validated, layer-aware tuning across materials, parameters, infills, and complex geometries in FDM.

4.6 Author Contributions

Conceptualization, A.Z.; Formal analysis, M.H. and A.Z.; Funding acquisition, M.H. and S.K.; Investigation, A.Z.; Methodology A.Z.; Software, A.Z.; Data collection: A.Z., Y.A., and S.Y.; Supervision, M.H. and S.K.; Writing—original draft, A.Z.; Writing—review and editing, M.H and S.K. All authors have read and agreed to the published version of the manuscript.

4.7 Funding

Funding: The authors acknowledge the funding provided by the Natural Sciences and Engineering Research Council (NSERC) of Canada (grant number: CRSNG–RGPIN-2021-02846) and the Canada Research Chairs Program.

4.8 Data Availability Statement:

Data available under request.

4.9 Conflicts of Interest:

The authors certify that they have no affiliations with or involvement in any organization or entity with any financial interest or non-financial interest in the subject matter or materials discussed in this manuscript.

4.10 References

[1] M. Boulaala, D. Elmessaoudi, I. Buj-Corral, J. El Mesbahi, O. Ezbakhe, A. Astito, M. El Mrabet, A. El Mesbahi, Towards design of mechanical part and electronic control of multi-material/multicolor fused deposition modeling 3D printing, The International Journal of Advanced Manufacturing Technology 110 (2020) 45-55.

[2] A. Gosset, D. Barreiro-Villaverde, J.C. Becerra Permuy, M. Lema, A. Ares-Pernas, M.J. Abad López, Experimental and numerical investigation of the extrusion and deposition process of a poly (lactic acid) strand with fused deposition modeling, Polymers 12(12) (2020) 2885.

[3] Y. Wang, R.T. Mushtaq, A. Ahmed, A. Ahmed, M. Rehman, M. Rehman, A.M. Khan, S. Sharma, D.K. Ishfaq, H. Ali, Additive manufacturing is sustainable technology: citespace based bibliometric investigations of fused deposition modeling approach, Rapid Prototyping Journal 28(4) (2022) 654-675.

[4] S. Vyavahare, S. Teraiya, D. Panghal, S. Kumar, Fused deposition modelling: a review, Rapid Prototyping Journal 26(1) (2020) 176-201.

[5] C. Camposeco-Negrete, Optimization of printing parameters in fused deposition modeling for improving part quality and process sustainability, The International Journal of Advanced Manufacturing Technology 108(7) (2020) 2131-2147.

[6] M. Abas, T. Habib, S. Noor, B. Salah, D. Zimon, Parametric investigation and optimization to study the effect of process parameters on the dimensional deviation of fused deposition modeling of 3D printed parts, Polymers 14(17) (2022) 3667.

[7] K.I. Ismail, T.C. Yap, R. Ahmed, 3D-printed fiber-reinforced polymer composites by fused deposition modelling (FDM): fiber length and fiber implementation techniques, Polymers 14(21) (2022) 4659.

[8] Z. Abdelhamid, H. Mohamed, S. Kelouwani, The use of machine learning in process–structure–property modeling for material extrusion additive manufacturing: a state-of-the-art review, Journal of the Brazilian Society of Mechanical Sciences and Engineering 46(2) (2024) 70.

[9] M. Lalegani Dezaki, M.K.A. Mohd Ariffin, S. Hatami, An overview of fused deposition modelling (FDM): Research, development and process optimisation, Rapid Prototyping Journal 27(3) (2021) 562-582.

[10] K. Rajan, M. Samykano, K. Kadirgama, W.S.W. Harun, M.M. Rahman, Fused deposition modeling: process, materials, parameters, properties, and applications, The International Journal of Advanced Manufacturing Technology 120(3) (2022) 1531-1570.

[11] A. Ziadia, M. Habibi, S. Kelouwani, Digital twin-driven real-time optimization of layer-specific surface roughness in FDM 3D printing, Progress in Additive Manufacturing (2025) 1-24.

[12] M. Sudin, S. Shamsuddin, F. Ramli, N.M. Daud, A Brief Review of Factors Affecting the Mechanical Properties of Fused Deposition Modelling Part, Journal of Advanced Mechanical Engineering Applications 3(2) (2022) 1-13.

[13] H.R. Vanaei, M. Shirinbayan, S. Vanaei, J. Fitoussi, S. Khelladi, A. Tcharkhtchi, Multi-scale damage analysis and fatigue behavior of PLA manufactured by fused deposition modeling (FDM), Rapid Prototyping Journal 27(2) (2021) 371-378.

[14] Q. He, H. Wang, K. Fu, L. Ye, 3D printed continuous CF/PA6 composites: Effect of microscopic voids on mechanical performance, Composites science and technology 191 (2020) 108077.

[15] W. Han, M.A. Jafari, S.C. Danforth, A. Safari, Tool path-based deposition planning in fused deposition processes, Journal of manufacturing science and engineering 124(2) (2002) 462-472.

[16] H. Eiliat, J. Urbanic, Visualizing, analyzing, and managing voids in the material extrusion process, The International Journal of Advanced Manufacturing Technology 96(9) (2018) 4095-4109.

[17] D. Ding, Z. Pan, D. Cuiuri, H. Li, A practical path planning methodology for wire and arc additive manufacturing of thin-walled structures, Robotics and Computer-Integrated Manufacturing 34 (2015) 8-19.

[18] T. Kuipers, E.L. Doubrovski, J. Wu, C.C. Wang, A framework for adaptive width control of dense contour-parallel toolpaths in fused deposition modeling, Computer-Aided Design 128 (2020) 102907.

[19] D. Qiu, N.A. Langrana, Void eliminating toolpath for extrusion-based multi-material layered manufacturing, Rapid prototyping journal 8(1) (2002) 38-45.

[20] B. Akhoundi, A.H. Behravesh, Effect of filling pattern on the tensile and flexural mechanical properties of FDM 3D printed products, Experimental Mechanics 59(6) (2019) 883-897.

[21] W. Jo, O.-C. Kwon, M.-W. Moon, Investigation of influence of heat treatment on mechanical strength of FDM printed 3D objects, Rapid Prototyping Journal 24(3) (2018) 637-644.

[22] O.A. Mohamed, S.H. Masood, J.L. Bhowmik, Optimization of fused deposition modeling process parameters: a review of current research and future prospects, Advances in manufacturing 3(1) (2015) 42-53.

[23] F. Górski, R. Wichniarek, W. Kuczko, P. Zawadzki, P. Buń, Strength of ABS parts produced by Fused Deposition Modelling technology–a critical orientation problem, Advances in Science and Technology. Research Journal 9(26) (2015).

[24] N. Vidakis, M. Petousis, A. Vairis, K. Savvakis, A. Maniadi, A parametric determination of bending and Charpy's impact strength of ABS and ABS-plus fused deposition modeling specimens, Progress in Additive Manufacturing 4(3) (2019) 323-330.

[25] M. Galeja, A. Hejna, P. Kosmela, A. Kulawik, Static and dynamic mechanical properties of 3D printed ABS as a function of raster angle, Materials 13(2) (2020) 297.

[26] M. Samykano, S. Selvamani, K. Kadirgama, W. Ngui, G. Kanagaraj, K. Sudhakar, Mechanical property of FDM printed ABS: influence of printing parameters, The International Journal of Advanced Manufacturing Technology 102(9) (2019) 2779-2796.

[27] K. Chockalingam, N. Jawahar, J. Praveen, Enhancement of anisotropic strength of fused deposited ABS parts by genetic algorithm, Materials and Manufacturing Processes 31(15) (2016) 2001-2010.

[28] M.S. Priya, K. Naresh, R. Jayaganthan, R. Velmurugan, A comparative study between in-house 3D printed and injection molded ABS and PLA polymers for low-frequency applications, Materials Research Express 6(8) (2019) 085345.

[29] J. Torres, J. Cotelo, J. Karl, A.P. Gordon, Mechanical property optimization of FDM PLA in shear with multiple objectives, Jom 67(5) (2015) 1183-1193.

[30] K. Elhattab, S.B. Bhaduri, P. Sikder, Influence of fused deposition modelling nozzle temperature on the rheology and mechanical properties of 3d printed β-tricalcium phosphate (tcp)/polylactic acid (pla) composite, Polymers 14(6) (2022) 1222.

[31] S. Garzon-Hernandez, D. Garcia-Gonzalez, A. Jérusalem, A. Arias, Design of FDM 3D printed polymers: An experimental-modelling methodology for the prediction of mechanical properties, Materials & Design 188 (2020) 108414.

[32] R.A. Wach, P. Wolszczak, A. Adamus-Wlodarczyk, Enhancement of mechanical properties of FDM-PLA parts via thermal annealing, Macromolecular Materials and Engineering 303(9) (2018) 1800169.

[33] P. Han, A. Tofangchi, A. Deshpande, S. Zhang, K. Hsu, An approach to improve interface healing in FFF-3D printed Ultem 1010 using laser pre-deposition heating, Procedia Manufacturing 34 (2019) 672-677.

[34] A. Deshpande, A. Ravi, S. Kusel, R. Churchwell, K. Hsu, Interlayer thermal history modification for interface strength in fused filament fabricated parts, Progress in Additive Manufacturing 4(1) (2019) 63-70.

[35] P. Han, A. Tofangchi, S. Zhang, A. Desphande, K. Hsu, Effect of in-process laser interface heating on strength isotropy of extrusion-based additively manufactured PEEK, Procedia Manufacturing 48 (2020) 737-742.

[36] D. Bhalodi, K. Zalavadiya, P. Gurrala, Influence of temperature on polymer parts manufactured by fused deposition modeling process. J Brazilian Soc Mech Sci Eng 41: 1–11, 2019.

[37] D. Ravoori, H. Prajapati, V. Talluru, A. Adnan, A. Jain, Nozzle-integrated pre-deposition and post-deposition heating of previously deposited layers in polymer extrusion based additive manufacturing, Additive Manufacturing 28 (2019) 719-726.

[38] G. Bräuer, K. Sachsenhofer, R.W. Lang, Material and process engineering aspects to improve the quality of the bonding layer in a laser-assisted fused filament fabrication process, Additive Manufacturing 46 (2021) 102105.

[39] N. Sabyrov, A. Abilgaziyev, M.H. Ali, Enhancing interlayer bonding strength of FDM 3D printing technology by diode laser-assisted system, The International Journal of Advanced Manufacturing Technology 108(1) (2020) 603-611.

[40] G. Li, J. Zhao, J. Jiang, H. Jiang, W. Wu, M. Tang, Ultrasonic strengthening improves tensile mechanical performance of fused deposition modeling 3D printing, The International Journal of Advanced Manufacturing Technology 96(5) (2018) 2747-2755.

[41] W. Wu, J. Li, J. Jiang, Q. Liu, A. Zheng, Z. Zhang, J. Zhao, L. Ren, G. Li, Influence mechanism of ultrasonic vibration substrate on strengthening the mechanical properties of fused deposition modeling, Polymers 14(5) (2022) 904.

[42] N. Jayanth, P. Senthil, C. Prakash, Effect of chemical treatment on tensile strength and surface roughness of 3D-printed ABS using the FDM process, Virtual and Physical Prototyping 13(3) (2018) 155-163.

[43] B. Li, J. Yang, H. Gu, J. Jiang, J. Zhang, J. Sun, Surface roughness of PLA parts by FDM with chemical treatment, Journal of Physics: Conference Series, IOP Publishing, 2021, p. 012199.

[44] A. Garg, A. Bhattacharya, A. Batish, Chemical vapor treatment of ABS parts built by FDM: Analysis of surface finish and mechanical strength, The International Journal of Advanced Manufacturing Technology 89(5) (2017) 2175-2191.

[45] D. Castro-Casado, Chemical treatments to enhance surface quality of FFF manufactured parts: a systematic review. Prog Addit Manuf 6: 307–319, 2021.

[46] T. Kozior, A. Mamun, M. Trabelsi, L. Sabantina, A. Ehrmann, Quality of the Surface Texture and Mechanical Properties of FDM Printed Samples after Thermal and Chemical Treatment, Journal of Mechanical Engineering/Strojniški Vestnik 66(2) (2020).

[47] T. Gajjar, R. Yang, L. Ye, Y. Zhang, Effects of key process parameters on tensile properties and interlayer bonding behavior of 3D printed PLA using fused filament fabrication, Progress in Additive Manufacturing 10(2) (2025) 1261-1280.

[48] F. Lambiase, F. Pace, E. Andreucci, A. Paoletti, Flow rate-dependent interlayer adhesion in FDM: a thermal and mechanical analysis, The International Journal of Advanced Manufacturing Technology 136(3) (2025) 1703-1716.

[49] K.L. Snapp, A.E. Gongora, K.A. Brown, Increasing throughput in fused deposition modeling by modulating bed temperature, Journal of Manufacturing Science and Engineering 143(9) (2021).

[50] Y. Niranjan, S. Krishnapillai, R. Velmurugan, S.K. Ha, Effect of annealing time and temperature on dynamic mechanical properties of FDM printed PLA, Composite Materials for Extreme Loading: Proceedings of the Indo-Korean Workshop on Multi Functional Materials for Extreme Loading 2021, Springer, 2021, pp. 143-160.

[51] J. Mazur, P. Sobczak, M. Panasiewicz, P. Łusiak, M. Krajewska, P. Findura, S. Obidziński, W. Żukiewicz-Sobczak, Mechanical properties and biodegradability of samples obtained by 3D printing using FDM technology from PLA filament with by-products, Scientific Reports 15(1) (2025) 5847.

[52] E.H. Tümer, H.Y. Erbil, Extrusion-based 3D printing applications of PLA composites: a review, Coatings 11(4) (2021) 390.

[53] S. Bhagia, K. Bornani, R. Agrawal, A. Satlewal, J. Ďurkovič, R. Lagaňa, M. Bhagia, C.G. Yoo, X. Zhao, V. Kunc, Critical review of FDM 3D printing of PLA biocomposites filled with biomass resources, characterization, biodegradability, upcycling and opportunities for biorefineries, Applied materials today 24 (2021) 101078.

[54] A. Ziadia, M. Habibi, S. Kelouwani, Machine learning study of the effect of process parameters on tensile strength of FFF PLA and PLA-CF, Eng 4(4) (2023) 2741-2763.

[55] S.I. Scipioni, F. Lambiase, Yielding and post-yielding behavior of FDM parts under compression stress at different strain rates, The International Journal of Advanced Manufacturing Technology 128(3) (2023) 1199-1211.

[56] R.A. Hamid, S.N.H. Husni, T. Ito, Effect of printing orientation and layer thickness on microstructure and mechanical properties of PLA parts, Malaysian Journal on Composites Science and Manufacturing 8(1) (2022) 11-23.

[57] C. Le, K. Kolasangiani, P. Nayyeri, H. Bougherara, Experimental and numerical investigation of 3D-Printed bone plates under four-point bending load utilizing machine learning techniques, Journal of the Mechanical Behavior of Biomedical Materials 143 (2023) 105885.

Partie II : Vers le pilotage en ligne et le jumeau numérique

Chapitre 5: Jumeaux numériques et reconstruction 3D en fabrication additive : Revue de l'état de l'art

Digital Twins and 3D Reconstruction in Additive Manufacturing: A State-of-the-Art Review. Abdelhamid ZIADIA, Mohamed HABIBI, and Sousso KELOUWANI.

La Partie 2 prolonge logiquement la Partie 1. Les modèles prédictifs, les surfaces de réponse et les réglages robustes établis hors ligne deviennent des consignes dynamiques. Ils sont alimentés par un monitoring in situ fondé sur la vision, le scan 3D et des capteurs, puis orchestrés par un jumeau numérique afin de fermer la boucle de contrôle. Pour ancrer cette transition, la Partie 2 s'ouvre sur une revue qui dresse une synthèse de l'intégration des jumeaux numériques et de la reconstruction 3D en fabrication additive, et montre comment la combinaison capteurs, simulation et IA rend possible le suivi temps réel, la prédiction et l'action sur le procédé.

La revue définit le jumeau numérique comme un modèle virtuel dynamique d'une machine, d'une pièce ou d'un procédé, synchronisé avec des données in situ et des résultats de simulation, utilisable en ligne pour corriger pendant l'impression ou hors ligne pour valider et prédire. Elle organise l'état de l'art en cinq axes fonctionnels. Conception et optimisation avec topologie, tranchage adaptatif pour réduire le coût de calcul. Monitoring de procédé avec fusion d'imagerie optique et infrarouge, signaux machine et modèles thermo-mécaniques pour suivre bain de fusion, champs thermiques, distorsions et dérives. Maintenance prévisionnelle avec détection précoce des dérives et estimation d'endommagement via modèles réduits et probabilistes. Assurance qualité avec prédiction de rugosité, contraintes résiduelles, déformations et traçabilité couche par couche. Commande en boucle fermée, apprentissage par renforcement, logique floue et pipelines scanner, analyser, corriger pour ajuster automatiquement les paramètres d'impression.

La reconstruction 3D est la couche d'observation du jumeau numérique. La classification retenue distingue la géométrie de surface et le recalage des trajectoires, les états internes reconstruits à partir de capteurs et de modèles physiques allégés, la cartographie des défauts en volumes voxels ou maillages, ainsi que des reconstructions algorithmiques et physiques qui convertissent des voxels en géométries fabriquables. Ces sorties fournissent des états observables et des indicateurs décisionnels qui alimentent le jumeau et rendent possible la commande adaptative.

La revue met en avant des démonstrateurs issus de plusieurs familles de procédés et montre une fermeture progressive de la boucle entre exécution physique et modèle numérique, depuis la surveillance jusqu'à la correction automatique. Elle identifie toutefois des verrous à lever pour un passage à l'échelle industrielle. Latence et synchronisation des flux multi-capteurs, compromis entre fidélité et coût de calcul qui motivent les modèles réduits et les surrogates informés par la physique, interopérabilité incomplète entre machines et logiciels, standardisation encore hétérogène des formats et des données.

En perspective, l'article appelle des jumeaux plus autonomes capables d'ajuster en temps réel énergie, vitesse, température et trajectoires pour stabiliser le procédé, réduire les rebuts et qualifier les pièces en ligne. Il plaide pour des reconstructions plus rapides et plus automatisées, avec des IA intégrant des lois physiques et nourries par des flux de données en ligne. Ce cadre jumeau numérique et reconstruction 3D constitue la porte d'entrée de la Partie 2. Il fait le pont entre les métriques qualité et PSP établies précédemment et leur mise en action via des boucles de contrôle temps réel.

Digital Twins and 3D Reconstruction in Additive Manufacturing: A State-of-the-Art Review

Abdelhamid Ziadia[1], Mohamed Habibi[1, *]& Sousso Kelouwani[1]

Affiliation 1; University of Quebec in Trois-Rivieres, (Department of Mechanical Engineering), Trois-Rivieres, (Quebec), Canada

*Correspondence: erima@uqtr.ca

5.1 Abstract

Additive manufacturing is gaining prominence across industries for its capacity to produce complex, customized components. However, ensuring reliability and quality across diverse AM processes remains a challenge. This article provides a state-of-the-art review of digital twin and 3D reconstruction technologies in additive manufacturing, which have emerged as key enablers for real-time monitoring, predictive analysis, and data-driven control throughout the AM lifecycle. The review organizes recent advancements into five major functional areas: design optimization, process monitoring, predictive maintenance, quality assurance, and closed-loop control. For each category, the role of digital twins in enhancing simulation fidelity, sensor fusion, fault detection, and lifecycle traceability is analyzed. In addition, a structured classification of 3D reconstruction approaches is proposed, encompassing geometric surface tracking, internal state recovery, defect mapping, and algorithm-driven modeling. By examining both real-time and offline strategies, this study highlights the growing synergy between physical sensing, machine learning, and simulation in creating responsive and intelligent AM systems. Current limitations including standardization, scalability, and model generalizability, are also discussed to outline directions for future research.

Keywords: Additive manufacturing, Digital twin, 3D Reconstruction, Real-time Monitoring

Abbreviations:

AM: Additive Manufacturing

AR: Augmented Reality

HPD: Heterogeneous Pore Design

BJT: Binder Jetting Technology

BSE: Backscattered Electron

CA: Cellular Automata

CAD: Computer-Aided Design

CAM: Computer-Aided Manufacturing

CFD: Computational Fluid Dynamics

CM 247 LC: Cobalt-based Superalloy

CNN: Convolutional Neural Network

CP: Crystal Plasticity

CSAM: Cold Spray Additive Manufacturing

CT: Computed Tomography

DED: Directed Energy Deposition

DEM: Discrete Element Method

DIC: Digital Image Correlation

DL: Deep Learning

DLP: Digital Light Processing

DT: Digital Twin

EBSD: Electron Backscatter Diffraction

FDM: Fused Deposition Modeling

FEA: Finite Element Analysis

FEM: Finite Element Method

GPR: Gaussian Process Regression

hDIC: height Digital Image Correlation

ICP: Iterative Closest Point

iCT: industrial Computed Tomography

IR: Infrared

LARM: Laser Additive Manufacturing

L-DED: Laser-Directed Energy Deposition

LCD: Liquid Crystal Display

LCNN: Lightweight Convolutional Neural Network

LFAM: Large Format Additive Manufacturing

LMD: Laser Metal Deposition

LPBF: Laser Powder Bed Fusion

MDACNN: Multi-fidelity Defect reconstruction strategy using A Convolutional Neural Network

ML: Machine Learning

ML-EM: Maximum Likelihood Expectation Maximization

MPAV: Meltpool Area Volume

MPC: Model Predictive Control

MPIV: Meltpool Intensity Volume

OICP: Offset Iterative Closest Point

PADL: Physics-Aware Deep Learning

PF: Phase Field

RBF: Radial Basis Function

RL: Reinforcement Learning

RNN: Recurrent Neural Network

SEM: Scanning Electron Microscope

SL: Structured Light

SLM: Selective Laser Melting

SVD: Singular Value Decomposition

SiL: Simulation-in-the-Loop

TED: Thermal Emission Distribution

TEP: Thermal Energy Profile

TLBM: thermal lattice Boltzmann modeling

U-Net: U-shaped Neural Network

VAM: volumetric additive manufacturing

VR: Virtual Reality

WAAM: Wire Arc Additive Manufacturing

XCT: X-ray Computed Tomography

5.2 Introduction

Since its beginnings as prototype, AM, also known as 3D printing, has advanced significantly [1-3]. These days, it is becoming more and more important in industries like aerospace, healthcare, and automotive, where there is a strong need for efficiency, complexity, and customization [2, 4]. AM lowers material waste and tooling costs while enabling lightweight and geometrically complex products through layer-by-layer component construction [2, 5]. However, despite its benefits, AM still faces obstacles that prevent its wider industrial implementation [6, 7].

A primary obstacle is guaranteeing consistent reliability and quality [8, 9]. Because AM is layer-wise, it introduces variability in mechanical response, material behavior, and thermal conditions, factors that are sometimes difficult to regulate and predict [10-13]. AM usually necessitates customized changes, repeated testing, and careful inspection, in contrast to traditional manufacturing processes where standards are well-established [14, 15]. Production is slowed down as a result, and quality control becomes more difficult, especially when parts are meant for vital applications like aviation or medical devices [16-20].

Digital twins are starting to alter that environment [21]. Digital twins are dynamic, constantly updated virtual models that replicate their physical counterparts, in contrast to traditional simulations [22, 23]. By combining information from sensors, simulations, and machine feedback, they assist AM in tracking the construction of a part in real time [24-26]. By optimizing process parameters, providing better insight into production outcomes, and informing operators of faults before they arise, this live connection not only makes monitoring possible but also allows for prediction and even intervention [27-31].

In addition to digital twins, 3D reconstruction methods are becoming more and more significant [32-34]. These techniques use information from CT scans, optical sensors, melt pool imaging, and other sources to reconstruct the interior structure or shape of printed items [35, 36]. Reconstruction aids in finding flaws, evaluating dimensional accuracy, and guiding decisions about quality or repair, whether it occurs during construction or after it is finished [24, 37]. These technologies enable the closure of the loop between quality control, real-time manufacturing, and virtual design when combined with digital twins [23, 38]. While prior reviews have examined digital twins or reconstruction techniques separately, a comprehensive state-of-the-art review that integrates both perspectives within additive manufacturing is still lacking.

Given the rapid advancements in this domain, this article provides a state-of-the-art review that consolidates how digital twins and 3D reconstruction are applied in additive manufacturing. The literature on digital twins is organized into five functional categories: design optimization, process monitoring, predictive maintenance, quality assurance, and closed-loop control. Each part delves deeply into recent work, showing how engineers and academics are addressing some of AM's most enduring problems [28, 29, 39].

The paper focuses heavily on specific examples, demonstrating the various applications of various technologies, ranging from multiscale simulation and adaptive feedback systems to sensor fusion

and AI-based prediction. Throughout the review, summary tables are used to aggregate various approaches, providing a clear glimpse of the methods, aims, and outcomes connected with each category.

Particular focus is also placed on 3D reconstruction techniques, which are investigated at several levels, ranging from mapping internal flaws and microstructural characteristics to capturing surface geometry. These tools are becoming more and more recognized as crucial parts of stronger, data-driven digital twin systems, in addition to being helpful on their own.

Finally, the review concludes with a discussion of ongoing challenges and future directions. Among the key issues are the difficulty of real-time parameter updates, limited standardization across platforms, and the need for more automated, high-resolution reconstruction solutions. Overcoming these obstacles will be key to scaling digital twin technologies and unlocking their full potential in advanced manufacturing.

By compiling and critically analyzing the most recent research, this study aims to serve as a state-of-the-art reference and roadmap, guiding researchers and practitioners in advancing intelligent and reliable additive manufacturing.

5.3 Digital Twins in Additive Manufacturing

5.3.1 Concept and Definition

A digital twin is a virtual representation of a physical object, process, or system that captures its characteristics and behavior across its lifecycle [40]. In the context of AM, digital twins are used to mirror the design, production, and post-processing stages of printed parts, offering a bridge between the physical and digital realms [41-43]. Depending on the application, this connection can range from fully dynamic, real-time synchronization to offline simulations and reconstructions that guide design or quality validation.

Unlike traditional simulations, which are typically static and restricted to specific phases, digital twins offer a more integrated view. They can be continuously updated with live data from sensors, or operate in offline mode, using experimental, scanned, or inferred information to predict outcomes or assess performance [44]. This flexibility allows digital twins to function as powerful tools for both real-time process control and post-process analysis [45].

When real-time data is available, digital twins enable continuous updates and adaptive feedback, forming the backbone of closed-loop control and in-situ optimization. Even in offline scenarios, they support key applications such as design validation, predictive modeling, and geometric

reconstruction. Across both modes, digital twins provide value through the following capabilities [45-47]:

- Data-Driven Insight: Whether updated in real time or post-process, digital twins integrate process data to enable informed decision-making.
- Lifecycle Coverage: They represent the entire product or process journey, from digital design to physical output and beyond [45].
- Interactivity and Adaptability: In more advanced setups, bidirectional communication allows the system to respond to deviations and improve outcomes in real time [46].
- Predictive Capabilities: Leveraging simulations, machine learning, and analytics, digital twins can anticipate failures, optimize parameters, or recommend corrective actions [47].

A digital twin consists of three core components that work together to create a seamless connection between the physical and virtual worlds [48, 49]:

- Physical Entity: The physical entity is the real-world object, process, or system being represented. In additive manufacturing, this could be the 3D printer, the part being produced, or the entire production line. The physical entity is equipped with sensors, IoT devices, and other data collection tools that capture real-time information about its state and performance [49, 50].
- Virtual Model: The virtual model is the digital counterpart of the physical entity. It is a detailed, data-driven representation that simulates the behavior, characteristics, and performance of the physical system. In AM, the virtual model may include CAD designs, material properties, process parameters, and environmental conditions. It is continuously updated with data from the physical entity to ensure accuracy [51, 52].
- Data Connection: The data connection is the link between the physical entity and the virtual model. It enables the seamless exchange of data in real time, ensuring that the digital twin remains synchronized with the physical system. This connection relies on advanced communication technologies, such as IoT, cloud computing, and edge computing, to handle large volumes of data and enable rapid decision-making [53].

Digital twins represent a paradigm shift in how additive manufacturing processes are designed, monitored, and optimized. By integrating real-time data, advanced simulations, and predictive analytics, digital twins enable a deeper understanding of the AM process and drive continuous

improvement. As AM technologies continue to evolve, digital twins will play an increasingly critical role in unlocking their full potential.

5.3.2 Applications in AM

The applications of digital twins in AM are examined in this section using a functionality-driven classification. The chosen works fall into five main categories: quality assurance, process monitoring, predictive modeling, design and simulation support, and closed-loop control (Figure 33). Every category represents a significant phase in the AM lifecycle and demonstrates how digital twins aid in risk reduction, performance optimization, and improved decision-making. This framework helps place the examined studies within a larger system-level knowledge and clarifies how the digital twin notion develops from passive monitoring tools to active control systems.

Figure 33.Classification of Digital Twin applications in Additive manufacturing.

5.3.2.1 Design Optimization

Design optimization is a critical phase in AM, leveraging generative design, topology optimization, and virtual prototyping to enhance the functional and structural performance of printed parts. Qu et al. [54] introduced a HPD algorithm tailored for filament diameter–adjustable 3D printing, significantly improving pore structures through customized filament widths, optimized G-code, and adaptive printhead velocities (Figure 34). Building upon similar optimization principles, Wu et al. [55] utilized machine learning–assisted digital twins integrated with multiscale finite element models to design optimized functionally graded lattice structures for biomedical implants, enhancing mechanical properties while drastically reducing computational resources.

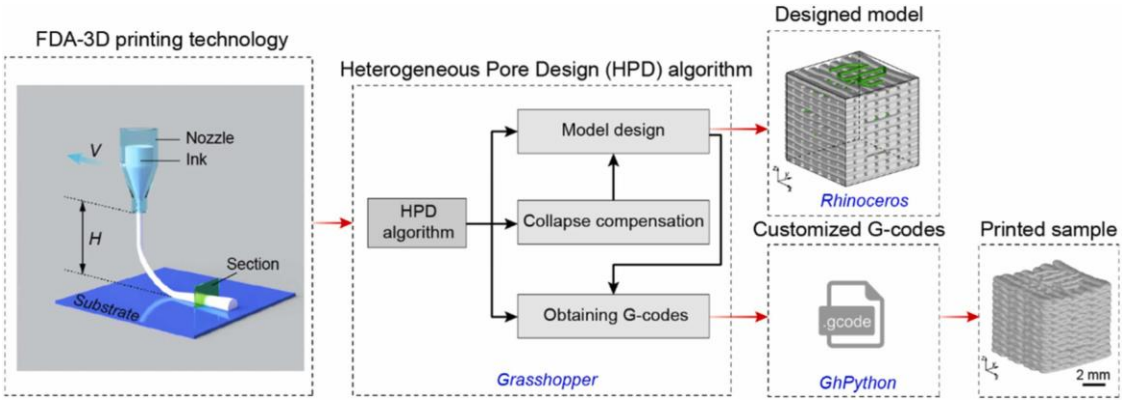

Figure 34. Workflow from FDA-3D printing technology to model design, model visualization and sample fabrication [54].

Kim et al. [56] presented a sophisticated framework linking laser path generation with predictive simulations, enabling precise predictions of deformation and residual stresses during LPBF. Complementing simulation-driven methods, Auyeskhan et al. [57] employed virtual reality-based digital twins combined with axiomatic design theory, guiding manufacturers toward optimal assembly strategies through immersive interactions and real-time performance feedback.

Further advancements by Hilbig et al. [58] incorporated CNNs trained on signed distance fields, significantly refining adaptive slicing strategies. Similarly, Risse et al. [59] focused on stiffness-optimized implants through iterative numerical modeling and AM, demonstrating improved compatibility and fatigue resistance. Chen et al. [60, 61] further extended optimization approaches, using multi-fidelity neural models and topology optimization methods integrated with parametric Voronoi structures, achieving substantial weight reduction without compromising mechanical performance.

Additionally, Zhou et al. [62] introduced topology optimization specifically tailored for manufacturable geometries, ensuring structural integrity and reduced support requirements. Xu et al. [63] offered a complementary approach by developing an adaptive slicing algorithm driven by digital twins, optimizing build orientation and minimizing geometric deviations, thereby enhancing print accuracy and efficiency

Table 16 highlights the growing use of DTs for optimizing structural and process parameters in AM. A dominant trend is the integration of topology optimization and neural network-based surrogate models, particularly for lattice structures and functionally graded components. While several approaches [56, 58] enable adaptive slicing and geometry refinement. Many of these

studies remain in the design or pre-print phase, indicating a need for stronger coupling between DT-driven design and in-process adaptation.

Table 16. Summary of Design Optimization methods

Ref.	Optimization Goal	AM Technology	Design Approach	Digital Twin Role	Validation Method
[54]	Pore/filament control	FDA-3D	HPD algorithm	Real-time G-code mapping	Fabrication
[55]	Lattice elasticity	LPBF	DANN + FEM	Neural surrogate	Simulation
[56]	Stress/temp prediction	LPBF	Scan path + FEM	Thermal-mechanical sim	Simulation
[57]	Assembly efficiency	Metal AM	VR + axiomatic design	Human-in-the-loop	Task metrics
[58]	Slicing by shape	Generic AM	3D-CNN on voxel data	Shape-based prediction	IoU > 88%
[59]	Implant stress shielding	SLM	Parametric FEA	Iterative DT tuning	ISO fatigue test
[60]	Pore shape control	LPBF	CNN + optimizer	CT-informed DT	Sphericity
[62]	Support-free design	Generic AM	TO with overhang filters	Overhang-aware DT	Printing trial
[61]	Lightweight structure	FDM	TO + Voronoi pattern	Structural sim	Mechanical tests
[63]	Hole accuracy	Generic AM	Genetic algo + fuzzy AHP	Orientation & slicing sim	Hole deviation <5%

5.3.2.2 Process Monitoring

Real-time process monitoring is crucial to ensuring high-quality, consistent outcomes AM, as it allows immediate feedback and corrective actions during production. Zheng et al. [64] pioneered an advanced digital twin synchronized in real-time with an LCD-based AM system, utilizing Arduino sensors. Their virtual model dynamically updates with Z-axis movement and UV exposure data, enabling real-time detection of surface deviations during layer-by-layer printing.

Extending this real-time capability, a SiL framework introduced by Fu et al. [65] was applied to DED to track material behavior and stress accumulation dynamically, offering early warnings about potential mechanical failures based on ongoing structural simulations.

Bevans et al. [66] further enriched process monitoring by integrating real-time optical and thermal imaging with a graph-based thermal simulation, enabling precise in-situ quality predictions in LPBF. Their hybrid digital twin system could predict critical properties, such as porosity, melt pool depth, grain size, and microhardness, achieving accuracies exceeding 90% for detecting lack-of-fusion porosity. Complementing this advanced digital twin framework, Chheang et al. [35] transformed digital twin inspections into immersive, multi-user activities using VR. Their approach leveraged multimodal overlays (toolpaths, CT scans, in-process images) and real-time annotation tools, significantly enhancing defect localization, collaborative decision-making, and training efficiency in distributed teams.

Horr [67] addressed computational efficiency in real-time monitoring within WAAM, combining reduced-order modeling through SVD with radial basis function neural networks. This integration enabled predictions of temperature and stress fields with computational speeds over 2,800 times faster than conventional finite element methods. Further advancing geometric monitoring, Pratt et al. [68] developed the ASDF framework, using real-time structured light or laser scanning data to immediately detect geometric deviations. Meanwhile, Mu et al. [69] introduced a method to dynamically predict layer-wise distortions in WAAM, integrating historical data and real-time scanning feedback with minimal latency, achieving impressive accuracy (RMSE < 0.9 mm).

Chen et al. [70] proposed a service-oriented digital twin architecture emphasizing modularity, scalability, and reusability across various AM systems. Their framework, organized into service, model, data, and interface layers, effectively supported real-time anomaly detection and warping predictions. Moretti et al. [71] enhanced defect monitoring in FDM by integrating laser line scanning with voxel-based simulations, allowing effective real-time identification of defects such as stringing and bridging. Similarly, Cabral et al. [72] created a robust, low-cost digital twin for robotic WAAM, adhering to ISO 23247 standards. This framework provided comprehensive real-time monitoring through cloud-based dashboards and full 3D simulations, significantly increasing process transparency and control.

Innovating in image reconstruction, Lu et al. [73] introduced the FB-PCADL framework, employing compressed sensing and active dictionary learning to reconstruct high-resolution

thermal and optical images from sparse sensor measurements. Li et al. [74] advanced LPBF monitoring with a high-fidelity multi-physics digital twin, using adaptive mesh refinement techniques to capture detailed melt pool dynamics efficiently. Rossi et al. [75] developed neural-network-powered digital twins for extrusion processes in FDM, significantly improving real-time detection and anomaly handling, notably in cases of nozzle clogging.

Sampedro et al. [27] provided a comprehensive Unity-based digital twin (3D-AmplifAI) (Figure 35 (A)), integrating an ensemble learning model to predict nozzle failures and thermal drift accurately, achieving an impressive F1-score of 0.8. Jyeniskhan et al. [76] expanded these capabilities through a Unity-based digital twin framework combining real-time temperature tracking, interactive control, and image-based defect detection using the EfficientDet-Lite model, which demonstrated precision up to 94% (Figure 35 (B)).

In addressing defect formation in LPBF, Yeung et al. [77] combined consistent laser power density scanning with in-situ melt pool imaging, developing voxel-based MPIV and MPAV to identify defect-prone regions. Corradini and Silvestri [24] significantly enhanced monitoring capabilities in FDM with a digital twin offering comprehensive real-time visualization, sensor synchronization, and detailed error diagnostics. Meanwhile, Dvorak et al. [78] established a hybrid WAAM and CNC milling digital twin integrating physical measurements and structured light scanning to enhance machining stability and accuracy.

Scime et al. [79] created a scalable digital twin platform capturing the digital thread from design to post-processing, using AI-driven anomaly detection adaptable to multiple AM processes. Liu et al. [80] used structured-light scanning to precisely track and reconstruct geometry layer-by-layer, enabling accurate mesoscale modeling and performance prediction. Reisch et al. [81] developed a context-aware digital twin for WAAM, employing autoencoder models to spatially map voltage signal anomalies effectively.

Additionally, Liu et al. [82] proposed a collaborative digital twin architecture (MANUELA project) integrating distributed edge-based monitoring and centralized cloud analytics, optimizing lifecycle management for metal powder bed fusion processes. Yi et al. [83] introduced AR visualizations to digital twins, presenting real-time geometry and sustainability metrics, significantly enhancing user interaction and understanding (Figure 35 (C)). Yavari et al. [84] combined rapid thermal simulations and melt pool monitoring for early flaw detection in LPBF, with robust validation through XCT and SEM analyses. Lu et al. [85] utilized physics-based

compressive sensing methods to reconstruct thermal fields in real-time with minimal sensor requirements and high accuracy.

Sieber et al. [86] emphasized high-resolution optical component fidelity, integrating tactile surface profilometry and digital twin feedback for precise corrective actions. Finally, Wu et al. [87] introduced the OICP method into a WAAM-CNC digital twin, significantly improving adaptive mold repair precision through effective real-time point cloud registration.

Together, these works showcase the rapid evolution and sophistication of process monitoring techniques, from fundamental imaging approaches to advanced multi-sensor digital twins, underscoring their indispensable role in enhancing AM efficiency, reliability, and overall product quality.

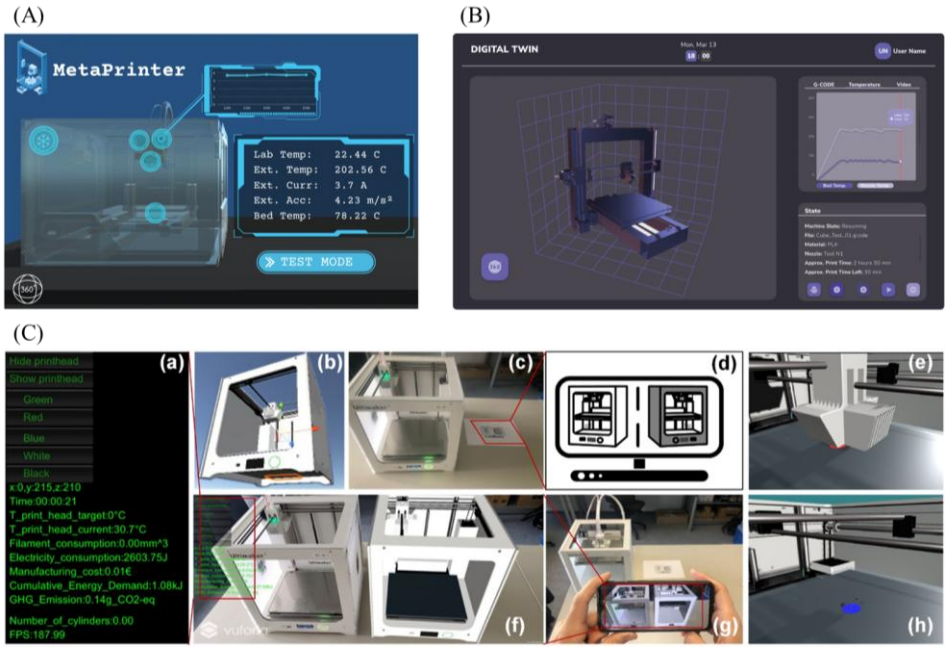

Figure 35. Examples of the Process Monitoring methods: (A) Sampedro et al. [27], (B) Jyeniskhan et al. [76], (C) Yi et al. [83].

Table 17 consolidates the various digital twin strategies for Process Monitoring, where real-time sensing, defect detection, and anomaly classification are the core focus. The table illustrates the widespread utilization of thermal, acoustic and visual data streams, which are frequently analyzed using ensemble classifiers, CNNs, or GRUs as machine learning models. While Liu et al. [82] and Sampedro et al. [27] incorporate real-time sensor fusion for quality tracking, some research, such as those by Li et al. [74], Lu et al. [85], and Moretti et al. [71], show simulation-enhanced

monitoring frameworks. The poor ability to detect subsurface anomalies and the platform-specificity of the majority of implementations are two significant gaps among these works.

Table 17. Summary of the Process Monitoring methods.

Ref.	Area of Application	AM Technology	Sensors	Monitoring Targets	Ref	Area of Application	AM Technology	Sensors	Monitoring Targets
[64]	Surface defect detection	Light-Curing AM	G-code data	Surface deviation	[76]	Image-based defect detection	FDM	Camera, temp sensors	Warping, clogging
[65]	Stress monitoring	DED	Thermal camera, stress sensors	Stress, strain	[77]	Flaw mapping	LPBF	Laser, imaging	Porosity, keyhole
[66]	Thermal/microstructure prediction	LPBF	IR, melt pool sensors	Porosity, melt pool depth	[24]	Full process tracking	FDM	Sensors + encoder	Execution path
[35]	VR-based inspection	Generic AM	CT, G-code	Defect localization	[78]	Stability in hybrid AM	WAAM + CNC	FRF, audio	Tool chatter
[67]	Reduced-order thermal modeling.	WAAM	Thermal sensors	Temp/stress fields	[79]	Multi-process monitoring	Binder Jet, LPBF	Voxel data, images	Local strength
[68]	Geometric error detection	FDM	Laser scanner	Deviation errors	[80]	Performance prediction	FDM	Light scanner	Stiffness, shape
[69]	Distortion tracking	WAAM	Scan sensor	Distortion	[81]	Anomaly clustering	WAAM	Voltage sensors	Defect zones
[70]	Anomaly detection	FDM	Camera, sensors	Warping, anomalies	[82]	Edge-cloud DT	PBF	CT, melt pool	Process health
[71]	Defect detection	FDM	Laser scanner	Bridging, stringing	[83]	AR monitoring	FDM	Phone sensors	GHG, energy
[72]	Process transparency	WAAM	19 sensors	Bead formation, toolpath	[84]	Thermal-based flaw detection	LPBF	Thermal camera	Porosity
[73]	Thermal/optical monitoring	FDM, LPBF	Thermal, optical sensors	Melt pool, spatter.	[85]	Thermal reconstruction	FDM	Sparse sensors	3D temp field
[74]	Melt pool simulation	LPBF	Mesh overlays	Melt pool shape	[86]	Feedback correction	Inkjet	Profiler	Height deviation
[75]	Extrusion defect detection	FDM	Force, temp sensors	Extrudate behavior	[87]	Adaptive repair	WAAM-CNC	Laser scanner	Geometry deviation
[27]	Thermal drift prediction	FDM	Multiple sensors	Nozzle fault					

5.3.2.3 Predictive Maintenance

In the realm of additive manufacturing, downtime and unexpected equipment failures can significantly disrupt production efficiency. Digital twins offer a powerful solution to this challenge by enabling predictive maintenance, using continuous monitoring and intelligent forecasting to prevent failures before they occur.

At the heart of predictive maintenance strategies is equipment health monitoring, where sensor data is integrated with advanced simulation models to assess machine condition and forecast potential failures. Liu and Wang [88] developed a hybrid simulation–ML framework combining PF and TLBM with a physics-constrained neural network surrogate. The model predicts microstructure evolution based on thermal inputs while reducing computational cost by over 36,000×, supporting real-time predictive maintenance by enabling efficient process–structure relationship modeling. Similarly, Li et al. [89] used a thermo-mechanical finite element model to simulate stress and distortion during laser-based repair, helping to anticipate component deformation.

Several studies focused on enhancing predictive insight through multivariate process modeling. Klingaa et al. [90] modeled the effects of gas flow variables on LPBF quality metrics, while Heo et al. [91] developed a multiscale physics-informed digital twin capable of predicting grain morphology, dislocation density, and elastic anisotropy. These frameworks highlight the growing role of Gaussian Process regression and surrogate modeling in bridging the gap between real-time simulation and predictive insight.

Repair planning is another crucial area benefiting from predictive modeling. Zhang et al. [92] employed voxelized geometry comparison to generate toolpaths for AM-based repair, demonstrating how digital twins can anticipate the scope of restoration needed. Similarly, Beckman et al. [93] combined filter geometry and simulation to forecast flow resistance and optimize media structure for high-performance applications.

In addition to complex multiphysics simulations, accessible and flexible modeling tools remain essential for wider industrial uptake. Yang and Özel [94] offered an open MATLAB-based framework for melt pool prediction across multiple metals, while Montoya-Zapata et al. [95] demonstrated that even simplified FEM models can yield thermal predictions with high fidelity, facilitating fast decision-making in early-stage design.

The contributions from the Predictive Maintenance area are compiled in Table 18, which emphasizes the use of digital twins to predict problems, adjust process parameters, and minimize downtime. To anticipate results like residual stress, porosity, or repair volume, the reported works including those by Liu and Wang [88], Klingaa et al. [90], and Zhang et al. [92]

use ML surrogates in conjunction with thermal and mechanical modeling. Using reduced-order models and Bayesian optimization to manage trade-offs between computational efficiency and model fidelity is a recurring pattern. Their responsiveness in dynamic production contexts is limited, nevertheless, by the fact that the majority of these predictive frameworks are not yet integrated with adaptive control systems or real-time sensor data. Broader generalization is further limited by the use of case-specific datasets and the absence of conventional validation techniques.

Table 18. Summary of Predictive Maintenance methods.

Ref.	Area of Application	AM Technology	Approach	Sensors	Prediction Target	Real-time / Offline	Validation / Outcome
[88]	Microstructure modeling	Metal AM	PF-TLBM + PCNN-MM	Thermal history	Dendrites, segregation	Offline	36,000x faster than direct sim
[89]	Residual stress prediction	LDMD	Coupled FEA	Thermocouple, XRD	Stress, deformation	Offline	Valid against exp data
[90]	Process-quality relation	LPBF	DoE + RSM	CT, hardness	Porosity, hardness	Offline	Validated via tests
[91]	P-S-P prediction	LPBF	Multiscale physics + GP surrogate	X-ray, In-situ imaging	Grain size, elasticity	Hybrid	Supports grain refinement
[92]	Repair optimization	Repair AM	Voxel comparison	3D scanner	Repair zone geometry	Offline	Confirmed interfacial fidelity
[93]	Filtration design	Filter media DT	SFE model + iteration	SEM, flow test	Filtration FOM	Offline	Reverse engineering filters
[94]	Thermal field prediction	LPBF	2D FEM model	Thermal properties	Overmelting, fusion zones	Offline	Literature validation
[95]	Thermal simulation	Laser-based AM	2D linear FEM	Heat flux BCs	HAZ dimension	Offline	<5% deviation from non-linear

5.3.2.4 Quality Assurance

Ensuring the quality of AM parts is of paramount importance, especially in safety-critical sectors like aerospace, healthcare, and energy. Digital twins provide a robust framework for quality assurance by virtually replicating the build process, enabling early defect detection, predictive testing, and comprehensive traceability across the manufacturing lifecycle.

In light-curing AM, surface integrity plays a pivotal role in overall part quality. Zheng et al. [64] tackled surface defects such as the “stair-step” effect by developing a digital twin system that generates high-fidelity virtual replicas of printed parts. This system uses slice profile data, cured layer thickness, and resin shrinkage to simulate surface deviations before the print begins, allowing for preemptive process adjustments that reduce material waste and improve surface accuracy.

To address real-time defect detection in WAAM, Kang et al. [96] proposed an edge-computing DT framework. It integrates a CNN-based image analysis pipeline with live camera feeds, identifying anomalies in bead formation. AR via HoloLens projects alerts directly into the operator’s workspace, facilitating prompt intervention and minimizing response time.

Further extending simulation-driven quality assurance, Castelló-Pedrero et al. [97] introduced a digital twin for LFAM using carbon fiber composites. Their approach simulates thermal strain and warpage before printing through voxel-based layer deposition modeling, streamlining process planning and minimizing trial-and-error.

For hybrid additive–subtractive processes, Denkena et al. [38] developed a Digital Workpiece Twin (DWT) that models geometry, roughness, and hardness evolution during LMD and micro-milling. Although not live-updated, the DWT supports adaptive NC code generation using predictive simulations and cutting force estimations, enhancing process flexibility.

A more granular approach was proposed by Hartmann et al. [98], who designed a multiscale digital twin for L-DED. Their architecture combines global thermal tracking with local melt pool simulation, offering high-resolution predictions of clad geometry and thermal gradients with less than 5% error. The results are validated via in-situ sensors and metallography.

In the context of LARM, Huang et al. [99] introduced a multi-task deep learning digital twin using high-speed and IR imaging to predict both surface cracks and internal thermal damage (Figure 36). The outcomes are rendered in a real-time quality map, enabling continuous monitoring of part integrity throughout production.

A knowledge-driven approach was advanced by Qin et al. [100], whose bidirectional digital twin for DED combines FEA and domain-informed machine learning. The model accurately predicts thermal gradients and melt pool dimensions and can infer optimal process parameters from observed metrics with sub-7% error.

Returning to LFAM, Castelló-Pedrero et al. [101] expanded their digital twin framework by incorporating anisotropy and thermal deformation modeling at micro, meso, and macro scales. Using Digimat-AM, they simulate residual stress and warpage in fiber-reinforced ABS molds, validated against both tensile testing and geometry outcomes.

For filament-based processes, Ochoa et al. [102] reverse-engineered the extrusion process to construct a digital twin from G-code and real filament profiles. This replica was analyzed via finite element simulations, yielding up to 97% alignment with experimental mechanical data, an effective means of quality prediction without destructive testing.

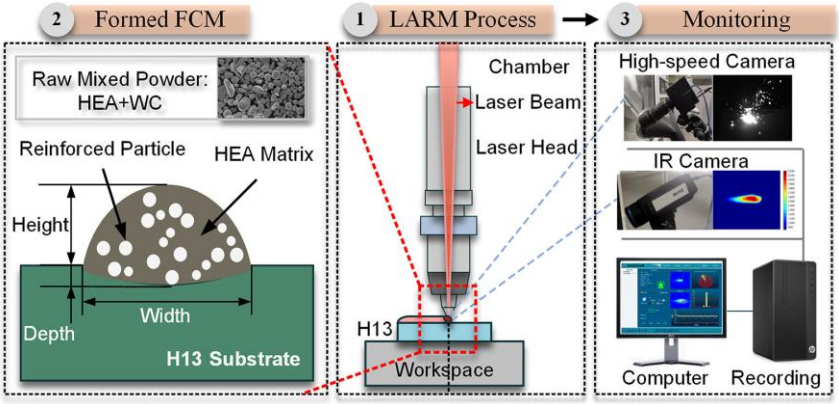

Figure 36. Image acquisition system in the LARM process [99].

In LPBF, Marks et al. [103] created a simulation-based digital twin that correlates laser parameters with fatigue life and mechanical properties using COMSOL. This enables prediction of part performance based on limited experimental inputs, a critical tool when destructive testing is constrained.

Patuelli et al. [104] developed a voxel-based FEM workflow for predicting distortions in SLM calibration artifacts. Simulations were compared with industrial CT scans at 40 reference points, achieving 65% correlation and validating the twin's effectiveness for thermal deformation assessment.

Dharmadhikari et al. [105] introduced a reinforcement learning system for L-DED melt pool control, using Q-learning with a digital twin built on the Eagar–Tsai model. The system optimizes process parameters iteratively, maintaining melt pool depth within 50 µm of the target.

For cold spray AM, Li et al. [106] proposed a MATLAB-based twin that simulates multi-layer coating using cylindrical jet distribution and deposition efficiency modeling. With coating height errors under 2%, the system accurately forecasts geometric evolution for various substrates.

Garfias et al. [107] offered a Metal Knitting strategy for CSAM to improve geometry and cohesion. Their controlled circular deposition reduced defects, while post-deposition annealing further improved microstructure, demonstrating a hybrid strategy for producing high-quality metal components.

Attariani et al. [108] developed a digital twin for LPBF using a circular laser array and thermal modeling in MOOSE. Their model predicts grain morphology through a Hunt-criterion-based solidification map, showing how power and scan speed shape microstructure, ultimately optimizing equiaxed grain formation.

Yavari et al. [84] integrated temperature readings with thermal simulation to detect flaws like porosity and voids in LPBF. Their hybrid approach enabled real-time fault localization, validated via XCT, positioning the twin as a vital QA component.

Miller et al. [109] created digital replicas of LPBF turbine blades based on scanned geometry and experimental data. Their simulations achieved tenfold accuracy improvement in strain prediction compared to CAD-based models, emphasizing the impact of real production data on mechanical validation.

Pantelidakis et al. [110] proposed a Unity-based digital twin for FDM machines, integrating firmware APIs and external sensors to support real-time visualization and performance tracking. With ±3 mm and ±2.2 °C accuracy in position and temperature, the ecosystem offers reliable in-process monitoring.

Finally, Wu et al. [111] introduced a failure criterion for BCC lattice structures based on post-process CT reconstructions. By defining angular deviation thresholds, their model supports quantitative inspection for service-loaded lattices.

Together, these diverse contributions underscore how digital twins are revolutionizing quality assurance in AM. From process simulation and real-time defect tracking to offline validation and structural health monitoring, these frameworks provide the foundation for data-driven decision-making and ensure that manufactured parts meet stringent industry standards.

Table 19 highlights the role of digital twins in defect detection, predictive testing, and process traceability. The works presented here cover a variety of AM modalities, such as L-DED, WAAM, and LFAM, with a focus on early defect detection, including dimensional drift, porosity, and bead abnormalities. The growing usage of AR and edge computing to improve operator feedback is one noteworthy trend. Combining simulation and empirical data, as demonstrated by Hartmann et al. [98] and Denkena et al. [38], is another strength that aids in predicting roughness and thermal warpage. Nevertheless, there are still issues with guaranteeing real-time application and combining predictions with automated remedial measures. Additionally, there aren't many unified platforms that can manage internal and external quality assurance parameters at the same time.

Table 19. Summary of Quality Assurance methods.

Ref.	Area of application	AM technology	Sensors	Lifecycle Phase	Output / Metrics Tracked
[64]	Surface quality evaluation	Light-Curing AM	Slice profile data	Pre-Process	Surface quality
[96]	Bead defect detection	WAAM	Camera	In-Process	Bead shape anomaly
[97]	Warp prediction	LFAM	Simulation-based	Pre-Process	Deformation, warpage
[38]	Hybrid LMD and milling planning	LMD + Micro-Milling	Cutting force	Pre-Process	Hardness, surface roughness
[98]	Melt pool and geometry prediction	Laser-DED	IR and CMOS cameras	In-Process	Temperature, clad geometry
[99]	Defect monitoring	LARM	High-speed camera, IR camera	In-Process	Cracks, thermal damage
[100]	Thermal control and planning	DED	Simulation + metadata	Pre-Process	Thermal field, melt pool geometry
[101]	Stress prediction	LFAM	simulation-based FEM	Pre-Process	Residual stress, warpage
[102]	Geometric validation	FDM	Microscopic imaging (cross-section)	Post-Process	Part geometry, mechanical response
[103]	P-S-P correlation	LPBF	Tensile, fatigue, elastic, resonance tests	Post-Process	Elastic modulus, fatigue
[104]	Distortion prediction	SLM	Industrial CT scanner	Post-Process	Displacement
[106]	Coating prediction	CSAM	simulation-based MATLAB	Pre-Process	Coating height, edge loss
[107]	Improved microstructure via post-treatment	CSAM	Observation-based post-treatment	Post-Process	Porosity, cohesion
[108]	Grain morphology optimization	LPBF	Simulation-based thermal model	Pre-Process	Grain morphology
[84]	Flaw localization via thermal deviation	Generic AM	Thermal imaging, XCT	In-Process	Flaws, voids, porosity
[109]	Turbine blade validation	LPBF	3D scanner, fatigue test	Post-Process	Stress, strain, fatigue life

[110]	Real-time status tracking	FDM	IR distance sensor, thermocouple	In-Process	Position, temperature
[111]	Lattice structure inspection	BCC lattice AM	Geometry inspection, microscopy	Post-Process	Rod angle deviation

5.3.2.5 Closed-Loop Control

Digital twins enable closed-loop control systems in AM, where real-time data from the physical process is continuously exchanged with its virtual counterpart. This bidirectional flow of information ensures that the process remains dynamically aligned with design intent and allows for immediate adaptation to internal variations or external disturbances. Such systems support not only adaptive manufacturing but also promote continuous improvement by analyzing historical data to refine parameters, reduce variability, and enhance part quality over time.

Y. Fu et al. [112] initiated the move toward intelligent structural validation by integrating FEA with U-net-based defect segmentation. Their simulation-in-the-loop framework updates the digital twin layer-by-layer, capturing inconsistencies as they occur and predicting failure strength within 5% accuracy. However, they also acknowledged challenges in detecting subsurface defects, suggesting the need for future multi-sensor integration.

Pushing the concept further, a 4D reconstruction pipeline was proposed for robotic cold spray AM [113], where a laser scanner and camera mounted on the robot capture each newly deposited layer. This real-time data enables immediate trajectory correction, forming a self-correcting control loop that improves accuracy and robustness of deposition.

Girard and Zhang [114] contributed with a structured light–based error detection system that identifies deposition anomalies by comparing real-time phase images with G-code-derived expectations. Detected discrepancies trigger corrective G-code generation, with experimental validation showing a fourfold improvement in surface accuracy after correction.

Real-time control in WAAM was explored by Mahdi et al. [23], who integrated cloud-based CNN defect classification with robotic path feedback. The system achieved 97% accuracy in weld anomaly detection and dynamically adjusted motion paths, showcasing the synergy of cloud computing and local robotics (Figure 37).

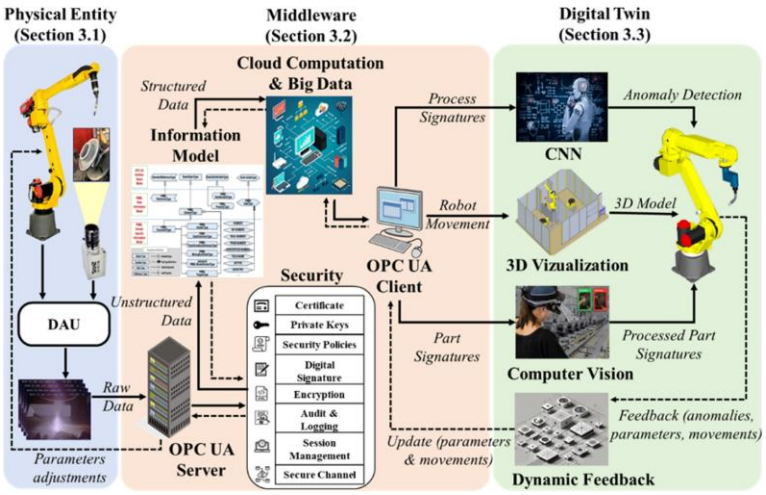

Figure 37. The proposed architecture of WAAM DT using OPC UA [23].

Malik et al. [115] implemented a reinforcement learning–driven digital twin in LPBF to reduce lack-of-fusion defects. Combining FEA, sensor-based sequential data, and RNNs, the system trains an RL agent to adaptively tune process parameters during printing, achieving strong performance in melt pool monitoring and decision-making.

In a probabilistic modeling approach, Karkaria et al. [116] introduced a Bayesian LSTM-based digital twin for DED. Coupled with model predictive control, the system forecasts future temperature distributions and adjusts laser power accordingly. Its hybrid nature, merging statistical learning with simulation, demonstrates one of the most comprehensive bidirectional feedback systems in AM.

On the construction scale, the RoBétArmé system [117] exemplifies cognitive digital twins that integrate sensor data, BIM models, and robotic execution. It adapts nozzle operation in real time while allowing AR-based human collaboration, showing the wide applicability of DTs in complex, multi-agent environments.

Ali et al. [118] further expanded the paradigm with a secure, real-time DT for FDM. Their architecture incorporates CNN-based anomaly detection, automatic print interruption, and augmented reality visualization via HoloLens. It offers a holistic cyber-physical solution to enhance quality and resilience in AM.

Focusing on sensor fusion, Chen et al. [119] built a digital twin that combines visual, acoustic, and thermal data with robot tracking in L-DED. Though currently limited to defect prediction, this system lays the groundwork for autonomous hybrid repair by enabling precise defect localization in 3D.

Rachmawati et al. [120] developed a lightweight FDM monitoring system using CNNs and a Unity interface for live printer tracking. This twin allows remote halting of faulty prints, illustrating that even low-cost platforms can support effective closed-loop control.

In LPBF, Phua et al. [121] tackled powder recoating variability with a Smart Recoating digital twin. Using Bayesian optimization and surrogate models trained on DEM/CFD simulations, their system suggests real-time corrections that include non-intuitive vertical adjustments to stabilise powder spread.

Visual feedback was central to Xiong et al. [122], who implemented a fuzzy controller for GMA-AM based on real-time molten pool imaging. This system dynamically adjusts arc current to maintain layer width, achieving impressive geometric accuracy even under variable process conditions.

Nath and Mahadevan [123] introduced a probabilistic DT for porosity control in LPBF. Using thermal images to update a Gaussian Process surrogate model, the system dynamically re-optimizes scan parameters, demonstrating the strength of Bayesian calibration in layer-wise defect reduction.

Corradini and Silvestri [24] developed a modular extrusion DT incorporating mechanical load monitoring, vision-based positioning, and fault response protocols. It not only pauses the print upon error detection but also tracks component wear for predictive maintenance, emphasizing comprehensive lifecycle monitoring.

A standards-based approach was proposed by Kim et al. [124], who built a WAAM DT aligned with ISO 23247. Their system uses CNNs for anomaly detection and supports OPC UA–based parameter control, enabling scalable, interoperable DT architectures for industrial AM.

The CyAMIS framework by Balu et al. [125] innovatively combines PDE-constrained neural networks with deep learning surrogates to predict full-field states in real time. By learning from sensor data while adhering to physical laws, it achieves simulation-grade accuracy without traditional computational overhead.

Xu et al. [126] created a closed-loop correction system for DED using point cloud analysis. A laser line scanner detects dimensional deviations, and machine learning modules generate new

toolpaths on-the-fly, eliminating the need for CAD regeneration (Figure 38). This cycle of scan–analyze–correct reduces surface error by 80% while maintaining part integrity.

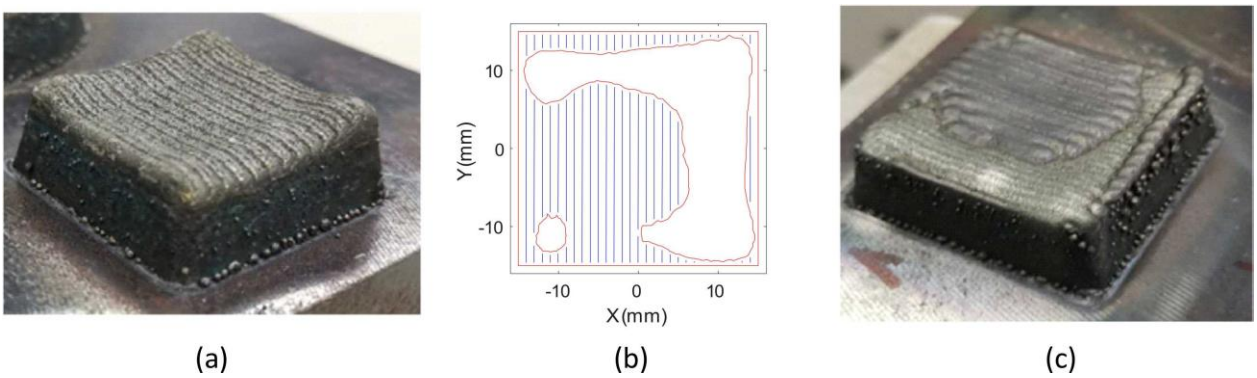

Figure 38 point cloud-based tool-path generation and dimension correction for one sliced layer: (a) original part with severe geometric distortions, (b) generated correction tool-path (laser-on segments), and (c) part after one layer of dimension correction [126].

Gunasegaram et al. [127] developed a supervisory control-oriented DT combining high-fidelity simulation and ML surrogates. It enables feedforward control through synthetic data generation and early fault prediction, paving the way for anticipatory decision-making in AM.

Stavropoulos et al. [128] implemented robust control theory in a DT for LPBF temperature regulation. Using dynamic system identification and LMI-optimized controllers, their system improves melt pool temperature stability by 68%, outperforming classical PID methods.

Complementing these approaches, Sieber et al. [86] applied a closed-loop DT in high-resolution inkjet printing. Based on tactile surface metrology, the system feeds back surface deviation maps to adjust parameters, ensuring ±10 μm surface fidelity and demonstrating the viability of feedback control in precision printing.

Together, these innovations highlight the growing maturity of closed-loop digital twins in AM. From powder spreading and thermal stabilization to adaptive slicing and autonomous repair, these systems close the loop between physical execution and digital design, elevating AM toward more intelligent, resilient, and self-correcting production platforms.

Table 20 synthesizes the advanced digital twin systems described in the Closed-Loop Control section, where bidirectional data exchange enables real-time parameter updates and adaptive control. The summarized works, including those by Malik et al. [115], Karkaria et al. [116], and Xu et al. [126], demonstrate the integration of simulation, sensing, and control algorithms,such as reinforcement learning, model predictive control, and fuzzy logic to manage deposition quality and respond to anomalies on the fly. Several studies, like those by Ali et al. [118] and Chen et al. [119], also incorporate sensor fusion for more informed decision-making. However, widespread deployment is still limited by challenges in sensor latency, control loop

tuning, and hardware compatibility. Furthermore, many solutions are validated in lab-scale settings, with fewer examples of robust industrial applications or standardized deployment pathways.

5.4 3D Reconstruction in Additive Manufacturing

Digital twins in AM increasingly rely on 3D reconstruction techniques to accurately model the evolving geometry, internal structure, and physical properties of parts throughout the fabrication process. These reconstruction approaches enable real-time monitoring, defect detection, mechanical validation, and process planning.

To help understand the changing landscape of 3D reconstruction in additive manufacturing, this section proposes a structured classification based on purpose, modality, and data granularity (Figure 39). With a focus on how these reconstructions feed digital twins or function independently for in-situ or post-process evaluations, this structure enables a thorough investigation of both offline and real-time reconstruction techniques hoping to draw attention to the operational diversity and increasing incorporation of 3D reconstruction pipelines in AM processes by presenting the literature in this manner.

Table 20. Summary of the Closed-loop Control methods.

Ref.	Area of application	AM technology	Sensors	Control Strategy	Correction Level
[112]	Real-time structural validation	FDM	Camera	Simulation-in-the-loop	Layer-wise FEA update
[113]	Trajectory correction in robotic cold spray	Robotic Cold Spray	Laser scanner, camera	Visual feedback	Toolpath correction
[114]	Pixel-wise error correction	SL-based AM	Structured light camera	Image analysis + logic	Layer correction
[23]	Welding anomaly feedback in WAAM	WAAM	Camera	CNN classification	Robot path correction
[115]	Fusion quality control	LPBF	Thermal sensors	Reinforcement Learning	Parameter tuning
[116]	DED temperature control	DED	Thermal sensors	Model Predictive Control	Laser power tuning
[117]	Robot shotcrete control	Shotcrete Construction	IoT sensors, camera	Sensor feedback loop	Nozzle motion

[118]	Cyber-physical FDM	FDM	Embedded sensors, camera	Anomaly classification + MPC	Process halt/tuning
[119]	Defect prediction in L-DED	Robotic L-DED	Vision, thermal, acoustic	Defect classification	Planning support
[120]	Multi-printer fault control	FDM	Temperature, humidity	CNN fault detection	Automatic stop
[121]	Recoater optimization	PBF	Recoater	Surrogate-driven control	Recoater stage tuning
[122]	Melt pool width control	GMA-WAAM	Passive vision sensor	Fuzzy logic	Arc current adjustment
[123]	Porosity control via GP	LPBF	Thermal camera	Bayesian control	Scan speed, laser power
[24]	Extrusion anomaly response	FDM	Encoders, thermistors	Rule-based fault logic	Pause + recovery
[124]	WAAM anomaly detection	WAAM	Voltage/current, HDR camera	Anomaly CNN	Parameter tuning
[125]	Physics-Aware DL feedback	Generic AM	IR camera	PDE-constrained DL	Thermal state feedback
[126]	Laser correction from scans	DED	Laser scanner	Point cloud-based	Geometry repair
[127]	Proactive defect control	Metal AM	Pyrometer	Feedforward ML	Temperature adjustment
[128]	Temperature control in LPBF	LPBF	Temperature sensors	Robust MPC	Laser power tuning
[86]	Surface feedback correction	Inkjet	3D scanner	Geometric error loop	Simulation-based tuning

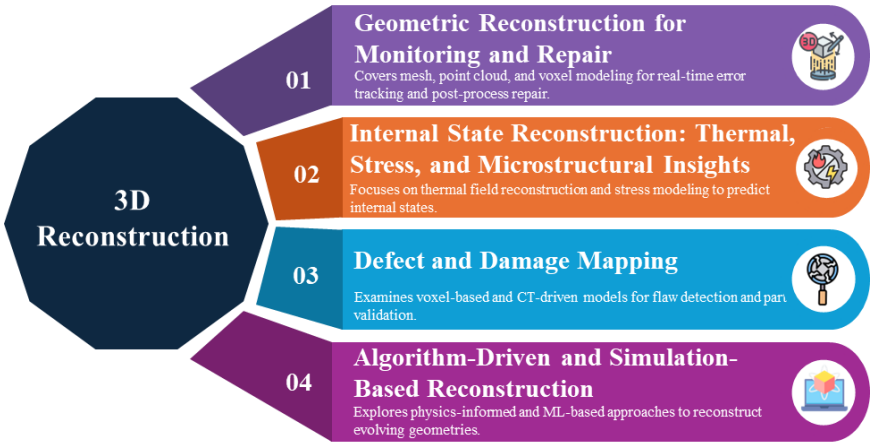

Figure 39. Classification of 3D Reconstruction methods in Additive manufacturing.

5.4.1 Geometric Reconstruction for Monitoring and Repair

This section consolidates digital twin approaches that focus on geometric reconstruction for both in-process monitoring and post-process repair. Although the objectives differ, real-time error correction versus restoration of damaged parts, the core techniques often rely on mesh generation, point cloud registration, and voxel-based geometry modeling.

Y. Fu et al. [112] incorporated real-time 3D reconstruction into their digital twin framework by employing high-resolution imaging and deep learning segmentation to detect and track defects throughout the AM process. The study leveraged U-net-based segmentation to identify voids and layer defects, updating a real-time FEA model to dynamically adjust material properties and stress distribution. Their image-driven reconstruction approach allowed for continuous defect tracking and stress analysis, bridging the gap between visual defect detection and mechanical validation (Figure 40(A)). However, they noted that accuracy limitations in their segmentation model, particularly for small or irregular defects, could impact the reliability of structural assessments, highlighting the need for higher-resolution imaging and alternative defect mapping techniques.

Building on real-time validation efforts, Girard and Zhang [114] developed a hybrid 2D-3D error detection strategy specifically tailored for FDM. By utilizing structured light imaging and fringe-based phase maps derived from sliced G-code, they detect anomalies in 2D and selectively reconstruct only erroneous regions into 3D (Figure 40(B)). This selective reconstruction significantly reduces computational overhead while enabling prompt geometric correction.

Complementing these in-situ strategies, Ochoa et al. [102] proposed a geometry-based digital twin generation method for FDM using reverse-engineered G-code and filament cross-section profiling. This virtual reconstruction mirrors actual deposition paths and is validated through mechanical testing and FE simulations, making it a valuable offline tool for structural validation.

Corradini and Silvestri [24] pursued a different offline reconstruction approach, generating 3D meshes from nozzle trajectory data, extrusion volume, and encoder feedback. By comparing reconstructed meshes to ideal STL models via point cloud analysis, their method facilitates quantitative defect localization and dimensional analysis.

Shifting to post-process analysis, Wu et al. [111] employed CT-based 3D point cloud reconstruction to evaluate deformation in SLM-fabricated lattices after mechanical loading. Skeleton extraction and angular deviation metrics allowed for detailed failure assessment, particularly suited to high-strain lattice structures.

On the microscale, Liu et al. [80] combined structured-light scanning with clustering and meshing algorithms to recreate the geometry of honeycomb structures layer by layer. These meshes were used in multiscale finite element models, enriching the fidelity of simulation-based property predictions (Figure 40(C)).

For repair-driven reconstruction, Li et al. [89] designed a workflow that aligns nominal and damaged gear geometries and extracts the repair volume using slicing and ray-casting. The resulting STL guides LDMD repair toolpaths, reducing human intervention in defect recovery (Figure 40(D)).

Zhang et al. [92] offered an extension of this repair strategy by adopting voxelization and Boolean operations to distinguish between additive and subtractive volumes. Their voxel-based method proved robust across multiple geometries and scan qualities, and it was experimentally validated (Figure 40(E)).

Finally, Wu et al. [87] enhanced scan registration for damaged molds in WAAM using a custom Offset ICP algorithm. By introducing translation offsets into the ICP framework, they achieved accurate alignment under conditions of minimal scan overlap, an essential improvement for practical, real-time repair workflows.

Together, these diverse yet interconnected contributions illustrate how digital twin-enabled geometric reconstruction plays a central role in both ensuring build accuracy and extending the lifespan of critical AM components.

Table 21 highlights the growing sophistication of surface-level 3D reconstruction techniques tailored for real-time and post-process monitoring in AM. These works primarily focus on reconstructing toolpath geometry, bead shape, and printed layer deviations using structured light, stereo imaging, and point cloud registration. A notable trend is the shift toward in-situ, scan-correct cycles, which close the loop between geometric deviation detection and corrective toolpath generation. Still, challenges remain in generalizing reconstruction workflows across different AM platforms and integrating them with downstream simulation or control modules.

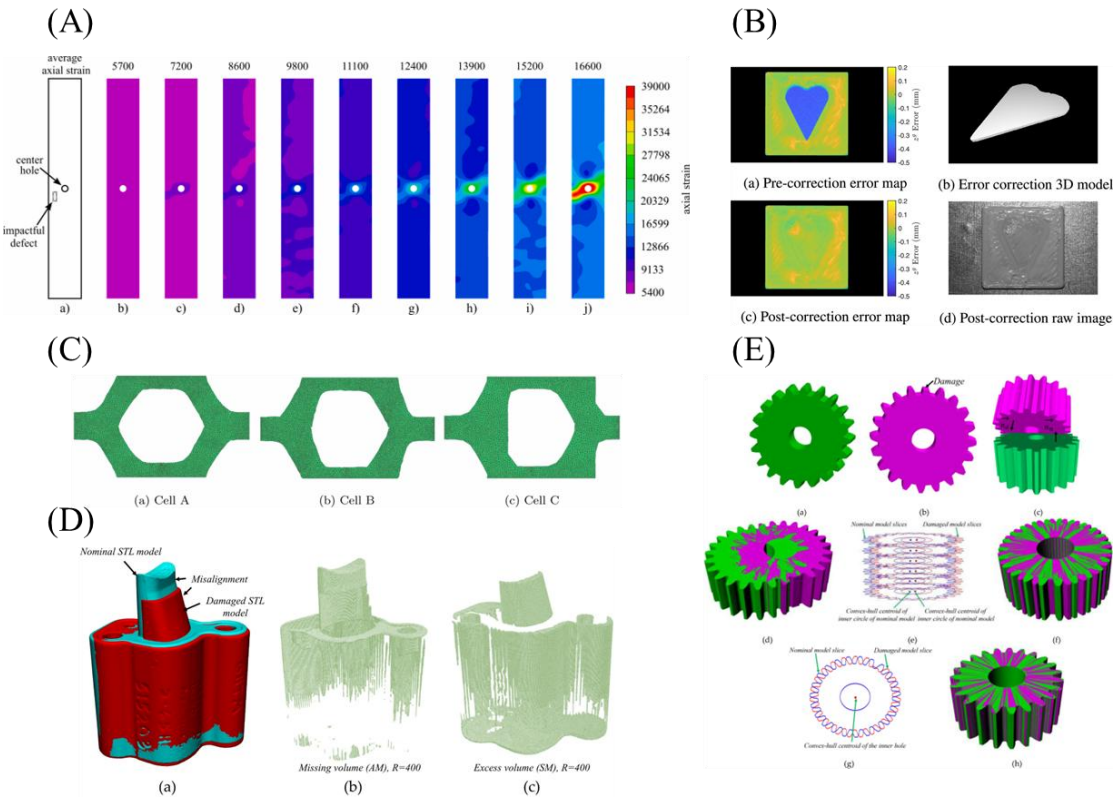

Figure 40. Examples of results of the Geometric Reconstruction for Monitoring and Repair: (A) Y. Fu et al. [112], (B) Girard and Zhang [114] , (C) Liu et al. [80], (D) Li et al. [89], (E) Zhang et al. [92].

Table 21. Summary of the Geometric Reconstruction for Monitoring and Repair methods.

Ref	AM Technology	Approach	Reconstruction Target	Online/ Offline	Application
[112]	FDM	Real-time imaging + U-Net segmentation + FEA	Geometry, mechanical defects	Online	Monitoring, stress analysis
[114]	FDM	Fringe SL + phase image + selective recon	Local geometry error	Online	Layer correction
[102]	FDM	G-code reverse engineering	Layer deposition path	Offline	Mechanical validation
[24]	FDM	Nozzle volume + encoder mesh	Print geometry	Offline	Dimensional quality map
[80]	FDM	Structured-light scan + mesh	Unit cell shapes	Online	Multiscale modeling
[111]	SLM	CT-based skeleton analysis	Lattice rod angles	Offline	Deformation assessment
[89]	Metal AM	Ray-casting + centroid alignment	Damage volume	Offline	Repair automation
[92]	AM-based repair	Voxel Boolean operations	Repair zones	Offline	Toolpath generation
[87]	WAAM	Offset ICP + point cloud	Surface geometry	Online	Real-time mold repair

5.4.2 Repair Internal State Reconstruction: Thermal, Stress, and Microstructural Insights

While geometric fidelity is crucial, an equally important dimension of AM quality lies in understanding and controlling the internal states of parts, specifically thermal gradients, residual stresses, and microstructural evolution. Several advanced digital twin implementations now focus on reconstructing these internal states, offering critical insights that directly influence performance and reliability.

Bevans et al. [66] laid foundational work in this domain by integrating real-time optical and thermal sensors with a graph-based simulation engine. Their hybrid digital twin for LPBF enables in-situ prediction of porosity, meltpool behavior, grain size, and hardness with high accuracy, moving AM toward a "born qualified" paradigm that verifies part integrity during fabrication (Figure 41(A)).

Extending into WAAM, Chen et al. [129] utilized boundary IR measurements and trained graph convolutional networks to reconstruct full-field temperature maps. This graph-based inpainting technique permits reconstruction even with sparse sensor data, making it especially viable for large-scale processes where dense sensor networks are impractical (Figure 41(B)).

In FDM processes, Lu et al. [85] proposed a physics-based compressive sensing technique that recovers 3D thermal fields from sparse measurements by solving an inverse heat transfer problem. By integrating Gaussian Process Regression to compensate for modeling errors, their method provides a low-cost yet high-accuracy alternative to full thermal imaging (Figure 41(C)).

Similarly focused on meltpool behavior, Yeung et al. [77] developed MPIV and MPAV volumetric reconstructions to capture spatial and temporal thermal features in LPBF. These voxelized datasets allow detection of pore-forming conditions such as keyhole instabilities, validated against XCT results (Figure 41(D)).

Zooming into the microstructure, Heo et al. [91] demonstrated a multiscale modeling framework that reconstructs grain growth, dislocation structures, and anisotropy using CA, PF, and CP models. This provides a deep insight into how microstructure evolves through the build and links these features to mechanical performance.

For stress analysis, Uzun et al. [130] employed voxel-based tomographic eigenstrain reconstruction to generate full-field stress and displacement maps using sparse X-ray diffraction data. Their approach overcomes the limitations of traditional stress mapping by covering all six stress components and validating them with multiple techniques (Figure 41(F)).

Furthering this, another work [131] applied height-based DIC to reconstruct triaxial displacements in CM 247 LC alloys, enabling stress mapping without plane simplifications. The method provides detailed insight into stress development from build to release.

In the context of process validation, Hartmann et al. [98] used CMOS-based in-situ imaging to capture melt pool and clad profiles during DED. These reconstructions inform and calibrate multiscale thermal and geometric simulations, enhancing predictive accuracy (Figure 41(E)).

Chapman et al. [132] delivered perhaps the most detailed microstructural reconstruction, combining 1000 serial sections with EBSD and BSE imaging to produce benchmark voxel data for LPBF IN625 samples. This dataset aligned using DREAM.3D, serves as a gold standard for validating image-based simulations of AM processes.

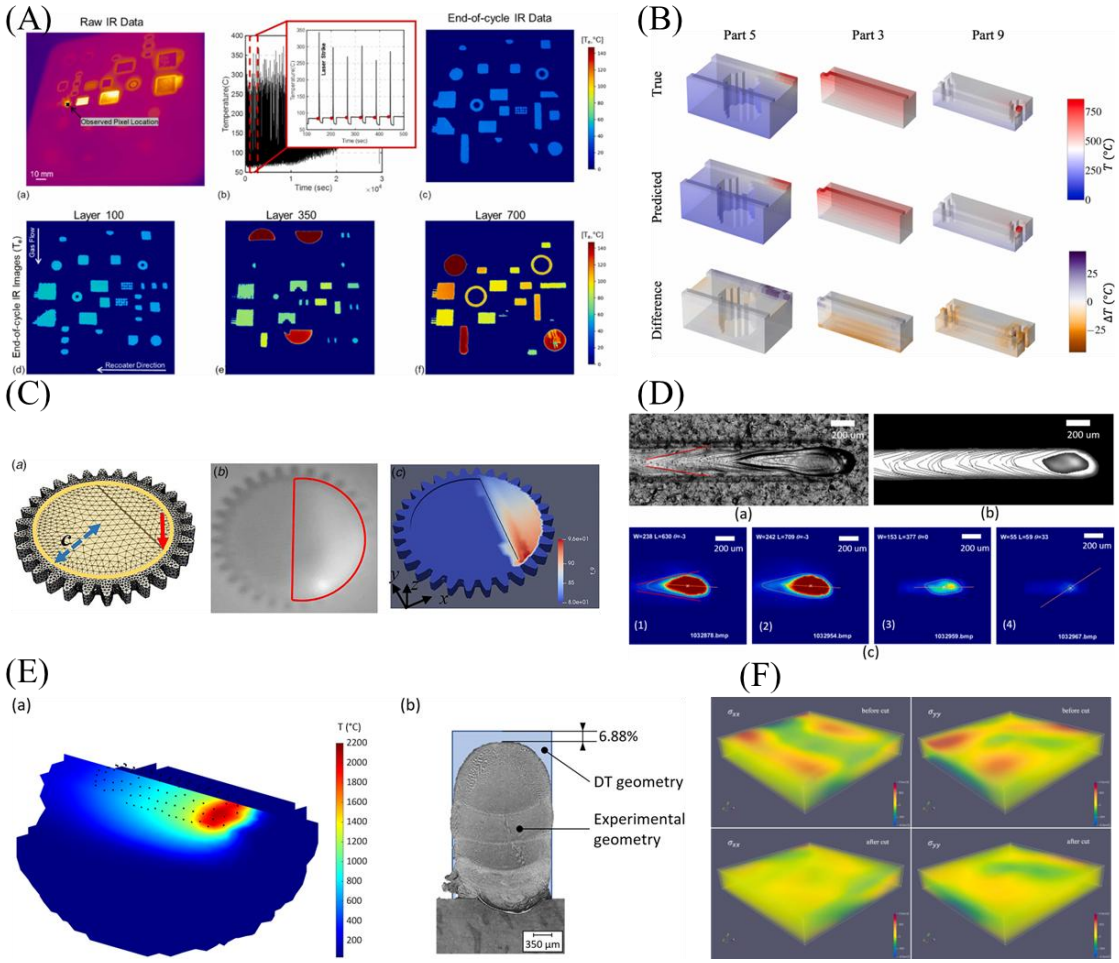

Figure 41. Example of the Internal State Reconstruction: (A) Bevans et al. [66], (B) Chen et al. [129], (C) Lu et al. [85], (D) Yeung et al. [77], (E) Hartmann et al. [98], (F) Uzun et al. [130].

Collectively, these efforts illustrate how internal state reconstruction serves as a cornerstone for truly predictive and quality-aware digital twins in additive manufacturing.

Table 22 summarizes contributions aimed at visualizing and understanding internal phenomena such as residual stress, thermal gradients, and microstructure evolution within AM builds. A

key strength of these studies is the integration of multi-physics models with sparse measurement data to reconstruct spatially resolved thermal or stress fields. Methods such as graph-based inpainting, eigenstrain inversion, and multiscale physics-informed modeling enable high-fidelity internal reconstructions. However, these efforts are mostly computationally intensive, highlighting a gap in real-time capability and sensor fusion for full-field internal state monitoring.

Table 22. Summary of the Internal State Reconstruction methods.

Ref	AM Technology	Approach	Reconstruction Target	Online/Off line	Application
[66]	LPBF	Graph-based sim + IR & optical sensors	Porosity, meltpool, hardness	Online	Quality prediction
[129]	WAAM	GCN with boundary temps	Interior temperature	Online	Thermal control
[85]	FDM	PDE-based compressed sensing + GPR	3D transient temperature	Online	Simulation-informed DT
[77]	LPBF	MPIV + MPAV	Meltpool energy fields	Offline	Defect-prone zones
[91]	LPBF	CA + PF + CP model chain	Microstructure, defects	Simulation	Process-property link
[130]	LPBF	hDIC + eigenstrain inversion	Residual stress, strain	Offline	Full-field stress map
[131]	LPBF	RBF mapping on displacement	Elastic strain	Offline	Cut-induced stress recovery
[98]	Laser-DED	CMOS image + meltpool fit	Layer profile	Online	Model calibration
[132]	LPBF	BSE/EBSD stack + image fusion	Grain morphology	Offline	Microstructure benchmark

5.4.3 Defect and Damage Mapping

Complementing geometric and thermal reconstructions, a vital class of digital twin applications focuses on detecting, characterizing, and localizing defects and damage throughout the AM lifecycle. These methods harness data-rich imaging, CT scanning, and deep learning to reconstruct internal flaw structures and understand defect formation under varied process conditions. The research in this area reveals a steady convergence between imaging fidelity, algorithmic intelligence, and process-specific tuning.

The effort by Gourley et al. [133] provides a notable example of image-driven defect identification. Their U-Net–based segmentation pipeline, developed for binder jetting additive manufacturing, identifies critical recoating anomalies such as streaking and short spreading. These 2D segmentations are stacked into a voxel-based volume, allowing the system to visualize and localize defect evolution across layers. This workflow not only facilitates post-build inspection but also builds correlations with process parameters, establishing a feedback loop for defect prevention (Figure 42 (A)).

Building on this emphasis on internal features, Qu et al. [54] introduced a heterogeneous pore design algorithm for FDA-3D printing. In their method, fabricated parts are scanned using micro-CT, and pores are reconstructed and quantified using Boolean operations and voxel-based processing in ImageJ and BoneJ. This detailed reconstruction enables high-resolution pore analysis, both radial and embedded, supporting structure–property studies and offering design insights grounded in actual print outcomes.

Ziabari et al. [134] advanced this concept with a CAD-assisted deep learning framework designed to reconstruct high-resolution XCT volumes from sparse scanning data. Their system, CAD-DLMBIR, integrates beam hardening correction and residual U-Net architectures to surpass traditional filtered back projection in both speed and accuracy. By reconstructing fine pore geometries with reduced scanning requirements, this approach supports both rapid part certification and porosity-informed process optimization.

Addressing similar goals in LPBF, Chen et al. [60] developed a MDACNN. Their model fuses low- and high-resolution CT scan data to extract critical pore features, volume, orientation, and sphericity, which are then used to inform downstream design and optimization. This enables the reconstruction of rich internal structure profiles from limited experimental data (Figure 42(B)).

In the context of metal lattice structures, Wu et al. [111] proposed a deformation evaluation method using CT-based point cloud reconstruction. After mechanical loading, lattice structures are scanned, and central rod skeletons are extracted via a 1L median filter. By analyzing inter-rod angles, their framework can identify deformation and failure thresholds with high spatial precision. This post-process technique eliminates the need for mesh modeling and manual tracking, offering a fast and scalable defect assessment tool.

A process-integrated approach is demonstrated by Corradini and Silvestri [24], who reconstructed printed geometries from nozzle movement data, extrusion volume, and encoder feedback. The resulting mesh models, based on approximated hexagonal cross-sections, are aligned with nominal STL files to detect dimensional drift and under-extrusion. Their method not only quantifies geometric deviations but also computes a quality index, transforming process monitoring data into actionable quality metrics.

In ceramic additive manufacturing, Zhang et al. [135] performed an in-depth defect evolution study using X-ray CT on alumina ceramics produced via DLP. They analyzed how variables such as atmosphere and heating rate during debinding influenced porosity, delamination, and crack formation. The volumetric reconstructions revealed strong correlations between thermal

profiles and internal defect morphology, underlining the value of CT-based analysis for process design and optimization.

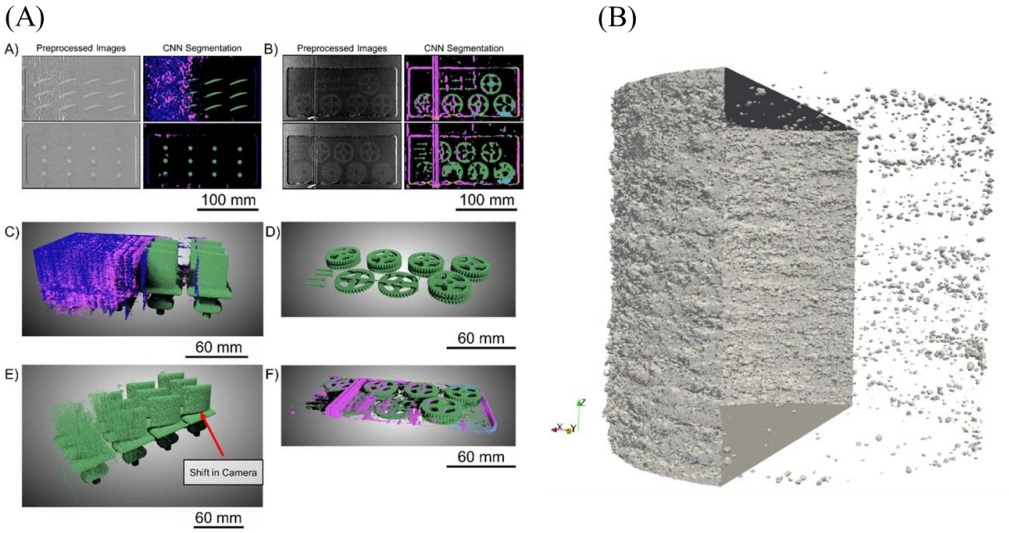

Figure 42. Examples of results of the Defect and Damage Mapping methods: (A) Gourley et al. [133], (B) Chen et al. [60].

Together, these investigations represent a sophisticated cross-section of defect-aware digital twins. By embedding CT data, neural models, and voxel-level analysis into AM workflows, they enable not just post-process verification but forward-looking defect mitigation strategies. The synergy between imaging, computation, and digital design is laying the groundwork for more resilient, optimized, and intelligent additive manufacturing systems. Whether driven by CT data, deep learning, or hybrid modeling approaches, defect and damage reconstruction enables part validation, process tuning, and the development of robust, fault-tolerant AM strategies. in digital twins. By shifting the focus from external form to internal heat-driven dynamics, they open pathways for smarter, thermally informed process monitoring and control, foundational for improving consistency, part integrity, and AM predictability.

Table 23 focuses on the detection, localization, and quantification of defects, including pores, cracks, and delamination, using 3D reconstruction strategies. Many works here employ CT-based volumetric imaging or image-stacking techniques for reconstructing defect-prone zones. Noteworthy advances include voxel-level inspection frameworks and AI-assisted segmentation, which enable accurate mapping of internal anomalies. These reconstructions are critical for post-process validation and for correlating defect morphology with process parameters. Nonetheless, the dependency on high-resolution CT data and offline processing presents a bottleneck for scaling to production environments or supporting continuous process control.

Table 23. Summary of the Defect and Damage Mapping methods.

Ref.	Area of Application	AM Technology	Reconstruction Approach	Data Source	Use Case
[133]	Recoating defect identification	Binder Jetting AM	U-Net 2D segmentation + voxel stacking	Optical images	Layer-wise defect evolution and process feedback
[54]	Pore structure quantification	FDA	CT-based voxel ops using ImageJ/BoneJ	Micro-CT	Pore analysis and structure-property studies
[134]	Sparse-view XCT reconstruction	Metal AM	CAD-DLMBIR: Beam-hardening + Res-UNet	Sparse XCT + CAD	Rapid, accurate pore detection and optimization
[60]	Pore feature extraction in Ti–6Al–4V	LPBF	Multi-fidelity CNN	CT high- & low-res	Pore metrics for design and optimization
[111]	Post-load deformation detection in lattices	SLM	CT + skeleton line analysis	CT scans	Angular deviation-based failure analysis
[24]	Dimensional accuracy and defect quantification	FDM	G-code + mesh + point cloud analysis	Encoder, nozzle data	STL deviation index for QA
[135]	Defect morphology vs. process condition	DLP	XCT of crack, pore, delam distribution	X-ray CT	Thermal profile impact on internal defect forms

5.4.4 Algorithm-Driven and Simulation-Based Reconstruction

Algorithm-driven and simulation-based reconstruction techniques represent a powerful class of digital twin strategies in additive manufacturing, enabling high-fidelity modeling of complex geometries, energy distributions, and build processes without relying solely on sensor data. These approaches integrate numerical algorithms, inverse modeling, and optimization routines to simulate or predict the reconstructed state of AM parts with high spatial and temporal accuracy.

Chen et al. [132] present a volumetric 3D reconstruction framework within tomographic additive manufacturing, driven by an expectation-maximization algorithm. The algorithm generates optimized exposure patterns to reproduce target light dose distributions, enabling volumetric photopolymerization from all directions simultaneously. This strategy significantly enhances geometric fidelity in challenging scenarios such as high-attenuation materials or large-volume prints, mitigating overcuring and edge blur. Moreover, the system's innovative hardware configuration, with stationary resin and rotating optics, further ensures uniform curing. The result is a robust simulation-based reconstruction strategy well suited for support-free, complex part fabrication.

Zhou et al. [62] introduced a reconstruction pipeline tailored for transforming voxel-based topology optimization outputs into smooth, manufacturable geometries. Their boundary representation process extracts iso-surfaces while integrating strict manufacturing constraints,

including minimum feature size and allowable overhang angles. By enforcing localized span control, the method produces support-free infill and shell structures, which are validated through FDM printing. The reconstructed geometries maintain the design intent while meeting AM feasibility criteria, illustrating how algorithmic post-processing bridges generative design and production.

In another example of predictive, simulation-driven reconstruction, Li et al. [106] developed a geometry-based algorithm to model layer evolution in CSAM. By simulating ray-jet impacts and mesh patching, their method captures the deposition process in high spatial detail, reflecting realistic coating topology with edge losses and asymmetries. Though not based on measured data, this reconstruction provides valuable foresight into expected part morphology and helps refine process parameters before manufacturing begins (Figure 43(B)).

Chen et al. [131] further expanded the realm of tomographic reconstruction with a statistically grounded algorithm for VAM. Their Maximum Likelihood–Expectation Maximization approach generates strictly positive, physically realizable projection patterns for light-based curing processes. Implemented with GPU acceleration, the method achieves high-speed and high-fidelity dose simulations even under significant optical attenuation. Comparative tests on complex models demonstrated superior accuracy and stability versus traditional reconstruction methods, reinforcing the method's potential for real-time or batch pattern optimization in photopolymer-based AM.

The work by Patuelli et al. [104] utilizes offline 3D reconstruction through iCT to validate simulated distortions in a voxel-based FEM model of an SLM-manufactured artifact. iCT scans provide sub-100 μm resolution volumetric data, which is aligned with the nominal STL geometry for accurate deviation analysis. The reconstructed volume is compared with simulation outputs across 40 points, enabling quantitative validation of the digital twin simulation.

Zhang et al. [92] proposed a voxel-based geometry reconstruction framework for additive manufacturing-based repair of damaged metallic components. The method begins by aligning damaged and nominal models using convex-hull centroid slicing and least-squares fitting. Both models are voxelized using the Marching Cubes algorithm, and Boolean operations extract the repair volume: missing regions for additive restoration and excess material for subtractive removal. This voxel approach supports accurate reconstruction even from non-ideal 3D scans and enables automated repair volume generation for complex parts such as aero-engine blades and casting dies. The method was validated across multiple geometries and resolutions, and its accuracy was confirmed via signed distance errors and tensile testing.

Zhou et al. [62] introduced a robust reconstruction method for converting voxel-based topology optimization results into smooth, manufacturable geometries for additive manufacturing. The reconstruction pipeline includes a boundary representation process that not only extracts iso-surfaces from the optimized density field but also enforces strict overhang span limits, ensuring all internal infill regions remain self-supporting. The algorithm accounts for AM-specific constraints like minimum feature size and overhang angle using localized span control during the voxel-to-CAD conversion. Final geometries generated from coarse TO meshes were validated with FDM printing, confirming the feasibility of the method for support-free manufacturing (Figure 43(C)).

Niu et al. [136] proposed a CT-based digital reconstruction and analysis framework for evaluating the geometric integrity of AM-fabricated micromixers. Their method reconstructs 3D models of square wave and 3D circular micromixers using high-resolution CT scans and AVIZO software, followed by extracting the central channel axis and generating orthogonal cross-sectional planes. A custom contour extraction algorithm is used to obtain the channel profile at any location, allowing precise measurement of width, height, and area. The algorithm includes an efficient winged-edge triangular mesh search and geometric transformations to improve processing speed. Through statistical and uncertainty analyses, the method demonstrated measurement errors below 6%, validating its reliability for nondestructive internal inspection of microfluidic features. The proposed approach can be extended to other microscale AM components with internal channels, like grooves or cantilevers.

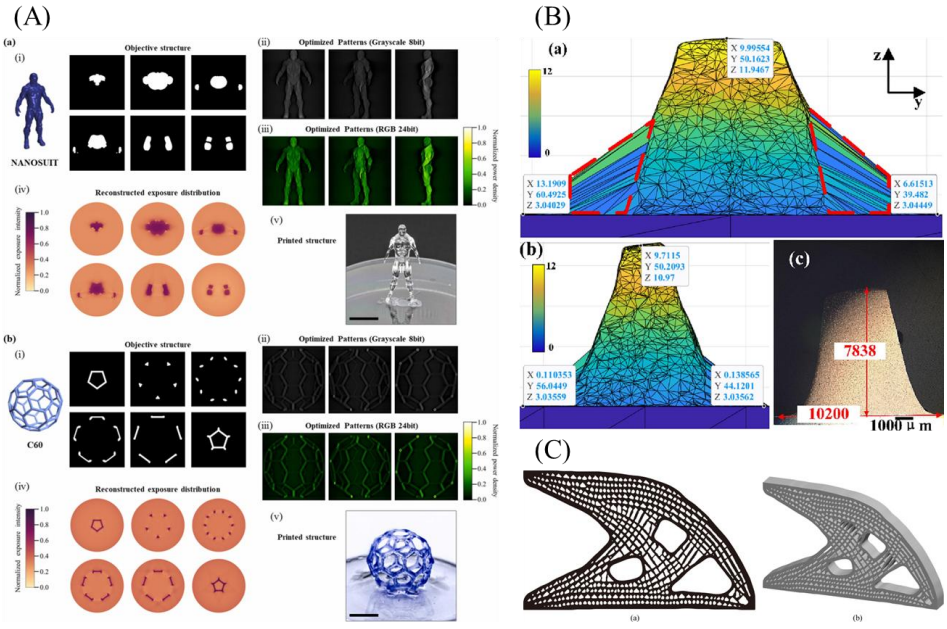

Figure 43. Examples of results of the Algorithm-Driven and Simulation-Based Reconstruction methods: (A) Chen et al. [132], (B) Li et al. [106], (C) Zhou et al. [62].

Together, these works exemplify how simulation and algorithm-based reconstructions empower digital twins to model the AM process with remarkable resolution and flexibility. By moving beyond sensor-bound reconstructions, they enable a deeper understanding of material exposure, geometry formation, and design manufacturability, essential capabilities for the future of intelligent, autonomous additive manufacturing systems.

Table 24 brings together works that rely primarily on modeling, simulation, or topology-based methods to reconstruct AM geometries. These methods include thermal simulations, ray-jet models, compressed sensing, and topology-to-CAD conversion pipelines. The standout feature of these approaches is their ability to generate or validate geometry without relying on physical scans, often enabling reconstruction before or during the build. These algorithmic reconstructions are particularly valuable in early design stages or for defect prediction under uncertain conditions. However, the abstraction from real measurement data may limit accuracy in some applications, and further efforts are needed to couple these models with live feedback for closed-loop implementation.

Table 24. Summary of the Algorithm-Driven and Simulation-Based Reconstruction methods.

Ref	AM Technology	Approach	Reconstruction Target	Online/Offline	Application
[132]	VAM	EM + grayscale photomasks	Exposure dose field	Offline	Volumetric fidelity
[62]	Generic AM	Voxel to B-rep surface	Optimized topology	Offline	Manufacturable CAD
[106]	CSAM	Ray simulation + mesh patching	Deposit layers	Offline	Cold spray prediction
[131]	VAM	ML-EM projection + GPU	Light dose convergence	Offline	Fast 3D exposure control
[104]	SLM	iCT validation of FEM	Deformation fields	Offline	Simulation validation
[136]	Microfluidics AM	CT + contour profile extraction	Channel shape	Offline	Microfeature QA
[131]	FDM	Voronoi lattice reconstruction	Cellular structures	Offline	TO-to-AM workflow

These diverse 3D reconstruction strategies significantly enhance the capabilities of digital twins in AM, supporting real-time monitoring, simulation-driven feedback, defect analysis, and design optimization. Each modality, whether image-based, thermal, structural, or simulated, contributes to a more complete and reliable digital representation of the additive manufacturing process and its outputs.

5.5 Challenges, and Future Outlook

5.5.1 Challenges, and Future Outlook

While the preceding sections showcase significant technical advancements, this final section synthesizes the cross-cutting challenges that persist in implementing digital twins and 3D

reconstruction in AM. It categorizes limitations by technological bottlenecks and workflow-level barriers. It also outlines a future outlook that advocates for real-time parameter optimization, intelligent reconstruction pipelines, and standardized frameworks, paving the way for more autonomous and reliable AM systems.

5.5.2 Challenges in Digital Twin Development

One of the foremost challenges in developing digital twins lies in achieving seamless real-time data synchronization. The task of integrating data streams from diverse sources such as thermal cameras, structured light sensors, and acoustic devices proves to be technically demanding, especially when these systems must scale across different additive manufacturing platforms. This complexity is evident in the works of Corradini and Silvestri [41] and Mahdi et al. [23], who successfully implemented such systems but emphasized their highly application-specific nature.

In addition, developers often grapple with balancing computational cost and model fidelity. High-fidelity simulations like those introduced by Malik et al. [115] and Stavropoulos et al. [128] can deliver accurate predictions and process control but typically require reduced-order modeling or surrogate networks to meet the constraints of real-time performance.

Another significant concern is cybersecurity. The always-connected architecture of digital twin environments, such as those developed by Ali et al. [118] and Nath and Mahadevan [123], inherently increases their exposure to cyber-physical threats. As a result, these systems demand advanced anomaly detection methods and secure communication protocols to maintain operational integrity.

Finally, the lack of universal standards and scalable architectures hinders broader adoption. While Kim et al. [124] made notable strides with an ISO-aligned, modular approach for WAAM systems, most industrial platforms still operate on proprietary infrastructure, impeding interoperability and cross-platform deployment.

5.5.3 Challenges in 3D Reconstruction

Achieving high-resolution and accurate 3D reconstruction remains an elusive goal in many AM contexts. Image-based strategies such as those developed by Y. Fu et al. [112] and Xiong et al. [122], perform well in identifying surface defects but fall short when it comes to detecting internal flaws that can compromise structural integrity.

Moreover, the immense data volumes generated during reconstruction add another layer of complexity. Systems like those proposed by Chapman et al. [132] and Liu et al. [80] rely on voxel-based or point cloud models that are computationally intensive, placing significant demands on memory and processing throughput.

Sensor fusion, while promising, is not yet mature. Approaches such as those presented by Chen et al. [119] and Yeung et al. [77] incorporate multiple sensor modalities to capture rich spatial and temporal features. However, challenges in aligning these data streams, ensuring temporal coherence, and mitigating sensor noise continue to limit their effectiveness.

Finally, many existing 3D reconstruction workflows still require manual alignment or human-guided corrections. Automated techniques developed by Li et al. [89] and Xu et al. [126] reduce this need but do not eliminate it entirely, hindering the feasibility of real-time or fully autonomous deployment in manufacturing environments.

5.5.4 Future Outlook

In the future, 3D reconstruction and digital twins will play an increasingly important role in additive manufacturing. The creation of systems that not only continuously monitor the printing process but also automatically modify the printing parameters, such as temperature, feed rate, or laser power, in response to actual build conditions is one of the most promising avenues. Production might become more reliable and effective with this type of real-time optimization, which could also significantly increase part quality, cut waste, and stop issues before they arise. Simultaneously, there is an increasing interest in improving the accuracy and practicality of 3D reconstruction techniques. Existing systems frequently require adjustments by humans to align scans and models, or struggle with the trade-off between resolution and speed. Future methods must concentrate on quicker and more automated methods that can record internal and external features, ideally with fewer sensors and less computational effort. Combining machine learning and intelligent scanning techniques, for instance, may make it simpler to identify issues early and modify the procedure as necessary.

As these technologies advance, improved methods for integrating various hardware and software platforms can be anticipated, which will facilitate the deployment of digital twin systems in factories and organizations. A fully integrated and intelligent manufacturing environment is the long-term goal, where each machine, part, and decision is directed by a real-time digital replica that continuously learns and gets better. In addition to helping businesses produce parts more precisely, this would also make the entire process more visible, traceable, and flexible enough to meet changing needs.

5.6 Conclusion

The integration of digital twin technologies and 3D reconstruction methods is fundamentally reshaping how additive manufacturing is understood, monitored, and controlled. As this review has demonstrated, these tools are gradually finding their way into real-world, industrial

applications and are no longer limited to research labs or proof-of-concept demonstrations. Smarter, more robust manufacturing ecosystems are being made possible by the convergence of virtual models and physical builds, whether it is through simulation-informed repair in directed energy deposition, real-time melt pool monitoring in laser powder bed fusion, or predictive quality evaluation in fused filament fabrication.

A growing number of studies show the concrete benefits of integrating sensor data, machine learning, and physics-based simulation within a digital twin framework across the five application areas studied: design optimization, process monitoring, predictive maintenance, quality assurance, and closed-loop control. Similar to this, 3D reconstruction methods have changed from static post-build inspections to layer-by-layer, dynamic tools that integrate seamlessly with digital twin systems. When combined, these technologies enable more agile responses to variability, deeper process understanding, and quicker defect detection.

Despite the promising advancements, challenges remain. The field is still struggling with problems like cross-platform standardization, computational cost, and data synchronization. To push the boundaries further, it will be essential to achieve more fully automated, high-resolution reconstruction and real-time, closed-loop optimization of process parameters.

In the end, 3D reconstruction and digital twins are not merely supplements to the AM workflow; rather, they are the cornerstones of a new manufacturing paradigm. These technologies will be crucial in advancing additive manufacturing toward a future characterized by intelligence, adaptability, and reliability as long as research into bridging the gap between design and production continues and as industrial adoption increases.

The goal of this review is to offer a thorough summary, assessing, and extending future innovations. Opportunities are numerous on the horizon, and additive manufacturing is well on its way to reaching its full potential with digital twins and 3D reconstruction at its core.

5.7 Author Contributions

Conceptualization, A.Z.; Formal analysis, M.H. and A.Z.; Funding acquisition, M.H. and S.K.; Investigation, A.Z.; Methodology A.Z.; Supervision, M.H. and S.K.; Writing—original draft, A.Z.; Writing—review and editing, M.H and S.K. All authors have read and agreed to the published version of the manuscript.

5.8 Funding

Funding: The authors acknowledge the funding provided by the Natural Sciences and Engineering Research Council (NSERC) of Canada (grant number: CRSNG–RGPIN-2021-02846) and the Canada Research Chairs Program.

5.9 Declarations

Competing interests: The authors declare no competing interests.

5.10 References

[1] B.V. Vasishta, T.H. Preetham, U. Akhil, N. Radhika, An overview of the evolution of additive manufacturing from 3d to 5d printing in biomedical applications, Progress in Additive Manufacturing (2024) 1-17.

[2] A. Mahmood, T. Akram, H. Chen, S. Chen, On the evolution of additive manufacturing (3D/4D printing) technologies: materials, applications, and challenges, Polymers 14(21) (2022) 4698.

[3] T.S. Tamir, G. Xiong, Z. Shen, J. Leng, Q. Fang, Y. Yang, J. Jiang, E. Lodhi, F.-Y. Wang, 3D printing in materials manufacturing industry: A realm of Industry 4.0, Heliyon 9(9) (2023).

[4] A. Hakami, S.A. Ojo, D.V. Abere, F.D. Uzuh, R.A. Robert, Advancements in metal additive manufacturing: opportunities, limitations, impact on properties, and potential solutions: a review, Progress in Additive Manufacturing (2024) 1-49.

[5] F.A.C. Sanchez, H. Boudaoud, M. Camargo, J.M. Pearce, Plastic recycling in additive manufacturing: A systematic literature review and opportunities for the circular economy, Journal of Cleaner Production 264 (2020) 121602.

[6] H. Kim, Y. Lin, T.-L.B. Tseng, A review on quality control in additive manufacturing, Rapid Prototyping Journal 24(3) (2018) 645-669.

[7] Q. Fang, G. Xiong, M. Zhou, T.S. Tamir, C.-B. Yan, H. Wu, Z. Shen, F.-Y. Wang, Process monitoring, diagnosis and control of additive manufacturing, IEEE Transactions on Automation Science and Engineering 21(1) (2022) 1041-1067.

[8] S. Romano, S. Miccoli, S. Beretta, A new FE post-processor for probabilistic fatigue assessment in the presence of defects and its application to AM parts, International Journal of Fatigue 125 (2019) 324-341.

[9] A. Coro, L.M. Macareno, J. Aguirrebeitia, L.N. López de Lacalle, A methodology to evaluate the reliability impact of the replacement of welded components by additive manufacturing spare parts, Metals 9(9) (2019) 932.

[10] J. Rao, S. Leong Sing, P. Liu, J. Wang, H. Sohn, Non-destructive testing of metal-based additively manufactured parts and processes: a review, Virtual and Physical Prototyping 18(1) (2023) e2266658.

[11] K. Zhu, J.Y.H. Fuh, X. Lin, Metal-based additive manufacturing condition monitoring: A review on machine learning based approaches, IEEE/ASME Transactions on Mechatronics 27(5) (2021) 2495-2510.

[12] M.M. Ahsan, S. Raman, Y. Liu, Z. Siddique, Defect analysis of 3D printed object using transfer learning approaches, Expert Systems with Applications 253 (2024) 124293.

[13] Z. Abdelhamid, H. Mohamed, S. Kelouwani, The use of machine learning in process–structure–property modeling for material extrusion additive manufacturing: a state-of-the-art review, Journal of the Brazilian Society of Mechanical Sciences and Engineering 46(2) (2024) 70.

[14] P. Charalampous, I. Kostavelis, D. Tzovaras, Non-destructive quality control methods in additive manufacturing: a survey, Rapid Prototyping Journal 26(4) (2020) 777-790.

[15] S. Inayathullah, R. Buddala, Review of machine learning applications in additive manufacturing, Results in Engineering (2024) 103676.

[16] K. Schnabel, J. Baumgartner, B. Möller, M. Scurria, Fatigue assessment of additively manufactured AlSi10Mg structures using effective stress concepts based on the critical distance approach, Welding in the World 65 (2021) 2119-2133.

[17] A.-F. Obaton, Y. Wang, B. Butsch, Q. Huang, A non-destructive resonant acoustic testing and defect classification of additively manufactured lattice structures, Welding in the World 65(3) (2021) 361-371.

[18] S. Usha, In situ monitoring of metal additive manufacturing process: a review, additive manufacturing (2021) 275-299.

[19] A. Megdich, M. Habibi, L. Laperrière, Z. Li, Y. Abdin, Advanced nanocomposites for 4D printing: High-performance electroactive shape memory polymers for smart applications, Applied Materials Today 44 (2025) 102702.

[20] K. Bouguermouh, M. Habibi, L. Laperrière, Z. Li, Y. Abdin, Designing advanced 4D printing thermo-sensitive shape memory polymer blends for enhanced mechanical and shape memory performances, Progress in Additive Manufacturing (2025) 1-20.

[21] U. Tariq, R. Joy, S.-H. Wu, M.A. Mahmood, A.W. Malik, F. Liou, A state-of-the-art digital factory integrating digital twin for laser additive and subtractive manufacturing processes, Rapid Prototyping Journal 29(10) (2023) 2061-2097.

[22] M. Kamali, B. Atazadeh, A. Rajabifard, Y. Chen, Advancements in 3D digital model generation for digital twins in industrial environments: Knowledge gaps and future directions, Advanced Engineering Informatics 62 (2024) 102929.

[23] M.M. Mahdi, M.S. Bajestani, S. Do Noh, D.B. Kim, Digital twin-based architecture for wire arc additive manufacturing using OPC UA, Robotics and Computer-Integrated Manufacturing 94 (2025) 102944.

[24] F. Corradini, M. Silvestri, Design and testing of a digital twin for monitoring and quality assessment of material extrusion process, Additive Manufacturing 51 (2022) 102633.

[25] M. Biehler, R. Mock, S. Kode, M. Mehmood, P. Bhardwaj, J. Shi, AUDIT: Functional Qualification in Additive Manufacturing Via Physical and Digital Twins, Journal of Manufacturing Science and Engineering 146(2) (2024).

[26] A. Ziadia, M. Habibi, S. Kelouwani, Digital twin-driven real-time optimization of layer-specific surface roughness in FDM 3D printing, Progress in Additive Manufacturing (2025) 1-24.

[27] G.A.R. Sampedro, M.A.P. Putra, M. Abisado, 3D-AmplifAI: An ensemble machine learning approach to digital twin fault monitoring for additive manufacturing in smart factories, IEEE Access 11 (2023) 64128-64140.

[28] Q. Feng, Y. Zhang, B. Sun, X. Guo, D. Fan, Y. Ren, Y. Song, Z. Wang, Multi-level predictive maintenance of smart manufacturing systems driven by digital twin: A matheuristics approach, Journal of Manufacturing Systems 68 (2023) 443-454.

[29] R. Van Dinter, B. Tekinerdogan, C. Catal, Predictive maintenance using digital twins: A systematic literature review, Information and Software Technology 151 (2022) 107008.

[30] A. Ziadia, M. Habibi, S. Kelouwani, Machine learning study of the effect of process parameters on tensile strength of FFF PLA and PLA-CF, Eng 4(4) (2023) 2741-2763.

[31] A. Megdich, M. Habibi, L. Laperrière, Modeling and optimization of piezoelectric and dielectric properties of poled PVDF/BT nanocomposites, Polymer Bulletin 81(10) (2024) 9181-9201.

[32] J. Jin, H. Xu, B. Leng, Adaptive points sampling for implicit field reconstruction of industrial digital twin, Sensors 22(17) (2022) 6630.

[33] X. Chen, Y. Pan, V.J. Gan, K. Yan, 3D reconstruction of semantic-rich digital twins for ACMV monitoring and anomaly detection via scan-to-BIM and time-series data integration, Developments in the Built Environment 19 (2024) 100503.

[34] J. He, P. Li, X. An, C. Wang, A Reconstruction Methodology of Dynamic Construction Site Activities in 3D Digital Twin Models Based on Camera Information, Buildings 14(7) (2024) 2113.

[35] V. Chheang, S. Narain, G. Hooten, R. Cerda, B. Au, B. Weston, B. Giera, P.-T. Bremer, H. Miao, Enabling additive manufacturing part inspection of digital twins via collaborative virtual reality, Scientific Reports 14(1) (2024) 29783.

[36] C. Zhang, J. Shu, H. Zhang, Y. Ning, Y. Yu, Estimation of load-carrying capacity of cracked RC beams using 3D digital twin model integrated with point clouds and images, Engineering Structures 310 (2024) 118126.

[37] Y. Chen, X. Peng, L. Kong, G. Dong, A. Remani, R. Leach, Defect inspection technologies for additive manufacturing, International Journal of Extreme Manufacturing 3(2) (2021) 022002.

[38] B. Denkena, M. Wichmann, T. Malek, H.N. Nguyen, M. Kato, K. Isshiki, R. Koike, Y. Kakinuma, Digital twin in process planning of the additive and subtractive process chain for laser metal deposition and micro milling of stainless steel, Journal of Manufacturing Science and Engineering 146(7) (2024).

[39] W. Hu, X. Wang, K. Tan, Y. Cai, Digital twin-enhanced predictive maintenance for indoor climate: A parallel LSTM-autoencoder failure prediction approach, Energy and Buildings 301 (2023) 113738.

[40] F. Tao, H. Zhang, A. Liu, A.Y. Nee, Digital twin in industry: State-of-the-art, IEEE Transactions on industrial informatics 15(4) (2018) 2405-2415.

[41] T. Shen, B. Li, Digital twins in additive manufacturing: a state-of-the-art review, The International Journal of Advanced Manufacturing Technology 131(1) (2024) 63-92.

[42] W. Kritzinger, M. Karner, G. Traar, J. Henjes, W. Sihn, Digital Twin in manufacturing: A categorical literature review and classification, Ifac-PapersOnline 51(11) (2018) 1016-1022.

[43] F. Tao, J. Cheng, Q. Qi, M. Zhang, H. Zhang, F. Sui, Digital twin-driven product design, manufacturing and service with big data, The International Journal of Advanced Manufacturing Technology 94 (2018) 3563-3576.

[44] F. Tao, Q. Qi, Make more digital twins, Nature 573(7775) (2019) 490-491.

[45] B. Schleich, N. Anwer, L. Mathieu, S. Wartzack, Shaping the digital twin for design and production engineering, CIRP annals 66(1) (2017) 141-144.

[46] Y. Lu, C. Liu, I. Kevin, K. Wang, H. Huang, X. Xu, Digital Twin-driven smart manufacturing: Connotation, reference model, applications and research issues, Robotics and computer-integrated manufacturing 61 (2020) 101837.

[47] M.G. Kapteyn, J.V. Pretorius, K.E. Willcox, A probabilistic graphical model foundation for enabling predictive digital twins at scale, Nature Computational Science 1(5) (2021) 337-347.

[48] M. Grieves, J. Vickers, Digital twin: Mitigating unpredictable, undesirable emergent behavior in complex systems, Transdisciplinary perspectives on complex systems: New findings and approaches (2017) 85-113.
[49] Q. Qi, F. Tao, T. Hu, N. Anwer, A. Liu, Y. Wei, L. Wang, A.Y. Nee, Enabling technologies and tools for digital twin, Journal of Manufacturing Systems 58 (2021) 3-21.
[50] S. Liu, J. Bao, Y. Lu, J. Li, S. Lu, X. Sun, Digital twin modeling method based on biomimicry for machining aerospace components, Journal of manufacturing systems 58 (2021) 180-195.
[51] H. Zhang, Q. Liu, X. Chen, D. Zhang, J. Leng, A digital twin-based approach for designing and multi-objective optimization of hollow glass production line, Ieee Access 5 (2017) 26901-26911.
[52] X.V. Wang, L. Wang, Digital twin-based WEEE recycling, recovery and remanufacturing in the background of Industry 4.0, International Journal of Production Research 57(12) (2019) 3892-3902.
[53] L.D. Xu, E.L. Xu, L. Li, Industry 4.0: state of the art and future trends, International journal of production research 56(8) (2018) 2941-2962.
[54] H. Qu, K. Liu, J. Liu, C. Gao, C. Ruan, A heterogeneous pore design algorithm for material extrusion additive manufacturing, Additive Manufacturing 94 (2024) 104449.
[55] C. Wu, J. Luo, J. Zhong, Y. Xu, B. Wan, W. Huang, J. Fang, G.P. Steven, G. Sun, Q. Li, Topology optimisation for design and additive manufacturing of functionally graded lattice structures using derivative-aware machine learning algorithms, Additive Manufacturing 78 (2023) 103833.
[56] B. Kim, S. Lee, J. Sung, J. Lee, M. Lee, Development of additive strategy generator for metal additive manufacturing build prediction using laser path generation algorithm, International Journal of Precision Engineering and Manufacturing 24(11) (2023) 2113-2131.
[57] U. Auyeskhan, C.A. Steed, S. Park, D.-H. Kim, I.D. Jung, N. Kim, Virtual reality-based assembly-level design for additive manufacturing decision framework involving human aspects of design, Journal of Computational Design and Engineering 10(3) (2023) 1126-1142.
[58] A. Hilbig, L. Vogt, S. Holtzhausen, K. Paetzold, Enhancing three-dimensional convolutional neural network-based geometric feature recognition for adaptive additive manufacturing: A signed distance field data approach, Journal of Computational Design and Engineering 10(3) (2023) 992-1009.

[59] L. Risse, S. Woodcock, J.-P. Brüggemann, G. Kullmer, H.A. Richard, Stiffness optimization and reliable design of a hip implant by using the potential of additive manufacturing processes, BioMedical Engineering OnLine 21(1) (2022) 23.
[60] J. Chen, C. Meng, Y. Gao, Y. Liu, Multi-fidelity neural optimization machine for Digital Twins, Structural and Multidisciplinary Optimization 65(12) (2022) 340.
[61] J. Chen, Q. Chen, H. Yang, Additive manufacturing of a continuum topology-optimized palletizing manipulator arm, Mechanical Sciences 12(1) (2021) 289-304.
[62] M. Zhou, Y. Lu, Y. Liu, Z. Lin, Concurrent topology optimization of shells with self-supporting infills for additive manufacturing, Computer Methods in Applied Mechanics and Engineering 390 (2022) 114430.
[63] J. Xu, H. Sheng, S. Zhang, J. Tan, J. Deng, Surface accuracy optimization of mechanical parts with multiple circular holes for additive manufacturing based on triangular fuzzy number, Frontiers of Mechanical Engineering 16 (2021) 133-150.
[64] Z. Zheng, Y. Wang, J. Li, Z. An, Development of a digital twin system for acquiring surface features of solid models in light-curing additive manufacturing, The International Journal of Advanced Manufacturing Technology 135(1) (2024) 663-675.
[65] Y. Fu, A.R. Downey, L. Yuan, H.-T. Huang, E.A. Ogunniyi, Simulation-in-the-loop additive manufacturing for real-time structural validation and digital twin development, Additive Manufacturing 98 (2025) 104631.
[66] B.D. Bevans, A. Carrington, A. Riensche, A. Tenequer, C. Barrett, H.S. Halliday, R. Srinivasan, K.D. Cole, P. Rao, Digital twins for rapid in-situ qualification of part quality in laser powder bed fusion additive manufacturing, Additive Manufacturing 93 (2024) 104415.
[67] A.M. Horr, Real-Time Modeling for Design and Control of Material Additive Manufacturing Processes, Metals (2075-4701) 14(11) (2024).
[68] S. Pratt, T. Kosmal, C. Williams, Adaptively sampled distance functions: A unifying digital twin representation for advanced manufacturing, Robotics and Computer-Integrated Manufacturing 92 (2025) 102877.
[69] H. Mu, F. He, L. Yuan, H. Hatamian, P. Commins, Z. Pan, Online distortion simulation using generative machine learning models: A step toward digital twin of metallic additive manufacturing, Journal of Industrial Information Integration 38 (2024) 100563.
[70] Z. Chen, K. Surendraarcharyagie, K. Granland, C. Chen, X. Xu, Y. Xiong, C. Davies, Y. Tang, Service oriented digital twin for additive manufacturing process, Journal of Manufacturing Systems 74 (2024) 762-776.

[71] M. Moretti, A. Rossi, N. Senin, Optical tomography by laser line scanning and digital twinning for in-process inspection of lattice structures in material extrusion, Additive Manufacturing 93 (2024) 104424.
[72] J.V.A. Cabral, A.J. Álvares, G.C. de Carvalho, Digital Twin Implementation for an Additive Manufacturing Robotic Cell based on the ISO 23247 Standard, IEEE Latin America Transactions 22(8) (2024) 651-658.
[73] Y. Lu, Y. Wang, L. Pan, A feature-based physics-constrained active dictionary learning scheme for image-based additive manufacturing process monitoring, Journal of Manufacturing Processes 103 (2023) 261-273.
[74] M.-J. Li, J. Chen, Y. Lian, F. Xiong, D. Fang, An efficient and high-fidelity local multi-mesh finite volume method for heat transfer and fluid flow problems in metal additive manufacturing, Computer Methods in Applied Mechanics and Engineering 404 (2023) 115828.
[75] A. Rossi, M. Moretti, N. Senin, Neural networks and NARXs to replicate extrusion simulation in digital twins for fused filament fabrication, Journal of Manufacturing Processes 84 (2022) 64-76.
[76] N. Jyeniskhan, A. Keutayeva, G. Kazbek, M.H. Ali, E. Shehab, Integrating machine learning model and digital twin system for additive manufacturing, IEEe Access 11 (2023) 71113-71126.
[77] H. Yeung, F. Kim, M. Donmez, J. Neira, Keyhole pores reduction in laser powder bed fusion additive manufacturing of nickel alloy 625, International Journal of Machine Tools and Manufacture 183 (2022) 103957.
[78] J. Dvorak, A. Cornelius, G. Corson, R. Zameroski, L. Jacobs, J. Penney, T. Schmitz, A machining digital twin for hybrid manufacturing, Manufacturing Letters 33(Supplement) (2022).
[79] L. Scime, A. Singh, V. Paquit, A scalable digital platform for the use of digital twins in additive manufacturing, Manufacturing Letters 31 (2022) 28-32.
[80] X. Liu, C. Kan, Z. Ye, Real-time multiscale prediction of structural performance in material extrusion additive manufacturing, Additive Manufacturing 49 (2022) 102503.
[81] R.T. Reisch, T. Hauser, B. Lutz, A. Tsakpinis, D. Winter, T. Kamps, A. Knoll, Context awareness in process monitoring of additive manufacturing using a digital twin, The International Journal of Advanced Manufacturing Technology (2022) 1-18.
[82] C. Liu, L. Le Roux, C. Körner, O. Tabaste, F. Lacan, S. Bigot, Digital twin-enabled collaborative data management for metal additive manufacturing systems, Journal of Manufacturing Systems 62 (2022) 857-874.

[83] L. Yi, M. Glatt, S. Ehmsen, W. Duan, J.C. Aurich, Process monitoring of economic and environmental performance of a material extrusion printer using an augmented reality-based digital twin, Additive Manufacturing 48 (2021) 102388.

[84] R. Yavari, A. Riensche, E. Tekerek, L. Jacquemetton, H. Halliday, M. Vandever, A. Tenequer, V. Perumal, A. Kontsos, Z. Smoqi, Digitally twinned additive manufacturing: Detecting flaws in laser powder bed fusion by combining thermal simulations with in-situ meltpool sensor data, Materials & Design 211 (2021) 110167.

[85] Y. Lu, E. Shevtshenko, Y. Wang, Physics-based compressive sensing to enable digital twins of additive manufacturing processes, Journal of Computing and Information Science in Engineering 21(3) (2021) 031009.

[86] I. Sieber, R. Thelen, U. Gengenbach, Enhancement of high-resolution 3D inkjet-printing of optical freeform surfaces using digital twins, Micromachines 12(1) (2020) 35.

[87] R. Wu, Z. Yu, D. Ding, Q. Lu, Z. Pan, H. Li, OICP: an online fast registration algorithm based on rigid translation applied to wire arc additive manufacturing of mold repair, Materials 14(6) (2021) 1563.

[88] D. Liu, Y. Wang, Metal additive manufacturing process design based on physics constrained neural networks and multi-objective bayesian optimization, Manufacturing Letters 33 (2022) 817-827.

[89] L. Li, X. Zhang, T. Pan, F. Liou, Component repair using additive manufacturing: experiments and thermal modeling, The International Journal of Advanced Manufacturing Technology (2022) 1-14.

[90] C.G. Klingaa, S. Mohanty, C.V. Funch, A. Hjermitslev, L. Haahr-Lillevang, J.H. Hattel, Towards a digital twin of laser powder bed fusion with a focus on gas flow variables, Journal of Manufacturing Processes 65 (2021) 312-327.

[91] T.W. Heo, S.A. Khairallah, R. Shi, J. Berry, A. Perron, N.P. Calta, A.A. Martin, N.R. Barton, J. Roehling, T. Roehling, A mesoscopic digital twin that bridges length and time scales for control of additively manufactured metal microstructures, Journal of Physics: Materials 4(3) (2021) 034012.

[92] X. Zhang, W. Cui, F. Liou, Voxel-based geometry reconstruction for repairing and remanufacturing of metallic components via additive manufacturing, International Journal of Precision Engineering and Manufacturing-Green Technology (2021) 1-24.

[93] I.P. Beckman, G. Berry, H. Cho, G. Riveros, Digital twin geometry for fibrous air filtration media, Fibers 9(12) (2021) 84.

[94] L. Yang, T. Özel, Physics-based simulation models for digital twin development in laser powder bed fusion, International Journal of Mechatronics and Manufacturing Systems 14(2) (2021) 143-163.
[95] D. Montoya-Zapata, J.M. Rodríguez, A. Moreno, J. Posada, O. Ruiz-Salguero, 2D linear finite element simulation of laser metal heating for digital twins, International Journal for Simulation and Multidisciplinary Design Optimization 12 (2021) 11.
[96] M.-S. Kang, D.-H. Lee, M.S. Bajestani, D.B. Kim, S.D. Noh, Edge Computing-Based Digital Twin Framework Based on ISO 23247 for Enhancing Data Processing Capabilities, Machines 13(1) (2024) 19.
[97] P. Castelló-Pedrero, C. García-Gascón, J.A. García-Manrique, Multiscale numerical modeling of large-format additive manufacturing processes using carbon fiber reinforced polymer for digital twin applications, International Journal of Material Forming 17(2) (2024) 15.
[98] S. Hartmann, O. Murua, J.I. Arrizubieta, A. Lamikiz, P. Mayr, Digital Twin of the laser-DED process based on a multiscale approach, Simulation Modelling Practice and Theory 132 (2024) 102881.
[99] H. Huang, H. Xu, Z. Liu, Multi-task deep learning-empowered digital twin for functional composite materials fabricated by laser additive remanufacturing, CIRP Annals 73(1) (2024) 125-128.
[100] J. Qin, P. Taraphdar, Y. Sun, J. Wainwright, W.J. Lai, S. Feng, J. Ding, S. Williams, Knowledge-based bidirectional thermal variable modelling for directed energy deposition additive manufacturing, Virtual and Physical Prototyping 19(1) (2024) e2397008.
[101] P. Castelló-Pedrero, C. García-Gascón, J. Bas-Bolufer, J.A. García-Manrique, Integrated computational modeling of large format additive manufacturing: Developing a digital twin for material extrusion with carbon fiber-reinforced acrylonitrile butadiene styrene, Proceedings of the Institution of Mechanical Engineers, Part L: Journal of Materials: Design and Applications 238(2) (2024) 332-346.
[102] S. Ochoa, S. Ferrándiz, L. Garzón, C. Cobos, Digital Twin of Fused Filament Fabrication Prints for Finite Element Analysis via G-Code Reverse Engineering, 3D Printing and Additive Manufacturing (2024).
[103] M. Marks, K. Aswani, G. Weaver, F. Dababneh, H. Taheri, Applying Digital Twin Methods for Process-Structure-Property Correlation Assessment in Metal Additive Manufacturing with Limited Experimental Data, Research in Nondestructive Evaluation 36(2) (2025) 74-90.

[104] C. Patuelli, E. Cestino, G. Frulla, F. Valente, G. Servetti, F. Esposito, L. Barbero, FEM Simulation of AlSi10Mg Artifact for Additive Manufacturing Process Calibration with Industrial-Computed Tomography Validation, Materials 16(13) (2023) 4754.
[105] S. Dharmadhikari, N. Menon, A. Basak, A reinforcement learning approach for process parameter optimization in additive manufacturing, Additive Manufacturing 71 (2023) 103556.
[106] W. Li, H. Wu, M. Sokore, R.N. Raoelison, H. Liao, S. Costil, S. Deng, General-purpose numerical deposition modeling methodology based on mesh geometry reconstruction strategy in cold spray additive manufacturing system, Surface and Coatings Technology 464 (2023) 129563.
[107] A. Garfias, R. Vaz, V. Albaladejo-Fuentes, J. Sánchez, I.G. Cano, Geometry and microstructure control of remanufactured metallic parts by cold spray additive manufacturing, Materials 16(13) (2023) 4735.
[108] H. Attariani, S.R. Petitjean, M. Dousti, A digital twin of synchronized circular laser array for powder bed fusion additive manufacturing, The International Journal of Advanced Manufacturing Technology 123(5) (2022) 1433-1440.
[109] D. Miller, R. Kemnitz, R. Grandhi, L. Sheridan, Toward digital twin development for additively manufactured turbine blades with experimental and analytical methods, Structural and Multidisciplinary Optimization 65(8) (2022) 227.
[110] M. Pantelidakis, K. Mykoniatis, J. Liu, G. Harris, A digital twin ecosystem for additive manufacturing using a real-time development platform, The International Journal of Advanced Manufacturing Technology 120(9) (2022) 6547-6563.
[111] L. Wu, N. Dai, H. Wang, Evaluation of rods deformation of metal lattice structure in additive manufacturing based on skeleton extraction technology, Math Biosci Eng 18 (2021) 7525-7538.
[112] Y. Fu, A.R. Downey, L. Yuan, H.-T. Huang, E.A. Ogunniyi, Simulation-in-the-loop additive manufacturing for real-time structural validation and digital twin development, Additive Manufacturing (2025) 104631.
[113] S.Y. Chew, E. Asadi, A. Vargas-Uscategui, P. King, S. Gautam, A. Bab-Hadiashar, I. Cole, In-process 4D reconstruction in robotic additive manufacturing, Robotics and Computer-Integrated Manufacturing 89 (2024) 102784.
[114] J. Girard, S. Zhang, Fast error detection method for additive manufacturing process monitoring using structured light three dimensional imaging technique, Optics and Lasers in Engineering 184 (2025) 108609.

[115] A.W. Malik, M.A. Mahmood, F. Liou, Digital twin–driven optimization of laser powder bed fusion processes: a focus on lack-of-fusion defects, Rapid Prototyping Journal 30(10) (2024) 1977-1988.

[116] V. Karkaria, A. Goeckner, R. Zha, J. Chen, J. Zhang, Q. Zhu, J. Cao, R.X. Gao, W. Chen, Towards a digital twin framework in additive manufacturing: Machine learning and bayesian optimization for time series process optimization, Journal of Manufacturing Systems 75 (2024) 322-332.

[117] I. Kostavelis, L. Nalpantidis, R. Detry, H. Bruyninckx, A. Billard, S. Christian, M. Bosch, K. Andronikidis, H. Lund-Nielsen, P. Yosefipor, RoBétArmé Project: Human-robot collaborative construction system for shotcrete digitization and automation through advanced perception, cognition, mobility and additive manufacturing skills, Open Research Europe 4 (2024) 4.

[118] M.H. Ali, A. Malik, N. Jyeniskhan, M.A. Mahmood, E. Shehab, F. Liou, Development of Digital Twin for FDM Printer with Preventive Cyber-Attack and Control Algorithms, IEEE Access (2024).

[119] L. Chen, G. Bi, X. Yao, C. Tan, J. Su, N.P.H. Ng, Y. Chew, K. Liu, S.K. Moon, Multisensor fusion-based digital twin for localized quality prediction in robotic laser-directed energy deposition, Robotics and Computer-Integrated Manufacturing 84 (2023) 102581.

[120] S.M. Rachmawati, M.A.P. Putra, J.M. Lee, D.S. Kim, Digital twin-enabled 3D printer fault detection for smart additive manufacturing, Engineering Applications of Artificial Intelligence 124 (2023) 106430.

[121] A. Phua, P.S. Cook, C.H. Davies, G.W. Delaney, Smart recoating: a digital twin framework for optimisation and control of powder spreading in metal additive manufacturing, Journal of Manufacturing Processes 99 (2023) 382-391.

[122] J. Xiong, H. Chen, S. Zheng, G. Zhang, Feedback control of variable width in gas metal arc-based additive manufacturing, Journal of Manufacturing Processes 76 (2022) 11-20.

[123] P. Nath, S. Mahadevan, Probabilistic digital twin for additive manufacturing process design and control, Journal of Mechanical Design 144(9) (2022) 091704.

[124] D.B. Kim, G. Shao, G. Jo, A digital twin implementation architecture for wire+ arc additive manufacturing based on ISO 23247, Manufacturing Letters 34 (2022) 1-5.

[125] A. Balu, S. Sarkar, B. Ganapathysubramanian, A. Krishnamurthy, Physics-aware machine learning surrogates for real-time manufacturing digital twin, Manufacturing Letters 34 (2022) 71-74.

[126] P. Xu, X. Yao, L. Chen, C. Zhao, K. Liu, S.K. Moon, G. Bi, In-process adaptive dimension correction strategy for laser aided additive manufacturing using laser line scanning, Journal of Materials Processing Technology 303 (2022) 117544.
[127] D.R. Gunasegaram, A. Murphy, A. Barnard, T. DebRoy, M. Matthews, L. Ladani, D. Gu, Towards developing multiscale-multiphysics models and their surrogates for digital twins of metal additive manufacturing, Additive Manufacturing 46 (2021) 102089.
[128] P. Stavropoulos, A. Papacharalampopoulos, C.K. Michail, G. Chryssolouris, Robust additive manufacturing performance through a control oriented digital twin, Metals 11(5) (2021) 708.
[129] J. Chen, M. Khrenov, J. Jin, S.P. Narra, C. McComb, Data-driven inpainting for full-part temperature monitoring in additive manufacturing, Journal of Manufacturing Systems 77 (2024) 558-575.
[130] F. Uzun, H. Basoalto, K. Liogas, M.F. Slim, T.L. Lee, C. Besnard, Z.I. Wang, J. Chen, I.P. Dolbnya, A.M. Korsunsky, Tomographic eigenstrain reconstruction for full-field residual stress analysis in large scale additive manufacturing parts, Additive Manufacturing 81 (2024) 104027.
[131] F. Uzun, H. Basoalto, K. Liogas, J. Chen, I.P. Dolbnya, Z.I. Wang, A.M. Korsunsky, Voxel-based full-field eigenstrain reconstruction of residual stresses in additive manufacturing parts using height digital image correlation, Additive Manufacturing 77 (2023) 103822.
[132] M.G. Chapman, M.N. Shah, S.P. Donegan, J.M. Scott, P.A. Shade, D. Menasche, M.D. Uchic, AFRL additive manufacturing modeling series: challenge 4, 3D reconstruction of an IN625 high-energy diffraction microscopy sample using multi-modal serial sectioning, Integrating Materials and Manufacturing Innovation 10 (2021) 129-141.
[133] A. Gourley, J. Kaufman, B. Aman, E. Schwalbach, J. Beuth, L. Rueschhoff, B. Reeja-Jayan, Spreading anomaly semantic segmentation and 3D reconstruction of binder jet additive manufacturing powder bed images, The International Journal of Advanced Manufacturing Technology 134(7) (2024) 3139-3151.
[134] A. Ziabari, S.V. Venkatakrishnan, Z. Snow, A. Lisovich, M. Sprayberry, P. Brackman, C. Frederick, P. Bhattad, S. Graham, P. Bingham, Enabling rapid X-ray CT characterisation for additive manufacturing using CAD models and deep learning-based reconstruction, npj Computational Materials 9(1) (2023) 91.
[135] L. Zhang, J. Huang, Z. Xiao, Y. He, K. Liu, B. He, B. Xiang, J. Zhai, L. Kong, Effects of debinding condition on microstructure and densification of alumina ceramics shaped with

photopolymerization-based additive manufacturing technology, Ceramics International 48(10) (2022) 14026-14038.
[136] W. Niu, M. Yang, Y. Liu, Y. Gong, Y. Xu, Cross Section Contour Extraction Algorithm of Additive Manufacturing Micromixers, 3D Printing and Additive Manufacturing 10(3) (2023) 490-499.

Chapitre 6: Optimisation en temps réel, pilotée par jumeau numérique, de la rugosité de surface couche par couche en impression 3D FDM

Ce chapitre a fait l'objet d'une publication :

Digital twin-driven real-time optimization of layer-specific surface roughness in FDM 3D printing. Abdelhamid ZIADIA, Mohamed HABIBI, et Sousso KELOUWANI. *Progress in Additive Manufacturing*, 2025, p. 1-24.

Il peut être consulté en ligne à l'adresse suivante :

https://doi.org/10.1007/s40964-025-01227-w

La suite logique de la Partie 2 consiste à transformer les principes du jumeau numérique en un dispositif opérationnel qui réduit la rugosité de surface en temps réel. Le système observe la surface déposée à la fin de chaque couche, cartographie la topographie 3D locale de cette surface, prédit Ra par apprentissage automatique, puis ajuste automatiquement les paramètres de la couche suivante en modifiant le G code et affiche leurs progressions en temps réel. Les briques capteurs, modèles et optimisation deviennent un régulateur numérique répétable sur une machine de bureau.

Le banc de test s'appuie sur une imprimante FDM à buse de 0,4 millimètre et un capteur de vision 3D Gocator 3210 placé au-dessus du plateau. La chaîne logicielle pilote l'imprimante, acquiert la carte de surface de la couche courante, calcule la rugosité selon ASME B46.1 et applique les consignes optimisées. Une interface de suivi affiche en direct les paramètres d'impression et les mesures clés avec historique par couche et mode manuel sécurisé pour valider ou corriger une action avant écriture du G code.

Le plan d'expériences explore température d'impression, vitesse et épaisseur de couche à trois niveaux. Les nuages de points sont nettoyés par filtrage statistique pour obtenir une mesure fiable de la topographie de surface. Le jeu de données associe pour chaque couche les paramètres d'impression, le rang de couche et la rugosité mesurée sur la surface exposée.

Le modèle prédictif est un réseau de neurones qui prend en entrée les paramètres d'impression, le numéro de couche et la rugosité de la couche précédente afin de capter l'effet séquentiel du procédé. La précision élevée et l'inférence très rapide autorisent une mise à jour des consignes à chaque couche. L'optimisation en ligne est réalisée dans la fenêtre de décision disponible

entre deux couches. Le essaim de particules respecte mieux la contrainte de temps et converge de manière stable, ce qui le rend adapté au réglage couche par couche.

La validation expérimentale montre une diminution de la rugosité moyenne sur l'ensemble des couches et une baisse marquée de la rugosité finale. Le profil de consignes suit une logique lisible avec température plus élevée au démarrage pour l'adhésion et le lissage, ajustements intermédiaires selon l'historique de surface et légère réhausse finale pour atténuer les stries résiduelles. La vitesse est ralentie aux phases sensibles et revient vers le nominal au milieu.

L'apport par rapport à la revue est double. La métrologie de surface devient l'observable principal du régulateur. La décision d'optimisation est intégrée au pilotage et matérialise la boucle capter comprendre agir. L'interface relie l'algorithme à l'utilisateur en offrant visibilité traçabilité sur chaque ajustement ainsi que l'exploration visuelle des nuages de points et de leurs métriques.

Digital Twin-Driven Real-Time Optimization of Layer-Specific Surface Roughness in FDM 3D Printing

Abdelhamid Ziadia[1], Mohamed Habibi[1], *& Sousso Kelouwani[1]

Affiliation [1]; University of Quebec in Trois-Rivieres, (Department of Mechanical Engineering), Trois-Rivieres, (Quebec), Canada

6.1 Abstract

This paper presents a novel in-situ optimization approach for Fused Deposition Modeling (FDM) Additive Manufacturing which utilizes high-resolution data from a 3D scanner and Artificial Intelligence for minimizing layer-specific surface roughness. The procedure starts with the print head retracting post-layer deposition, which is followed by a 3D scanner creating a detailed point cloud of the surface. This data is then pre-processed to calculate the surface roughness, and a metaheuristic optimization algorithm, supported by a neural network, updates the print settings for the subsequent layer. The analysis of the different algorithms revealed that Particle Swarm Optimization was the most efficient, with a better fitness evaluation and faster convergence than the Genetic Algorithm. The study focuses on the effect of sequential layer deposition on surface roughness and shows that the quality of the previous layer has a significant impact on the quality of the next. In addition, a Digital Twin architecture is implemented that enables seamless integration between the FDM printer and the 3D scanner and provides a user-friendly interface for real-time parameter monitoring and surface visualization. This approach not only improves manufacturing precision, but also sets new standards for accuracy and reliability in Additive Manufacturing. It demonstrates the transformative potential of adaptive manufacturing techniques that integrate real-time data acquisition, advanced AI and robust optimization algorithms.

Keywords: FDM 3D Printing, Surface Roughness, Real-Time Optimization, Digital Twin, Machine Learning, Layer-Specific Control.

6.2 Introduction

The advent of Fused Deposition Modeling (FDM) 3D printing technology has revolutionized manufacturing, transitioning from simple prototyping to complex mass production applications [1-7]. This evolution has broadened the scope of modern manufacturing but has also introduced significant challenges, particularly in optimizing parameters that critically influence production quality and efficiency [8-12]. Among these challenges, surface roughness is a pivotal factor that affects mechanical performance, dimensional accuracy, and the aesthetic quality of printed

components [13, 14]. Consequently, optimizing surface roughness is essential to ensure the reliability and functionality of FDM-printed parts, making it a key area of focus for researchers and industry professionals alike.

FDM operates through a sequential, layer-by-layer deposition process, offering unique opportunities for optimization at multiple stages of production. In the pre-production phase, critical decisions regarding material selection, geometry design, and initial parameter settings influence the final print quality [15-21]. Research efforts have extensively explored optimization techniques for pre-production parameters to enhance surface roughness. For instance, Saad et al. [22] utilized advanced methodologies like response surface methodology combined with particle swarm optimization to refine parameters effectively. Similarly, Tura et al. [23] integrated artificial neural networks with symbiotic organism search algorithms to optimize surface roughness in ABS materials, achieving significant improvements. Pawar and Dolas [24] demonstrated the impact of parameter tuning on the flexural strength and surface roughness of PC-ABS components, highlighting the delicate balance between mechanical performance and aesthetic quality. Additionally, Patil et al. [25] emphasized the importance of multi-objective optimization in printing Polylactic Acid (PLA), advocating for fine-tuning process parameters to achieve optimal functionality and surface finish.

In the post-production phase, surface finishing techniques play a critical role in defining the ultimate surface quality of printed objects. Colpani et al. [26] investigated the effectiveness of acetone vapor smoothing on ABS parts, which significantly enhances their surface finish. This method notably reduces the perceptible roughness, rendering it an essential technique for elevating final product quality. Kozior et al. [27] elaborated on the advantages of thermal and chemical post-processing treatments that not only refine the surface texture but also enhance the mechanical properties of FDM prints. Furthermore, Akhouri et al. [28] examined various plating processes that can be applied after printing to enhance both the functional and aesthetic qualities of FDM parts, emphasizing the transformative impact of post-production treatments on surface enhancements. Additionally, Li et al. [29] employed machine learning to predict surface roughness in extrusion-based Additive Manufacturing. This predictive capability enables the fine-tune post-processing protocols, optimizing post-production efforts to achieve superior surface quality.

Digital Twin (DT) technology has emerged as a transformative approach in manufacturing, enabling real-time synchronization between physical and virtual systems for continuous monitoring, optimization, and predictive control[30-36]. In the context of FDM, DT provides a dynamic means of addressing in-process variations by allowing real-time adjustments to

critical printing parameters. Unlike conventional process control methods, which rely on static parameter tuning or post-production modifications, DT offers an interactive, adaptive system that can detect defects as they arise and implement corrective actions instantaneously. Henson et al. [37] proposed a DT-based strategy for FDM by comparing simulated and in-situ images from a multi-camera system. Their method identifies print distortions, enabling early print termination and reducing production waste. Expanding on defect detection capabilities, Jyeniskhan et al. [38] introduced a DT framework for Additive Manufacturing that integrates machine learning models. Using OctoPrint, Raspberry Pi, and Unity, their system enables real-time monitoring, control, and visualization with an average defect detection precision of 92%, reducing hardware redundancy through built-in sensor data integration. Focusing on process control, Moretti et al. [39] developed an extrusion simulation model for real-time monitoring and adaptive control in FDM. By integrating mechanical, thermal, and fluid dynamics sub-models, their model predicts filament temperature, flow rate, and compressive force during extrusion. Experimental validation using a multi-sensor FDM machine demonstrated the model's accuracy, supporting process optimization and failure detection. For fault detection based on sensor data, Rachmawati et al. [40] introduced a lightweight CNN-enabled DT using temperature sensor inputs. Their system achieved an F1-score of 0.9981, enabling near-real-time fault monitoring with minimal latency. In the context of predicting part performance, Butt and Mohaghegh [41] combined a DT of the extruder assembly with machine learning models. Their simulations correlated process parameters with mechanical properties using CNN and random forest classifiers. Advancing process monitoring further, Mourtzis et al. [42] designed a DT architecture integrating quality assessment modules, defect compensation algorithms, and an immersive augmented reality interface for remote monitoring. For simulation-based validation, Ochoa et al. [43] developed a DT of FDM prints by reverse-engineering G-code for finite element analysis. They reconstructed 3D models from printing trajectories, achieving a 90% similarity between simulations and experimental tensile tests. Similarly, Corradini and Silvestri [44] designed a DT for process and quality monitoring in material extrusion. By integrating sensor data with CAD models, their system allows real-time process monitoring and automated fault recovery, enhancing production accuracy. To detect performance anomalies, Balta et al. [45] presented a Digital Twin framework for performance monitoring and anomaly detection in FDM. They introduce a formal specification-based anomaly detection method, validated through experiments on a FDM printer. Considering cloud-based solutions, Guo et al. [46] proposed a cloud-edge collaborative DT system for FDM, addressing network

latency and data privacy issues in cloud manufacturing. Time-sensitive services are managed locally through edge computing, enabling real-time monitoring and control.

Despite significant advancements in surface roughness optimization and Digital Twin technology, several critical gaps persist, preventing the realization of fully adaptive, real-time process control in FDM 3D printing. Surface roughness optimization techniques remain limited to pre-production parameter selection or post-print refinements, failing to incorporate real-time adaptive control mechanisms. Traditional approaches rely on static parameter tuning, ignoring dynamic process variability caused by environmental fluctuations, material inconsistencies, and thermal effects. Furthermore, the layer-by-layer nature of FDM amplifies imperfections, requiring precise inter-layer control that current optimization methods fail to provide. Predictive models in existing literature are constrained by offline data processing, preventing real-time corrections and leading to cumulative print defects.

Simultaneously, Digital Twin implementations in FDM 3D printing remain largely underdeveloped in terms of real-time optimization and control. Many DT frameworks are limited to passive monitoring or offline optimization, lacking the real-time feedback loops necessary to make immediate, data-driven process adjustments. Existing Digital Twin solutions often do not incorporate advanced machine learning models capable of predictive analysis and proactive defect correction. Moreover, in-situ optimization capabilities remain largely unexplored, preventing real-time parameter tuning and failing to leverage direct G-code modifications for dynamic process control. Additionally, most DT frameworks primarily focus on backend data collection rather than real-time, interactive control, offering limited interfaces for real-time decision-making

To bridge these gaps, this study introduces a novel Digital Twin framework that integrates real-time surface roughness monitoring, predictive machine learning algorithms, and dynamic G-code modification to achieve adaptive, closed-loop optimization in FDM 3D printing. Unlike prior approaches, this framework actively monitors each printed layer in real time, leveraging high-resolution 3D scanning and AI-driven predictions to dynamically adjust printing parameters through Particle Swarm Optimization (PSO). This real-time feedback-driven correction mechanism mitigates cumulative surface defects and process variability, ensuring precise inter-layer control that traditional methods fail to achieve. Additionally, by incorporating direct G-code modifications, the framework enables in-situ adjustments rather than relying on post-print evaluations. The system also features an interactive operator interface, allowing users to visualize real-time print data, analyze surface roughness deviations, and receive feedback on process stability. This innovative approach bridges the gaps between

Digital Twin technology and real-time surface roughness optimization, transforming FDM 3D printing into a fully adaptive, data-driven manufacturing process.

This paper outlines the architecture of the proposed DT framework, describes the integration of real-time machine learning predictions with PSO-based optimizations, and evaluates the improvements in print quality. Comprehensive experiments and analyses reveal the transformative potential of combining DT technology with AI-driven optimization tools, showcasing a path toward more precise, efficient, and sustainable manufacturing practices in FDM 3D printing.

As illustrated in Figure 44, this paper is organized as follows: Section 2 describes the materials and methods employed, detailing the integration of machine learning algorithms and genetic optimization within a Digital Twin framework. Section 3 presents the results and performance evaluations of the developed algorithms, demonstrating their efficacy in improving layer-specific surface roughness and overall print quality. Section 4 concludes the paper by summarizing the contributions of our work and discussing its implications for future research and practical applications in the field of AM.

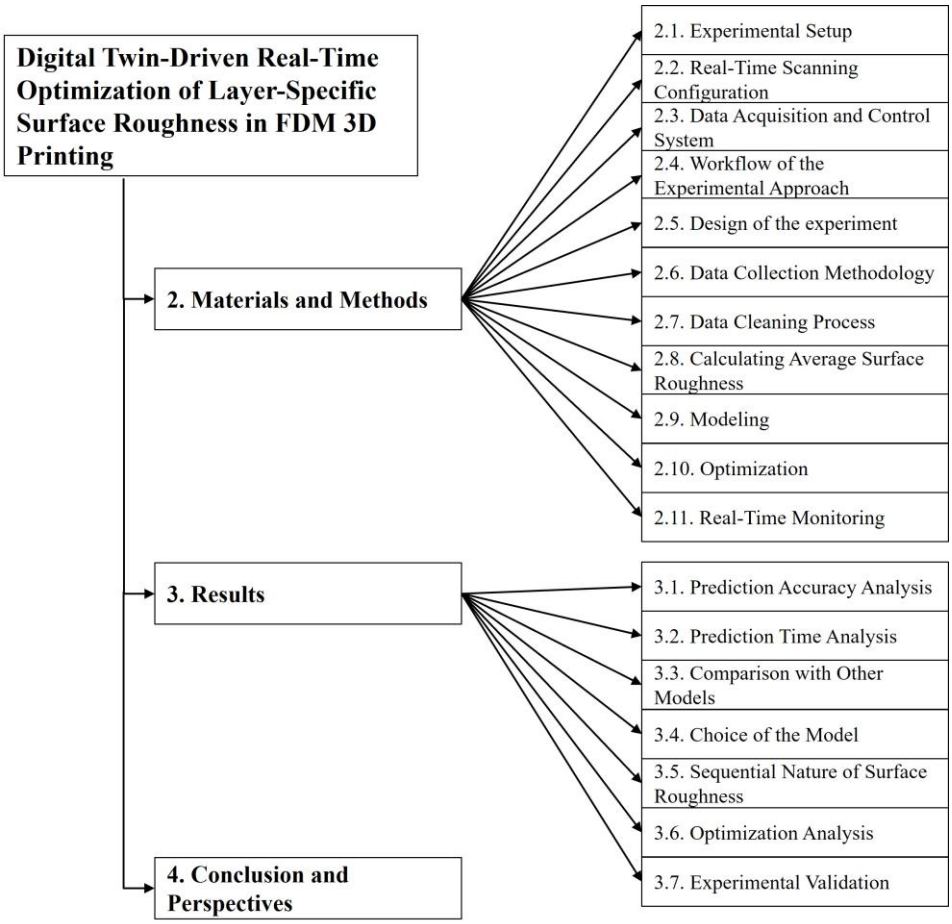

Figure 44. Schematic diagram of article content structure.

6.3 Materials and Methods

6.3.1 Experimental Setup

The core of our experimental setup involved the Prusa i3 MK3S+ desktop Fused Deposition Modeling (FDM) 3D printer, chosen for its reliability and precision in AM. This printer operates with a 0.4 mm nozzle, which dispenses 1.75 mm diameter polylactic acid (PLA) filament, a commonly used material in 3D printing due to its biodegradability and ease of use.

6.3.2 Real-Time Scanning Configuration

To monitor the quality of each printed layer, a Gocator 3210 Snapshot sensor from LMI Technologies was integrated into the printer setup. Positioned and fixed above the printing platform, the scanner was configured to perform vertical scans, capturing high-resolution images of each layer immediately after deposition. The design of the system allows the printer to pause automatically after each layer's completion, retracting the extruder to provide an unobstructed view for the scanner. The Gocator 3210 features a field of view ranging from 71 × 98 mm (near field) to 100 × 154 mm (far field), with a depth measurement range of 110 mm, a Z-repeatability of 4.7 μm, and adhering to the VDI/VDE 2634 part 2 accuracy class of 0.035 mm.

6.3.3 Data Acquisition and Control System

The control and data acquisition systems were centralized through a computer connected to the 3D printer via a serial port and to the Gocator scanner via an Ethernet connection. This computer, equipped with an Intel Core i7-9700K processor (3.6 GHz, 8 cores), 16 GB RAM and a Nvidia GeForce GTX 1050 GPU, ran a Python script responsible for orchestrating the printing process and handling data flow. The script managed the operational parameters of the printer through G-code commands, which are standard in the 3D printing industry, and processed the point cloud data collected from the Gocator scanner.

6.3.4 Workflow of the Experimental Approach

The experimental methodology developed in this study encompasses a comprehensive four-step process (Figure 45(a)), designed to enhance the surface quality of 3D printed objects through optimized parameters and real-time adjustments. Below is a detailed overview of each step involved:

6.3.4.1 Selection of Parameters and Design of Experiments (DOE)

The initial phase involves the careful selection of printing parameters. A Design of Experiments (DOE) approach is employed to systematically vary them and identify their impact on the layer-specific surface roughness.

6.3.4.2 Data Collection and Machine Learning Model Development

Once the DOE is set up, the next step is the real-time data collection of each printed layer's surface via a high-resolution 3D scanner. This collected data is then processed to calculate a precise surface roughness metric (Average Roughness). Using this dataset, machine learning models are developed to predict the surface roughness based on the varying printing parameters.

6.3.4.3 Optimization of Printings Parameters

With the predictive models in place, the study applies metaheuristic optimization algorithms, namely Particle Swarm Optimization (PSO) or Genetic Algorithms (GA), to determine the optimal printing settings for subsequent layers. The goal of this step is to dynamically adjust the printer settings in real-time to minimize surface roughness, based on the predictions made by the machine learning models.

6.3.4.4 Implementation of a Digital Twin Architecture

The final step involves the integration of a Digital Twin (DT) architecture that mirrors the physical printing process (Figure 45(b)). This digital replica is used for real-time monitoring and optimization of the printing process. It allows for the seamless adaptation of printing parameters, guided by the outputs from the machine learning models and optimization algorithms and the display of printing parameters and point cloud of the printed surfaces and its characteristics.

6.3.5 Design of the experiment

The experimental design for this study employs a Full Factorial approach, ensuring a comprehensive evaluation of the influence of key 3D printing parameters on surface roughness. As depicted in Table 25, three primary parameters were identified as having a significant impact on the surface roughness of the printed layers:

Printing Temperature: Determines the extrusion temperature of the material, with levels set at 200°C, 215°C, and 230°C.

Printing Speed: Controls the speed at which the printer operates, tested at 40 mm/s, 50 mm/s, and 60 mm/s.

Layer Thickness: Specifies the height of each printed layer, with options including 0.15 mm, 0.25 mm, and 0.35 mm.

Each of these parameters was carefully selected based on preliminary studies and literature indicating their potential impact on the quality of 3D printed objects.

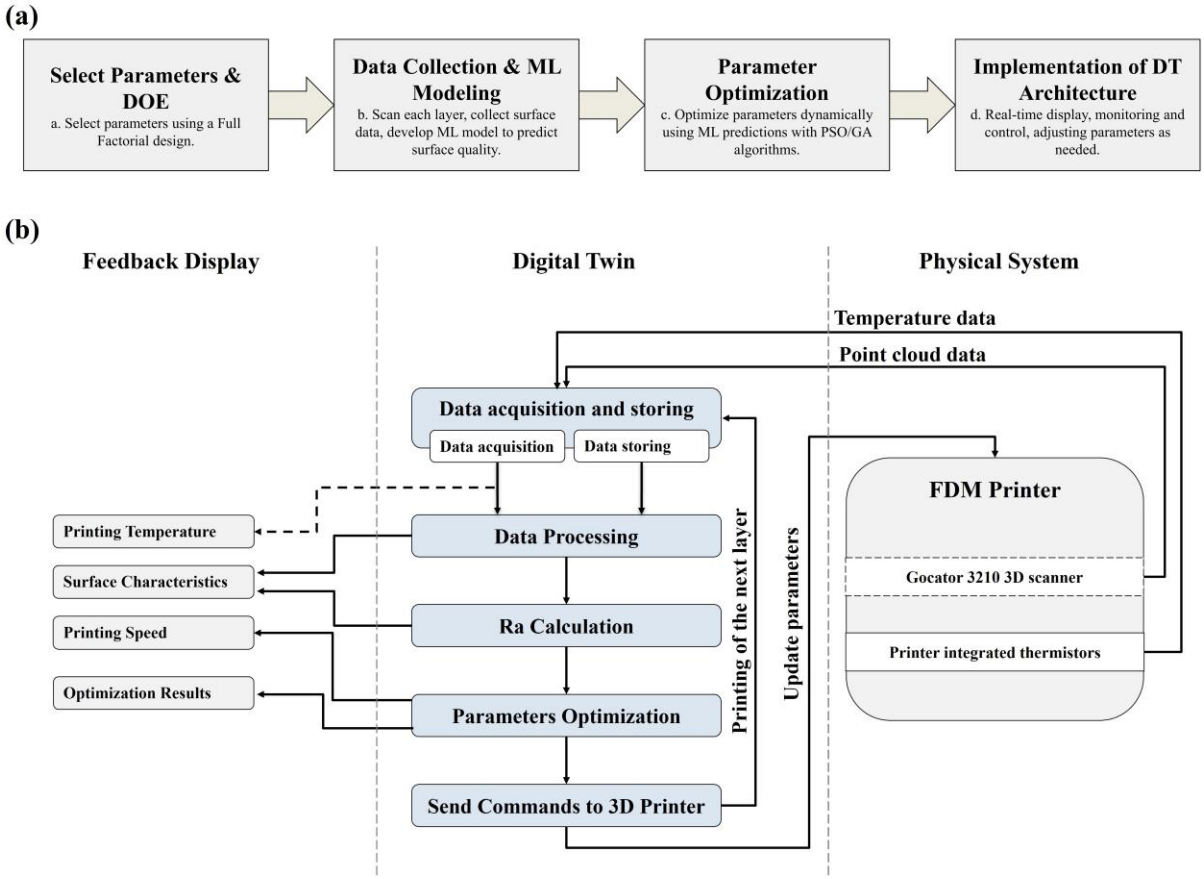

Figure 45. Illustrative Diagram of the Workflow Digital Twin and Experimental Workflow for Real-Time Optimization in FDM 3D Printing: (a) Workflow of the Experimental Approach and (b) Workflow of Digital Twin Integration in Real-Time Optimization of FDM 3D Printing.

The Full Factorial Design results in a total of 27 distinct combinations of the three parameters (3 levels of temperature × 3 levels of speed × 3 levels of thickness). To ensure the robustness of the results and mitigate the impact of any potential anomalies or variability in the printing process, each parameter setting combination was replicated three times. This led to a total production of 81 specimens. Each specimen has dimensions of 30mm x 20mm x 2mm to maintain consistency across tests.

While the focus of this experiment is on temperature, speed, and layer thickness, other factors such as infill density, infill pattern, infill angle, and bed temperature are also known to influence the final properties of the printed objects. For the purpose of this study, these variables were kept constant to isolate the effects of the tested parameters. The specific settings for these controls are detailed in Table 26.

Table 25. Varied parameters and their levels

Factors	Level 1	Level 2	Level 3
Printing Temperature (°C)	200	215	230
Layer Thickness (mm)	0.15	0.25	0.35
Printing Speed (mm/s)	40	50	60

Table 26. Fixed FFF process parameters and their description.

Parameters	Definition	Value
Bed Temperature (°C)	Used to heat the build platform	60
Infill density (%)	The amount of material used in the inside of the print	100
Infill Pattern	The form or structure of the material within the component	Lines
Infill Angle (°)	the orientation of the internal structures within a printed object	0
Number of contours	The number of contours surrounding the part	1

6.3.6 Data Collection Methodology

Data collection was meticulously organized to ensure comprehensive surface data capture for each printed specimen, facilitating detailed analysis of layer-specific surface roughness. The Gocator 3210 3D Smart Snapshot Sensor, mounted vertically above the printing area, was employed for scanning. Each layer of the printed specimens was scanned immediately after deposition and cooling to accurately capture the surface.

The scanning procedure involved the analysis of 27 specimens for each of the three layer thickness categories (0.15mm, 0.25mm, and 0.35mm), with each specimen replicated three times to ensure robust data. The total number of layers scanned varied with thickness; 13 layers for 0.15mm, 8 layers for 0.25mm, and 6 layers for 0.35mm, culminating in a grand total of 729 distinct scans across all categories. Each layer of each specimen was scanned three times, providing a dense dataset of surface scans (Table 27).

The scanning parameters of the Gocator 3210 were meticulously set to ensure optimal data quality: a single exposure of 9000µs, an X/Y spacing interval of 0.08mm, a uniform spacing option, and a diffuse type of material setting were used. To validate the uniformity of Ra measurements across the scan, each snapshot was segmented into four quadrants. Surface roughness was computed for each region, revealing a standard deviation of only 0.001. This consistency demonstrates that surface roughness values obtained from a representative area can reliably reflect the quality of the entire layer. Therefore, even in cases where the part is large and the full printed surface is not entirely covered within the scanner's field of view, analyzing a representative region remains sufficient to assess overall layer quality with high confidence.

Table 27. Number of scans corresponding to each layer thickness.

Layer thickness	Number of specimens	Number of layers for each specimen	Total number of scans
0.15mm	9x3	13	117x3
0.25mm	9x3	8	72x3
0.35mm	9x3	6	54x3

6.3.7 Data Cleaning Process

Point cloud data acquisition in real time is used for monitoring the surface quality of each layer during the 3D printing process. The captured data using the Gocator Sensor are exported via a Python script that interfaces directly with the scanning device before undergoing a critical cleaning phase to ensure its reliability and accuracy for subsequent analysis.

Statistical Outlier Removal (SOR): The primary technique employed for data cleaning is the Statistical Outlier Removal (SOR) method, facilitated by the Open3D Python library. SOR is designed to refine point cloud data by identifying and removing deviating points. These outliers often represent noise or erroneous data points that can skew the analysis and misrepresent the actual surface features of the printed layers.

Cleaning Mechanism:

- Neighborhood Analysis: Initially, the method analyzes each point in the point cloud by establishing a neighborhood defined by the nearest points. This neighborhood helps in assessing the local density and distribution of points.
- Distance Calculation: The average distance between a point and its neighbors is computed, providing a measure of how closely or sparsely points are grouped around a specific point.
- Statistical Evaluation: Following the distance calculations, the method employs statistical techniques to compute the mean and Standard Deviation of these distances across the entire point cloud.
- Outlier Detection: Points whose average distance to their neighbors exceeds a threshold—defined by multiplying the Standard Deviation by a factor (Standard Deviation ratio)—are classified as outliers. This threshold is crucial in distinguishing between normal variations in surface data and anomalies that are likely noise or errors.
- Outlier Removal: Points identified as outliers are removed from the dataset, resulting in a cleaned point cloud that more accurately represents the intended surface geometry of the printed object.

Parameters and Thresholds: For our specific application, the SOR parameters were set to include 20 nearest neighbors (nb_neighbors) to ensure a sufficiently dense sampling for reliable analysis, and a Standard Deviation ratio (std_ratio) of 1, establishing a stringent criterion for identifying outliers.

Visualization of Results: Figure 46 illustrate the transformation of the point cloud data before and after the cleaning process. It demonstrates the effectiveness of the cleaning process, with

Figure 46(b) and Figure 46(d) depicting a significantly more refined and accurate representation of the layer's surface post-cleaning.

This systematic approach to data cleaning is essential for maintaining the integrity of the data analysis part in our study, ensuring that only valid, accurate surface data is used to inform the optimization algorithms that adjust printing parameters in real time.

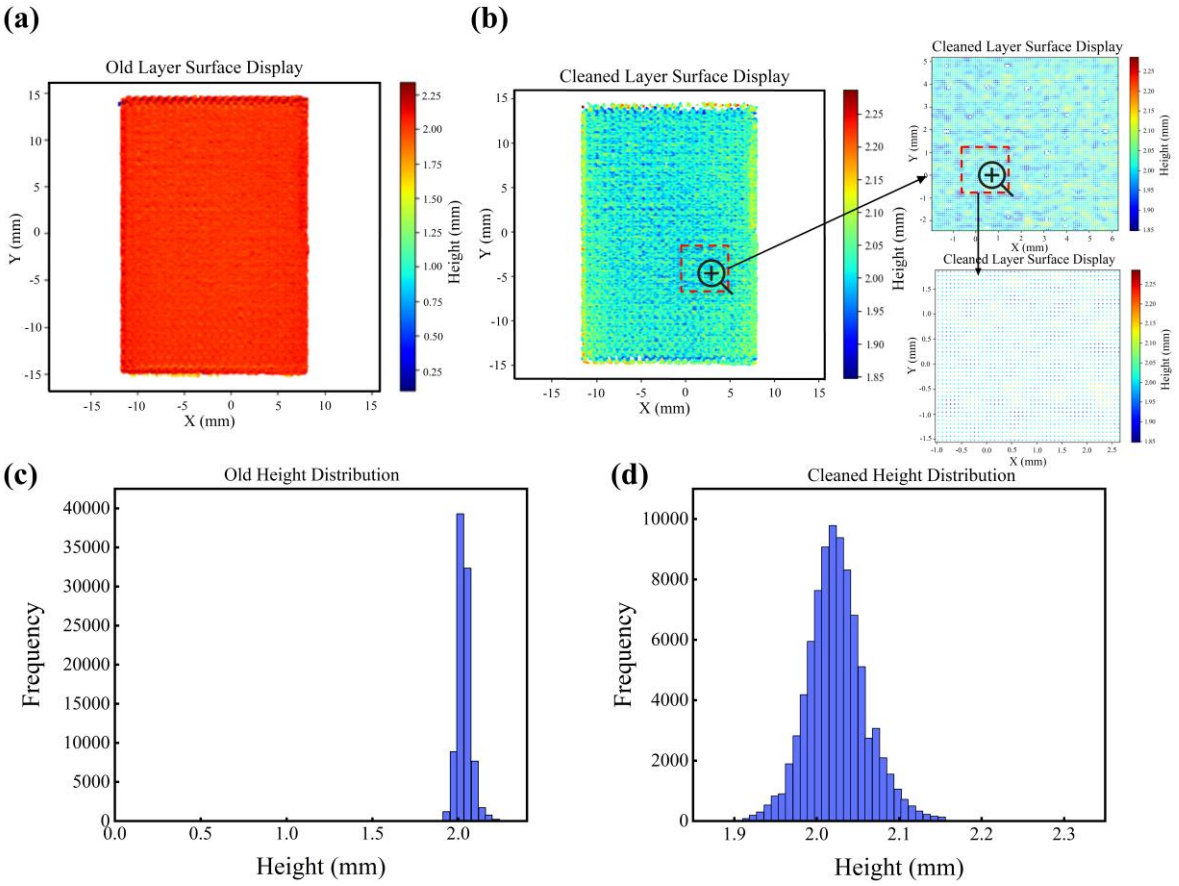

Figure 46. Comparison of Scanned Surface Before and After Point Cloud Cleaning: (a) Unprocessed Point Cloud, (b) Point Cloud Post-Cleaning, (c) Initial Height Distribution, (d) Height Distribution Post-Cleaning.

6.3.8 Calculating Average Surface Roughness

The Average Surface Roughness (Ra) is a critical parameter for quantifying an object's surface roughness. Ra measures the arithmetic average of absolute deviations from the mean surface line, providing a quantitative indication of surface irregularities. To accurately calculate Ra, the captured discrete data points across the surface of each layer immediately after printing is used. Ra is computed using Equation 19 which follows the standard definition provided in ASME B46.1-2019 [47], specifying it as the arithmetic mean of the absolute deviations from the mean surface line over the evaluated length as follow:

$$Ra = \frac{1}{N}\sum_{i=1}^{N} |z_i - \bar{z}| \quad (19)$$

Where *N* is the total number of sampled points. z_i represents the height at each sampled point (*i*). $\bar{z}$ is the average height across all sampled points, calculated as $\bar{z} = \frac{1}{N}\sum_{i=1}^{N} z_i$.

Throughout the study, 729 scans were conducted across different specimens, each represented thrice to account for variability, leading to a detailed dataset. Each set of three scans was analyzed to compute the mean and Standard Deviation of Ra, ensuring precision in our surface roughness measurements. Notably, the Standard Deviations were consistently below 8% of the mean Ra value, indicating a high degree of consistency across the printing process. This uniformity underscores the stability of the printing parameters, and the homogeneity of the material used, highlighting the effectiveness of this method in maintaining quality control.

The dataset thus comprises 243 unique observations of Ra, associated printing parameters, and the sequence of layer deposition, providing a comprehensive base for further analysis to refine FDM printing techniques. This methodical approach not only enhances understanding of layer-specific surface characteristics but also contributes significantly to the advancement of AM technology by optimizing surface quality in real-time.

6.3.9 Modeling

A variety of machine learning models were utilized to predict the surface roughness of each layer in the FDM 3D printing process, examining both independent and cumulative layer effects. The models tested include Random Forest (RF), Neural Networks (NN), Gradient Boosting, eXtreme Gradient Boosting (XGB), and Support Vector Machine Regressor (SVR). Two datasets were prepared to train the models to assess the impact of preceding layer roughness on subsequent layers: The primary features set consisted of four primary printing parameters: Printing Temperature (PT), Layer Thickness (LT), Printing Speed (PS), and Layer Number (LN). The enhanced features set included all the parameters from the primary set plus the Average Surface Roughness of the previous layer (PSR), providing insights into the sequential effects within the printing process.

For the Neural Network model, a TensorFlow/Keras framework was employed. The architecture featured an input layer depending on the dataset, with either four or five input neurons corresponding to the number of features. After evaluating several configurations, ranging from one to three hidden layers and 32, 64, or 128 neurons per layer, a single hidden layer with 64 neurons and ReLU (Rectified Linear Unit) activation was selected for both models. This setup achieved the best balance between training stability and predictive accuracy, showing no signs of overfitting or underfitting. The output layer contained a single neuron with a linear activation function, suitable for the regression task of predicting

continuous surface roughness values. The Adam optimizer was chosen for its robustness with sparse gradients and noisy data, and the loss function used was Mean Squared Error (MSE), which quantifies the accuracy by minimizing the deviation between predicted and actual values. Additional hyperparameters were also empirically tuned, learning rates of 0.01, 0.001, and 0.0005 were tested, with 0.001 selected based on convergence performance and batch sizes of 16, 32, and 64 were also evaluated, with 32 yielding the most stable results.

For the other models, Grid Search was systematically applied to fine-tune their hyperparameters. This technique evaluates multiple combinations of hyperparameters to find the optimal settings for each model, enhancing their predictive performance. Each model was trained on both datasets to determine the impact of including the roughness of the previous layer. The performance of the models was evaluated based on their ability to predict layer-specific surface roughness with high accuracy. The model that best minimized the MSE during testing was selected for practical implementation.

This modeling approach, integrating sophisticated ML algorithms with real-time data, aims to dynamically adjust printing parameters to optimize surface roughness layer by layer, thereby revolutionizing the precision and efficiency of the FDM 3D printing process.

6.3.10 Optimization

Optimization plays a pivotal role in refining the printing parameters to achieve minimal surface roughness in FDM 3D printing. The focus of the optimization in this study is on two key parameters: Printing Temperature (PT) and Printing Speed (PS). The objective is to minimize the predicted value of surface roughness (Ra), represented by the objective function in Equation 20:

$$f(PT, PS) = \widehat{Ra} \tag{20}$$

The bounds of the optimization variables are defined in Equation 3, where PT is constrained between 200°C and 230°C and PS between 40mm/s and 60mm/s. This defined range provides a controlled environment for the optimization algorithm to efficiently explore potential solutions within practical and experimentally validated settings. The rest of the parameters used in the predictive models are held as constants.

$$\begin{gathered}\text{minimize } f(PT, PS) \\ \text{subject to: } PT \in [200°\text{C}, 230°\text{C}], PS \in [40,60]\text{mm/s}\end{gathered} \tag{21}$$

The use of these algorithms is justified by their robustness and adaptability, which are essential for optimizing processes with intricate interactions between multiple parameters [48]. Particle Swarm Optimization (PSO) and Genetic Algorithm (GA) are particularly well-suited for the

dynamic and non-linear nature of FDM 3D printing, where parameters such as temperature, speed, and layer thickness interact in complex ways to influence surface quality [43-46][22]. Their ability to explore a vast solution space efficiently makes them valuable tools for addressing the multi-dimensional optimization challenges inherent in Additive Manufacturing [49].

Despite their strengths, these algorithms are not without weaknesses. PSO, for instance, is known to suffer from premature convergence in high-dimensional or complex landscapes, where the swarm may stagnate around local optima. Similarly, GA can be computationally intensive, especially when dealing with large populations or a high number of generations and may require careful tuning of its crossover and mutation rates to balance exploration and exploitation [39-42][56]. However, these weaknesses are mitigated in this study due to the specific nature of the problem and the constraints of the optimization framework.

For instance, the dimensionality of the parameter space in this study is relatively low, and the well-defined bounds of the search space reduce the likelihood of premature convergence in PSO. Furthermore, the computational overhead of GA is managed by leveraging a tailored population size and convergence criteria, ensuring efficient exploration without excessive resource consumption.

These algorithms have demonstrated success across a wide range of optimization tasks in diverse fields, such as materials science, mechanical engineering, and computational biology, further underscoring their suitability for improving the print quality in this study [50]. For instance, PSO's fast convergence and effective handling of continuous variables have been leveraged to optimize energy efficiency in manufacturing systems, while GA's versatility in exploring global optima has been utilized in tasks ranging from structural design to logistics optimization [48]. These prior applications highlight the versatility and reliability of these algorithms, making them ideal candidates for real-time adjustments during the FDM process [39-42][51].

Particle Swarm Optimization (PSO)

Particle Swarm Optimization (PSO) is an algorithm inspired by the social behavior of animals, such as birds flocking or fish schooling, and is particularly suitable for optimizing continuous problems like adjusting 3D printing parameters to minimize surface roughness [22, 52]. This study integrates PSO to refine the process settings in real-time, enhancing the Digital Twin capabilities in the context of Fused Deposition Modeling (FDM).

The way PSO has been specially designed for this application is as follows:

- Initialization: The process begins with the initialization of a swarm of particles, where each particle represents a potential set of printing parameters. Each particle is randomly assigned a position and velocity within the defined parameter space.
- Evaluation: Each particle's position corresponds to a specific combination of printing parameters. The fitness of each particle is evaluated based on the resulting surface roughness of the printed layer predicted by the neural network model developed from previous print data.
- Update Personal and Global Best: Each particle keeps track of its personal best position (Pbest), the position where it achieved its lowest surface roughness. The algorithm also tracks the global best position among all particles (Gbest), which represents the overall lowest surface roughness achieved by the swarm.
- Velocity and Position Update: Each particle updates its velocity and position based on its current velocity, the distance from its Pbest, and the distance from the Gbest. This is done using a formula that incorporates cognitive and social components:
  -The cognitive component (c1) reflects the particle's tendency to return to its Pbest.
  -The social component (c2) reflects the tendency to move towards the Gbest.
  -An inertia component (w) maintains a part of the previous velocity to ensure exploration of the search space.
- Iteration: These steps repeat for each particle until a stopping criterion is met, which could be a set number of iterations, or a minimal improvement threshold in surface roughness across iterations.
- Real-time Adjustment: The final Gbest after the completion of iterations is used as the optimal set of printing parameters for the next layer. This ensures that each layer is printed with parameters that are continually optimized based on real-time feedback and predictive modeling.

  Genetic Algorithm (GA)

Genetic Algorithms (GA) are evolutionary computing techniques that mimic natural selection processes to solve complex optimization problems, which can be highly effective in optimizing 3D printing parameters to minimize surface roughness [53-56]. In the context of this study, GA helps in dynamically adjusting printing settings based on the performance outcomes measured by the layer-specific surface roughness.

The implementation of GA in this research involves the following key steps tailored to the specifics of 3D printing optimization:

- Initial Population: The algorithm begins with a randomly generated population of individuals, where each individual represents a set of 3D printing parameters encoded as a chromosome.
- Fitness Evaluation: Each individual's fitness is evaluated based on how well the chosen parameters result in a printed layer with minimal surface roughness. This evaluation uses the predictive model developed from the machine learning analysis of historical print data.
- Selection: Individuals are selected for reproduction based on their fitness scores, with higher fitness individuals having a greater probability of being chosen. This selection process ensures that the best solutions are carried forward.
- Crossover and Mutation: Crossover operations mix the parameter sets of paired individuals to produce new offspring, introducing new parameter combinations to the population. Mutations are randomly applied to some individuals to explore new areas of the solution space and prevent the algorithm from becoming trapped in local optima.
- Replacement: New offspring replace less fit individuals in the population, continuously improving the population's overall quality in terms of achieving lower surface roughness.

Comparative Methodology

To evaluate the efficacy of the Particle Swarm Optimization (PSO) and Genetic Algorithm (GA) for real-time optimization in Fused Deposition Modeling (FDM) 3D printing, a systematic comparative analysis will be conducted. The objective is to determine the best algorithm for dynamically optimizing layer-specific surface roughness during the printing process. The comparison will focus on the following key criteria:

- Solution Quality: This involves assessing the algorithms' ability to consistently find optimal or near-optimal printing parameters that result in the lowest possible surface roughness. It will involve analyzing the average surface roughness values achieved by each algorithm and comparing them.
- Processing Time: Since the optimization needs to occur in real-time, the computational speed of each algorithm is crucial. This criterion will measure the time each algorithm takes to reach the termination criteria.
- Convergence Speed: This refers to how quickly each algorithm can find an optimal or satisfactory solution. Faster convergence is preferable in a production setting to ensure that adjustments to printing parameters can be made swiftly without disrupting the

ongoing manufacturing process. The convergence criterion used involves a threshold of 1e-6 with a patience of 15.

- Robustness Against Local Optima: An effective algorithm should avoid getting trapped in local optima-suboptimal solutions that a less robust algorithm might mistake for the best possible solution. The robustness will be evaluated by running each algorithm multiple times with different initial conditions to see if they consistently converge to the same or similar solutions.

The setup will involve the following steps:

- Implementation: Each algorithm will be configured to optimize a predefined set of Printing Speed, and Printing Temperature.
- Testing: Algorithms will be tested under identical conditions to challenge their optimization capabilities. The testing environment was configured to simulate real-time optimization, with processing times measured to reflect the computational effort required for one optimization cycle. 30 cycles were conducted with a fixed termination criterion of 100 iterations.
- Parameter Tuning: To ensure a fair and effective comparison, algorithmic parameters for both GA and PSO were empirically tuned through preliminary experimentation. For GA, population sizes of 5, 10, 30, and 50 were tested in combination with mutation rates (mutpb) from 0.1 to 0.3 and crossover probabilities (cxpb) between 0.5 and 0.8. For PSO, swarm sizes of 5, 10, 30, and 50 were evaluated along with inertia weights (w) from 0.4 to 0.6 and acceleration coefficients (c1, c2) ranging from 1.0 to 2.0.
- Data Collection: Performance data, including surface roughness measurements, computational time, and iteration counts, will be collected.
- Statistical Analysis: The collected data were subjected to statistical analysis to compare the performance of GA and PSO across different population (or swarm) sizes. For each population size (5, 10, 30, and 50), the best-performing parameter configuration for each algorithm, based on prior tuning, was used. Metrics such as final fitness value, execution time, and convergence speed were analyzed using mean and standard deviation over 30 independent runs. This approach ensured that each algorithm was evaluated under its most favorable settings for a fair comparison at each population level.

Figure 47 illustrates the methodology, showcasing how each algorithm will be evaluated against these criteria. This comparative study aims to provide clear insights into which

algorithm offers the best combination of precision, speed, and reliability for real-time optimization in FDM 3D printing.

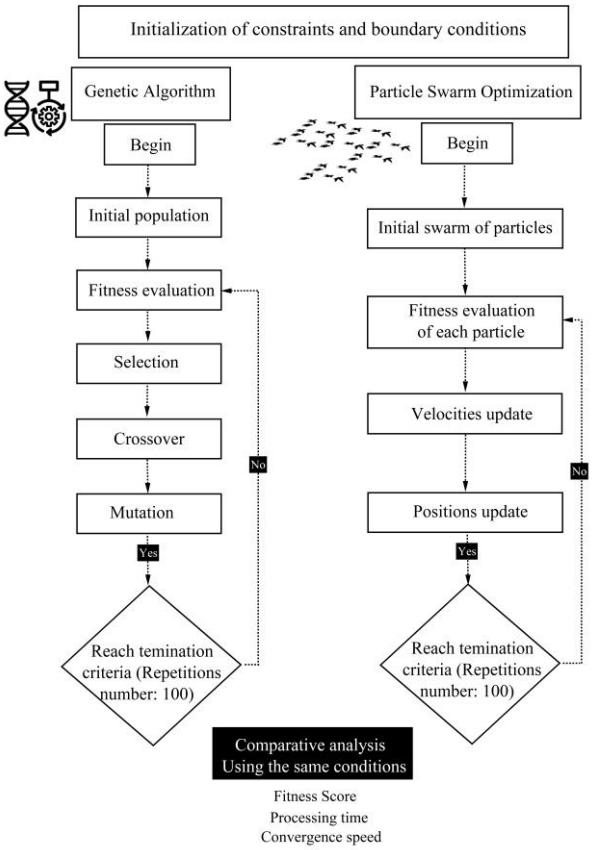

Figure 47. Methodology of the comparison between the optimization algorithms.

6.3.11 Real-time monitoring

The cornerstone of this research involves the deployment of a sophisticated Digital Twin framework to facilitate real-time monitoring and optimization of the FDM 3D printing process. The Digital Twin is crafted to synchronize seamlessly with the physical 3D printer, mirroring parameters of the printing process in real-time. This integration not only allows for the continuous tracking of printing parameters but also enables real-time adjustments to optimize layer-specific surface roughness and overall printing quality.

6.3.11.1 Key Features of the Digital Twin in FDM 3D Printing:

The architecture of the Digital Twin system incorporates several high-fidelity sensors, including thermistors embedded within the printer to continuously monitor the temperatures of the extruder and the print bed. These temperatures are vital as they directly affect the filament's melting and adhesion properties, thereby influencing the structural integrity and surface quality of the printed object. The system is designed to update temperature data every three seconds, ensuring swift responses to any deviations from the optimal thermal conditions.

Additionally, the Digital Twin is tasked with managing the printing speed, dynamically optimizing it upon the completion of each layer based on predictive adjustments recommended by the optimization algorithm. This proactive strategy ensures that each new layer commences under the most favorable conditions, enhancing the synergy between speed and temperature to achieve the best possible surface finish.

Furthermore, the Digital Twin offers an interactive surface monitoring interface that enables real-time visualization of point cloud data collected from scanned layers. This interface decodes the received point cloud data, calculates surface roughness metrics, and provides a detailed graphical representation of the layer's surface quality. By integrating this feature, operators can assess real-time deviations, surface inconsistencies, and overall print quality trends.

6.3.11.2 Software Implementation

The Digital Twin is implemented using a PyQt5 desktop application, providing a robust and user-friendly interface for operators to monitor real-time data and control the system effectively. Key features of the software include:

- Communication Method: The controlling algorithm and Digital Twin interfaces communicate by means of two named pipes that insure an efficient exchange of real-time data. The first pipe is dedicated to printing parameters, which transmits Printing Temperature, Bed Temperature, and Printing Speed. The second pipe is dedicated to surface monitoring and visualization, and it is in charge of transmitting the extracted point cloud data obtained from scanning each printed layer throughout the 3D scanning process.

  The controlling algorithm and the printer communicate via a serial connection where a Python script feeds the G-code instructions and other directives line by line. In order to keep the workflow between the printing, scanning, visualization, and optimization processes synchronized, the script not only handles the sequential printing instructions but also includes the important control instructions like leading the printer to pause after the print of each layer, moving the print head away from the printed part so that scanning can be applied and optimization can be performed, and collecting data from the sensors.
- Data Synchronization: The Digital Twin continuously syncs with the physical printer, gathering data on printing speed, and temperatures. By sending the G-code command 'M155 S3' to the printer via serial port, the algorithm keep on receiving temperature

data that include Target Printing Temperature, Actual Printing Temperature, Target bed Temperature, and Actual Bed Temperature from the printer every 3 seconds (Figure 48(a)). The Printing Speed is set after the optimization of each layer and is sent with the Temperature parameters. Moreover, after the print of each layer, Point Cloud data generated from the 3D scanner is collected via a Python script (Figure 48(b)). The two named pipes responsible for sending and receiving data are employed to process data in the background and allow constant monitoring without interfering with direct commanding of the printer. This real-time data collection is crucial for assessing the current state of the print and for making informed decisions on parameter adjustments.

- Optimization of Printing Parameters: Based on the collected data from the scanner, using the optimization algorithm and the prediction models, the Digital Twin generates new optimized values of Printing Temperature and Printing Speed and updates the printer accordingly. In the current implementation, the optimized print speed is applied uniformly across each layer. The optimization cycle is executed layer-by-layer, using feedback from the previous layer's scan to update parameters for the next. Real-time intra-layer speed variation during deposition is not active in this version of the system.
- Visualization and User Interface: The Digital Twin provides user-friendly interfaces that display both the current and previous state of the print. It includes a display of the Printing Parameters (Figure 48(a)) that include the temperatures-time graph, and the Printing Speed resulted from the optimization of the current layer, and a display of the Point Cloud of the printed layer and resulted Surface quality metrics (Figure 48(b)).
- Historical Data Analysis: Beyond real-time monitoring, the Digital Twin archives all collected data for each print job. This historical analysis aids in identifying long-term trends, potential systematic errors, and areas for further optimization.

The integration of the Digital Twin into the FDM 3D printing process not only elevates the precision and adaptability of the operations but also significantly curtails material waste by preventing print failures. It enhances the aesthetic and structural quality of the final products. This continuous optimization of key printing parameters like temperature and speed epitomizes the transformative potential of incorporating advanced digital tools in manufacturing settings.

6.4 Results

This section presents the findings related to the accuracy of prediction models and the performance of optimization algorithms.

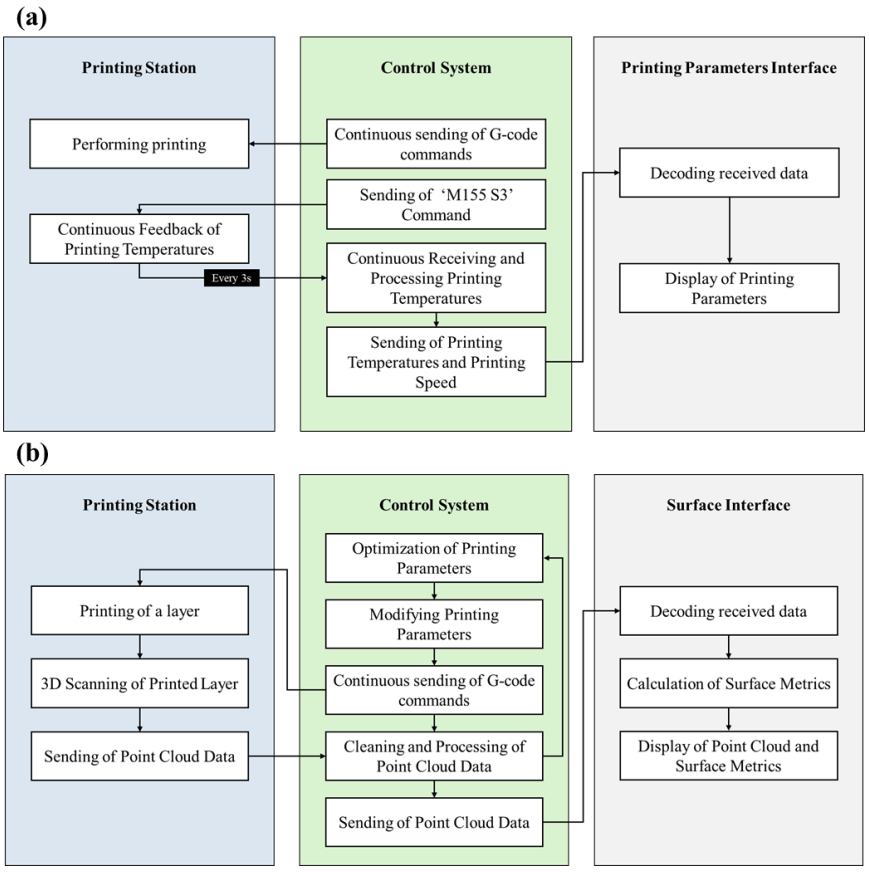

Figure 48. Real-Time Data Synchronization and Monitoring in the Digital Twin: (a) Temperature-Time Graph and Printing Speed Display, (b) Point Cloud Visualization of Printed Layer and Sur-face Quality Metrics.

6.4.1 Prediction accuracy analysis

The results of the prediction accuracy analysis of the Neural Network models are summarized in Table 28. The Neural Network (NN) model exhibited the highest prediction accuracy compared to the other models tested. When trained with four features, Printing Temperature (PT), Layer Thickness (LT), Printing Speed (PS), and Layer Number (LN), the NN model achieved a Testing R^2 of 86.12% and a Training R^2 of 93.84%. Upon adding a fifth feature, Previous Surface Roughness (PSR), the Testing R^2 improved to 92.19%, while the Training R^2 increased to 95.8%. These results suggest that the inclusion of PSR as an additional feature enhances the NN model's ability to predict layer-specific surface roughness with greater precision, as illustrated in Figure 49(a) and Figure 49(b).

A comprehensive SHAP analysis was performed on the full held-out test set (Figure 49(c)), revealing each feature's directional impact on predicted surface roughness. Layer Number shows that later layers predominantly decrease Ra, while early layers increase it. The best smoothing lever appears to be printing temperature, as high temperatures provide negative SHAP values and consistently reduce roughness across samples. Layer Thickness and Printing Speed both exhibit near-linear effects on predicted roughness. Thicker layers consistently drive

SHAP values negative indicating lower Ra, while thinner layers increase it. On the other hand, faster printing speeds increase predicted roughness, and slower speeds decrease it, with little evidence of a neutral mid-range. Although Previous Surface Roughness has a smaller mean-absolute SHAP compared to these parameters, its red points mostly lie to the right of zero demonstrating that high prior-layer roughness leads to higher predicted roughness in the subsequent layer. This behavior validates the inclusion of a memory term in the model, ensuring that identical process settings will yield increased Ra when carried over from a rough surface.

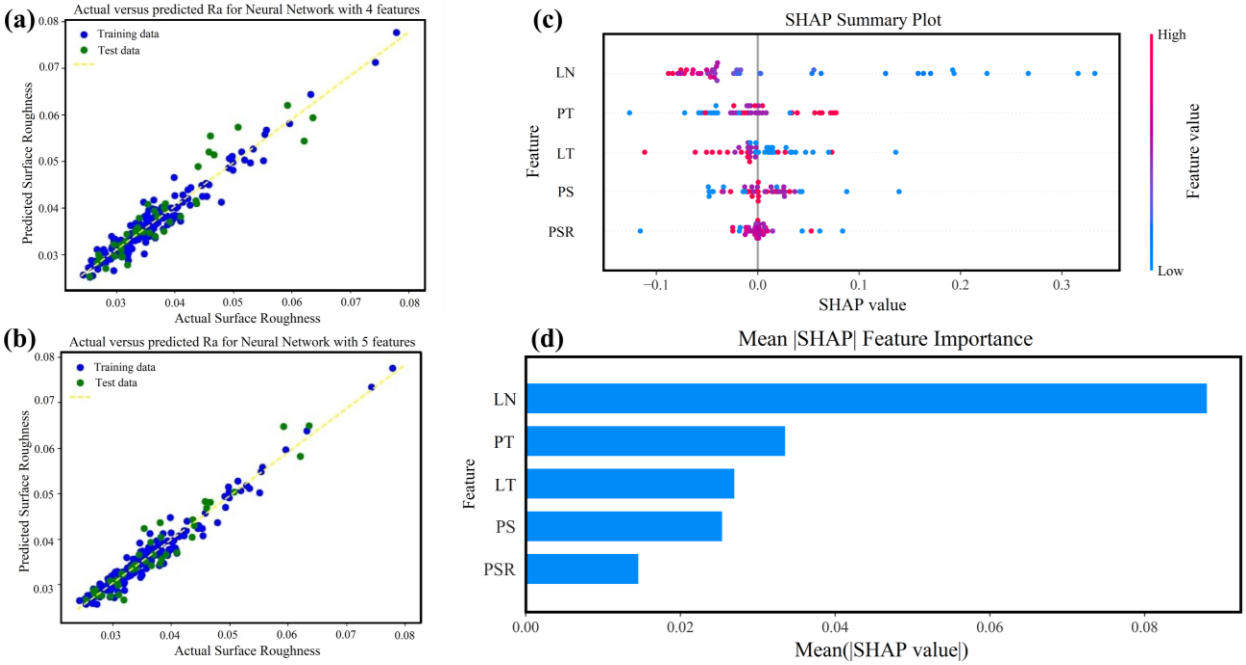

Figure 49. Observed versus predicted average surface roughness for the Neural Network models: (a) NN with 4 features, (b)NN with 5 features, (c) SHAP beeswarm summary plot, (d) Mean - |SHAP| Feature Importance bar chart.

6.4.2 Prediction time analysis

The prediction time of the Neural Network (NN) model is a crucial factor in assessing its effectiveness for real-time applications. The inference latency of the trained models was evaluated using the full dataset as input. A custom Python script employing the time module recorded the average inference time over 1000 iterations. Although the model's accuracy improved with the inclusion of the fifth feature (Previous Surface Roughness), the prediction time remained largely stable, slightly decreasing from 68.47 ms to 67.75 ms. This minor reduction in prediction time, coupled with the enhanced accuracy, highlights the NN model's efficiency and suitability for real-time optimization tasks in FDM 3D printing. When evaluated on an Nvidia GeForce GTX 1050 GPU, the average inference time dropped significantly to 0.0511 ms for the model with 5 features and 0.0528 for the model with 4 features, highlighting

the model's scalability and potential for accelerated deployment using embedded GPUs or multi-core environments. The performance details for both configurations of the NN model are summarized in Table 28.

Table 28. Performances of the NN models.

Model	Features	Testing R^2	Training R^2	Prediction Time	Prediction Time Using GPU
Neural Network	4	86.12%	93.84%	68.47 ms	0.0528 ms
Neural Network	5	92.19%	95.80%	67.75 ms	0.0511 ms

6.4.3 Comparison with other models

In this study, several machine learning models were employed to predict the surface roughness of each layer in the FDM 3D printing process and to compare their performances against the Neural Network (NN) models. These models included Random Forest (RF), Gradient Boosting (GB), eXtreme Gradient Boosting (XGB), and Support Vector Regressor (SVR). A grid search method was used to optimize the hyperparameters of each model to achieve the best performance.

The comparison showed that tree-based models, such as Random Forest, Gradient Boosting, and eXtreme Gradient Boosting, provided good accuracy and faster execution times compared to the NN model. However, these models struggled with generalization, as reflected in the discrepancy between their training and testing R^2 values (Figure 50). This discrepancy indicated a tendency to overfit the training data, which reduced their performance on unseen data. Table 29 summarizes the accuracy and prediction times of each model.

Table 29. Accuracy of ML models compared to NN.

Model	Testing R^2	Training R^2	Prediction Time
Random Forest (RF)	88.94%	95.93%	26.82 ms
Gradient Boosting (GB)	90.38%	94.91%	1.51 ms
eXtreme Gradient Boosting (XGB)	91.85%	95.55%	1.48 ms
Support Vector Regressor (SVR)	69.36%	70.92%	1.32 ms

In contrast, the NN model, with its ReLU activation function and regularization techniques, demonstrated better generalization capabilities. The NN model’s ability to incorporate non-linearity enabled it to capture more intricate relationships within the data, resulting in more balanced performance across both training and testing datasets. While the NN model had a

longer prediction time than the tree-based models, it consistently produced more accurate predictions, making it a more robust choice for real-time optimization in FDM 3D printing.

This trade-off between prediction speed and accuracy highlights the need for careful consideration of both computational efficiency and prediction reliability when selecting models for real-time optimization tasks.

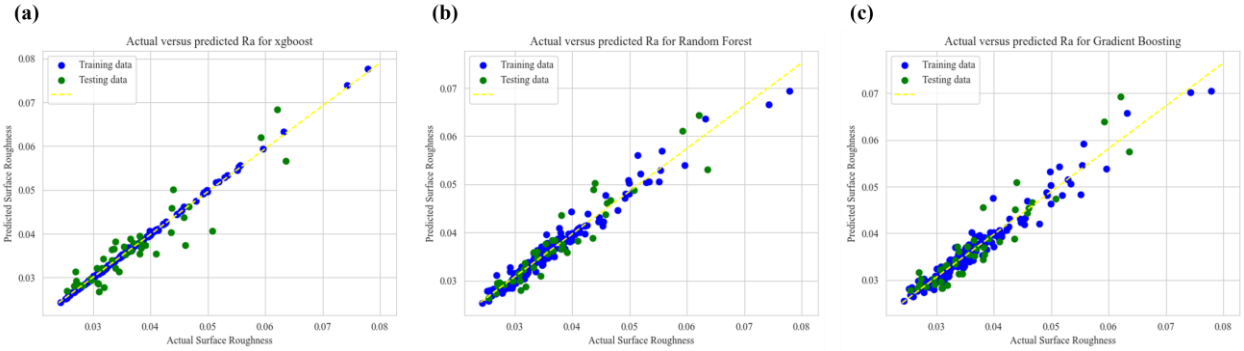

Figure 50. Observed versus predicted average surface roughness for the tree-based models: (a) xgboost, (b) Random Forest, (c) Gradient Boosting.

6.4.4 Choice of the model

For real-time optimization, the selection of a prediction model must balance both accuracy and prediction time. In this study, the Neural Network (NN) model with five features (including the Previous Surface Roughness) emerged as the most suitable choice. This model demonstrated high accuracy, with a Testing R^2 of 92.19% and a Training R^2 of 95.8%, indicating its strong predictive performance for unseen data. Additionally, the NN model maintained a reasonable prediction time of 67.75 ms, which is critical for real-time applications.

Given its ability to provide precise predictions within a short time frame, the NN model is well-suited for real-time optimization tasks in FDM 3D printing. The balance it strikes between fast computational performance and high accuracy ensures that it can effectively respond to dynamic changes in printing conditions, optimizing the printing parameters in real-time without sacrificing the quality of predictions. Therefore, the NN model stands out as the most viable option for enhancing the surface roughness control and overall quality of the FDM printing process in real-time applications.

6.4.5 Sequential nature of surface roughness

Our analysis of feature importance across several tree-based machine learning models revealed that Previous Surface Roughness (PSR) consistently emerges as a key predictor in determining the surface roughness of subsequent layers (Figure 51). This was particularly evident in the Random Forest (RF) and Gradient Boosting (GB) models, where PSR was ranked as the second

most influential feature, with importance values of 33.50% for RF and 27.15% for GB. Even in the eXtreme Gradient Boosting (XGB) model, PSR was recognized, although with a lower importance of 11.23%. These results highlight the strong impact that the surface roughness of one layer has on the next in the FDM 3D printing process.

Alongside PSR, Layer Number (LN) also proved to be a significant feature, especially in the XGB model, where it was the most important factor (50.80%). LN was similarly important in RF (36.60%) and GB (41.44%) models, demonstrating that the sequential order of layers plays a crucial role in the surface quality of the printed part. This sensitivity to layer number emphasizes the importance of capturing the sequential nature of the 3D printing process, where each new layer builds on the previous one.

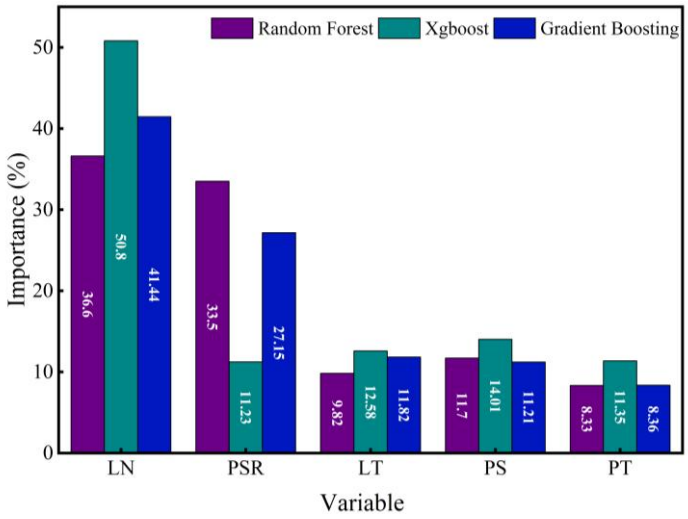

Figure 51. Feature importance of the Tree-based ML algorithms that have the best performances.

Other features such as Layer Thickness (LT), Printing Speed (PS), and Printing Temperature (PT) contributed to the prediction models, but to a lesser extent than PSR and LN. These findings underscore the complex interplay between the physical aspects of 3D printing and the data-driven insights provided by machine learning. Specifically, the relationship between the surface quality of preceding layers and subsequent ones is a critical determinant of the final print quality.

The mean |SHAP| bar chart (Figure 49(d)) confirms that Layer Number has by far the greatest average impact on predicted roughness using NN model, reflecting the buildup of surface deviations over successive layers. Meanwhile, the remaining inputs all contribute meaningfully but at lower levels.

In the context of FDM 3D printing, the physical deposition of each new layer on top of the previous one means that any surface imperfections in the lower layer directly influence the layer above it. The 3D printer's extruder follows the contour of the preceding layer, which

means that deviations in flatness or texture can propagate through the entire print, compounding surface roughness over time. Additionally, as the number of layers increases, heat dissipation and cooling dynamics shift due to the increasing mass of the printed part. These thermal changes can affect how each new layer adheres and solidifies, which further impacts surface roughness.

By including the PSR in our machine learning models, the models can account for these sequential effects, allowing them to adjust their predictions based on the roughness of the previous layer. A greater roughness value in one layer tends to correlate with specific changes in the roughness of the next, enabling more accurate predictions and allowing for real-time adjustments to printing parameters.

The inclusion of the layer number as a feature serves a similar function, helping the model recognize patterns associated with different stages of the printing process. Early layers, which are closer to the heated print bed, often cool at different rates compared to middle or top layers. This change in cooling dynamics as the print progresses further supports the importance of the layer number in predicting surface roughness. Thus, accounting for the layer number allows the model to refine its predictions based on its position in the printing sequence.

Figure 52 visually illustrates the relationship between sequential layers by showing the surface roughness profiles for eight consecutive layers of a printed object. The red dashed boxes and arrows highlight areas where the surface roughness of one layer visibly influences the next. Peaks and valleys in one layer often correspond to similar features in the layer above, showing a clear transmission of imperfections from layer to layer. These regions emphasize that the roughness is not random but is driven by the conditions in preceding layers, confirming the importance of accounting for sequential effects when optimizing 3D printing processes.

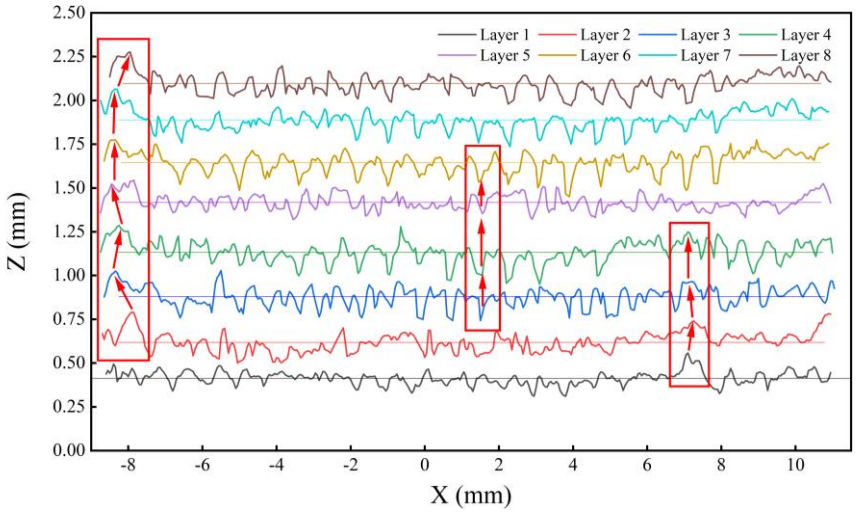

Figure 52. Sequential influence of the layer's surface roughness in FDM.

6.4.6 Optimization analysis

This section provides an in-depth analysis of the Genetic Algorithm (GA) and the Particle Swarm Optimization (PSO), to assess their suitability for real-time optimization of layer-specific surface roughness in FDM 3D printing. Both algorithms were evaluated based on key criteria, including final fitness values, execution time, and convergence speed, with the goal of identifying the most effective method for enhancing surface quality while maintaining computational efficiency.

The results from multiple runs (30 repetitions with 100 iterations per run) are summarized in Table 30, which highlights the performance differences between the two algorithms under the best possible parameter settings for each population size. For each population or swarm size, the results presented correspond to the best-performing parameter settings identified during the preliminary tuning phase described in the methodology. This ensures that the comparison between GA and PSO at each size level reflects their optimized performance under fair and equivalent conditions.

The *Genetic Algorithm* (GA) demonstrated robust performance, particularly with larger population sizes, achieving high-quality fitness values and moderate execution times. For instance, GA with a population size of 50 (GA50) achieved a final fitness value of 0.0287±1.1×10−5, an execution time of 11.93±0.6511.93±0.65 seconds, and a convergence speed of 33.17±23.22 generations. These results underscore GA's ability to explore a wide search space thoroughly, leveraging its processes of selection, crossover, and mutation to achieve superior solutions. However, GA's relatively slower convergence speed, compared to PSO, highlights a potential limitation for real-time applications that demand rapid adjustments.

Conversely, *Particle Swarm Optimization* (PSO) exhibited strong performance, particularly in terms of execution speed and consistency across varying population sizes. PSO with a population size of 30 (PSO30) emerged as a standout configuration, achieving a final fitness value of 0.0287±3.46×10−18, an execution time of 5.17±0.25 seconds, and a convergence speed of 27.63±4.64 generations. These results highlight PSO30's ability to combine precision and rapid convergence, making it an excellent choice for real-time optimization tasks. Compared to PSO10, PSO30 maintains similar computational efficiency while slightly improving its convergence consistency, as reflected by its lower Standard Deviation in convergence speed. Additionally, PSO's inherent strength lies in its ability to dynamically adjust particle positions by effectively balancing exploration and exploitation through local and global best-known solutions.

The comparison highlights the unique strengths of both algorithms in optimizing printing parameters to minimize surface roughness. GA is particularly well-suited for tasks requiring high precision and extensive solution exploration, while PSO's rapid convergence and computational efficiency make it ideal for real-time optimization.

As shown in Figure 53, the response surface illustrates the performance of both algorithms, emphasizing the benefits of increased population size for achieving lower surface roughness. PSO consistently exhibited lower Standard Deviations at population sizes of 10 and 30, indicating its ability to converge within a tightly bounded neighborhood of the global minimum. In contrast, GA, particularly at population sizes of 10 and 30, demonstrated superior exploration of the optimization space, avoiding premature convergence to local minima.

Table 30. Comparative analysis of the optimization algorithms

Optimization Algorithm	Population/Sworm size (parameters)	Final fitness	Execution time (s)	Execution time using GPU (s)	Convergence speed (generations)
GA	5 (mutpb=0.2, cxpb=0.8)	0.0290 ±9.76E-4	9.17 ±0.65	0.0587±0.0109	41.41 ± 31.76
	10 (mutpb=0.2, cxpb=0.5)	0.0290 ±30.2E-5	10.39±0.53	0.0633±0.0155	50.50 ± 29.64
	30 (mutpb=0.1, cxpb=0.5)	0.0288 ±10.8E-5	11.13±0.96	0.0950±0.0145	38.97 ± 25.41
	50 (mutpb=0.1, cxpb=0.5)	0.0287 ±1.1E-5	11.93±0.65	0.1228±0.0211	33.17 ± 23.22
PSO	5 (w=0.6, c1=2, c2=1.5)	0.0288 ±4.72E-9	4.98 ±0.25	0.0452± 0.009	41.33 ± 7.78
	10 (w=0.5, c1=2, c2=1.5)	0.0287 ±3.47E-18	5.03 ±0.8	0.0549±0.008	28.90 ± 7.91
	30 (w=0.5, c1=1.5,c2=1.5)	0.0287 ±3.46E-18	5.17 ±0.25	0.0962±0.009	27.63 ± 4.64
	50 (w=0.5, c1=1.5,c2=1.5)	0.0287 ±5.04E-17	6.11 ±0.84	0.1293±0.016	25.97 ± 4.30

In real-time optimization applications, balancing all evaluation criteria, such as final fitness value precision, execution time, and convergence speed, is essential. Based on the findings, PSO with a population size of 30 (PSO30) is the recommended approach for real-time optimization tasks in FDM 3D printing. It achieves an optimal balance between precision, execution time, and convergence speed, making it an excellent choice for applications requiring dynamic adjustments. With an execution time of 5.17±0.25 seconds, PSO30 outpaces GA50 while maintaining comparable precision and significantly faster convergence. The parameter configuration of the chosen method (PSO30) include an inertia weight of 0.5 and cognitive and social weights of 1.5, ensuring an effective optimization of printing parameters.

To explore scalability and acceleration potential, the optimization algorithms were also executed using GPU-based inference on a Nvidia GTX 1050. While the scan–predict–optimize loop was originally run on CPU, this GPU integration serves as a forward-looking perspective for further improving responsiveness. Notably, PSO with a population size of 5 achieved a mean processing time of 0.045 s ± 0.009, while GA5 reached 0.059 s ± 0.011. Even at higher population sizes, total processing times remained below 0.13 s. These findings confirm the

feasibility of real-time optimization under constrained hardware and highlight the opportunity for additional speedups using embedded or more advanced GPUs, particularly beneficial for scaling up to complex or larger builds.

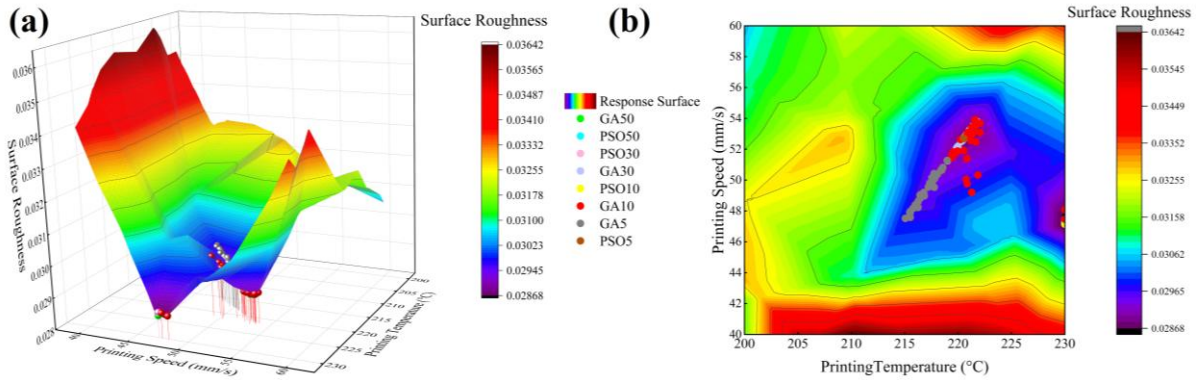

Figure 53. Response Surface of the optimization space and results of the optimization algorithms: (a) 3D response surface, (b) 2d response surface.

These results are consistent with existing research findings, which also underscore the effectiveness of GA and PSO in optimizing FDM 3D printing parameters. Feng et al. [49] demonstrated that a hybrid of GA and PSO could successfully minimize material waste in FDM printing, reinforcing the effectiveness of these algorithms, particularly with larger population sizes. Furthermore, Saad et al. [22] highlighted PSO's superior convergence speed and final fitness values, underscoring its suitability for real-time applications where quick and accurate optimization is required. Clarke et al. [57] also reported that PSO's adaptability enhanced both the mechanical properties and surface finish of printed parts, affirming PSO's utility for real-time FDM 3D printing optimization.

6.4.7 Experimental validation

To assess the efficacy of the optimization algorithm implemented through the Digital Twin, an experimental comparison was conducted between layer-specific surface roughness of parts printed using standard parameters for PLA and parts printed with dynamically optimized parameters. As detailed in Table 31, the recommended standard parameters for PLA included a printing temperature of 215°C and a printing speed of 50 mm/s, with a layer thickness of 0.35 mm chosen for this validation. Other parameters remained consistent as specified in Table 26.

Table 31. Recommended parameters for PLA

Parameters	Recommended Parameters	Optimized parameters
Printing Temperature (°C)	215	Adjusted dynamically
Printing Speed (mm/s)	50	Adjusted dynamically

The layer-specific roughness comparison between parts printed with standard parameters and those printed using the Digital Twin's optimized parameters demonstrates a significant enhancement in surface finish. This improvement is reflected by the consistently lower surface roughness (Ra) values in the optimized prints across all layers (Figure 54(a)). The optimized parameters result in visibly smoother prints, with the surface roughness (Ra) values notably lower than those produced using standard parameters. This finding highlights the effectiveness of the Digital Twin's real-time adjustments in minimizing surface irregularities during the printing process.

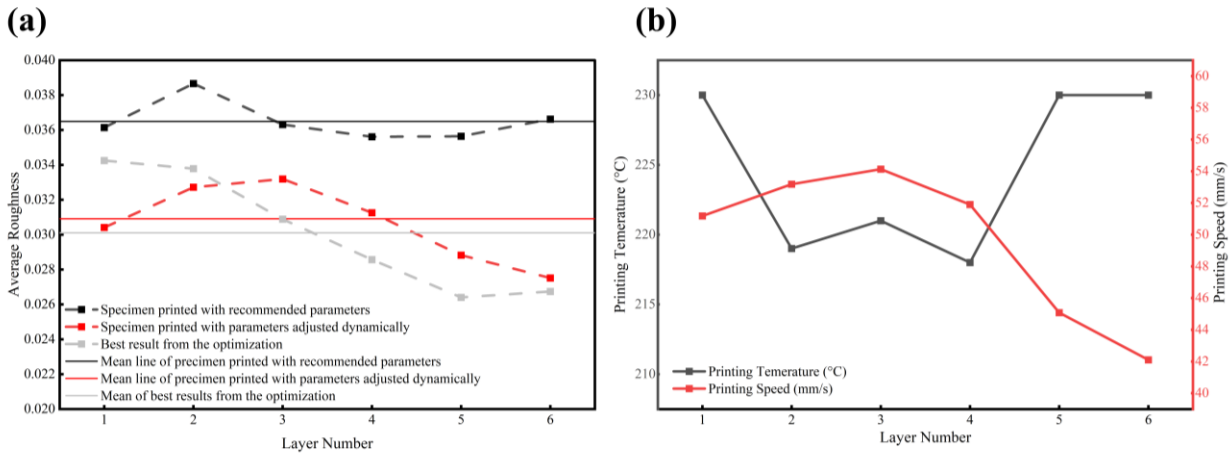

Figure 54. Impact of Real-Time Optimization on Surface Roughness and Printing Parameters: (a) Comparison of Surface Roughness Between Standard and Dynamically Optimized Printing Parameters, (b) Evolution of Printing Temperature and Speed as Determined by the Optimization Algorithm.

Furthermore, the average surface roughness for parts printed with standard parameters was approximately 0.03649mm, whereas parts printed with optimized parameters achieved an average Ra of 0.03058mm. This difference represents a substantial reduction of 16.196% in layer-specific Ra and more importantly, of 24.877% of the Ra of the last layer, translating directly to a smoother surface finish. These results validate the Digital Twin's capability to enhance print quality significantly by dynamically optimizing the printing process for each layer.

When compared to earlier studies that used offline optimization techniques, these results show a notable improvement in surface roughness. The real-time optimization technique employed here has shown to be more successful in dynamically modifying print settings in real time, even though numerous studies have obtained reductions by pre-determined parameter adjustment [13, 22, 58]. This validates the benefits of online optimization over conventional offline techniques by confirming that adaptive parameter adjustment throughout the printing process results in higher surface quality.

Figure 54(a) also presents the comparison between the predicted and observed average surface roughness values. The small deviation between the two sets of points indicates a high prediction accuracy of the model, it suggests that the model effectively captures the key patterns in surface roughness variations. The slight deviations observed in some layers could be attributed to minor external disturbances such as environmental fluctuations like ambient temperature changes or material inconsistencies. These results confirm the reliability of the model in real-time applications, as it consistently provides accurate predictions that can guide optimal parameter adjustments.

Figure 54(b) illustrates the variation of printing temperature and printing speed across the printed layers, showing how the optimization algorithm adapts these parameters in real time to compensate for surface roughness trends and enhance print stability. The results show high printing temperature at the beginning of the print which could be explained by the need of high temperatures to ensure proper adhesion to the print bed and to compensate for heat loss due to direct contact with the bed surface. It also improves the flow of the material reducing the risk of warping. This result aligns with the research of Sanatgar et al. [59] that found that higher Printing Temperatures enhance adhesion by improving the wetting of the material on the print surface and the research of Thumsorn et al. [60] that confirmed that it improves the overall strength of the first layer. The temperatures of the middle layers remain close to the recommended temperature for PLA as long as there is not a significant deviation in the preceding surface due to environmental fluctuations or material inconsistencies. The optimization algorithm suggests high printing temperatures for the last layers to prevent the material from cooling too quickly and to guarantee good inter-layer fusion, which addresses the problem of weak interlayer bonding in later layers of FDM printing caused by cooling effects because they are farther from the heated print bed than the other layers [61-63].

The optimization algorithm also suggests relatively low speed for the first layer to ensure its strong to the print bed. In fact, lower speeds allow the material to be deposited more precisely, ensuring that the first layers bond securely to prevent warping or detachment [60]. For the middle layers, the printing speed remained close to the recommended parameters. For the last layers, the printing speed is reduced to values close to the minimum of the optimization space for this parameter.

The experimental validation of the Digital Twin system revealed several critical performance metrics that underscore its efficiency and responsiveness in optimizing the FDM 3D printing process.

- Temperature Transition Time: The time required for the Digital Twin to adjust printing temperatures affects the system's adaptability to new parameters, impacting overall responsiveness. Transitioning the print head temperature from 200°C to 230°C requires about 27 seconds, while cooling from 230°C to 200°C takes approximately 55 seconds. This discrepancy results from the printer's heating system, which facilitates quick temperature increases, whereas cooling relies only on the print head's fans, slowing the process. These transition times represent worst-case scenarios where the temperature changes across the full range of the optimization space.
- Surface Scan Process: For each layer scan, the printing must pause, and the print head moves to a secure location. This procedure takes around 30 seconds, divided as follows:
  - Moving the print head to a secure position: 5 seconds
  - Scanning the layer: 15 seconds
  - Acquiring data: 10 seconds
  - Processing data and sending it via the pipe: less than 1 second
- Optimization Process: Particle Swarm Optimization (PSO) with a population size of 30 was selected for the optimization. A convergence-based termination criterion was employed, whereby the process would end if the fitness score remained unchanged for 15 iterations. This setup led to an average optimization completion time of 2.83 seconds and an average stopping at 53.16 iterations for the presented validation test, ensuring rapid adjustments without compromising print quality.
- Temperature Data Monitoring and Transfer: Fast data transfer is essential for the real-time monitoring capacity of the Digital Twin. Transferring temperature data from the printer's sensor to the Digital Twin is almost instantaneous, enabling timely temperature updates that support real-time optimization. The temperature monitoring interface within the Digital Twin is shown in Figure 55(a).
- Surface Scan Data Display: Displaying surface scan data in the Digital Twin takes approximately 2 seconds, split between data transfer and data display (Figure 55(b)).

These performance metrics illustrate the Digital Twin system's capability to manage and optimize the FDM 3D printing process efficiently, enabling dynamic adjustments to printing parameters with minimal delay. This system not only enhances the quality of the printed layers by reducing surface roughness but also demonstrates the potential for achieving high efficiency and responsiveness in real-time AM optimization.

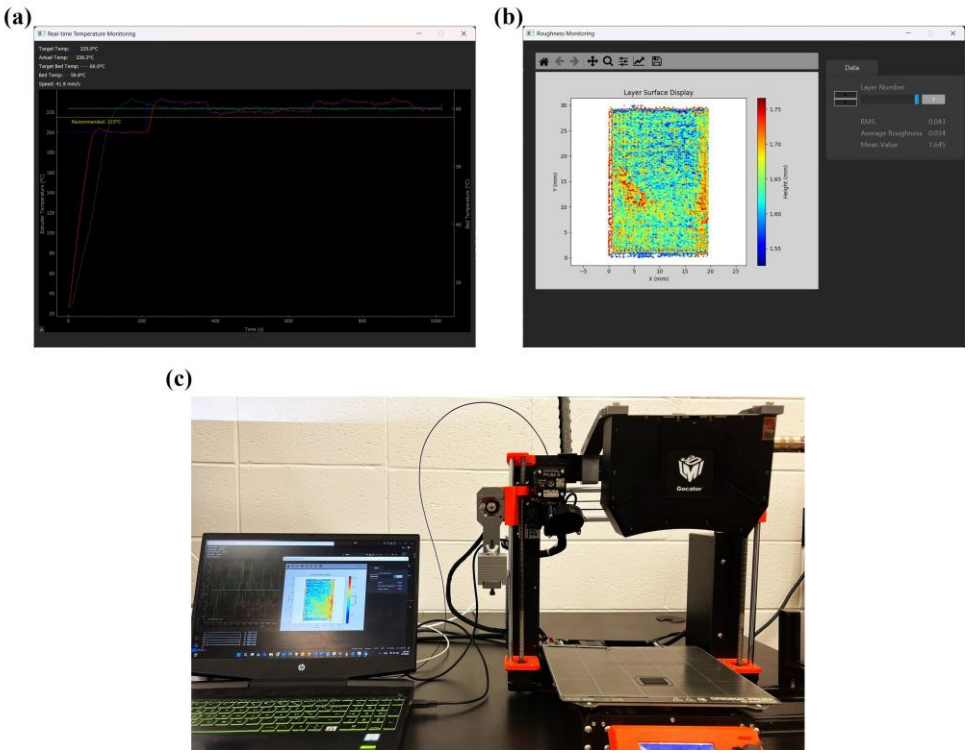

Figure 55. Monitoring Interfaces of the Digital Twin in Real-Time Optimization: (a) Temperature and Speed Interface, (b) Surface Display Interface, (c) Digital Twin Setup.

The Digital Twin's real-time monitoring and optimization capabilities, while requiring relatively long process times for parameter adjustments and surface scans, contribute substantially to enhanced print quality, improved layer adhesion, and reinforced structural integrity of printed components. These real-time adjustments help minimize variability and increase reliability throughout the FDM process, resulting in more consistent output quality [64, 65]. The benefits of this approach are notable: reduced material waste, fewer print defects, and increased overall process efficiency [66, 67].

In an industrial setting, these improvements directly translate into cost savings, quicker production cycles, and the ability to produce superior-quality products with fewer resources, significantly boosting competitiveness and operational efficiency [68, 69]. The strategic advantages of incorporating a Digital Twin into the manufacturing process thus extend beyond individual prints, establishing a foundation for optimized workflows and resource management in AM.

6.5 Conclusion and perspectives

This article has introduced a novel approach to FDM 3D printing, where layer-specific surface roughness is dynamically optimized using real-time data acquired through 3D scanning. By integrating advanced scanning technology with sophisticated optimization algorithms,

specifically Genetic Algorithm (GA) and Particle Swarm Optimization (PSO), a new method emerges that effectively bridges fabrication processes with real-time quality control.

The optimization process includes a Neural Network model trained to predict surface roughness based on essential printing parameters: Printing Temperature, Printing Speed, Layer Thickness, Layer Number, and the Surface Roughness of the preceding layer. This model achieved impressive accuracy, with R^2 values of 95.8% on training data and 92.19% on testing data. While alternative machine learning models demonstrated faster execution times, they lacked generalization capacity, underscoring the Neural Network's superior predictive reliability.

The investigation into feature importance highlighted the critical role of Layer Number and Previous Surface Roughness in training tree-based algorithms. These findings demonstrate that the quality of each layer is substantially influenced by the roughness of the previous layer; deviations in flatness or texture can propagate, compounding imperfections throughout the print.

A comparative analysis of optimization algorithms revealed that while GA excels in thoroughly exploring the optimization space, it requires larger population sizes and exhibits slower convergence speeds. In contrast, PSO achieved high fitness scores with rapid convergence and efficient processing times, making it the most suitable algorithm for real-time optimization in this FDM 3D printing application.

A Digital Twin system has been developed in this context to monitor and visualize printing parameters and printed surfaces in real-time, while integrating optimization algorithms. This system is implemented as a PyQt5 desktop application, providing a user-friendly interface for real-time data display and monitoring. The Digital Twin communicates with a script that controls the printer by sending g-code commands line by line, reading temperature data from the thermistors embedded in the printer, and interfacing with the 3D scanner to receive scans of each layer.

The temperature data, collected from the printer, is displayed in the Digital Twin interface almost instantaneously. After each layer is printed, the printing process pauses, and the print head moves to a secure position, allowing the 3D scanner to capture a snapshot of the printed surface. The system then extracts the average surface roughness from the point cloud data generated by the scanner. An optimization process follows, adjusting the printing temperature and speed to achieve the best surface quality for the next layer. This entire process, from scanning to optimization, takes approximately 35 seconds, after which the system waits for the printing temperature to reach its target value as determined by the optimization algorithm.

Although each scan–predict–optimize cycle introduces a modest 35-second pause per layer, this delay yields substantial benefits in surface integrity, even when printing parts with hundreds of layers. By correcting deviations at each layer boundary, the system prevents roughness buildup, ensuring that minor surface defects do not propagate into larger structural inconsistencies. The result is a significantly smoother finish, minimizing or even eliminating post-processing, which is highly advantageous for applications requiring high precision or critical surface quality.

Looking ahead, future work will explore alternative scanning configurations and accelerated data-processing techniques to further reduce this layer-by-layer pause. In particular, integrating lightweight LiDAR sensors mounted directly on the print head could enable simultaneous scanning during deposition, eliminating the need to pause after each layer. This advancement would support localized, in-situ adjustments to parameters such as printing speed and material flow in response to surface deviations or complex geometries, improving both surface quality and process efficiency, especially for high-layer-count or large-scale builds.

The demonstrated effectiveness of these real-time algorithms underscores the potential of adaptive manufacturing strategies, where printing parameters are dynamically refined using immediate feedback. Such strategies pave the way for unprecedented precision in producing complex geometries, redefining quality standards in Additive Manufacturing.

This work not only deepens the understanding of real-time optimization in FDM 3D printing but also establishes a new benchmark for the field. By uniting predictive machine learning models with fast, layer-level data acquisition, it opens pathways to more intelligent, autonomous AM systems capable of higher efficiency and superior part quality.

Future investigations will expand the optimization framework to include a broader set of process parameters and materials. Integrating these insights into adaptive slicing strategies and topology optimization techniques, particularly for multi-material printing, will help tailor layer thickness and part design to specific material behaviors, further enhancing performance.

Additionally, upcoming studies will examine how surface roughness trajectories relate to functional properties such as mechanical strength, dimensional accuracy, and internal defects. Finally, implementing multi-objective optimization, incorporating both quality and production time, will increase the practicality and industrial relevance of the proposed approach.

6.6 Author Contributions

Conceptualization, A.Z.; Formal analysis, M.H. and A.Z.; Funding acquisition, M.H. and S.K.; Investigation, A.Z.; Methodology A.Z.; Software, A.Z.; Supervision, M.H. and S.K.;

Writing—original draft, A.Z.; Writing—review and editing, M.H and S.K. All authors have read and agreed to the published version of the manuscript.

6.7 Funding

Funding: The authors acknowledge the funding provided by the Natural Sciences and Engineering Research Council (NSERC) of Canada (grant number: CRSNG–RGPIN-2021-02846).

6.8 Data Availability Statement

Data available under request.

6.9 Conflicts of Interest

The authors certify that they have no affiliations with or involvement in any organization or entity with any financial interest or non-financial interest in the subject matter or materials discussed in this manuscript.

6.10 References

[1] Wang S, Ma Y, Deng Z, Zhang S, Cai J. Effects of fused deposition modeling process parameters on tensile, dynamic mechanical properties of 3D printed polylactic acid materials. Polymer testing. 2020;86:106483.

[2] Cailleaux S, Sanchez-Ballester NM, Gueche YA, Bataille B, Soulairol I. Fused Deposition Modeling (FDM), the new asset for the production of tailored medicines. Journal of controlled release. 2021;330:821-41.

[3] Ismail KI, Yap TC, Ahmed R. 3D-printed fiber-reinforced polymer composites by fused deposition modelling (FDM): fiber length and fiber implementation techniques. Polymers. 2022;14:4659.

[4] Megdich A, Habibi M, Laperrière L, Li Z, Abdin Y. Enhanced piezoelectric performance of PVDF/MWCNTs energy harvester through a 3D-printed multimodal auxetic structure for smart security systems. Materials Today Sustainability. 2024;27:100847.

[5] Melocchi A, Uboldi M, Cerea M, Foppoli A, Maroni A, Moutaharrik S, et al. A graphical review on the escalation of fused deposition modeling (FDM) 3D printing in the pharmaceutical field. Journal of Pharmaceutical Sciences. 2020;109:2943-57.

[6] Acierno D, Patti A. Fused deposition modelling (FDM) of thermoplastic-based filaments: process and rheological properties—an overview. Materials. 2023;16:7664.

[7] Kumar S, Kolekar T, Patil S, Bongale A, Kotecha K, Zaguia A, Prakash C. A low-cost multi-sensor data acquisition system for fault detection in fused deposition modelling. Sensors. 2022;22:517.

[8] Karima B, Habibi M, Laperrière L. 4D printing of fiber-reinforced auxetic structures: the building blocks: a review. Smart Material Structures. 2024;33:063001.
[9] Quero RF, da Silveira GD, da Silva JAF, de Jesus DP. Understanding and improving FDM 3D printing to fabricate high-resolution and optically transparent microfluidic devices. Lab on a Chip. 2021;21:3715-29.
[10] Camposeco-Negrete C. Optimization of printing parameters in fused deposition modeling for improving part quality and process sustainability. The International Journal of Advanced Manufacturing Technology. 2020;108:2131-47.
[11] Abdelhamid Z, Mohamed H, Kelouwani S. The use of machine learning in process–structure–property modeling for material extrusion additive manufacturing: a state-of-the-art review. Journal of the Brazilian Society of Mechanical Sciences and Engineering. 2024;46:70.
[12] Bouguermouh K, Habibi M, Laperrière L, Li Z, Abdin Y. 4D-printed PLA-PETG polymer blends: comprehensive analysis of thermal, mechanical, and shape memory performances. Journal of Materials Science. 2024:1-18.
[13] Vyavahare S, Kumar S, Panghal D. Experimental study of surface roughness, dimensional accuracy and time of fabrication of parts produced by fused deposition modelling. Rapid Prototyping Journal. 2020;26:1535-54.
[14] Nugroho WT, Dong Y, Pramanik A. Dimensional accuracy and surface finish of 3D printed polyurethane (PU) dog-bone samples optimally manufactured by fused deposition modelling (FDM). Rapid Prototyping Journal. 2022;28:1779-95.
[15] Ferretti P, Leon-Cardenas C, Santi GM, Sali M, Ciotti E, Frizziero L, et al. Relationship between FDM 3D printing parameters study: parameter optimization for lower defects. Polymers. 2021;13:2190.
[16] Tamir TS, Xiong G, Fang Q, Dong X, Shen Z, Wang F-Y. A feedback-based print quality improving strategy for FDM 3D printing: an optimal design approach. The International Journal of Advanced Manufacturing Technology. 2022;120:2777-91.
[17] Durão LFC, Barkoczy R, Zancul E, Lee Ho L, Bonnard R. Optimizing additive manufacturing parameters for the fused deposition modeling technology using a design of experiments. Progress in Additive Manufacturing. 2019;4:291-313.
[18] Dey A, Yodo N. A systematic survey of FDM process parameter optimization and their influence on part characteristics. Journal of Manufacturing and Materials Processing. 2019;3:64.

[19] Jayanth N, Senthil P, Prakash C. Effect of chemical treatment on tensile strength and surface roughness of 3D-printed ABS using the FDM process. Virtual and Physical Prototyping. 2018;13:155-63.

[20] Singh D, Singh R, Boparai KS. Development and surface improvement of FDM pattern based investment casting of biomedical implants: A state of art review. Journal of Manufacturing Processes. 2018;31:80-95.

[21] Taufik M, Jain PK. Part surface quality improvement studies in fused deposition modelling process: a review. Australian Journal of Mechanical Engineering. 2022;20:527-51.

[22] Saad MS, Nor AM, Baharudin ME, Zakaria MZ, Aiman A. Optimization of surface roughness in FDM 3D printer using response surface methodology, particle swarm optimization, and symbiotic organism search algorithms. The International Journal of Advanced Manufacturing Technology. 2019;105:5121-37.

[23] Tura AD, Mamo HB, Gemechu WF. Mathematical modeling and parametric optimization of surface roughness for evaluating the effects of fused deposition modeling process parameters on ABS material. International Journal of Advanced Engineering Research and Science. 2021;8:049-57.

[24] Pawar S, Dolas D. Effect of process parameters on flexural strength and surface roughness in fused deposition modeling of PC-ABS material. Journal of Micromanufacturing. 2022;5:164-70.

[25] Patil P, Singh D, Raykar SJ, Bhamu J. Multi-objective optimization of process parameters of Fused Deposition Modeling (FDM) for printing Polylactic Acid (PLA) polymer components. Materials Today: Proceedings. 2021;45:4880-5.

[26] Colpani A, Fiorentino A, Ceretti E. Characterization of chemical surface finishing with cold acetone vapours on ABS parts fabricated by FDM. Production Engineering. 2019;13:437-47.

[27] Kozior T, Mamun A, Trabelsi M, Sabantina L, Ehrmann A. Quality of the Surface Texture and Mechanical Properties of FDM Printed Samples after Thermal and Chemical Treatment. Journal of Mechanical Engineering/Strojniški Vestnik. 2020;66.

[28] Akhouri D, Banerjee D, Mishra SB. A review report on the plating process of fused deposition modelling (FDM) built parts. Materials Today: Proceedings. 2020;26:2140-2.

[29] Li Z, Zhang Z, Shi J, Wu D. Prediction of surface roughness in extrusion-based additive manufacturing with machine learning. Robotics and Computer-Integrated Manufacturing. 2019;57:488-95.

[30] Chen L, Zhang X. Modification the surface quality and mechanical properties by laser polishing of Al/PLA part manufactured by fused deposition modeling. Applied Surface Science. 2019;492:765-75.

[31] Nadeem H, Ghazali N, Nabeel M, Ahsan M, Khurram A. Experimental assessment of surface roughness of fused deposition modelling parts and method of improvement. Journal of Thermoplastic Composite Materials. 2024;37:1187-201.

[32] Radhwan H, Shayfull Z, Farizuan M, Effendi M, Irfan A. Optimization parameter effects on the quality surface finish of the three-dimensional printing (3D-printing) fused deposition modeling (FDM) using RSM. AIP conference proceedings: AIP Publishing; 2019.

[33] Heshmat M, Adel M. Investigating the effect of hot air polishing parameters on surface roughness of fused deposition modeling PLA products: ANOVA and regression analysis. Progress in Additive Manufacturing. 2021;6:679-87.

[34] Kothandaraman L, Balasubramanian NK. Optimization of the Printing Parameters to Improve the Surface Roughness in Fused Deposition Modeling. E3S Web of Conferences: EDP Sciences; 2023. p. 03003.

[35] Nagendra J, Srinath M, Sujeeth S, Naresh K, Prasad MG. Optimization of process parameters and evaluation of surface roughness for 3D printed nylon-aramid composite. Materials Today: Proceedings. 2021;44:674-82.

[36] Tura A, Mamo H, Jelila Y, Lemu HG. Experimental investigation and ANN prediction for part quality improvement of fused deposition modeling parts. IOP Conference Series: Materials Science and Engineering: IOP Publishing; 2021. p. 012031.

[37] Henson CM, Decker NI, Huang Q. A Digital Twin strategy for major failure detection in fused deposition modeling processes. Procedia Manufacturing. 2021;53:359-67.

[38] Jyeniskhan N, Keutayeva A, Kazbek G, Ali MH, Shehab E. Integrating machine learning model and Digital Twin system for additive manufacturing. IEEE Access. 2023.

[39] Moretti M, Rossi A, Senin N. In-process simulation of the extrusion to support optimisation and real-time monitoring in fused filament fabrication. Additive Manufacturing. 2021;38:101817.

[40] Rachmawati SM, Putra MAP, Lee JM, Kim DS. Digital twin-enabled 3D printer fault detection for smart additive manufacturing. Engineering Applications of Artificial Intelligence. 2023;124:106430.

[41] Butt J, Mohaghegh V. Combining Digital Twin and machine learning for the fused filament fabrication process. Metals. 2022;13:24.

[42] Mourtzis D, Togias T, Angelopoulos J, Stavropoulos P. A Digital Twin architecture for monitoring and optimization of fused deposition modeling processes. Procedia CIRP. 2021;103:97-102.

[43] Ochoa S, Ferrándiz S, Garzón L, Cobos C. Digital Twin of Fused Filament Fabrication Prints for Finite Element Analysis via G-Code Reverse Engineering. 3D printing and additive manufacturing. 2024.

[44] Corradini F, Silvestri M. Design and testing of a Digital Twin for monitoring and quality assessment of material extrusion process. Additive Manufacturing. 2022;51:102633.

[45] Balta EC, Tilbury DM, Barton K. A Digital Twin framework for performance monitoring and anomaly detection in fused deposition modeling. 2019 IEEE 15th International Conference on Automation Science and Engineering (CASE): IEEE; 2019. p. 823-9.

[46] Guo L, Cheng Y, Zhang Y, Liu Y, Wan C, Liang J. Development of cloud-edge collaborative Digital Twin system for FDM additive manufacturing. 2021 IEEE 19th international conference on industrial informatics (INDIN): IEEE; 2021. p. 1-6.

[47] (ASME) ASoME. Surface Texture (Surface Roughness, Waviness, and Lay). New York, NY2019.

[48] Dhadwal MK, Jung SN, Kim CJ. Advanced particle swarm assisted genetic algorithm for constrained optimization problems. Computational Optimization and Applications. 2014;58:781-806.

[49] Feng R, Jiang J, Sun Z, Thakur A, Wei X. A hybrid of genetic algorithm and particle swarm optimization for reducing material waste in extrusion-basedadditive manufacturing. Rapid Prototyping Journal. 2021;27:1872-85.

[50] Gong Y-J, Li J-J, Zhou Y, Li Y, Chung HS-H, Shi Y-H, Zhang J. Genetic learning particle swarm optimization. IEEE transactions on cybernetics. 2015;46:2277-90.

[51] Saad MS, Mohd Nor A, Zakaria MZ, Baharudin ME, Yusoff WS. Modelling and evolutionary computation optimization on FDM process for flexural strength using integrated approach RSM and PSO. Progress in Additive Manufacturing. 2021;6:143-54.

[52] Qin J, Liu Y, Grosvenor R, Lacan F, Jiang Z. Deep learning-driven particle swarm optimisation for additive manufacturing energy optimisation. Journal of Cleaner Production. 2020;245:118702.

[53] Ziadia A, Habibi M, Kelouwani S. Machine Learning Study of the Effect of Process Parameters on Tensile Strength of FFF PLA and PLA-CF. Eng. 2023;4:2741-63.

[54] Leirmo TS, Martinsen K. Evolutionary algorithms in additive manufacturing systems: Discussion of future prospects. Procedia CIRP. 2019;81:671-6.

[55] Megdich A, Habibi M, Laperrière L. Modeling and optimization of piezoelectric and dielectric properties of poled PVDF/BT nanocomposites. Polymer Bulletin. 2024:1-21.
[56] Megdich A, Habibi M, Laperrière L, Li Z, Abdin Y. Advanced 3D-printed PVDF/BT piezoelectric energy harvester with a bio-inspired 3D structure for a self-powered smart mouse. Nano Energy. 2024:109876.
[57] Clarke J, McLay L, McLeskey Jr JT. Comparison of genetic algorithm to particle swarm for constrained simulation-based optimization of a geothermal power plant. Advanced Engineering Informatics. 2014;28:81-90.
[58] Wang P, Zou B, Ding S. Modeling of surface roughness based on heat transfer considering diffusion among deposition filaments for FDM 3D printing heat-resistant resin. Applied Thermal Engineering. 2019;161:114064.
[59] Sanatgar RH, Campagne C, Nierstrasz V. Investigation of the adhesion properties of direct 3D printing of polymers and nanocomposites on textiles: Effect of FDM printing process parameters. Applied surface science. 2017;403:551-63.
[60] Thumsorn S, Prasong W, Kurose T, Ishigami A, Kobayashi Y, Ito H. Rheological behavior and dynamic mechanical properties for interpretation of layer adhesion in FDM 3D printing. Polymers. 2022;14:2721.
[61] Thumsorn S, Prasong W, Ishigami A, Kurose T, Kobayashi Y, Ito H. Influence of Ambient Temperature and Crystalline Structure on Fracture Toughness and Production of Thermoplastic by Enclosure FDM 3D Printer. Journal of Manufacturing and Materials Processing. 2023;7:44.
[62] Sabyrov N, Abilgaziyev A, Ali MH. Enhancing interlayer bonding strength of FDM 3D printing technology by diode laser-assisted system. The International Journal of Advanced Manufacturing Technology. 2020;108:603-11.
[63] Bengfort P, Stracke D, Künne B. Establishment of a rotary print head to effect residual stresses and interlayer bonding in an FLM-process. Journal of Manufacturing and Materials Processing. 2021;5:82.
[64] Wang Z, Liu P, Xiao Y, Cui X, Hu Z, Chen L. A data-driven approach for process optimization of metallic additive manufacturing under uncertainty. Journal of Manufacturing Science and Engineering. 2019;141:081004.
[65] Bayat S, Mohseni M, Behnami D, Abolmaesumi P. Real-time prediction of temperature distribution in additive manufacturing processes based on machine learning. ASME International Mechanical Engineering Congress and Exposition: American Society of Mechanical Engineers; 2020. p. V02ATA031.

[66] Liu L, Jo E, Vaidya U, Kim S, Ju F. An Integrated Offline and Online Optimization Framework for Large Scale Additive Manufacturing. 2023 IEEE 19th International Conference on Automation Science and Engineering (CASE): IEEE; 2023. p. 1-6.

[67] Dharmadhikari S, Menon N, Basak A. A reinforcement learning approach for process parameter optimization in additive manufacturing. Additive Manufacturing. 2023;71:103556.

[68] Pandit A, Sekhar R, Shah P. Simulation based process optimization for additive manufacturing. International Journal of Innovative Technology and Exploring Engineering (IJITEE). 2019;8:3405-10.

[69] Pan Y, Yu X, Liu Y. Improved Particle Swarm Localization Algorithm Based on Evolutionary Mechanism. Journal of Physics: Conference Series: IOP Publishing; 2022. p. 012034.

Chapitre 7: Amélioration de la qualité d'impression et des propriétés mécaniques par optimisation en temps réel et tranchage adaptatif en impression 3D FDM

Optimizing Printing Quality and Mechanical Properties Through Real-Time Optimization and Adaptive Slicing in FDM 3D Printing. Abdelhamid ZIADIA, Mohamed HABIBI, and Sousso KELOUWANI.

Dans la continuité du chapitre précédent, qui a montré qu'une boucle capter comprendre agir pouvait réduire la rugosité de surface par des ajustements couche par couche de la température et de la vitesse, cette article étend la boucle fermée vers un pilotage multicritère. L'objectif est d'améliorer simultanément la qualité de surface, la précision dimensionnelle et les propriétés mécaniques en FDM. Pour y parvenir, la chaîne capter comprendre agir est enrichie par un tranchage adaptatif qui ajuste l'épaisseur de couche dans des bornes imprimables, par des prédicteurs spatio-temporels de type CNN-LSTM entraînés sur des données couche par couche, et par une optimisation multi-objectifs NSGA-III qui choisit à chaque couche le meilleur compromis puis le traduit immédiatement en G-code. Les règles univariées deviennent ainsi des consignes coordonnées agissant sur température buse et lit, débit et hauteur de couche.
Le dispositif expérimental repose sur une imprimante Prusa i3 MK3S plus avec buse de 0,4 millimètre, filament PLA et un capteur 3D Gocator 3210 placé au-dessus du plateau pour acquérir la topographie de surface après chaque couche. Un jumeau logiciel orchestre la séquence pause, acquisition, nettoyage des nuages, calcul des indicateurs et mise à jour des consignes, puis envoie un G-code modifié pour la couche suivante. La boucle comporte une optimisation multi-objectifs NSGA-III, alimentée par des prédicteurs rapides CNN-LSTM, qui sélectionne à chaque couche un point de Pareto et fournit l'ensemble des consignes coordonnées température buse et lit, débit, et hauteur de couche. Le tranchage adaptatif applique la hauteur de couche décidée par NSGA-III, dans des bornes imprimables et sous contrainte de conserver la hauteur finale, au moyen d'une vérification progressive et d'un rattrapage cumulé.
Le plan d'expériences suit un Box–Behnken à quatre facteurs et trois niveaux couvrant température d'extrusion, température de lit, épaisseur de couche et débit. Les acquisitions couche par couche alimentent trois volets. La rugosité Ra est mesurée sur la surface scannée

après nettoyage statistique des nuages de points. La précision dimensionnelle est quantifiée par recalage ICP entre la surface scannée et la surface de référence issue de la CAO. Les propriétés mécaniques sont mesurées sur éprouvettes ASTM D638 Type IV imprimées selon le plan d'experience.

Les performances des modèles CNN-LSTM sont élevées. Pour Ra, les coefficients de détermination atteignent environ 93,73 % en entraînement et 88,35 % en test. Pour les propriétés mécaniques, la généralisation est quasi parfaite avec environ 99,94 % en entraînement et 99,84 % en test. L'analyse des corrélations met en évidence un point central. Le débit d'extrusion est le facteur le plus influent sur les propriétés étudiées. L'épaisseur de couche présente une corrélation négative avec la résistance à la traction et surtout avec le module d'Young, ce qui indique que des couches plus fines favorisent de meilleures propriétés mécaniques, tandis que son effet sur Ra et la déviation géométrique demeure plus modéré. Les températures de buse et de lit ont un effet relativement faible au regard des autres paramètres. Du côté des relations entre propriétés, on observe une corrélation positive entre Ra et la résistance ultime, ainsi qu'une forte interdépendance entre les propriétés mécaniques. Surtout, la corrélation est très élevée entre Ra et la précision dimensionnelle, ce qui justifie de concentrer la prédiction et l'optimisation sur Ra et sur les propriétés mécaniques, l'amélioration de la rugosité contribuant fortement à une meilleure fidélité géométrique.

NSGA-III explore en continu des bornes imprimables pour minimiser Ra tout en maximisant résistance et module. Les fronts de Pareto offrent des compromis équilibrés immédiatement traduits en G-code, y compris la mise à jour de l'épaisseur de couche avec conservation de la hauteur finale. Trois effets concrets se dégagent des trajectoires optimales. Un raffinement des couches vers les zones critiques qui améliore de concert surface, précision et rigidité. Une gestion thermique qui élève la température de lit au démarrage pour l'adhésion, la stabilise ensuite puis la rehausse en fin de pièce pour consolider la fusion inter-couches. Une modulation du débit autour de 98 à 105 % qui renforce l'adhésion là où nécessaire tout en préservant la définition géométrique des parois.

Les résultats quantifiés valident l'apport simultané sur les trois critères. La rugosité moyenne passe d'environ 0,0425 mm à environ 0,0295 mm, soit une réduction d'environ 30,59% par rapport aux réglages standards PLA. La déviation dimensionnelle moyenne diminue d'environ 0,06326 mm à environ 0,05989 mm, soit un gain d'environ 5,33 % alors même que la précision n'était pas explicitement optimisée. La résistance ultime augmente d'environ 9,12 % et le module d'Young progresse en moyenne d'environ 3,25 %, ce qui montre qu'on peut améliorer les propriétés mécaniques tout en lissant la surface et en gagnant en précision dimensionnelle.

L’articulation avec les chapitres précédents est nette. Par rapport à la revue jumeaux numériques et observation de surface, ce travail opérationnalise une boucle multicritère avec tranchage adaptatif et compromis Pareto. Par rapport à la boucle fermée centrée rugosité, il étend la portée en ajoutant la mécanique et la précision dimensionnelle et en faisant du tranchage adaptatif un levier majeur, piloté par des prédicteurs spatio-temporels et une optimisation multi-objectifs capable de choisir le meilleur compromis à chaque couche. Les limites tiennent au temps de décision et aux transitions thermiques ainsi qu’à la dépendance à une acquisition fiable et rapide. Les perspectives portent sur l’accélération des calculs en edge ou sur GPU, l’embarquement de capteurs pour réduire les pauses, l’extension à d’autres matériaux et objectifs combinant qualité, temps et énergie, et la fusion avec des observables thermiques pour tendre vers un jumeau numérique plus autonome.

Optimizing Printing Quality and Mechanical Properties Through Real-Time Optimization and Adaptive Slicing in FDM 3D Printing

Abdelhamid Ziadia[1], Mohamed Habibi[1,*]& Sousso Kelouwani[1]

1 Affiliation 1; University of Quebec in Trois-Rivieres, (Department of Mechanical Engineering), Trois-Rivieres, (Quebec), Canada

*Correspondence: erima@uqtr.ca

7.1 Abstract

This study presents a digital twin for Fused Deposition Modeling (FDM) that embeds an advanced real-time optimization framework to enhance layer-specific surface quality and mechanical performance. By integrating in-situ 3D scanning, machine learning, and multi-objective optimization, the method adjusts printing parameters layer by layer to address surface roughness, dimensional accuracy, and strength. The digital twin couples a Convolutional Neural Network–Long Short-Term Memory (CNN–LSTM) model with a Non-dominated Sorting Genetic Algorithm III (NSGA-III) optimizer that selects the best trade-offs in real-time. Experimental results showed a 30.59 % reduction in surface roughness, a 9.12 % increase in ultimate tensile strength, a 5.3% improvement in dimensional accuracy, and a 3.25% enhancement in Young's modulus compared to parts printed using standard parameters. The CNN-LSTM model demonstrated high predictive accuracy, achieving R^2 values of 93.73% for training and 88.35% for testing in surface roughness prediction, as well as 99.94% for training and 99.84% for testing in mechanical property prediction. These findings support the broader adoption of FDM in precision-demanding industries by providing a robust framework for real-time quality control and process optimisation.

Keywords: Additive manufacturing, Fused Deposition Modeling, Digital twin, Machine Learning, Real-time optimization, Adaptive slicing

7.2 Introduction

Fused deposition modeling (FDM) is among the most prevalent additive manufacturing techniques due to its simplicity, low cost, and ability to fabricate complex geometries rapidly. In this process, a thermoplastic filament is melted and extruded through a heated nozzle, depositing successive layers that solidify to form a three-dimensional part [1-3][4-6][7, 8].

The technique's appeal lies in its versatility and accessibility. FDM supports numerous polymers, from commodity materials such as PLA and ABS to engineering composites, allowing its adoption across sectors ranging from consumer products to functional mechanical

components [9-13][14][15-19]. Compared with other additive processes, FDM systems remain relatively inexpensive and easy to operate, which has accelerated their use in both research and industry [20-22].

Beyond rapid prototyping, FDM is increasingly employed to produce functional and end-use components exhibiting adequate mechanical strength [23-25]. Its versatility has driven widespread adoption in the automotive, aerospace, and biomedical sectors for applications such as customized tools, fixtures, and patient-specific implants [4, 26, 27]. The capability to manufacture parts on demand and at lower cost than conventional processes further strengthens its industrial relevance [28-30].

Nevertheless, several limitations constrain its use in precision applications. The layer-by-layer deposition process can generate visible stair-stepping on curved surfaces, dimensional deviations from warping or shrinkage, and imperfect interlayer adhesion. Among these, surface roughness and mechanical anisotropy remain the most critical factors affecting quality [31-33] [34, 35]. Such issues originate from incomplete fusion between adjacent extruded filaments, which produces interfacial voids and weak bonding across layers.

To address these limitations, many studies have focused on improving the surface finish and mechanical properties of FDM parts through process optimization. Surface quality can be enhanced at different stages of manufacturing, before printing, during deposition, or through post-processing treatments. In the pre-printing phase, the adjustment of key parameters such as layer thickness, infill density, extrusion temperature, and printing speed plays a decisive role in determining the final surface texture and part integrity [36-42]. These parameters are usually kept constant once the print starts, even though they strongly affect surface quality. Previous works using design of experiments (DOE) and statistical optimization have shown that inadequate parameter selection often leads to severe surface irregularities [38, 42-44]. When advanced optimization approaches such as response surface methodology (RSM) or genetic algorithms are applied, a significant reduction in surface roughness can be achieved [42, 43, 45, 46]. Post-processing remains one of the most efficient approaches for improving the surface quality of FDM parts, especially when high dimensional accuracy is required. Techniques such as acetone vapor exposure and thermal reflow have been shown to lower surface roughness to around 0.3 μm while also enhancing the visual and functional quality of printed components [47, 48].

The optimization of mechanical properties follows a similarly structured strategy. In the prefabrication phase, material selection is crucial in determining the part's strength and durability. Composite filaments, such as PLA reinforced with carbon fiber, graphene, or short

glass fibers, have been extensively explored for their enhanced tensile and flexural performance [26, 35, 41, 49-54]. Moreover, adjustments of process parameters such as layer height, raster angle, and nozzle temperature directly affect interlayer bonding and the overall mechanical strength of printed parts [41, 49-54]. Post-fabrication techniques, such as annealing and hot-air jet polishing, are also widely applied to address anisotropic weaknesses and enhance interlayer adhesion. These treatments significantly enhance tensile strength and reduce brittleness, thereby extending the suitability of FDM parts to demanding applications in the aerospace and medical sectors [39, 55]. Additionally, chemical smoothing can be employed to simultaneously improve mechanical integrity and surface quality, offering a holistic enhancement of part performance [48]. In contrast, during fabrication, the ability to optimize surface and mechanical properties remains inherently limited by the sequential, layer-by-layer deposition nature of FDM. Although machine learning-based error detection systems have shown promise for in-process monitoring, their capability to actively improve print quality in real time remains constrained [45, 56-60].

Despite continuous progress in improving surface finish and mechanical strength in FDM, several challenges still limit its deployment in precision manufacturing. Real-time optimization during printing remains largely unexplored, current approaches such as closed-loop feedback control and machine-learning-based defect detection can monitor deviations but rarely apply effective corrections on the fly [45, 56-60]. The dependence on predefined, static parameters reduces adaptability to unexpected process variations, emphasizing the need for adaptive frameworks capable of dynamic adjustment.

Moreover, optimization strategies often treat surface quality and mechanical strength as isolated targets, neglecting their interdependence [49, 61-64]. For instance, while post-fabrication techniques such as annealing and chemical smoothing can enhance surface finish, they may also adversely affect mechanical performance due to alterations in material properties [65, 66]. This trade-off highlights the need for holistic approaches that jointly optimize both aspects without compromising either. In addition, most post-processing techniques, such as vapor smoothing and annealing, remain labor-intensive and lack scalability for industrial-scale production [66, 67]. Their dependence on manual intervention poses practical constraints for high-throughput manufacturing. The development of automated, integrated solutions for enhancing both surface quality and mechanical integrity represents a promising direction for extending the industrial applicability of FDM.

One promising approach to overcoming these limitations is the implementation of adaptive slicing techniques. In FDM 3D printing, adaptive slicing refers to the dynamic adjustment of

layer thickness according to the model's geometry. Several studies have investigated this method to enhance part quality while preserving printing efficiency.

For example, one study introduced adaptive layering algorithms that calculate layer thickness by minimizing volume error, aiming to improve surface accuracy and forming efficiency, particularly for geometrically complex parts [68]. Another work revisited adaptive slicing strategies by integrating slope and curvature analysis into the optimization process, focusing on reducing printing time while controlling discretization error. The approach was validated using slicing software such as Ultimaker Cura and 3D scanning tools [69]. In addition, real-time adaptive slicing systems have been proposed, incorporating sensor-based feedback to adjust layer height during the printing process. These systems demonstrated marked improvements in both surface finish and geometric precision, and were evaluated using tools such as coordinate measuring machines [70]. A comprehensive review of FDM further highlighted the benefits of adaptive slicing in adjusting slice thickness according to local geometric features, leading to reductions in print time while maintaining part integrity and quality [71]. Taken together, these advances underscore the transformative potential of adaptive slicing in addressing FDM's inherent limitations, offering a viable path toward broader industrial adoption in precision-driven domains.

In this context, the present study builds upon our previous digital-twin framework for real-time surface optimization [86] and addresses key limitations of FDM 3D printing by introducing a new adaptive and multi-objective approach. A 3D laser scanner is employed to analyze each printed layer, enabling dynamic adjustment of process parameters through adaptive slicing and NSGA-III-based optimization, with the objectives of minimizing surface roughness, maximizing mechanical strength, and preserving dimensional accuracy. The methodology is supported by a comprehensive correlation analysis to quantify the relationships among process parameters, surface roughness, mechanical strength, and dimensional accuracy within a Design of Experiments (DOE) framework. Standard ASTM D638 Type IV specimens are used to validate the influence of the proposed strategy on both surface quality and mechanical performance, aiming to extend the industrial applicability of FDM for engineering components.

To implement this strategy, a digital twin was developed for FDM processes, integrating laser-based 3D scanning, a CNN–LSTM predictive model, adaptive slicing, and NSGA-III multi-objective optimization. The architecture leverages the spatial feature extraction capabilities of Convolutional Neural Networks (CNN) and the temporal sequence learning strengths of Long Short-Term Memory (LSTM) networks, enabling accurate prediction of layer-specific surface roughness and mechanical behavior [72, 73]. This integration allows real-time decision-making

for parameter tuning, contributing to a closed-loop control system for quality-aware additive manufacturing.

To optimize the printing parameters, this study employs the NSGA-III multi-objective optimization algorithm, which balances competing objectives such as surface quality, mechanical strength, and dimensional accuracy [74, 75]. The optimization outcomes are represented using Pareto fronts, allowing the visualisation of trade-offs and the selection of the most suitable compromise for each layer.

The proposed digital-twin framework establishes a continuous link between the physical printer and its virtual counterpart, enabling real-time monitoring and adaptive control to improve part quality. This capability broadens the applicability of FDM to high-precision fields.

The structure of the paper is as follows:

- Section 2 describes the methodology, including the experimental setup, the design of experiments, data acquisition procedures, and the integration of machine learning, multi-objective optimization, adaptive slicing, and digital twin algorithms.
- Section 3 presents the results of the developed framework, analyzes the correlations between process parameters and part properties, and discusses experimental validations.
- Section 4 concludes the paper by summarizing key contributions and outlining potential directions for future research in additive manufacturing.

7.3 Methodology

7.3.1 Experimental setup and Real-Time Scanning Configuration

The experimental platform combined a Prusa i3 MK3S+ desktop FDM printer and a Gocator 3210 snapshot 3D scanner (LMI Technologies), forming the basis of the real-time digital-twin system previously introduced by our group [86]. In this study, the setup was upgraded with adaptive-slicing and multi-objective optimization modules to enable layer-wise adjustment of printing parameters.

To enable layer-by-layer quality assessment, a Gocator 3210 snapshot 3D sensor (LMI Technologies) was installed above the build plate to acquire a height map immediately after each deposition pass. The device covers a 71 × 98 mm to 100 × 154 mm field of view depending on working distance, offers a 110 mm depth range, and achieves 4.7 µm Z-repeatability, consistent with VDI/VDE 2634-2 accuracy class 0.035 mm. The printer was scripted to pause at the end of every layer and retract the nozzle, ensuring an unobstructed scan of the freshly printed surface.

Data flow and motion were managed by a central control computer that communicated with the printer via serial link and with the scanner over Ethernet. A custom Python program synchronized the print–scan sequence, ingested the sensor point clouds, performed surface processing, and issued updated G-code to adjust process settings in real time.

7.3.2 Design of the Experiment

The primary objective of this experimental design is to systematically investigate the influence of key printing parameters on the surface roughness, dimensional accuracy, and mechanical properties of FDM-printed parts. A Box-Behnken Design (BBD) was selected to ensure a comprehensive and efficient evaluation of these effects, enabling the study of main effects and interactions while minimizing the number of experimental runs.

Four process parameters were selected based on prior studies and literature evidence regarding their significant impact on part quality [22, 41, 46, 51, 62, 76-85]:

- Printing temperature (°C): 200, 215, 230
- Bed temperature (°C): 50, 60, 70
- Layer thickness (mm): 0.15, 0.25, 0.35
- Flow rate (%): 95, 100, 105

These parameters are detailed in Table 32. All other printing settings were held constant at their recommended values to isolate the effects of the selected variables on the responses of interest.

Table 32. Selected process parameters and their levels.

Factor	Level 1	Level 2	Level 3
Printing Temperature (°C)	200	215	230
Layer Thickness (mm)	0.15	0.25	0.35
Bed Temperature (°C)	50	60	70
Flow Rate (%)	95	100	105

The Box–Behnken Design offers a robust statistical framework for exploring both linear and interaction effects among these variables. With four factors at three levels, the design required 27 experimental runs, offering a good trade-off between accuracy and efficiency when compared to a full factorial design. For each combination, dog-bone specimens based on the ASTM D638 Type IV standard were printed and later evaluated for surface roughness, dimensional accuracy, and tensile strength.

7.3.3 Data collection

Data collection plays a critical role in this study, enabling real-time monitoring of the FDM process and the acquisition of high-resolution data reflecting the interactions between printing parameters and resulting part quality. All specimens were fabricated based on the Box–

Behnken Design (BBD), and layer-wise scans were acquired using a Gocator snapshot 3D scanner. Mounted above the build platform, the scanner captures detailed point cloud data after the deposition of each layer, which is used to assess dimensional accuracy and detect deviations during printing.

7.3.3.1 Average Surface Roughness Measurement

Average surface roughness (Ra) was selected as the primary quantitative index for assessing the layer-wise surface quality of the printed specimens. It corresponds to the arithmetic mean of the absolute deviations from the mean surface height. As illustrated in Figure 56(a)(i), the surface roughness measurement process involved the following steps:

–*Layer-specific point cloud acquisition:* Following the deposition of each layer, the Gocator 3210 3D snapshot sensor captured the corresponding point cloud to generate a detailed topographical map of the layer (Figure 56(a)(iii)). Scanning parameters were optimized for precision, single exposure (20,000 µs), X/Y resolution of 0.05 mm, uniform point spacing, and diffuse material mode, to ensure a consistent and reliable surface profile.

–*Point cloud processing:* The acquired data were denoised using the Statistical Outlier Removal (SOR) filter in the Open3D Python library. This algorithm computes the mean distance between each point and its neighboring points and eliminates statistical outliers exceeding a set deviation threshold. In this work, 15 nearest neighbors and a standard deviation ratio of 1.0 were applied, producing a clean and accurate surface representation (Figure 56(a)(iv)).

– *Roughness calculation:* The filtered point cloud was analyzed to calculate Ra according tothe formula:

$$Ra = \frac{1}{N}\sum_{i=1}^{N} \left|h_i - \bar{h}\right| \text{ with } \bar{h} = \frac{1}{N}\sum_{i=1}^{N} h_i \quad (22)$$

where N is the number of points, h_i is the height of the i^{th} point, and $\bar{h}$ is the average height across all points.

This protocol was repeated for each layer and parameter combination in the design of experiments, yielding a dataset of 375 surface roughness measurements used for statistical and machine-learning analyses.

7.3.3.2 Dimensional Accuracy Data Collection

Dimensional accuracy was assessed by comparing the top surface of each printed part with the corresponding reference geometry from the CAD model (STL), using 3D point cloud data (Figure 56(a)(ii)). The evaluation was performed using a combination of Python libraries, including Open3D and NumPy, following the steps below:

–Point cloud and reference model loading: Preprocessed point cloud data from the 3D scan and the reference STL model were imported into the Open3D environment.

–Reference surface extraction and alignment: From the STL model, only the top surface at a specific Z-height was extracted to isolate the relevant geometry. The scanned point cloud and the reference surface were then aligned using the Iterative Closest Point (ICP) algorithm, which adjusts the position and orientation of the scanned data to best fit the reference.

–Deviation computation: After alignment, point-wise deviations between the scanned surface and the reference surface were calculated using nearest-neighbor matching. The mean deviation (D_{mean}) was then computed as:

$$D_{\text{mean}} = \frac{1}{N}\sum_{i=1}^{N} d_i \quad \text{with } d_i = \sqrt{(x_i - x_r)^2 + (y_i - y_r)^2 + (z_i - z_r)^2} \tag{23}$$

Where N is the total number of points, (x_i, y_i, z_i) and (x_r, y_r, z_r) are the coordinates of the scanned and reference points, respectively.

This procedure was repeated for each printed layer across all experimental runs, resulting in a total of 375 dimensional accuracy observations, corresponding to each layer and parameter combination in the DOE.

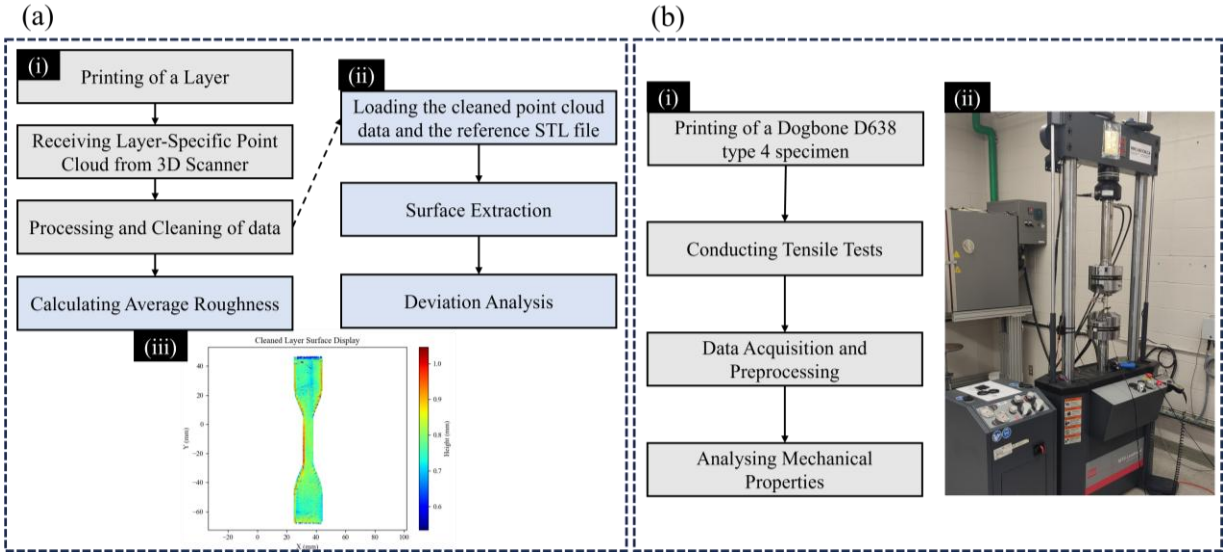

Figure 56. Data collection workflow: (a) Data collection for Surface roughness and Dimensional accuracy, (b) Data collection for Mechanical properties.

7.3.3.3 Mechanical Properties Collection

Tensile testing is a widely used method to assess the mechanical properties of polymer parts, including tensile strength, and elastic modulus. As shown in Figure 56(b)(i), in this study, mechanical performance was evaluated through the following procedure:

–Tensile testing procedure: Dog-bone specimens were fabricated in accordance with the ASTM D638 Type IV standard. Tensile tests were conducted using a universal testing machine

(MTS system (Figure 56(b)(ii))), with a crosshead speed set to 2 mm/min, a standard rate for evaluating 3D-printed polymer samples. The setup included calibrated specimen grips and a strain gauge to accurately measure elongation during testing.

–*Data acquisition and preprocessing:* The raw data collected during testing were exported and manually curated. Files were saved in CSV format to ensure compatibility with downstream analysis tools. Preprocessing included unit consistency checks, noise filtering, and alignment of force–displacement curves.

–*Mechanical property extraction:* The final step involved computing key mechanical properties, including ultimate tensile strength (UTS) and modulus of elasticity (E) for each specimen. These values were later correlated with process parameters and surface metrics to support the machine learning and optimization tasks.

7.3.4 Predictive algorithms

The predictive modeling component of this study employs a deep learning framework based on a CNN–LSTM architecture, designed to forecast layer-specific surface roughness and mechanical properties (Young's modulus and tensile strength). The network architectures follow the same overall structure, with slight variations in the output layer depending on the prediction target. This architecture was selected because CNNs are highly effective in extracting spatial correlations between process parameters, while LSTMs are well suited for capturing sequential dependencies across layers in FDM printing [86]. The combination allows the model to learn both local parameter interactions and temporal evolution of properties with relatively limited data.

–*CNN layers* are used for spatial feature extraction. Although surface roughness (Ra) is ultimately a scalar, the CNN captures complex interactions between process parameters, learning non-linear correlations that influence part quality.

–*MaxPooling layers* are introduced after each convolutional block to reduce the dimensionality of the feature maps, enhancing computational efficiency and reducing overfitting.

–*LSTM layers* are responsible for temporal modeling. Given that the quality of a printed layer is influenced by preceding layers, LSTM networks are well suited to capture such sequential dependencies over time.

–*Fully connected (dense) layers* merge spatial and temporal features to generate final predictions.

This architecture allows robust modeling of the relationships between input parameters and both surface and mechanical outputs. A schematic overview of the model is presented in Figure 57, and the network flow is summarized below:

i. Input Layer

- For mechanical property prediction, the input includes layer-wise printing parameters along with the measured surface roughness (Ra).
- For surface roughness prediction, the input includes printing parameters, the current layer index, and the sequence of surface roughness values from preceding layers to capture temporal dependencies.

This input layer consolidates relevant features required to predict the surface quality and mechanical behavior of the printed parts.

ii. Convolutional Layers (CNN)

- Multiple convolutional layers extract spatial correlations from the input data.
- Each convolution operation is followed by a ReLU (Rectified Linear Unit) activation to introduce non-linearity and allow the model to capture complex interactions.
- MaxPooling layers are applied to reduce the dimensionality of feature maps, enhancing computational efficiency and mitigating overfitting.

iii. Flattening Layer

- The output from the CNN is flattened into a one-dimensional feature vector to prepare the data for sequential modeling by the LSTM.
- This transformation bridges spatial analysis and temporal modeling within the architecture.

iv. LSTM Layers

- The flattened CNN features are passed to one or more Long Short-Term Memory (LSTM) layers.
- These layers capture dependencies between layers in the print sequence, modeling how variations in earlier layers affect subsequent outcomes.
- This is particularly important in FDM, where interlayer adhesion and geometry affect final properties.

v. Dense Layers

- The output of the LSTM layers is fed into one or more fully connected (dense) layers.
- These layers combine the learned spatial and temporal features to generate robust property predictions.

vi. Output Layer

- The architecture diverges based on the prediction objective:
- For mechanical properties, the output layer contains two nodes corresponding to Young's modulus and tensile strength.
- For surface roughness, a single output node predicts the average surface roughness (Ra).

This layer-by-layer configuration ensures that the model captures both the internal relationships among process parameters and the sequential influence of prior layers, making it well suited for real-time layer-wise prediction during FDM printing.

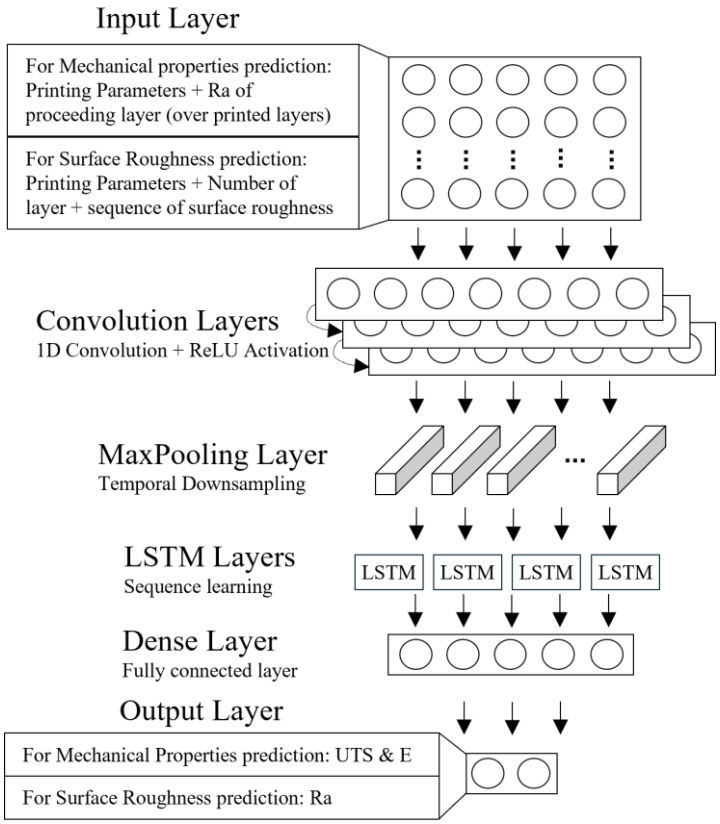

Figure 57. Architecture of the CNN-LSTM Model; Illustration of the deep learning architecture combining convolutional neural networks (CNN) and long short-term memory (LSTM) layers for the prediction of layer-specific surface roughness and mechanical properties in FDM 3D printing.

7.3.5 Multi-Objective Optimization

To ensure optimal print quality, this study employs the Non-dominated Sorting Genetic Algorithm III (NSGA-III), a state-of-the-art multi-objective optimization algorithm well-suited for handling multiple conflicting objectives. NSGA-III operates by identifying a set of Pareto-optimal solutions, i.e., solutions for which no other solution is better in all objectives.

The optimization process involves the following steps:

i. *Initial Population:* A population of candidate solutions is randomly initialized. Each individual represents a unique combination of printing parameters: printing temperature, bed temperature, layer thickness, and flow rate.

ii. *Fitness Evaluation:* Each candidate is evaluated using the predictive models described earlier, based on three performance objectives: average surface roughness, tensile strength, and Young's modulus.

iii. *Selection:* NSGA-III uses non-dominated sorting and crowding distance to retain a diverse and high-performing subset of solutions for the next generation.

iv. Crossover and Mutation

Genetic operators are applied to selected solutions:

- Crossover combines two parent solutions to generate offspring by mixing their parameters.
- Mutation introduces small random changes to explore new regions of the search space.

v. *Replacement:* A new generation of candidate solutions is formed by combining the offspring and current population and eliminating the least fit individuals. This iterative refinement guides the population toward more optimal trade-offs.

vi. *Convergence and Solution Selection:* Over successive generations, the algorithm converges to an optimized Pareto front that visualizes the trade-offs between objectives. A final solution is then selected based on its proximity to a target point, which represents the desired balance between surface quality and mechanical performance. The Euclidean distance is computed between each solution on the Pareto front and the target point, and the closest solution is chosen for implementation.

This strategy enables the layer-by-layer adjustment of process parameters in real-time, guided by predictive feedback from the digital twin. The use of NSGA-III not only optimizes surface and mechanical properties simultaneously but also provides users with a spectrum of non-dominated solutions, offering flexibility in selecting the most appropriate compromise for each application [74, 75].

7.3.6 Real-Time Adjustment and Execution Process

The real-time adjustment and execution strategy is central to this study, enabling adaptive control of the printing process on a layer-by-layer basis. The approach relies on a closed-loop digital twin system that integrates adaptive slicing, real-time sensing, predictive modeling, and multi-objective optimization to enhance print quality dynamically throughout fabrication.

i. Data Acquisition: At the beginning of each new layer, a 3D scan of the previously printed surface is captured using the Gocator sensor, providing detailed point cloud data. This data is preprocessed to remove noise and is then used to compute layer-specific indicators such as average surface roughness (Ra) and geometric deviations from the reference CAD model.

ii. Predictive Modeling and Optimization: The real-time optimization process relies on predictive models, specifically CNN–LSTM neural networks, to support decision-making by estimating key quality metrics of the current layer, such as average surface roughness, tensile strength, and Young's modulus. These predictions provide insight into the evolving state of the printed part and are essential for guiding the NSGA-III algorithm. Based on both the predicted quality indicators and real-time measurements, NSGA-III identifies the optimal set of printing parameters for the upcoming layer. The optimization aims to minimize surface roughness while maximizing mechanical performance, thereby achieving a balanced trade-off between competing objectives in real-time.

iii. Adaptive Slicing and Parameter Adjustment: The adaptive slicing method is based on the initial slicing of the specimen. The optimized layer thickness, generated by the NSGA-III algorithm, is used to update the extrusion value (E) in each line of the G-code. This value represents the amount of filament extruded, measured in millimeters.

To apply the new layer thickness, the algorithm extracts the original layer thickness ($LT_{original}$) and the corresponding original extrusion value ($E_{original}$) from the initial G-code. By reverse-engineering the slicing logic, the adjusted extrusion value can be calculated using the following equation:

$$E_{new} = E_{original} \times \frac{LT_{new}}{LT_{original}} \quad (3)$$

Where E_{new} is the updated extrusion amount based on the optimized layer thickness, E_{original} is the original extrusion amount from the slicer, LT_{new} is the optimized layer thickness from NSGA-III and $LT_{original}$ is the original sliced layer thickness.

Alongside extrusion, the nozzle height is dynamically adjusted after each layer. The total part height is fixed at the beginning of the print, and the remaining height is updated after each layer is completed. To ensure the printed part terminates exactly at the target height without violating minimum or maximum layer thickness constraints, a forward-checking strategy is applied in real time. At each layer, the algorithm accepts the proposed thickness if the remaining height after printing that layer is either greater than or equal to the minimum allowed (0.15 mm) or falls within the valid range [0.15 mm, 0.35 mm], in which case it can be printed as the final layer. If subtracting the proposed thickness would leave a remainder smaller than 0.15 mm, the

algorithm reserves exactly 0.15 mm for the final layer and adjusts the current layer to print the remaining height − 0.15, but only if that adjusted value remains within [0.15 mm, 0.35 mm]. If reserving 0.15 mm is not feasible and the total remaining height is itself within [0.15 mm, 0.35 mm], the algorithm prints the entire remaining height as a valid final layer. This ensures that all layers, including the last, comply with the prescribed bounds while achieving exact height closure without backtracking. Figure 58 summarises the workflow of the adaptative slicing approach.

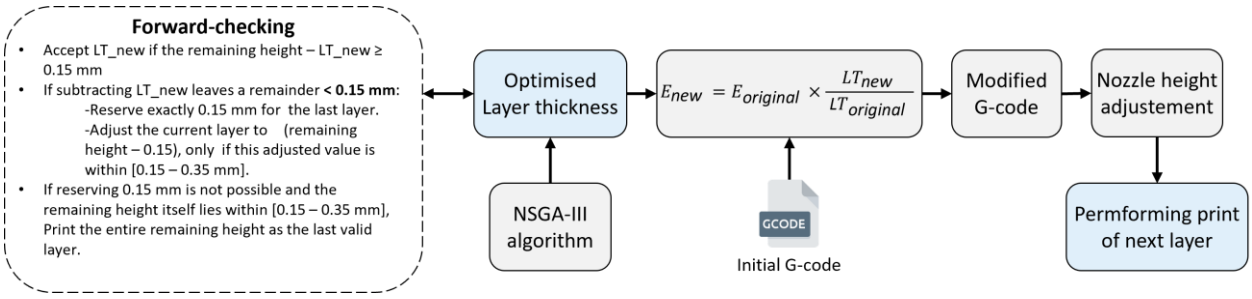

Figure 58. Workflow of Adaptive Slicing with Forward-Checking in FDM

Beyond layer thickness, other process parameters are adjusted using G-code commands:

- Printing temperature: M104 S{new_PT} sets the value, and M109 S{new_PT} waits for stabilization.
- Bed temperature: M140 S{new_BT} sets the value, and M190 S{new_BT} confirms stability.
- Flow rate: M221 S{new_F} updates the extrusion multiplier as a percentage.
- and Z-axis adjustments for nozzle height.

These instructions ensure that the optimized parameters are correctly implemented for each layer, thereby enhancing both print quality and process efficiency in real-time.

iv. Execution: Once all parameter adjustments have been made, the modified G-code is transmitted line by line to the 3D printer via a serial connection. The printer then proceeds to fabricate the next layer using the optimized process settings determined by the predictive and optimization modules. This ensures that each layer is printed under conditions specifically tailored to its predicted behavior.

v. Iterative Feedback Loop: The entire process, comprising scanning, prediction, optimization, parameter update, and execution, is repeated for every layer. This iterative, closed-loop architecture enables the adaptive control of the printing process in real-time. By continuously integrating real-time measurements and model-based predictions, the system ensures consistent print quality throughout the build, resulting in improved mechanical performance, dimensional accuracy, and surface finish layer after layer.

7.3.7 Validation and Testing

To validate the effectiveness of the proposed methodology, a series of experiments were conducted using ASTM D638 Type IV tensile specimens. These specimens were printed using the optimized layer-wise parameters generated by the digital twin framework, which integrates real-time sensing, predictive modeling, and adaptive slicing.

Following fabrication, the parts were subjected to standard mechanical tests to assess tensile strength and Young's modulus. In addition, surface roughness and dimensional accuracy were measured using the 3D scanning and data analysis pipeline described earlier.

To quantify the benefits of the proposed approach, the results were compared with a control group of specimens printed using fixed, non-adaptive parameters, which reflect conventional slicing strategies. This comparative analysis allows for a clear evaluation of the gains in surface quality, mechanical performance, and dimensional fidelity achieved through the integration of the digital twin and real-time optimization process.

7.4 Results

7.4.1 Surface Roughness Analysis

The correlation analysis between the key printing parameters and the average surface roughness (Ra) is presented in Figure 59(a). This analysis quantifies the relative influence of each parameter on surface quality during the FDM process.

The flow rate exhibits a moderate correlation with Ra (38 %), indicating its critical role in determining surface finish. Incorrect flow settings can result in under-extrusion or over-extrusion, leading to surface defects such as gaps, blobs, or ripples [87].

Other parameters, including printing temperature (8%), layer thickness (7%), %), and bed temperature (4.27%), also contribute to surface quality, albeit to a lesser extent. Their effects, while smaller in direct correlation, interact with each other and the printing dynamics in non-trivial ways.

- Bed temperature affects adhesion of the initial layers, indirectly influencing the flatness and uniformity of the upper surface.
- Printing temperature controls material flow consistency: even slight deviations may alter the bonding quality between layers.
- Layer thickness plays a dual role, influencing both the geometric resolution and the bonding quality.

Thinner layers typically result in a finer surface finish and better layer fusion. The use of adaptive slicing enables this parameter to be optimized in real-time based on print conditions, thereby reducing surface inconsistencies.

Also, although not represented in Figure 59, the Ra of the previous layer shows the highest correlation with the current Ra compared to the printing parameters, with a value of 86 %. This result highlights the strong inter-layer dependency in FDM: imperfections in earlier layers tend to propagate to subsequent ones, reinforcing the need for layer-wise quality control throughout the build.

These findings highlight the necessity of a multi-parameter approach to surface quality control, with a particular focus on inter-layer roughness propagation and flow rate management. Integrating real-time monitoring and corrective adjustments based on the Ra of previous layers could significantly enhance the final surface finish. Simultaneously, optimizing flow rate, temperature, and layer thickness dynamically during the print contributes to a more consistent and high-quality output.

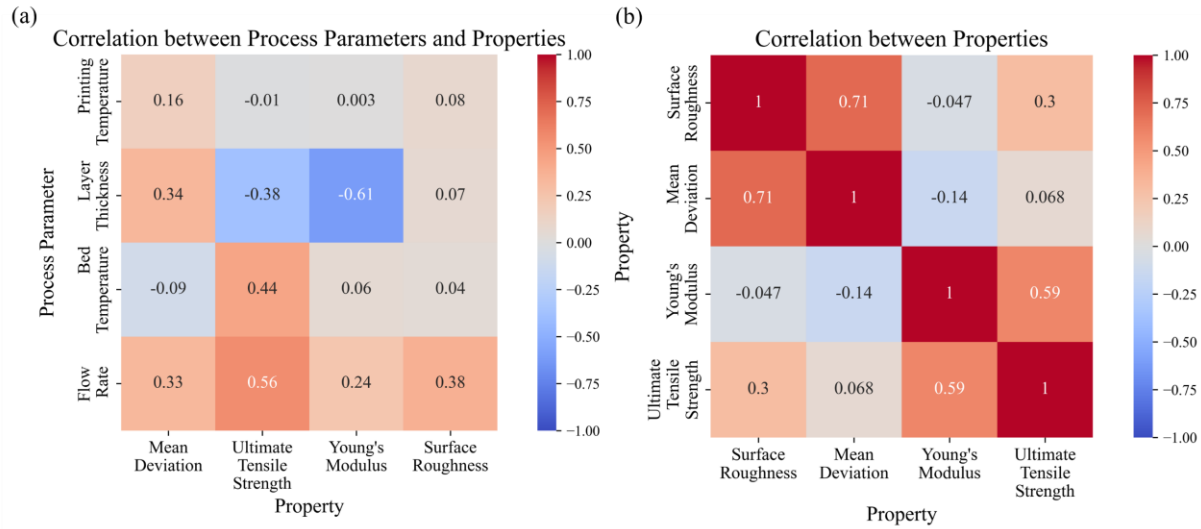

Figure 59. Correlation Matrices of Printing Parameters and Printed Part Properties. (a) Correlation matrix between printing process parameters and resulting part properties, (b) Correlation matrix among the studied properties themselves.

7.4.2 Dimensional Accuracy Analysis

The analysis of the correlation between printing parameters and dimensional accuracy, used here as a metric for dimensional accuracy, is also presented in Figure 59(a).

Among all evaluated factors, layer thickness exhibits the highest correlation with dimensional accuracy, at 34 %. This confirms that it plays a decisive role in the uniformity of layer deposition. Variations in layer height can accumulate over successive layers, leading to pronounced deviations from the intended geometry. Therefore, implementing real-time layer

thickness adjustment is essential for minimizing geometric errors and maintaining dimensional consistency throughout the build.

The flow rate, with a correlation of 33 %, is the second most influential parameter. An improper flow setting can result in over-extrusion (causing bulging and excess material) or under-extrusion (creating gaps and voids), both of which directly impact the precision of the final geometry [36, 87]. Dynamic regulation of flow rate is thus a critical element for accurate volumetric deposition.

The printing temperature presents a moderate correlation of 16% with a dimensional accuracy. While less impactful than layer thickness and flow rate, it still plays a meaningful role. Inconsistent temperature control can affect filament viscosity and extrusion stability, resulting in variable layer heights and subtle distortions during printing [88]. Interestingly, bed temperature shows a negative correlation of -9 %, suggesting that increasing the bed temperature can slightly reduce dimensional deviation. This may be attributed to improved first-layer adhesion and reduced warping, particularly in the early stages of printing. Although its direct influence is weaker, it contributes to stabilizing the base layers and supports geometric integrity over time.

Together, layer thickness (34 %), flow rate (33 %), and printing temperature (16 %) account for approximately 83% of the explained variance in dimensional deviation. This reinforces the importance of optimizing them simultaneously. Moreover, although not explicitly represented in Figure 59, the interaction between layer thickness and flow rate is known to exacerbate deviations when miscalibrated, such as excessive material in thicker layers or poor bonding in thinner ones. Addressing these effects jointly is crucial for achieving reliable print accuracy.

In summary, these findings validate the strategy of adaptive, layer-wise parameter optimization, particularly for layer thickness and flow rate, as a robust method for controlling dimensional accuracy in FDM processes. The digital twin's real-time feedback loop ensures continuous correction, helping to maintain geometric fidelity throughout the fabrication cycle.

7.4.3 Mechanical Properties Analysis

The analysis of Figure 59(a) also provides insight into the relationship between key FDM printing parameters and the two primary mechanical properties of printed parts: Ultimate Tensile Strength (UTS) and Young's Modulus.

Among all parameters, flow rate stands out as the most influential, showing strong positive correlations with both UTS (56 %) and Young's Modulus (24 %). This confirms that accurate flow control is essential for achieving uniform material deposition and consistent layer fusion.

Adequate flow rate helps reduce voids and delamination, thereby increasing both the tensile strength and stiffness of the printed part [36, 87].

In contrast, layer thickness exhibits a marked negative correlation with mechanical properties: -38 % for UTS and -61 % for Young's Modulus. These results imply that increasing the thickness of deposited layers tends to degrade mechanical performance. Thicker layers can lead to weaker interlayer bonding and higher chances of internal defects or porosity. Consequently, reducing layer thickness, especially in structurally critical regions, can effectively enhance the mechanical integrity of the part [89].

Bed temperature shows a positive correlation with UTS (44 %) and a moderate correlation with Young's Modulus (6 %). This suggests that higher bed temperatures improve interlayer adhesion, particularly in the early stages of the print, resulting in enhanced tensile properties. However, its limited influence on stiffness implies that bed temperature primarily contributes to bonding quality rather than altering the bulk material response.

Surprisingly, printing temperature exhibits minimal correlation with either mechanical property (UTS: -1 %, Young's Modulus: 0.3 %). While this indicates a lesser direct influence, maintaining a stable extrusion temperature remains important to ensure flow stability and avoid anomalies such as stringing or under-extrusion during printing [88].

Overall, this analysis reinforces the importance of dynamic adjustment of flow rate and layer thickness, as enabled by the digital twin framework. Their significant impact on mechanical behavior justifies their selection as optimization targets in the multi-objective algorithm. Bed temperature also plays a supporting role in reinforcing tensile strength, particularly in the initial bonding phase.

7.4.4 Cross-Property Correlation and Interpretation

Figure 59(b) presents a cross-correlation analysis between the four main quality metrics studied in this work: dimensional accuracy, ultimate tensile strength (UTS), Young's modulus, and average surface roughness (Ra). These results highlight critical interdependencies that can guide the optimization strategy for FDM 3D printing.

The strong positive correlation between dimensional accuracy and average surface roughness (71 %) indicates a close relationship between geometric precision and surface finish. This suggests that improving surface roughness could simultaneously enhance dimensional accuracy, making Ra a proxy metric for both surface quality and geometric fidelity. In practical terms, this correlation simplifies the optimization task: by prioritizing surface roughness control, dimensional deviations can be reduced as a secondary benefit.

In terms of mechanical performance, Young's modulus shows a moderate correlation with UTS (59 %), which is expected given their shared dependence on material continuity and interlayer adhesion. However, Young's modulus has weak or negligible correlations with Ra (−4.7%) and dimensional accuracy (−14 %), suggesting that stiffness is relatively independent of geometric or surface-level variations. This implies that stiffness is primarily influenced by internal bonding quality and deposition consistency, rather than external shape fidelity.

Conversely, UTS is moderately affected by both Ra and dimensional accuracy, reinforcing the idea that tensile strength bridges surface quality and internal cohesion. Parts that are geometrically accurate and smooth tend to exhibit higher tensile strength, likely due to better interlayer bonding and fewer surface-initiated failure points.

These insights support a focused optimization strategy that targets:

- Surface roughness (Ra): as a dominant driver of both visual quality and dimensional accuracy.
- Ultimate tensile strength (UTS): as a key mechanical property influenced by both geometry and material deposition.
- Young's modulus: as a distinct objective linked primarily to material and thermal parameters.

Rather than optimizing all four properties independently, this prioritization allows for a reduced-complexity multi-objective formulation, where Ra and UTS and Young's modulus serve as principal targets. The strong Ra–dimensional accuracy correlation ensures that dimensional control is implicitly addressed.

7.4.5 Models Training and Evaluation

7.4.5.1 Prediction of Surface Roughness

This section presents the evaluation of the revised CNN–LSTM model in predicting the average surface roughness (Ra), with an in-depth analysis of the architecture, data preparation strategy, and model performance across both training and testing phases.

The model was trained using a dataset generated from the Design of Experiment (DoE), which included 375 rows. Each row contained key printing parameters, including printing temperature, layer thickness, bed temperature, flow rate, and the layer number within the printed specimen. This comprehensive dataset was constructed to reflect a wide range of process conditions, enabling the model to generalize across different parts of the printing cycle.

To capture temporal dependencies between successive layers, a moving window approach was employed. Specifically, for each layer to be predicted, the model considered the Ra values of

the previous 20 layers. This sequence of historical roughness values formed the temporal context for the prediction. In cases where fewer than 20 previous layers were available (e.g., early layers), the sequence was padded with zeros to maintain a consistent input shape. This method allowed the model to learn how roughness evolves over time and how earlier layers influence subsequent surface quality.

The dataset was partitioned into training (80 %) and testing (20 %) sets to rigorously evaluate model generalization. The input sequences included not only the roughness history but also static printing parameters, enabling the model to simultaneously exploit temporal and spatial features.

The CNN–LSTM model architecture comprised multiple components:

- A 1D Convolutional Layer with 64 filters and a kernel size of 3 was used to extract spatial features from the input matrix. This layer processed both Ra histories and printing parameters to uncover local patterns.
- A MaxPooling1D layer with a pool size of 2 was employed after convolution to reduce dimensionality and retain essential features, thereby mitigating the risks of overfitting.
- Two LSTM layers followed the CNN module:
  - The first LSTM layer consisted of 128 units and returned sequences, enabling the network to propagate time-dependent patterns.
  - The second LSTM layer had 64 units and returned the final output sequence, which was passed to a dense feedforward network.
- A Dense Layer with 64 neurons and ReLU activation aggregated the learned features from both CNN and LSTM branches.
- The final Output Layer consisted of a single neuron with a linear activation, providing a continuous-valued prediction for Ra.

To avoid overfitting and ensure model robustness, early stopping was activated, halting training if validation loss failed to improve after 75 consecutive epochs. Additionally, model checkpoints were used to automatically save the best-performing weights during training, ensuring that the final model represented an optimal balance between bias and variance.

The trained model was evaluated using standard regression metrics:

- Coefficient of Determination (R^2):
  - Training R^2: 93.73 %
  - Testing R^2: 88.35 %
- Mean Squared Error (MSE):
  - Training MSE: 1.17×10^{-6}

- Testing MSE: 3.97×10^{-6}

These results demonstrate that the model achieved excellent accuracy in both training and testing phases, indicating strong generalization to unseen layer sequences (Figure 60(a)).

This robust performance highlights the CNN–LSTM architecture's strength in simultaneously capturing spatial parameter interactions and temporal evolution, making it a valuable predictive tool for closed-loop control of print quality in digital twin implementations.

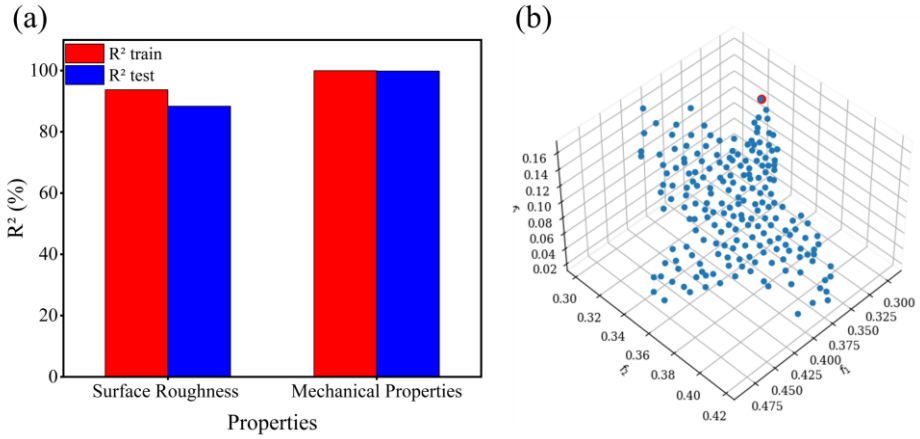

Figure 60. Performance of Predictive Models and Optimization Outcome; (a) R^2 of the prediction models, (b) Example of the Pareto front generated by the NSGA-III algorithm, illustrating trade-offs between surface quality and mechanical properties.

7.4.5.2 Prediction of Mechanical Properties

The prediction of mechanical properties using the CNN–LSTM architecture was conducted in parallel with the surface roughness model, leveraging the same dataset of 375 experimental samples. Each sample included the main process parameters, printing temperature, layer thickness, bed temperature, flow rate, and the average surface roughness (Ra), which was included as an additional predictor to account for the surface–structure–mechanical interaction. As with surface roughness prediction, a moving window approach was implemented to construct temporal input sequences that captured the variation of properties across layers. This allowed the model to learn how the mechanical behavior of the printed part evolves with respect to both parameter changes and surface quality trends throughout the build.

The CNN–LSTM model adopted for mechanical prediction comprised the following architecture:

- A 1D convolutional layer (64 filters) to extract spatial features from the printing parameters and Ra values across the temporal window,
- A MaxPooling1D layer to downsample the feature maps, helping reduce overfitting and computational complexity,

- A single LSTM layer (64 units), which modeled the sequential dependencies in the data and output a fixed-size latent vector,
- Fully connected dense layers, culminating in an output layer with two neurons, corresponding to the Ultimate Tensile Strength (UTS) and Young's Modulus (E).

The training and evaluation followed the same protocol as before, using 80 % of the data for training and 20 % for testing, and employing early stopping and model checkpointing to retain the best model based on validation loss.

The trained model demonstrated excellent predictive performance:

- R^2 (training): 99.94 %, indicating that the model explains virtually all variance in the mechanical properties,
- R^2 (testing): 99.84 %, confirming near-perfect generalization to unseen samples,
- MSE (training): 3.77, and MSE (testing): 11.38, which are both low and within acceptable ranges for regression tasks in experimental material modeling.

These performance metrics reflect the model's ability to simultaneously capture the complex relationships between multiple process variables, surface quality indicators, and final mechanical outcomes (Figure 60(a)).

This performance confirms that the proposed model can be reliably used within the digital twin framework to provide real-time, layer-wise predictions of mechanical properties, enabling adaptive decision-making during the print process.

7.4.6 Multi-objective optimization

This section presents the results of the multi-objective optimization applied to the FDM 3D printing process, targeting the simultaneous optimization of surface quality and mechanical performance. Specifically, the optimization objectives include minimizing the average surface roughness (Ra) while maximizing the Ultimate Tensile Strength (UTS) and Young's Modulus (E). These conflicting goals reflect the inherent trade-offs in FDM: improving surface finish may come at the cost of structural integrity, and vice versa.

To address this challenge, the Non-dominated Sorting Genetic Algorithm III (NSGA-III) was employed due to its effectiveness in solving many-objective problems and generating diverse, high-quality Pareto fronts. The optimization variables were bounded based on practical operating ranges derived from preliminary experimental results and literature:

- Printing Temperature: 200 °C – 230 °C
- Bed Temperature: 50 °C – 70 °C
- Layer Thickness: 0.15 mm – 0.35 mm
- Flow Rate: 98 % – 105 %

The optimization process leveraged the previously trained CNN–LSTM predictive models for Ra, UTS, and E, which served as fast surrogate models to evaluate candidate solutions across the design space without requiring physical experimentation.

The outcome of the NSGA-III optimization is visualized in Figure 60(b), which displays the Pareto front obtained after convergence. Each point on the surface corresponds to a non-dominated solution, i.e., a parameter set where no objective can be improved without degrading at least one of the others. The well-distributed nature of the Pareto front demonstrates the algorithm's ability to maintain diversity across competing trade-offs.

This visualization allows users to explore solutions depending on the application-specific priority: for instance,

- Designs favoring minimal Ra are found on one edge of the surface,
- While those optimizing UTS and E occupy the opposing region.

In addition to visual inspection, a targeted selection process was implemented. A reference point in the objective space was defined as [0, 1, 1], representing the ideal configuration with zero surface roughness and maximum mechanical properties (normalized). The Euclidean distance from each Pareto-optimal solution to this reference point was computed. The solution with the minimum distance, highlighted in red in Figure 60(b), was selected as the most balanced compromise among all trade-offs.

This optimal configuration provides a valuable reference for real-time parameter tuning, especially in adaptive control scenarios where priorities may shift depending on part geometry, intended function, or application domain (e.g., medical vs. automotive).

Overall, the results confirm the efficacy of NSGA-III in generating a rich set of optimal parameter combinations tailored to different quality and performance goals. The integration of predictive modeling with multi-objective optimization enables an intelligent, data-driven decision-making framework for FDM printing, supporting on-the-fly adaptation and continuous process improvement.

7.4.7 Real-Time Optimization and Adaptive Slicing

The real-time optimization framework, supported by NSGA-III and the CNN–LSTM predictive models, enabled the adaptive selection of printing parameters on a layer-by-layer basis. This dynamic tuning aimed to simultaneously improve surface roughness, dimensional accuracy, and mechanical properties, in response to the evolving state of the printed part.

The adaptively generated G-code incorporated modifications in four key parameters across layers: printing temperature, layer thickness, bed temperature, and flow rate. These changes

were driven by real-time predictions and optimization decisions based on the performance of the previous layer.

Layer Thickness Adjustment: Figure 61(a) presents the variation in layer thickness for three optimized prints. Initial layers typically feature moderate thicknesses (around 0.25 mm), ensuring a stable foundation and good bed adhesion. As the print progresses, the thickness values are consistently reduced towards 0.15 mm, especially in critical structural zones. This aligns with our correlation analysis, which showed that decreasing layer thickness improves Ra, dimensional accuracy, and mechanical strength [89]. The optimizer thus favors fine layers for regions requiring high fidelity and strength, while allowing coarser layers where tolerances are less strict.

Bed Temperature Control: As shown in Figure 61(b), bed temperature is also adaptively managed:

– The first few layers maintain higher temperatures (65–70 °C) to ensure strong bed adhesion and avoid early warping, which is crucial for print stability [90]. In intermediate layers, temperatures stabilize around 50–55 °C, suggesting a controlled cooling phase that reduces thermal stress and layer misalignment.

– Towards the end, temperature increases again, reflecting a proactive approach to enhance bonding and reduce the risk of cracking as the printed volume grows.

– This thermal regulation strategy highlights the relevance of dynamic substrate control in high-fidelity, multi-layer builds.

Flow Rate Adaptation: Figure 61(c) illustrates the evolution of the flow rate, which oscillates between 98% and 105%. These fine-tuned variations are critical for adjusting the material deposition rate:

– Higher flow rates (closer to 105 %) are selectively applied to enhance interlayer adhesion, particularly in regions prone to delamination or void formation.

– Conversely, lower flow rates help prevent over-extrusion and maintain surface definition in outer shell regions.

This control strategy confirms the model's ability to balance mechanical integrity and dimensional consistency, particularly in complex geometries [91].

Printing Temperature Regulation: Figure 61(d) shows the printing temperature trajectory across the layers. Temperatures vary dynamically between 200 °C and 230 °C:

– Initial layers exhibit minor fluctuations, ensuring proper melting and extrusion consistency.

– In later stages, an upward trend is observed, likely to improve fusion between layers and counteract cooling effects that lead to poor bonding or warping.

These adjustments reflect the optimization system's capacity to react to real-time measurements, sustaining both material flow quality and structural continuity.

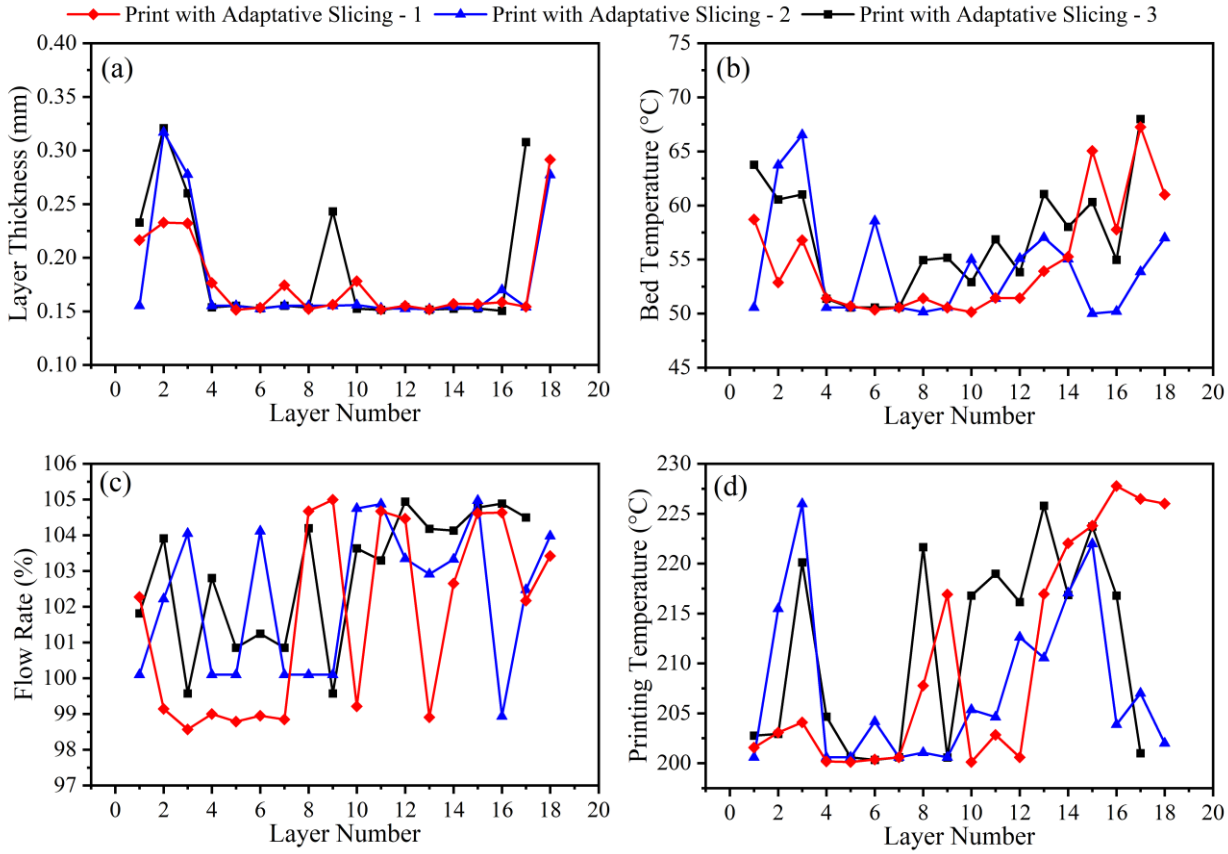

Figure 61. Adaptive Optimization of Printing Parameters Across Layers: (a) Printing Temperature, (b) Layer Thickness, (c) Bed Temperature, (d) Flow Rate.

7.4.8 Surface Roughness

To assess the effectiveness of the proposed real-time optimization and adaptive slicing strategy, a comparative analysis was performed between specimens printed using the developed method and a reference specimen produced with standard recommended parameters for PLA. These baseline parameters are commonly suggested in the FDM community and are detailed in Table 33 below.

As illustrated in Figure 62, specimens printed under adaptive slicing exhibited a consistent reduction in surface roughness (Ra) across all layers when compared to the reference specimen fabricated using fixed parameters. The layer-specific Ra evolution, shown in Figures 62(a) through 62(c), highlights the performance of three separate prints conducted under optimized, real-time parameter adjustments. Each is overlaid with the corresponding values obtained from

the reference print. Figure 62(d) further synthesizes these results by comparing the average surface roughness of each adaptively sliced part to that of the reference specimen.

Table 33. Recommended FDM process parameters for PLA

Printing Parameter	Value
Printing Temperature	215°C
Layer Thickness	0.25mm
Bed Temperature	60°C
Flow Rate	100%

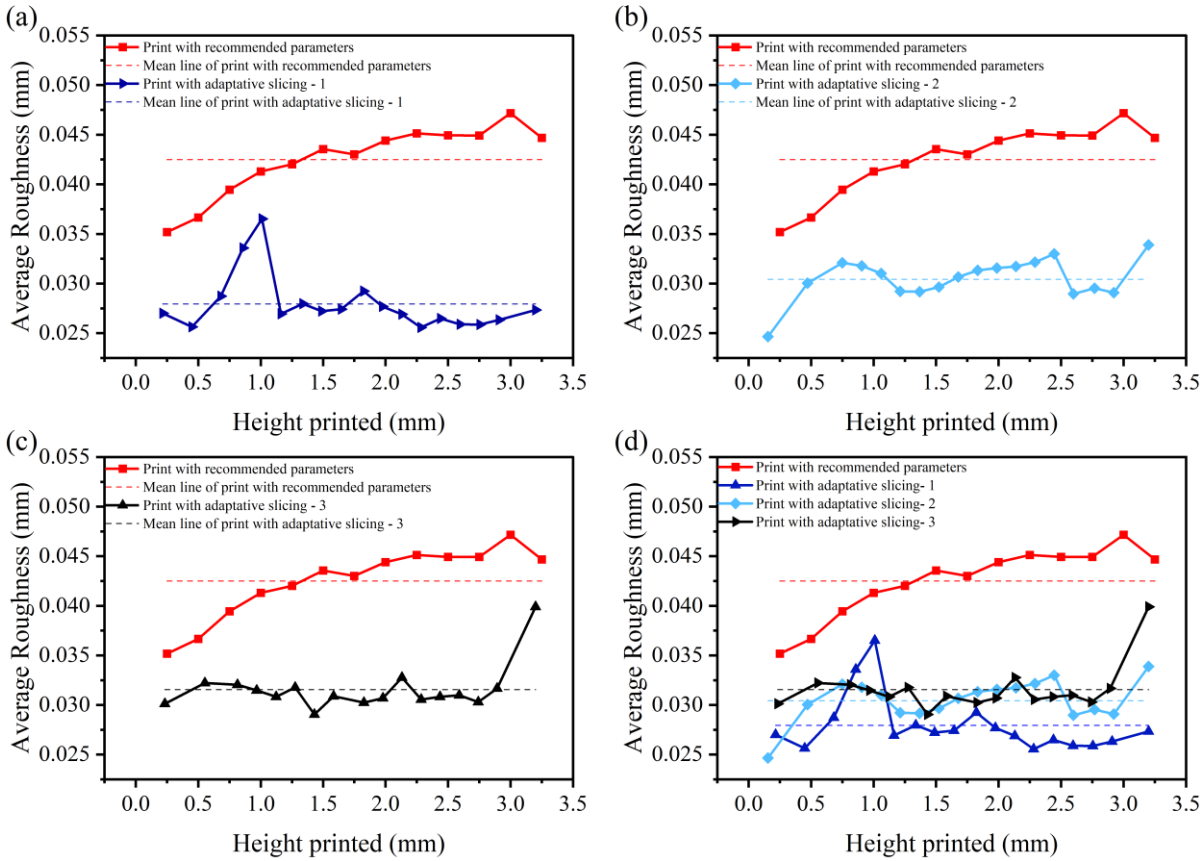

Figure 62. Impact of Adaptive Slicing on Surface Roughness Across Layers: (a–c) Evolution of Ra for three optimized prints compared to the reference print using standard parameters; (d) Aggregate comparison of average surface roughness between all adaptive sliced

Across all cases, the adaptively optimized parameter sets yielded visibly smoother surfaces. The layer-wise variation in Ra shows that the optimization system, leveraging predictive models and real-time feedback, was able to detect surface deviations and apply corrective adjustments, primarily through layer thickness and flow rate modulation. These two parameters, previously identified in the correlation analysis as major contributors to surface finish, were dynamically adapted to reduce roughness incrementally from one layer to the next. From a quantitative standpoint, the average surface roughness measured across all layers for the adaptively printed specimens was approximately 0.0295 mm, corresponding to a 30.59 %

reduction relative to the 0.0425 mm average Ra observed in the reference specimen. This substantial improvement validates the efficacy of the proposed method in minimizing surface irregularities during the printing process.

The results confirm that the integration of real-time optimization and adaptive slicing not only enhances surface quality but also provides a robust, automated strategy for ensuring consistent print quality across layers. This method allows for the reduction of surface roughness without relying on post-processing, while simultaneously improving material deposition control and layer adhesion, ultimately enabling the production of high-quality FDM parts suitable for applications requiring both dimensional precision and superior surface finish.

7.4.9 Dimensional Accuracy

Although dimensional accuracy was not explicitly incorporated as an objective in the multi-objective optimization process, primarily due to its strong correlation with surface roughness as demonstrated in Section 3.4, its variation was nonetheless closely monitored to evaluate the indirect effects of adaptive slicing and surface optimization on part fidelity.

As illustrated in Figure 63, comparing the mean deviation between the actual prints and their CAD reference geometries reveals a consistent enhancement in dimensional accuracy across all layers in the specimens printed with optimized parameters. These deviations were calculated using 3D point cloud alignment techniques, as detailed in Section 2.4, with the mean deviation reflecting the layer-by-layer geometrical error.

Figures 63(a) through 63(c) show the evolution of dimensional accuracy for three adaptively sliced prints, compared with the part printed under standard PLA settings. In each case, the optimized prints exhibit a downward trend or stabilization of error, while the reference part shows consistently higher deviations. Figure 63(d) aggregates these results, highlighting the layer-wise average deviation for all test cases.

Quantitatively, the average mean deviation across layers decreased from 0.06326 mm (recommended parameters) to 0.05989 mm (adaptive slicing), representing a reduction of approximately 5.33%. Although this reduction may appear modest, it is important to note that:

- The improvement was achieved without directly targeting dimensional accuracy in the optimization algorithm.
- The gain is cumulative and meaningful for precision-demanding applications in bio-medical or aerospace fields.
- It confirms the interdependence between surface finish and geometrical accuracy, as smoother layer deposition minimizes surface irregularities that typically propagate as dimen-sional drift over the build height.

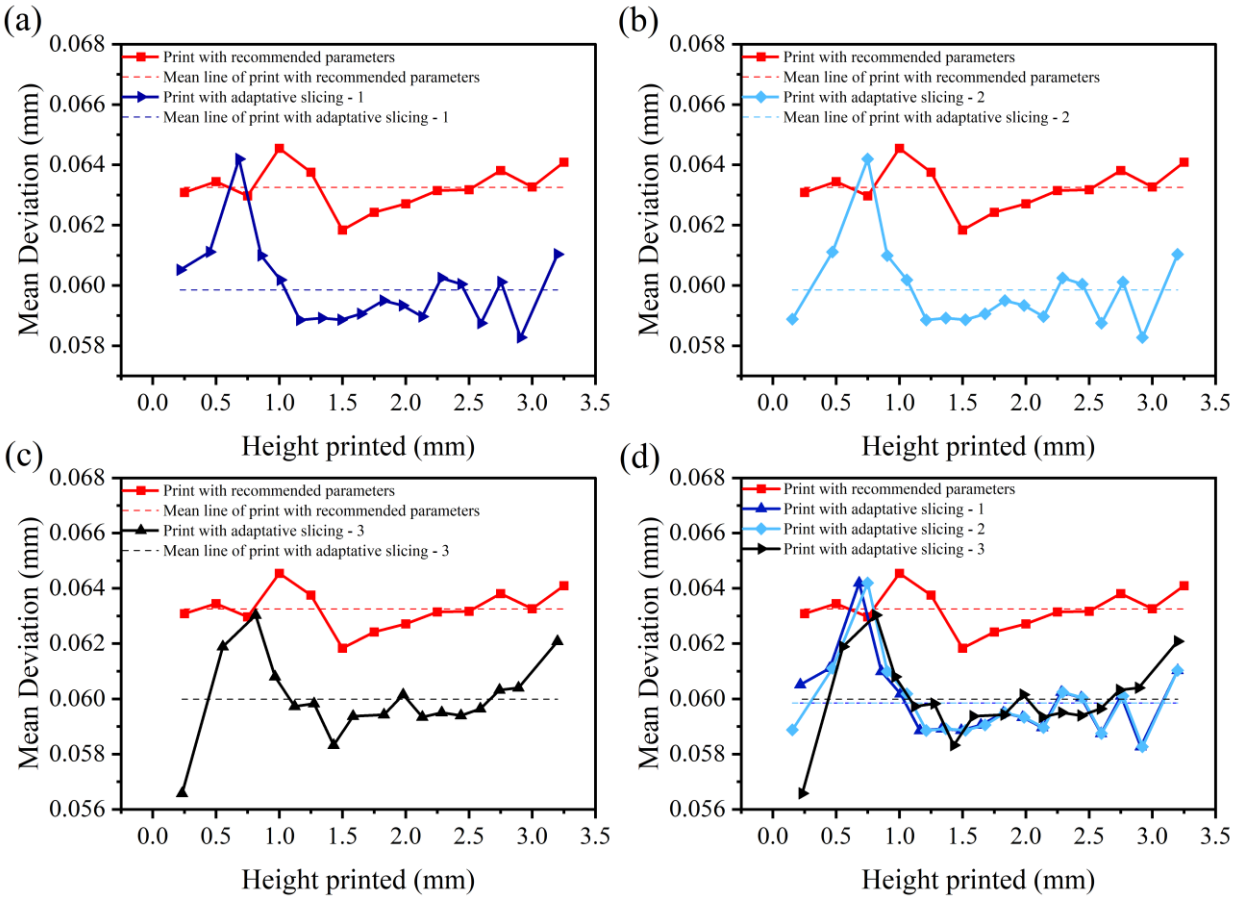

Figure 63. Effect of Adaptive Slicing on Dimensional Accuracy Across Printed Layers: (a–c) Evolution of mean deviation for three adaptive prints compared to the reference print; (d) Comparison of average mean deviation for all adaptively sliced prints and the print with recommended parameters.

These results reinforce the conclusion that optimizing surface roughness not only enhances aesthetic and functional surface properties but also contributes significantly to dimensional fidelity. The adaptive slicing method thus proves to be a robust and efficient approach to improve multiple performance criteria simultaneously, even when only a subset of objectives is explicitly optimized.

7.4.10 Mechanical Properties

The tensile testing of the printed specimens provided clear evidence of mechanical performance enhancement through real-time optimization. As shown in Figure 64, the ultimate tensile strength (UTS) of the specimens produced with optimized parameters showed a notable increase of 9.12% compared to those printed using standard recommended settings.

Specifically, the reference specimens exhibited an average UTS of 55.17 MPa, with the best-performing sample shown in red on the stress–strain plot. In contrast, the adaptively optimized prints reached an average UTS of 60.2 MPa across the three tests, highlighting the positive

effect of real-time parameter adaptation, articularly the improved layer adhesion achieved through better control of temperature, flow rate, and layer thickness.

In addition to tensile strength, Young's modulus was included as a key objective in the multi-objective optimization procedure. However, results indicate that although the average stiffness improved by 3.25% compared to the baseline configuration, not all optimized prints outperformed the reference in terms of modulus individually.

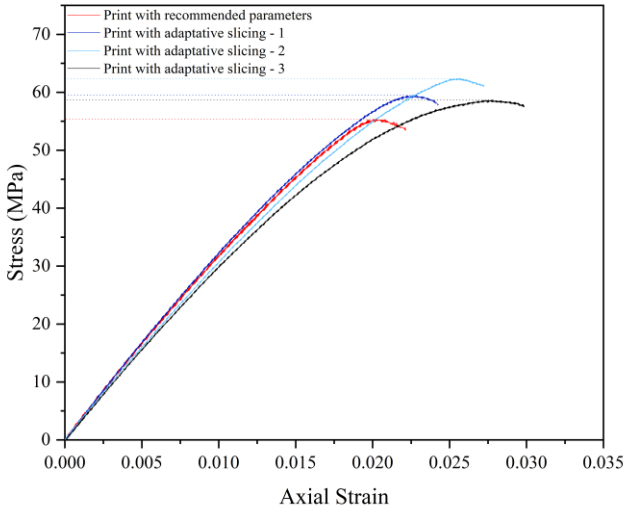

Figure 64. Stress–Strain Curves for Baseline and Optimized Prints; Comparison of tensile behavior for reference specimens (recommended PLA parameters) and adaptively optimized prints, highlighting gains in ultimate tensile strength and Young's modulus.

This observation highlights the inherent trade-offs in multi-objective optimization strategies, such as NSGA-III, which aim to identify Pareto-optimal compromises across competing goals, in this case, minimizing surface roughness while maximizing both ultimate tensile strength (UTS) and Young's modulus. Because increasing stiffness may sometimes be at odds with reducing surface irregularities or optimizing interlayer bonding, the algorithm prioritizes global balance over strict maximization of any single metric.

Quantitatively, the average Young's modulus across the optimized specimens was 3.335 GPa, with individual values of 3.476 GPa, 3.306 GPa, and 3.223 GPa. For the reference prints, the average was 3.229 GPa, with respective values of 3.307 GPa, 3.223 GPa, and 3.160 GPa. Despite slight dispersion, the overall improvement in modulus reflects the optimizer's success in enhancing mechanical rigidity while preserving surface quality and dimensional accuracy.

Furthermore, these findings align well with the cross-property correlation analysis presented in Section 3.4. In that earlier section, UTS and Young's modulus showed a strong mutual correlation (59.25%), while surface roughness and dimensional accuracy exhibited a high correlation (71.17%), reinforcing the idea that smoother layers improve both strength and

geometric fidelity. Interestingly, the correlation between surface roughness and Young's modulus was weak and negative (–4.66%), suggesting that stiffness can be improved independently of surface quality, a relationship clearly respected by the NSGA-III optimization in this study.

This convergence between the experimental outcomes and the inter-property correlations underscores the robustness of the proposed strategy. It validates the framework's framework to exploit latent dependencies (such as Ra ↔ deviation ↔ UTS) while navigating conflicting objectives to achieve optimized mechanical performance in FDM parts.

7.5 Conclusion and Perspectives

This study presents a novel real-time optimization approach for Fused Deposition Modeling 3D printing, leveraging advanced technologies such as 3D scanning, machine learning, and multi-objective optimization to enhance both the layer-specific quality and mechanical properties of printed parts. By integrating a digital twin framework, the research successfully demonstrated the potential of adaptive slicing and real-time parameter adjustments to address the inherent challenges of FDM, such as surface roughness, dimensional accuracy, and mechanical performance.

The key findings for Surface Roughness optimization include that the real-time adaptive slicing and parameter adjustments significantly reduced surface roughness by 30.59% compared to prints using standard parameters. This improvement highlights the effectiveness of the proposed method in minimizing surface irregularities and enhancing the overall surface finish of FDM-printed parts.

Although Dimensional Accuracy was not directly included in the optimization process, the study observed a 5.33% improvement in dimensional accuracy, indicating that optimizing Surface Roughness indirectly enhances Dimensional accuracy. The finding underscores the interconnected nature of surface quality and geometric precision in FDM printing.

The optimized prints showed a 9.12% increase in Ultimate Tensile Strength, demonstrating the potential of real-time optimization to improve mechanical performance. However, the trade-offs inherent in multi-objective optimization meant that Young's Modulus did not always show constant and significant improvement where in the proposed maximizing method, on average it did increase of about 3.25%.

The CNN-LSTM model proved highly effective in predicting both Surface Roughness and Mechanical Properties, with high R^2 values (93.73% for trainin and 88.35% for testing in

surface roughness prediction, and 99.94% for training and 99.84% for testing in mechanical properties prediction).

The NSGA-III algorithm successfully identified Pareto-optimal solutions that balanced surface roughness, tensile strength, and Young's modulus. This approach allows for dynamic adjustments based on real-time data, providing an efficient method for optimizing FDM printing parameters.

The proposed real-time digital-twin framework demonstrated simultaneous improvement of surface roughness, dimensional accuracy, and mechanical strength in FDM printing through adaptive slicing and NSGA-III optimization. The findings point to clear practical extensions. A first priority is scaling the method for industrial use by deploying it on high-speed printers, so real-time control remains effective at large production volumes. Although validation here used PLA, the same framework can be transferred to advanced composites, high-performance polymers, and multi-material builds. Upcoming experiments should examine how the controller adapts to material-dependent behaviors, with applications in aerospace, automotive, and biomedical components where material choice is critical.

The digital-twin architecture is also ready for smart-factory integration. It supports continuous monitoring, predictive analytics, and adaptive control, and can be connected to IoT-enabled printers with cloud or edge analytics. With printers, sensors, and optimization routines exchanging data in real time, production lines can gain efficiency, repeatability, and higher throughput.

Sustainability is another direction. Future work will quantify how closed-loop optimization reduces material waste, lowers energy consumption, and mitigates environmental impact during printing.

In summary, this work addresses persistent issues in FDM, surface quality, dimensional accuracy and mechanical performance, by combining machine learning, adaptive slicing, and multi-objective optimization within a real-time digital twin. The results demonstrate a viable path to in-process quality control and process improvement, positioning FDM for high-precision applications across multiple industries and providing a solid basis for broader deployment of data-driven additive manufacturing.

7.6 Author Contributions

Conceptualization, A.Z.; Formal analysis, M.H. and A.Z.; Funding acquisition, M.H. and S.K.; Investigation, A.Z.; Methodology A.Z.; Software, A.Z.; Supervision, M.H. and S.K.;

Writing—original draft, A.Z.; Writing—review and editing, M.H and S.K. All authors have read and agreed to the published version of the manuscript.

7.7 Funding

Funding: The authors acknowledge the funding provided by the Natural Sciences and Engineering Research Council (NSERC) of Canada (grant number: CRSNG–RGPIN-2021-02846) and the Canada Research Chairs Program.

7.8 Data Availability Statement

Data available under request.

7.9 Conflicts of Interest

The authors certify that they have no affiliations with or involvement in any organization or entity with any financial interest or non-financial interest in the subject matter or materials discussed in this manuscript.

7.10 References

[1] M. Abas, T. Habib, S. Noor, B. Salah, D. Zimon, Parametric investigation and optimization to study the effect of process parameters on the dimensional deviation of fused deposition modeling of 3D printed parts, Polymers 14(17) (2022) 3667.

[2] K.I. Ismail, T.C. Yap, R. Ahmed, 3D-printed fiber-reinforced polymer composites by fused deposition modelling (FDM): fiber length and fiber implementation techniques, Polymers 14(21) (2022) 4659.

[3] Z. Abdelhamid, H. Mohamed, S. Kelouwani, The use of machine learning in process–structure–property modeling for material extrusion additive manufacturing: a state-of-the-art review, Journal of the Brazilian Society of Mechanical Sciences and Engineering 46(2) (2024) 70.

[4] Y. Wang, R.T. Mushtaq, A. Ahmed, A. Ahmed, M. Rehman, M. Rehman, A.M. Khan, S. Sharma, D.K. Ishfaq, H. Ali, Additive manufacturing is sustainable technology: citespace based bibliometric investigations of fused deposition modeling approach, Rapid Prototyping Journal 28(4) (2022) 654-675.

[5] S. Vyavahare, S. Teraiya, D. Panghal, S. Kumar, Fused deposition modelling: a review, Rapid Prototyping Journal 26(1) (2020) 176-201.

[6] C. Camposeco-Negrete, Optimization of printing parameters in fused deposition modeling for improving part quality and process sustainability, The International Journal of Advanced Manufacturing Technology 108(7) (2020) 2131-2147.

[7] M. Boulaala, D. Elmessaoudi, I. Buj-Corral, J. El Mesbahi, O. Ezbakhe, A. Astito, M. El Mrabet, A. El Mesbahi, Towards design of mechanical part and electronic control of multi-material/multicolor fused deposition modeling 3D printing, The International Journal of Advanced Manufacturing Technology 110 (2020) 45-55.

[8] A. Gosset, D. Barreiro-Villaverde, J.C. Becerra Permuy, M. Lema, A. Ares-Pernas, M.J. Abad López, Experimental and numerical investigation of the extrusion and deposition process of a poly (lactic acid) strand with fused deposition modeling, Polymers 12(12) (2020) 2885.

[9] D.M. Baca Lopez, R. Ahmad, Tensile mechanical behaviour of multi-polymer sandwich structures via fused deposition modelling, Polymers 12(3) (2020) 651.

[10] M.G.M. Benal, P.K. GS, V. Tambrallimath, G. HR, T.Y. Khan, A.A. Rajhi, M.A.A. Baig, Influence of short glass fibre reinforcement on mechanical properties of 3D printed ABS-based polymer composites, Polymers 14(6) (2022) 1182.

[11] D. Veeman, S. Palaniyappan, G. Surendhar, R. Shanmugam, Process optimization of compressive property and dimensional error on wood polylactic acid gyroid-structured polymer composite, Journal of Reinforced Plastics and Composites (2022) 07316844221096486.

[12] B. Karima, M. Habibi, L. Laperrière, 4D printing of fiber-reinforced auxetic structures: the building blocks: a review, Smart Material Structures 33(6) (2024) 063001.

[13] A. Megdich, M. Habibi, L. Laperrière, Z. Li, Y. Abdin, Enhanced piezoelectric performance of PVDF/MWCNTs energy harvester through a 3D-printed multimodal auxetic structure for smart security systems, Materials Today Sustainability 27 (2024) 100847.

[14] T. Sathies, P. Senthil, M. Anoop, A review on advancements in applications of fused deposition modelling process, Rapid Prototyping Journal 26(4) (2020) 669-687.

[15] J.F.P. Lovo, C.A. Fortulan, M.M. da Silva, Optimal deposition orientation in fused deposition modeling for maximizing the strength of three-dimensional printed truss-like structures, Proceedings of the Institution of Mechanical Engineers, Part B: Journal of Engineering Manufacture 233(4) (2019) 1206-1215.

[16] P. Ferretti, G.M. Santi, C. Leon-Cardenas, M. Freddi, G. Donnici, L. Frizziero, A. Liverani, Molds with advanced materials for carbon fiber manufacturing with 3D printing technology, Polymers 13(21) (2021) 3700.

[17] A. Melocchi, F. Briatico-Vangosa, M. Uboldi, F. Parietti, M. Turchi, D. von Zeppelin, A. Maroni, L. Zema, A. Gazzaniga, A. Zidan, Quality considerations on the pharmaceutical applications of fused deposition modeling 3D printing, International Journal of Pharmaceutics 592 (2021) 119901.

[18] A. Megdich, M. Habibi, L. Laperrière, Z. Li, Y. Abdin, Advanced 3D-printed PVDF/BT piezoelectric energy harvester with a bio-inspired 3D structure for a self-powered smart mouse, Nano Energy (2024) 109876.

[19] K. Bouguermouh, M. Habibi, L. Laperrière, Z. Li, Y. Abdin, 4D-printed PLA-PETG polymer blends: comprehensive analysis of thermal, mechanical, and shape memory performances, Journal of Materials Science (2024) 1-18.

[20] V. Linares, M. Casas, I. Caraballo, Printfills: 3D printed systems combining fused deposition modeling and injection volume filling. Application to colon-specific drug delivery, European Journal of Pharmaceutics and Biopharmaceutics 134 (2019) 138-143.

[21] Z. Liu, Y. Wang, B. Wu, C. Cui, Y. Guo, C. Yan, A critical review of fused deposition modeling 3D printing technology in manufacturing polylactic acid parts, The International Journal of Advanced Manufacturing Technology 102 (2019) 2877-2889.

[22] E.U. Enemuoh, S. Duginski, C. Feyen, V.G. Menta, Effect of process parameters on energy consumption, physical, and mechanical properties of fused deposition modeling, Polymers 13(15) (2021) 2406.

[23] M. Goudswaard, B. Hicks, A. Nassehi, The creation of a neural network based capability profile to enable generative design and the manufacture of functional FDM parts, The International Journal of Advanced Manufacturing Technology 113 (2021) 2951-2968.

[24] S. Wickramasinghe, T. Do, P. Tran, FDM-based 3D printing of polymer and associated composite: A review on mechanical properties, defects and treatments, Polymers 12(7) (2020) 1529.

[25] A. Ziadia, M. Habibi, S. Kelouwani, Machine learning study of the effect of process parameters on tensile strength of FFF PLA and PLA-CF, Eng 4(4) (2023) 2741-2763.

[26] M.N. Ahmad, M.R. Ishak, M. Mohammad Taha, F. Mustapha, Z. Leman, D.D. Anak Lukista, Irianto, I. Ghazali, Application of Taguchi method to optimize the parameter of fused deposition modeling (FDM) using oil palm fiber reinforced thermoplastic composites, Polymers 14(11) (2022) 2140.

[27] A.-H. Ismail Mourad, A.H. Idrisi, J.V. Christy, D.T. Thekkuden, H. Al Jassmi, A. M. Ghazal, M. M. Syam, O.D. Ali Ahmed Al Qadi, Mechanical performance assessment of internally-defected materials manufactured using additive manufacturing technology, Journal of Manufacturing and Materials Processing 3(3) (2019) 74.

[28] S. Karimi, S. Kwon, F. Ning, Energy-aware production scheduling for additive manufacturing, Journal of Cleaner Production 278 (2021) 123183.

[29] C. Billings, M. Saha, Y. Liu, Development and Implementation of a High-Temperature FDM Machine for Additive Manufacturing of Thermoplastics, ASME International Mechanical Engineering Congress and Exposition, American Society of Mechanical Engineers, 2022, p. V003T04A001.

[30] N. Top, I. Sahin, S.K. Mangla, M.D. Sezer, Y. Kazancoglu, Towards sustainable production for transition to additive manufacturing: a case study in the manufacturing industry, International Journal of Production Research 61(13) (2023) 4450-4471.

[31] V.K. Tiwary, P. Arunkumar, A.S. Deshpande, N. Rangaswamy, Surface enhancement of FDM patterns to be used in rapid investment casting for making medical implants, Rapid Prototyping Journal 25(5) (2019) 904-914.

[32] O.A. Mohamed, S.H. Masood, J.L. Bhowmik, Modeling, analysis, and optimization of dimensional accuracy of FDM-fabricated parts using definitive screening design and deep learning feedforward artificial neural network, Advances in Manufacturing 9 (2021) 115-129.

[33] M. Samykano, S. Selvamani, K. Kadirgama, W. Ngui, G. Kanagaraj, K. Sudhakar, Mechanical property of FDM printed ABS: influence of printing parameters, The International Journal of Advanced Manufacturing Technology 102 (2019) 2779-2796.

[34] P. Zhang, Z. Wang, J. Li, X. Li, L. Cheng, From materials to devices using fused deposition modeling: A state-of-art review, Nanotechnology Reviews 9(1) (2020) 1594-1609.

[35] J.C. Camargo, Á.R. Machado, E.C. Almeida, E.F.M.S. Silva, Mechanical properties of PLA-graphene filament for FDM 3D printing, The International Journal of Advanced Manufacturing Technology 103 (2019) 2423-2443.

[36] P. Ferretti, C. Leon-Cardenas, G.M. Santi, M. Sali, E. Ciotti, L. Frizziero, G. Donnici, A. Liverani, Relationship between FDM 3D printing parameters study: parameter optimization for lower defects, Polymers 13(13) (2021) 2190.

[37] T.S. Tamir, G. Xiong, Q. Fang, X. Dong, Z. Shen, F.-Y. Wang, A feedback-based print quality improving strategy for FDM 3D printing: an optimal design approach, The International Journal of Advanced Manufacturing Technology 120(3) (2022) 2777-2791.

[38] A. Dey, N. Yodo, A systematic survey of FDM process parameter optimization and their influence on part characteristics, Journal of Manufacturing and Materials Processing 3(3) (2019) 64.

[39] D. Singh, R. Singh, K.S. Boparai, Development and surface improvement of FDM pattern based investment casting of biomedical implants: A state of art review, Journal of Manufacturing Processes 31 (2018) 80-95.

[40] M. Taufik, P.K. Jain, Part surface quality improvement studies in fused deposition modelling process: a review, Australian Journal of Mechanical Engineering 20(2) (2022) 527-551.

[41] S. Pawar, D. Dolas, Effect of process parameters on flexural strength and surface roughness in fused deposition modeling of PC-ABS material, Journal of Micromanufacturing 5(2) (2022) 164-170.

[42] L. Kothandaraman, N.K. Balasubramanian, Optimization of the Printing Parameters to Improve the Surface Roughness in Fused Deposition Modeling, E3S Web of Conferences, EDP Sciences, 2023, p. 03003.

[43] L.F.C. Durão, R. Barkoczy, E. Zancul, L. Lee Ho, R. Bonnard, Optimizing additive manufacturing parameters for the fused deposition modeling technology using a design of experiments, Progress in Additive Manufacturing 4 (2019) 291-313.

[44] A. Tura, H. Mamo, Y. Jelila, H.G. Lemu, Experimental investigation and ANN prediction for part quality improvement of fused deposition modeling parts, IOP Conference Series: Materials Science and Engineering, IOP Publishing, 2021, p. 012031.

[45] M.S. Saad, A.M. Nor, M.E. Baharudin, M.Z. Zakaria, A. Aiman, Optimization of surface roughness in FDM 3D printer using response surface methodology, particle swarm optimization, and symbiotic organism search algorithms, The International Journal of Advanced Manufacturing Technology 105 (2019) 5121-5137.

[46] P. Patil, D. Singh, S.J. Raykar, J. Bhamu, Multi-objective optimization of process parameters of Fused Deposition Modeling (FDM) for printing Polylactic Acid (PLA) polymer components, Materials Today: Proceedings 45 (2021) 4880-4885.

[47] A. Colpani, A. Fiorentino, E. Ceretti, Characterization of chemical surface finishing with cold acetone vapours on ABS parts fabricated by FDM, Production Engineering 13 (2019) 437-447.

[48] N. Jayanth, P. Senthil, C. Prakash, Effect of chemical treatment on tensile strength and surface roughness of 3D-printed ABS using the FDM process, Virtual and Physical Prototyping 13(3) (2018) 155-163.

[49] A.W. Gebisa, H.G. Lemu, Influence of 3D printing FDM process parameters on tensile property of ULTEM 9085, Procedia Manufacturing 30 (2019) 331-338.

[50] F.M. Othman, T. Fadhil, A.H.B. Ali, Influence of process parameters on mechanical properties and printing time of FDM PLA printed parts using design of experiment, J. Eng. Res 8 (2018) 2248-9622.

[51] A. Ouballouch, S. Ettaqi, A. Bouayad, M. Sallaou, L. Lasri, Evaluation of dimensional accuracy and mechanical behavior of 3D printed reinforced polyamide parts, Procedia Structural Integrity 19 (2019) 433-441.

[52] H. Chokshi, D.B. Shah, K.M. Patel, S.J. Joshi, Experimental investigations of process parameters on mechanical properties for PLA during processing in FDM, Advances in Materials and Processing Technologies 8(sup2) (2022) 696-709.

[53] A.W. Gebisa, H.G. Lemu, Investigating effects of fused-deposition modeling (FDM) processing parameters on flexural properties of ULTEM 9085 using designed experiment, Materials 11(4) (2018) 500.

[54] U.K.u. Zaman, E. Boesch, A. Siadat, M. Rivette, A.A. Baqai, Impact of fused deposition modeling (FDM) process parameters on strength of built parts using Taguchi's design of experiments, The international journal of Advanced Manufacturing technology 101 (2019) 1215-1226.

[55] T. Kozior, A. Mamun, M. Trabelsi, L. Sabantina, A. Ehrmann, Quality of the Surface Texture and Mechanical Properties of FDM Printed Samples after Thermal and Chemical Treatment, Journal of Mechanical Engineering/Strojniški Vestnik 66(2) (2020).

[56] A. Saluja, J. Xie, K. Fayazbakhsh, A closed-loop in-process warping detection system for fused filament fabrication using convolutional neural networks, Journal of Manufacturing Processes 58 (2020) 407-415.

[57] U. Delli, S. Chang, Automated process monitoring in 3D printing using supervised machine learning, Procedia Manufacturing 26 (2018) 865-870.

[58] C. Liu, A.C.C. Law, D. Roberson, Z.J. Kong, Image analysis-based closed loop quality control for additive manufacturing with fused filament fabrication, Journal of Manufacturing Systems 51 (2019) 75-86.

[59] H. Hu, K. He, T. Zhong, Y. Hong, Fault diagnosis of FDM process based on support vector machine (SVM), Rapid Prototyping Journal 26(2) (2020) 330-348.

[60] Y. Banadaki, N. Razaviarab, H. Fekrmandi, G. Li, P. Mensah, S. Bai, S. Sharifi, Automated quality and process control for additive manufacturing using deep convolutional neural networks, Recent Progress in Materials 4(1) (2021).

[61] S. Wang, Y. Ma, Z. Deng, S. Zhang, J. Cai, Effects of fused deposition modeling process parameters on tensile, dynamic mechanical properties of 3D printed polylactic acid materials, Polymer testing 86 (2020) 106483.

[62] R. Srinivasan, P. Prathap, A. Raj, S.A. Kannan, V. Deepak, Influence of fused deposition modeling process parameters on the mechanical properties of PETG parts, Materials Today: Proceedings 27 (2020) 1877-1883.

[63] M.S. Saad, A.M. Nor, M.E. Baharudin, M.Z. Zakaria, A. Aiman, Optimization of surface roughness in FDM 3D printer using response surface methodology, particle swarm optimization, and symbiotic organism search algorithms, The International Journal of Advanced Manufacturing Technology 105(12) (2019) 5121-5137.

[64] M.M. Manziuc, C. Gasparik, A.V. Burde, H.A. Colosi, M. Negucioiu, D. Dudea, Effect of glazing on translucency, color, and surface roughness of monolithic zirconia materials, Journal of Esthetic and Restorative Dentistry 31(5) (2019) 478-485.

[65] I. Hussain, Effects of Post-processing Treatments on the Mechanical Properties of FDM, biomaterials 93 45-111.

[66] A. Kantaros, T. Ganetsos, F.I.T. Petrescu, L.M. Ungureanu, I.S. Munteanu, Post-Production Finishing Processes Utilized in 3D Printing Technologies, Processes 12(3) (2024) 595.

[67] J.R.C. Dizon, C.C.L. Gache, H.M.S. Cascolan, L.T. Cancino, R.C. Advincula, Post-processing of 3D-printed polymers, Technologies 9(3) (2021) 61.

[68] N. Lv, X. Ouyang, Y. Qiao, Adaptive layering algorithm for FDM-3D printing based on optimal volume error, Micromachines 13(6) (2022) 836.

[69] F. Wasserfall, N. Hendrich, J. Zhang, Adaptive slicing for the FDM process revisited, 2017 13th IEEE Conference on Automation Science and Engineering (CASE), IEEE, 2017, pp. 49-54.

[70] P.M. Pandey, N.V. Reddy, S.G. Dhande, Real time adaptive slicing for fused deposition modelling, International Journal of Machine Tools and Manufacture 43(1) (2003) 61-71.

[71] G.A. Nisja, A. Cao, C. Gao, Short review of nonplanar fused deposition modeling printing, Material Design & Processing Communications 3(4) (2021) e221.

[72] H.S. Kim, K.M. Han, J. Yu, J. Kim, K. Kim, H. Kim, Development of a CNN+ LSTM hybrid neural network for daily PM2. 5 prediction, Atmosphere 13(12) (2022) 2124.

[73] M.S. Ibrahim, S.M. Gharghory, H.A. Kamal, A hybrid model of CNN and LSTM autoencoder-based short-term PV power generation forecasting, Electrical Engineering (2024) 1-17.

[74] X. Wang, J. Cao, A novel multi-objective optimization of 3D printing adaptive layering algorithm based on improved NSGA-II and fuzzy set theory, The International Journal of Advanced Manufacturing Technology 123(3) (2022) 957-972.

[75] J. Yang, F. Wang, Y. Dun, Z. Huang, A. Zhang, Y. Liu, Prediction-based multi-objective optimization method for 3D printing resource consumption, The International Journal of Advanced Manufacturing Technology 134(3) (2024) 1805-1843.
[76] D. Dakshinamurthy, S. Gupta, A study on the influence of process parameters on the viscoelastic properties of ABS components manufactured by FDM process, Journal of The Institution of Engineers (India): Series C 99(2) (2018) 133-138.
[77] A.A. Bakır, R. Atik, S. Özerinç, Effect of fused deposition modeling process parameters on the mechanical properties of recycled polyethylene terephthalate parts, Journal of Applied Polymer Science 138(3) (2021) 49709.
[78] L.P. Huynh, H.A. Nguyen, H.Q. Nguyen, L.K. Phan, T.T. Thanh, Effect of process parameters on mechanical strength of ffabricated parts using the fused deposition modelling method, (2019).
[79] O.A. Mohamed, S.H. Masood, J.L. Bhowmik, Mathematical modeling and FDM process parameters optimization using response surface methodology based on Q-optimal design, Applied Mathematical Modelling 40(23-24) (2016) 10052-10073.
[80] R. Venkatraman, S. Raghuraman, Experimental analysis on density, micro-hardness, surface roughness and processing time of Acrylonitrile Butadiene Styrene (ABS) through Fused Deposition Modeling (FDM) using Box Behnken Design (BBD), Materials Today Communications 27 (2021) 102353.
[81] A.D. Tura, H.B. Mamo, W.F. Gemechu, Mathematical modeling and parametric optimization of surface roughness for evaluating the effects of fused deposition modeling process parameters on ABS material, International Journal of Advanced Engineering Research and Science 8(5) (2021) 049-057.
[82] N. Vinoth Babu, N. Venkateshwaran, N. Rajini, S.O. Ismail, F. Mohammad, H.A. Al-Lohedan, S. Suchart, Influence of slicing parameters on surface quality and mechanical properties of 3D-printed CF/PLA composites fabricated by FDM technique, Materials Technology 37(9) (2022) 1008-1025.
[83] K.M. Agarwal, P. Shubham, D. Bhatia, P. Sharma, H. Vaid, R. Vajpeyi, Analyzing the impact of print parameters on dimensional variation of ABS specimens printed using fused deposition modelling (FDM), Sensors International 3 (2022) 100149.
[84] M.M. Hanon, L. Zsidai, Q. Ma, Accuracy investigation of 3D printed PLA with various process parameters and different colors, Materials Today: Proceedings 42 (2021) 3089-3096.

[85] M. Galetto, E. Verna, G. Genta, Effect of process parameters on parts quality and process efficiency of fused deposition modeling, Computers & Industrial Engineering 156 (2021) 107238.

[86] A. Ziadia, M. Habibi, S. Kelouwani, Digital twin-driven real-time optimization of layer-specific surface roughness in FDM 3D printing, Progress in Additive Manufacturing (2025) 1-24.

[87] J. Butt, R. Bhaskar, V. Mohaghegh, Investigating the influence of material extrusion rates and line widths on FFF-printed graphene-enhanced PLA, Journal of Manufacturing and Materials Processing 6(3) (2022) 57.

[88] M.-H. Hsueh, C.-J. Lai, K.-Y. Liu, C.-F. Chung, S.-H. Wang, C.-Y. Pan, W.-C. Huang, C.-H. Hsieh, Y.-S. Zeng, Effects of printing temperature and filling percentage on the mechanical behavior of fused deposition molding technology components for 3D printing, Polymers 13(17) (2021) 2910.

[89] K. Shergill, Y. Chen, S. Bull, An investigation into the layer thickness effect on the mechanical properties of additively manufactured polymers: PLA and ABS, The International Journal of Advanced Manufacturing Technology 126(7) (2023) 3651-3665.

[90] M. Spoerk, J. Gonzalez-Gutierrez, J. Sapkota, S. Schuschnigg, C. Holzer, Effect of the printing bed temperature on the adhesion of parts produced by fused filament fabrication, Plastics, Rubber and Composites 47(1) (2018) 17-24.

[91] F. Lambiase, F. Pace, E. Andreucci, A. Paoletti, Flow rate-dependent interlayer adhesion in FDM: a thermal and mechanical analysis, The International Journal of Advanced Manufacturing Technology (2024) 1-14.

Chapitre 8: Reconstruction 3D des pièces fabriquées par FDM basée sur l'intelligence artificielle

AI-based 3D reconstruction of FDM printed parts. Abdelhamid ZIADIA, Mohamed HABIBI, Sousso KELOUWANI, Sheena YAN & Yasmine ABDIN.

Ce chapitre prolonge le chapitre précédant en s'attaquant à l'état interne de la pièce. À partir des paramètres d'impression et des nuages de points acquis en fin de chaque couche, un cGAN 3D conditionnel génère des volumes de type micro-CT. L'objectif est d'estimer la géométrie et la porosité internes sans imagerie lourde pendant l'impression et d'alimenter le jumeau numérique avec un état interne prédictif.

Le plan d'expérience suit un Taguchi L9 sur quatre facteurs à trois niveaux. Débit 95, 100 et 105 %. Température d'extrusion 200, 215 et 230 °C. Température de lit 50, 60 et 70 °C. Épaisseur de couche 0,20, 0.30 et 0,40 mm. Les coupons 10 × 10 × 2 mm permettent des acquisitions de référence compactes. Chaque couche est scannée, les nuages sont nettoyés puis agrégés en un descripteur compact. En parallèle, les données micro-CT de référence sont prétraitées et normalisées, puis alignées dès l'amont aux scans in situ afin de constituer un jeu cohérent pour l'entraînement du conditional Generative Adversarial Network (cGAN) et pour l'évaluation des volumes générés.

Le modèle prend en entrée les paramètres normalisés et le descripteur des nuages de points et produit un volume 3D normalisé. La qualité est suivie à l'échelle voxel par des erreurs L_1, MSE et Dice La qualité est suivie à l'échelle voxel par L_1, MSE et Dice, et à l'échelle surface après alignement rigide via la distance de Hausdorff et l'écart moyen point-surface. Les résultats montrent une bonne conservation des contours externes et de la topologie interne avec des écarts résiduels localisés sur les arêtes vives et les zones minces.

L'apport est double. D'une part, la chaîne de pilotage multicritère fondée sur l'observation de surface se dote d'une observabilité volumique prédictive de la pièce entière. D'autre part, les cartes internes reconstruites à l'échelle du volume complet deviennent des critères et des contraintes supplémentaires pour les décisions de contrôle ultérieures.

Dans le cadre de cette thèse, la reconstruction 3D est introduite comme un volet complémentaire à l'observation de surface, avec l'objectif d'enrichir le jumeau numérique d'une lecture interne complète de la pièce. L'intégration directe de cette information dans une

stratégie décisionnelle en ligne n’a pas été explorée ici, car le travail visait en priorité à démontrer la capacité du modèle à anticiper la structure interne à partir des données disponibles en fabrication. Cette contribution fournit un socle robuste pour plusieurs développements futurs: pilotage exploitant simultanément surface et volume, analyse interne pour l’assurance qualité, intégration dans des simulations numériques plus fidèles, ou encore conception adaptative guidée par l’état prédictif de la pièce.

AI-based 3D reconstruction of FDM printed parts

Abdelhamid Ziadia[1], Mohamed Habibi[1, *], Sousso Kelouwani[1], Sheena Yan[2] & Yasmine Abdin[2]

Affiliation 1; University of Quebec in Trois-Rivieres, (Department of Mechanical Engineering), Trois-Rivieres, (Quebec), Canada

Affiliation 2; University of British Columbia, (Department of Materials Engineering), Vancouver, BC, Canada

*Correspondence: erima@uqtr.ca

8.1 Abstract

Additive manufacturing enables the fabrication of complex geometries, but quality control remains a major challenge, particularly in fused deposition modeling where variations in process settings introduce layer-wise defects and geometric drift. This work presents a multimodal framework for 3D reconstruction of FDM parts based on a Generative Adversarial Network that fuses process parameters with an in-situ point-cloud descriptor, while micro-CT volumes provide ground-truth supervision. Experiments were conducted on PLA coupons of 10 × 10 × 2 mm, fabricated with a Prusa MK3S+ under a Taguchi L9 design. The model achieved robust performance, with validation errors converging to L_1 = 0.1535 and MSE = 0.1402. On a strictly held-out specimen, alignment achieved a correspondence ratio of 1.000, an inlier RMSE of 0.0098, and a symmetric Hausdorff distance of 0.0455. These results demonstrate that process-aware, geometry-aware reconstruction can reach decision-grade accuracy, enabling quality assurance and digital-twin synchronization in material-extrusion AM, while paving the way toward in-situ monitoring via sparse, layer-wise inputs.

Keywords: Additive manufacturing, Fused Deposition Modeling, 3D reconstruction, Machine Learning, Quality assurance

8.2 Introduction

Additive Manufacturing (AM), or 3D printing, builds parts layer by layer from digital models, enabling complex geometries, reduced material waste, shorter production cycles, and mass customization [1, 2]. Among AM techniques, Fused Deposition Modeling (FDM) is widely used for its simplicity, low cost, and material versatility, moving from prototyping toward functional parts [3-6]. However, FDM is highly sensitive to process parameters such as temperature, speed, and layer thickness, often leading to defects including poor interlayer adhesion, surface irregularities, voids, and warping[7-10]. These challenges highlight the limitations of conventional monitoring methods and the need for advanced post-process evaluation tools capable of accurately recovering both surface and internal features of printed parts [11, 12].

To overcome the limits of conventional inspection, 3D reconstruction has become an essential tool in additive manufacturing, allowing recovery of both surface geometry and internal features from data such as CT, structured light, thermal imaging, and optical cameras. These reconstructions reveal pores, delamination, deformation, and geometric drift not visible externally, while also supporting dimensional verification, simulation validation, repair planning, and digital twin synchronization. In FDM, efforts have largely focused on surface recovery and toolpath tracking. Girard and Zhang [13] applied structured light and phase imaging for fast local error detection. Corradini and Silvestri [14] combined nozzle trajectory, extrusion volume, and encoder feedback to reconstruct meshes and define a quality index. Ochoa et al. [15] used G-code reverse engineering and filament profiling to build digital twins for finite element validation. Liu et al. [16] reconstructed lattice unit cells with structured light to enhance multiscale modeling. In metal AM, reconstruction has expanded to internal states and thermal history. Wu et al. [17] mapped lattice rod deformation from CT point clouds. Uzun et al. [18] introduced eigenstrain reconstruction from X-ray diffraction. Lu et al. [19] recovered 3D thermal fields in FDM via physics-based compressive sensing. Chen et al. [20] applied graph convolutional networks with IR boundaries for thermal mapping. Yeung et al. [21] developed voxel meltpool energy representations for pore detection. Hybrid approaches also progress defect mapping. Chen et al. [22] extracted pore features with a CT-driven CNN, Ziabari et al. [23] fused CAD and sparse XCT to accelerate volume reconstruction, and Zhang et al. [24] used voxel Boolean operations for automatic repair zone extraction.

While these studies demonstrate the growing capabilities of 3D reconstruction in additive manufacturing, several critical limitations remain. Many existing methods are restricted to post-process evaluation and rely heavily on high-resolution scanning equipment such as CT or structured light systems, which are not always feasible for in-situ applications. Additionally, most approaches focus on a single data modality, often neglecting the rich contextual information embedded in printing parameters, which significantly influence the final part geometry. Few reconstruction pipelines attempt to fuse process-aware, geometry-aware, and design-aware data into a unified framework. These methods often perform poorly when faced with incomplete, noisy, or irregular data and cannot adapt to variations across different parts or printing conditions. In contrast, learning-based models offer improved generalization and robustness by extracting underlying patterns from diverse training examples. These gaps highlight the need for a reconstruction framework that is multimodal, data-driven, and robust to uncertainty, capable of operating within digital twin ecosystems and supporting both post-process validation and future real-time integration.

To address the limitations of existing 3D reconstruction approaches, a conditional Generative Adversarial Network (cGAN) framework that reconstructs the 3D geometry of printed parts by integrating multiple sources of information is proposed. In contrast to prior methods that rely on single-modality inputs or post-process evaluation, our approach combines partial surface point clouds and process parameters, to generate 3D reconstructions that reflect the actual build. The model is trained using CT scan volumes as ground truth, enabling voxel-level supervision and high geometric fidelity. A complete training pipeline is presented, and the method is validated on a left out of training FDM-printed specimen. This work establishes a foundation for integrating deep learning-based 3D reconstruction into digital twin environments, offering new capabilities for geometry validation, quality assurance, and intelligent manufacturing feedback.

8.3 Methodology

The complete workflow adopted in this study is summarized in Figure 65. PLA specimens were printed according to a Taguchi L9 design, with process parameters recorded and top surfaces scanned layer by layer. After fabrication, micro-CT provided volumetric ground truth. All data sources were preprocessed to ensure consistent resolution, scale, and format. These multimodal representations formed the inputs to the conditional GAN reconstruction framework. The training dataset consisted of 9 volumetric micro-CT scans paired with their corresponding in-situ point-cloud descriptors. Among these, 8 specimens were used to train and tune the model, while 1 strictly held-out specimen served as the final evaluation case to assess true generalization. The dataset covers the full diversity induced by the Taguchi L9 design, including variations in flow rate, printing temperature, bed temperature, and layer thickness. All CT volumes were preprocessed to ensure consistent resolution (256^3 voxels), binarization, noise filtering, and spatial alignment with the in-situ scans. This setup guarantees that the cGAN reconstruction is evaluated not only on interpolation within the training space but also on its ability to predict complete volumetric geometry under fully unseen printing conditions. The reconstructed volumes were finally compared to CT using voxel-level and surface-level metrics to assess fidelity and geometric conformance.

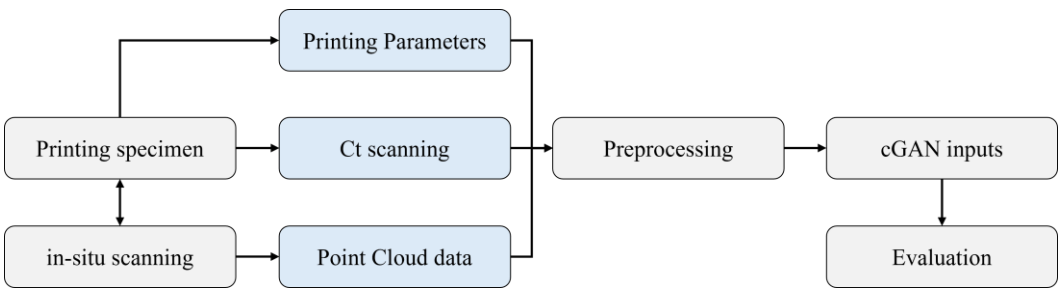

Figure 65. Overview of the experimental and computational workflow.

8.3.1 Printing Setup and Design of the Experiment

All experiments were conducted on a Prusa MK3S+ fused deposition modeling (FDM) printer. PLA was selected as the build material for all prints because it is bio-sourced and biodegradable, and is widely used in FDM studies, making the findings broadly applicable [25, 26].

A Taguchi L9 orthogonal array was adopted to study four key factors which are the Flow Rate, the Printing Temperature, the Bed Temperature, and the Layer Thickness, at three levels each (Table 34). This design reduces the number of combinations from 81 (full factorial) to 9, yielding substantial savings in print time, material consumption, and CT acquisition costs while preserving the ability to estimate the relative influence of each factor on reconstruction quality. Specimens were printed as compact coupons (10 × 10 × 2 mm). This geometry allows whole-part micro-CT imaging in a single acquisition, maximizing spatial resolution and avoiding stitching artifacts.

Table 34. Selected process parameters and their levels.

Factor	Level 1	Level 2	Level 3
Printing Temperature (°C)	200	215	230
Layer Thickness (mm)	0.2	0.3	0.4
Bed Temperature (°C)	50	60	70
Flow Rate (%)	95	100	105

8.3.2 Data acquisition and preprocessing

8.3.2.1 In-situ Point-Cloud Acquisition

For each DOE combination, the top surface deposited at every layer was scanned in real time using a Gocator 3210 snapshot 3D scanner from LMI Technologies mounted above the printing bed, producing high-resolution point clouds that capture the layer topography. The Gocator 3210 features a feld of view that ranges from 71×98 mm to 100×154 mm, a 110mm depth measurement range, and a 4.7 μm Z-repeatability. The printer was programmed to pause automatically at the end of each layer, retracting the extruder to not obscure the field of view of the scanner. The parameters set to the scanner included a single exposure of 20000 μs, a uniform spacing option, an X/Y spacing interval of 0.05 mm, and a diffuse type of material setting.

The raw scans were cleaned in several stages:

- Outlier removal: Statistical Outlier Removal followed by radius-based filtering to remove spurious points.
- Spatial cropping: A fixed bounding box to exclude supports and background.

— Vertical smoothing: Interquartile-range (IQR) filtering to attenuate residual surface irregularities and high-frequency noise.

For each specimen, layer point clouds were then aggregated and downsampled via Farthest Point Sampling (FPS) to a constant size of 2048 points. The cleaned, size-normalized cloud was encoded with a pretrained PointNet module to produce a 128-dimensional feature vector per layer. Layer vectors were averaged to yield a single specimen-level descriptor used throughout modeling.

8.3.2.2 Micro-CT Imaging and Volume Preparation

After printing, each specimen was imaged by micro-CT (voxel size 15 µm, 60 kV, 5 W, 0.4× objective, 1601 projections). A custom made python script was used for volumetric preprocessing:

— Fixed-threshold binarization at 0.5 to separate material from background across all samples.

— Morphological closing and removal of isolated regions to consolidate structures and discard speckle noise.

— Median and Gaussian filtering to reduce high-frequency noise.

Binary volumes were then resampled to 256^3 voxels by trilinear interpolation and normalized to 0,1.

Figure 66 shows a comparison between original and cleaned ct_scan result.

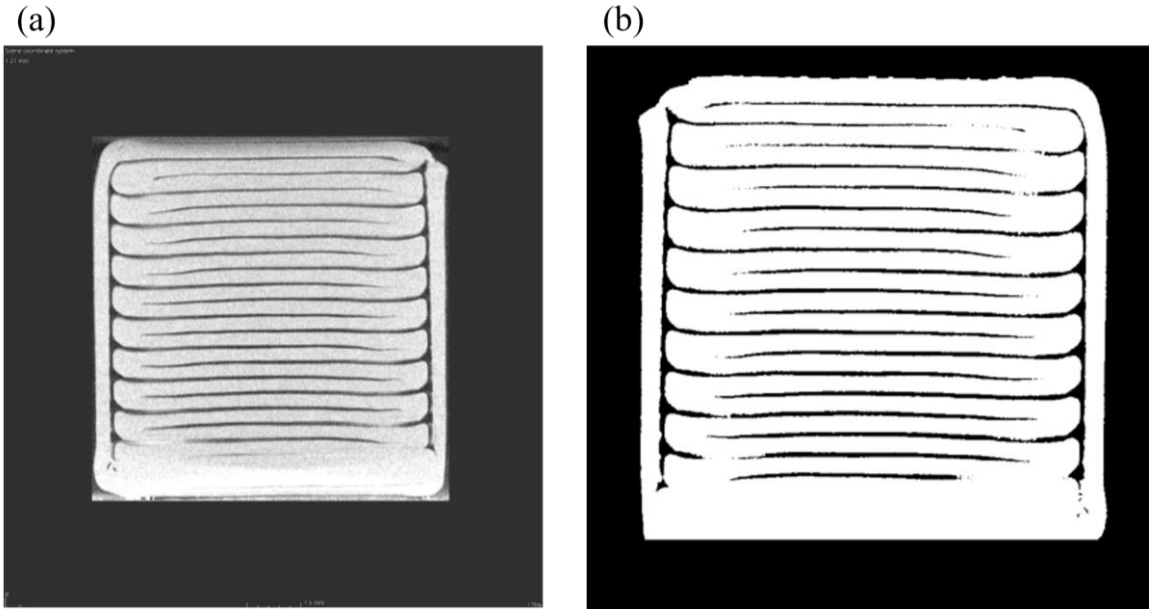

Figure 66. Example of micro-CT acquisition and preprocessing: (a) raw CT slice, (b) corresponding flipped and cleaned binary slice.

8.3.2.3 Alignment of Point Clouds and Micro-CT images

Because small orientation and position mismatches can remain between in-situ scans and CT volumes and to ensure spatial coherence between them, a rigid registration was performed prior to any metric evaluation. An isosurface was extracted from each cleaned CT volume by a marching-cubes procedure and uniformly sampled to obtain a CT-derived point set. The aggregated in-situ point cloud was downsampled to harmonize density and suppress noise. Rigid alignment used a point-to-point Iterative Closest Point (ICP) scheme with identity initialization and a normalized correspondence cutoff of 1.0 (distances expressed after the normalization described below). The algorithm iteratively minimized the mean squared distance between corresponding points until default convergence criteria were met, yielding a 4×4 rigid transform subsequently applied to the in-situ point cloud. Alignment quality was tracked by the correspondence ratio (fraction of accepted correspondences) and the inlier root-mean-square error (RMSE), and verified visually (Figure 67).

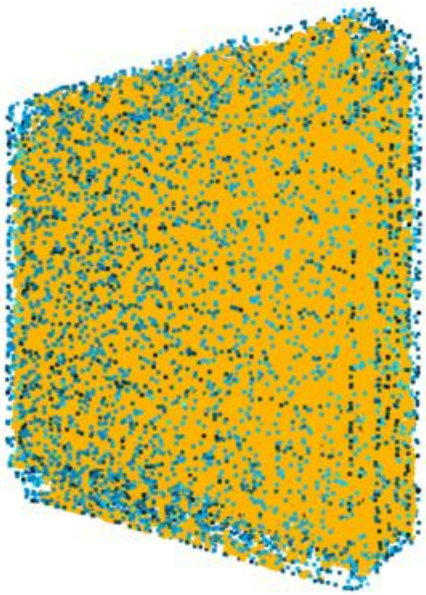

Figure 67. Example of rigid alignment between in-situ point cloud data and the CT data

8.3.3 Learning Framework, Training, and Evaluation

8.3.3.1 Conditional Inputs for Learning

Process parameters from the Prusa MK3S+ prints (nozzle temperature, bed temperature, layer thickness, flow) were min–max normalized to [0, 1] using observed bounds. The specimen-level PointNet 128-d descriptor was concatenated with the 4-d parameter vector to form a 133-dimensional conditional input consumed by both generator and discriminator.

8.3.3.2 Volumetric generative model

Reconstruction of CT-like volumes was performed with a 3D conditional adversarial model that accepts the multimodal condition described above.

Generator: The 133-d condition, concatenated with Gaussian noise, was projected to a latent tensor (512 channels, 4×4×4). A stack of residual 3D blocks with FiLM (feature-wise linear modulation) conditioned intermediate activations across scales. The volume was upsampled via transposed 3D convolutions (stride = 2) to 256^3, followed by a final transposed convolution with sigmoid to output [0, 1] volumes.

Discriminator: A projection-based conditional discriminator with spectral normalization on all 3D convolutions ingested the candidate volume. Six downsampling blocks with Leaky-ReLU and dropout yielded a compact embedding. The 133-d condition was encoded by a small MLP and fused via dot-product projection with aggregated features; a sigmoid estimated the realness probability.

8.3.3.3 Training Protocol

Optimisation used Adam with $\beta_1 = 0.5$ and $\beta_2 = 0.999$ with learning rates 2×10^{-4} for the generator and 5×10^{-5} for the discriminator. The objective combined BCE adversarial loss with an L_1 reconstruction loss between generated and ground-truth CT volumes. The L_1 weight was $\lambda_{l1} = 0.01$ for the first 300 epochs and 0.001 thereafter to favor perceptual realism after coarse convergence. Models were trained for 1000 epochs with batch size = 3, checkpointing every 10 epochs.

The dataset comprised nine specimens from the Taguchi L9 design. Eight specimens were used for model training, and one specimen was reserved as a hold-out validation case. The validation specimen was used for the quantitative and qualitative evaluations reported here unless otherwise noted.

8.3.3.4 Evaluation Metrics

Model performance was assessed using a combination of voxel-wise similarity indices, geometric distance metrics, and qualitative inspections. These complementary measures provide information at different scales, from local voxel accuracy to global surface fidelity.

— Voxel-wise overlap and error metrics:

- The mean absolute error (L_1) measured the average voxel-wise intensity difference, directly reflecting reconstruction fidelity across the entire volume.
- The mean squared error (MSE) penalized larger deviations more strongly than L_1, providing a sensitive indicator of discrepancies in fine details.

— Surface alignment indicators:

For the held-out validation specimen, surfaces derived from reconstructed and CT volumes were compared after rigid alignment. The rigid transform returned by the

registration procedure was characterized by two internal indicators: the correspondence ratio which is the fraction of points successfully matched within the cut-off distance and the inlier root-mean-square error (RMSE), both of which reflect the quality of alignment.

— Geometric deviation metrics:

After alignment, the symmetric Hausdorff distance (H) was computed between the surfaces, defined as the maximum of the two directed point-set distances. This metric reports the worst-case discrepancy and thus provides a strict upper bound on reconstruction error.

The reconstructed output is a TIFF stack at 256^3 with intensities in [0,1] is cleaned and resized to 800x800x153 voxels to match the original shape of the ct_scans and binarized and converted to a triangular surface by marching-cubes isosurface extraction. The resulting volume is exported in STL format. In parallel, the validation ct volume is also meshed and converted to an STL file.

Both STL files are converted to point-cloud (PCD) representations with comparable sampling density to enable point-set registration and distance calculations. For dimensionless reporting and cross-specimen comparability, each point set is normalized by the largest bounding-box extent of the reference surface and distances are thus expressed in normalized units.

The point cloud generated was rigidly aligned to the validation point cloud using a point-to-point ICP procedure with identity initialization and a normalized correspondence cut-off of 1.0. The alignment 4×4 transform, a correspondence ratio, and an inlier root-mean-square error (RMSE). The transform was applied to the candidate point set, and visual overlays of the aligned point clouds and their derived surfaces were inspected to verify superposition.

Following alignment, the aligned point sets and their surfaces were assessed using the metrics and conformance rule specified above.

8.4 Results

8.4.1 Convergence and volumetric fidelity

Training over 1000 epochs exhibited a rapid improvement during the initial phase. Validation losses L_1 and MSE decreased from 0.4865 and 0.2461 at initialization to approximately 0.13 and 0.11 by epoch 200, indicating fast capture of global structural features (Figure 68). Beyond this point, convergence proceeded more gradually, with losses stabilizing near 0.15 (L_1) and 0.14 (MSE) after roughly epoch 500, accompanied by small fluctuations. Adversarial dynamics remained balanced throughout: the discriminator's output for real and generated volumes

approached similar values (0.31 at the end of training), and the generator's adversarial term converged near 0.78, consistent with a stable equilibrium without mode collapse.

Final validation losses reached L_1 of 0.1535 and MSE of 0.1402, confirming faithful reproduction of volumetric geometry at voxel scale.

Qualitative inspections supported the quantitative behavior: central-slices overlays showed close agreement across the geometry of each specimen, and three-dimensional renderings displayed coherent global shapes. Residual mismatches were localized, most commonly at sharp edges and thin features (Figure 69).

Despite the strong voxel-level agreement with the micro-CT reference, the model shows localized deviations in specific regions. Small errors appear mainly near thin walls and sharp corners, where local topography variations can lead to slight thickness over- or under-estimation. Very small voids (below 2–3 voxels) are sometimes smoothed out, as their contrast approaches the CT noise floor. Low-contrast material–air transitions may also produce softened boundaries. These limitations indicate that higher-resolution descriptors or enhanced multi-scale conditioning could further improve reconstruction accuracy.

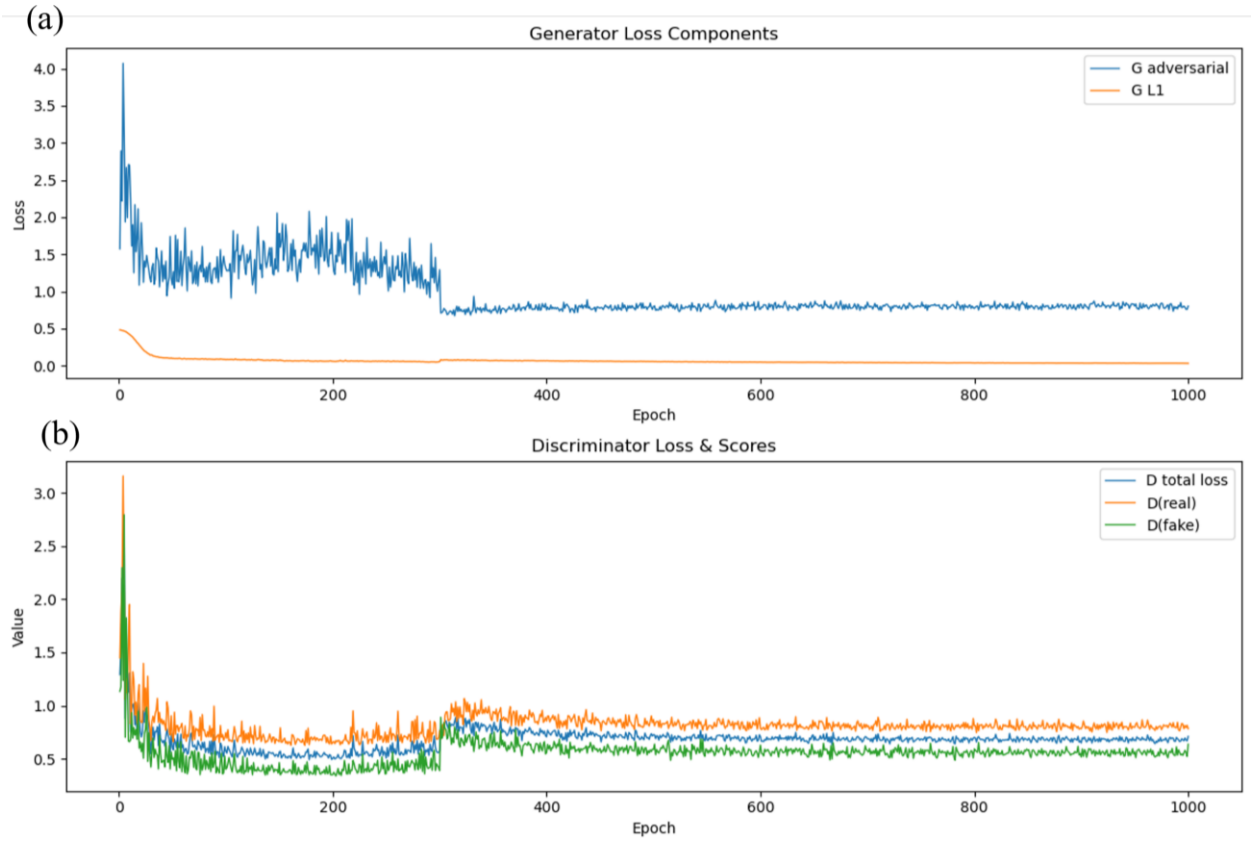

Figure 68. Training behavior of the conditional GAN framework: (a) Generator loss components, (b) Discriminator loss.

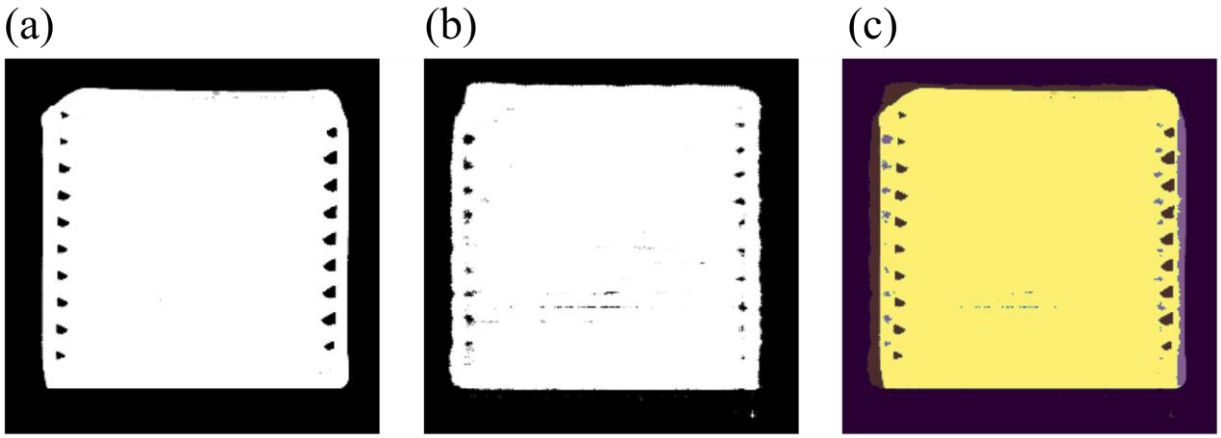

Figure 69. Central-slice comparison between reference and generated volumes: (a) binarized slice from the CT reference, (b) corresponding central slice from the reconstructed TIFF volume, (c) overlay of the generated slice and CT slice.

8.4.2 Alignment and surface conformance

For surface-level evaluation, the final reconstruction for the held-out validation specimen followed the workflow in the methodology, the generated volume was exported as a cleaned TIFF stack at 256^3, resized to 800 × 800 × 153, meshed to STL, converted to a point cloud with sampling density comparable to the CT-derived reference, and then rigidly aligned to that reference (Figure 70). The alignment achieved a correspondence ratio of 1.000 and an inlier RMSE of 0.0098 in normalized units, indicating near-perfect superposition within the accepted correspondence cut-off. Post-alignment geometric discrepancy, quantified by the symmetric Hausdorff distance, was H=0.0455 in normalized units.

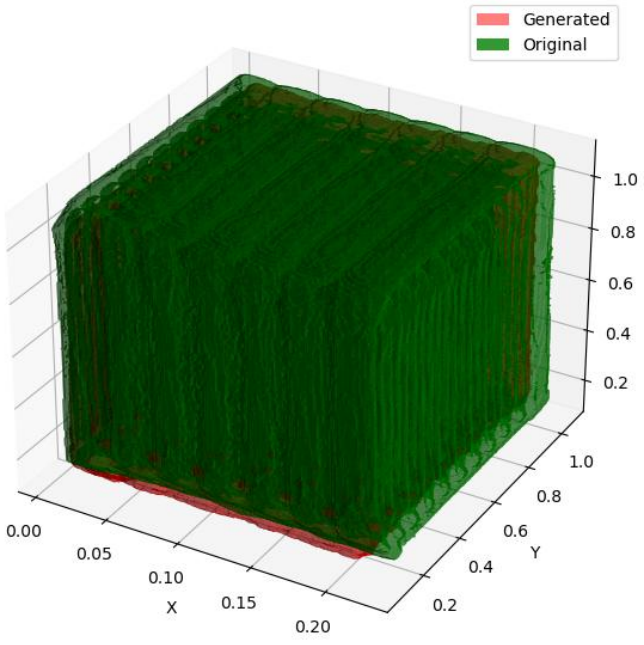

Figure 70. Surface overlay on the held-out specimen after rigid alignment.

To provide a more interpretable, part-level visualization of agreement, top view, side view, and cut view overlays of the reconstructed STL and the CT-derived STL are shown in Figure 71. These views illustrate that the two surfaces are broadly coincident, with small, spatially limited deviations concentrated at external corners and thin regions, consistent with the quantitative results. The cut view emphasizes internal/topological consistency through the section plane.

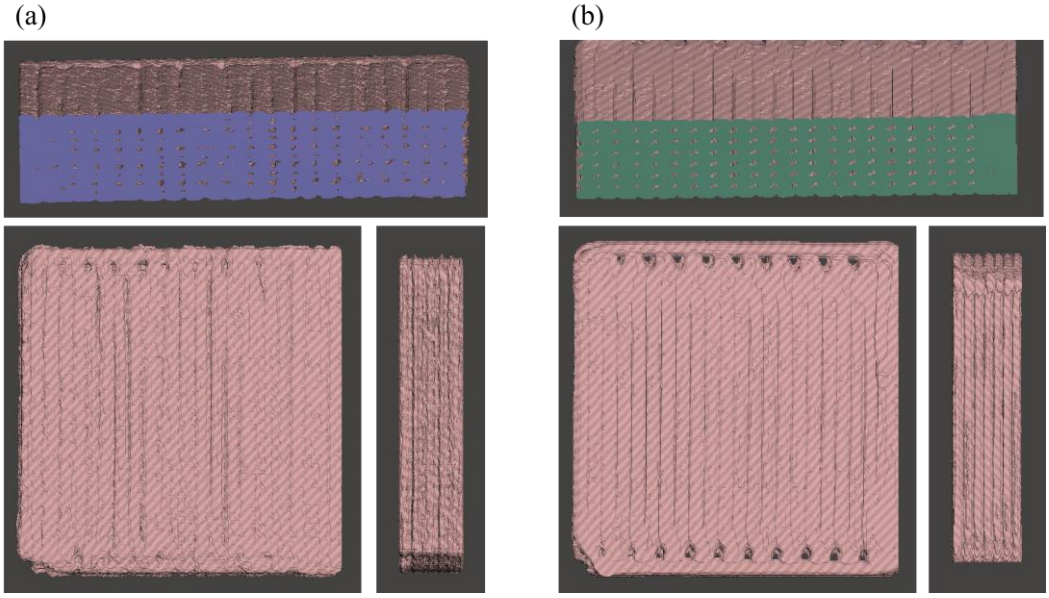

Figure 71. Multi-view overlays of the held-out specimen: (a) Reconstructed STL, (b) CT-derived STL.

8.4.3 Interpretation

The combined evidence indicates that the framework reconstructs FDM parts with high geometric fidelity under the tested conditions. At the voxel level, losses converged stably to L_1 = 0.1535 and MSE = 0.1402, and the Figure 70 confirmed sustained volumetric overlap consistent with qualitative overlays. At the surface level, the held-out specimen exhibited near-perfect alignment (correspondence ratio 1.000, inlier RMSE 0.0098) and conformance with H=0.0455. Multi-view surface overlays further corroborate that residual discrepancies are confined to edges and thin features. Together, the voxel-scale and surface-scale assessments support the conclusion that the reconstruction pipeline delivers quantitatively accurate and visually coherent geometry suitable for downstream quality assurance.

8.5 Conclusion and Perspectives

This study shows that a multimodal, data-driven framework can reconstruct the volumetric geometry of FDM-printed parts with high fidelity under practical conditions. Training over 1,000 epochs reduced the validation L_1 error from 0.4865 to 0.1535 and the MSE from 0.2461 to 0.1402, with most of the gain achieved around epoch 200 (L_1 = 0.13, MSE = 0.11) and stable convergence thereafter. On the held-out validation specimen, rigid alignment yielded a

correspondence ratio of 1.000 and an inlier RMSE of 0.0098 in normalized units. The symmetric Hausdorff distance was 0.0455 on normalized data, indicating geometric conformance. Qualitative overlays of slices and surfaces were consistent with these quantitative trends, with residual discrepancies confined to sharp edges and thin features.

Beyond the numerical improvements, the primary contribution of this work lies in demonstrating that process-aware, geometry-aware, and design-aware information can be fused into a unified, learning-based framework for volumetric reconstruction in material-extrusion printing. By integrating in-situ point clouds and process parameters with CT-supervised training, and validating the approach through both voxel-level metrics and surface-level conformance checks, the study establishes a reproducible pathway for bridging experimental data and digital twins. This dual emphasis on methodological rigor and application to quality assurance underscores the potential of machine-learning-driven reconstruction not only as a post-process diagnostic tool, but also as an enabling a potential technology for adaptive, real-time manufacturing.

Looking ahead, the most impactful next steps are to expand the dataset beyond the L9 design by incorporating a wider variety of geometries, printers, and materials to enhance generalization. Conditioning can be further enriched with complementary sensing such as thermal imaging, infrared, or acoustic signals, while streaming sparse, layer-wise inputs would pave the way for in-situ monitoring and adaptive control. Finally, reconstructions should be standardized for seamless integration into digital twins, ensuring that detection is directly linked to corrective actions and ultimately enabling real-time, data-driven printing.

8.6 Author Contributions

Conceptualization, A.Z.; Formal analysis, M.H. and A.Z.; Funding acquisition, M.H. and S.K.; Investigation, A.Z.; Methodology A.Z.; Software, A.Z.; Data collection: A.Z., Y.A., and S.Y.; Supervision, M.H. and S.K.; Writing—original draft, A.Z.; Writing—review and editing, M.H and S.K. All authors have read and agreed to the published version of the manuscript.

8.7 Funding

Funding: The authors acknowledge the funding provided by the Natural Sciences and Engineering Research Council (NSERC) of Canada (grant number: CRSNG–RGPIN-2021-02846) and the Canada Research Chairs Program.

8.8 Data Availability Statement:

Data available under request.

8.9 Conflicts of Interest

The authors certify that they have no affiliations with or involvement in any organization or entity with any financial interest or non-financial interest in the subject matter or materials discussed in this manuscript.

8.10 References

[1] P. Ferro, A. Fabrizi, H. Elsayed, G. Savio, Multi-material additive manufacturing: creating IN718-AISI 316L bimetallic parts by 3D printing, debinding, and sintering, Sustainability 15(15) (2023) 11911.

[2] Y. Lu, W. Xu, J. Leng, X. Liu, H. Xu, H. Ding, J. Zhou, L. Cui, Review and research prospects on additive manufacturing technology for agricultural manufacturing, Agriculture 14(8) (2024) 1207.

[3] N.N. Ahmad, Y.H. Wong, N.N.N. Ghazali, A systematic review of fused deposition modeling process parameters, Soft Science 2(3) (2022) N/A-N/A.

[4] N. Maqsood, M. Rimašauskas, Characterization of carbon fiber reinforced PLA composites manufactured by fused deposition modeling, Composites Part C: Open Access 4 (2021) 100112.

[5] A. Ziadia, M. Habibi, S. Kelouwani, Digital twin-driven real-time optimization of layer-specific surface roughness in FDM 3D printing, Progress in Additive Manufacturing (2025) 1-24.

[6] B. Mallikarjuna, P. Bhargav, S. Hiremath, K. Jayachristiyan, N. Jayanth, A review on the melt extrusion-based fused deposition modeling (FDM): background, materials, process parameters and military applications, International Journal on Interactive Design and Manufacturing (IJIDeM) 19(2) (2025) 651-665.

[7] A. Ziadia, M. Habibi, S. Kelouwani, Machine learning study of the effect of process parameters on tensile strength of FFF PLA and PLA-CF, Eng 4(4) (2023) 2741-2763.

[8] J.M. Barrios, P.E. Romero, Improvement of surface roughness and hydrophobicity in PETG parts manufactured via fused deposition modeling (FDM): An application in 3D printed self–cleaning parts, Materials 12(15) (2019) 2499.

[9] M. Altan, M. Eryildiz, B. Gumus, Y. Kahraman, Effects of process parameters on the quality of PLA products fabricated by fused deposition modeling (FDM): surface roughness and tensile strength, Materials Testing 60(5) (2018) 471-477.

[10] Z. Abdelhamid, H. Mohamed, S. Kelouwani, The use of machine learning in process–structure–property modeling for material extrusion additive manufacturing: a state-of-the-art

review, Journal of the Brazilian Society of Mechanical Sciences and Engineering 46(2) (2024) 70.

[11] A. Dey, N. Yodo, A systematic survey of FDM process parameter optimization and their influence on part characteristics, Journal of Manufacturing and Materials Processing 3(3) (2019) 64.

[12] A. Mathew, S.R. Kishore, A.T. Tomy, M. Sugavaneswaran, S.G. Scholz, A. Elkaseer, V.H. Wilson, A. John Rajan, Vapour polishing of fused deposition modelling (FDM) parts: a critical review of different techniques, and subsequent surface finish and mechanical properties of the post-processed 3D-printed parts, Progress in Additive Manufacturing 8(6) (2023) 1161-1178.

[13] J. Girard, S. Zhang, Fast error detection method for additive manufacturing process monitoring using structured light three dimensional imaging technique, Optics and Lasers in Engineering 184 (2025) 108609.

[14] F. Corradini, M. Silvestri, Design and testing of a digital twin for monitoring and quality assessment of material extrusion process, Additive Manufacturing 51 (2022) 102633.

[15] S. Ochoa, S. Ferrándiz, L. Garzón, C. Cobos, Digital Twin of Fused Filament Fabrication Prints for Finite Element Analysis via G-Code Reverse Engineering, 3D Printing and Additive Manufacturing (2024).

[16] X. Liu, C. Kan, Z. Ye, Real-time multiscale prediction of structural performance in material extrusion additive manufacturing, Additive Manufacturing 49 (2022) 102503.

[17] L. Wu, N. Dai, H. Wang, Evaluation of rods deformation of metal lattice structure in additive manufacturing based on skeleton extraction technology, Math Biosci Eng 18 (2021) 7525-7538.

[18] F. Uzun, H. Basoalto, K. Liogas, M.F. Slim, T.L. Lee, C. Besnard, Z.I. Wang, J. Chen, I.P. Dolbnya, A.M. Korsunsky, Tomographic eigenstrain reconstruction for full-field residual stress analysis in large scale additive manufacturing parts, Additive Manufacturing 81 (2024) 104027.

[19] Y. Lu, E. Shevtshenko, Y. Wang, Physics-based compressive sensing to enable digital twins of additive manufacturing processes, Journal of Computing and Information Science in Engineering 21(3) (2021) 031009.

[20] J. Chen, M. Khrenov, J. Jin, S.P. Narra, C. McComb, Data-driven inpainting for full-part temperature monitoring in additive manufacturing, Journal of Manufacturing Systems 77 (2024) 558-575.

[21] H. Yeung, F. Kim, M. Donmez, J. Neira, Keyhole pores reduction in laser powder bed fusion additive manufacturing of nickel alloy 625, International Journal of Machine Tools and Manufacture 183 (2022) 103957.
[22] J. Chen, C. Meng, Y. Gao, Y. Liu, Multi-fidelity neural optimization machine for Digital Twins, Structural and Multidisciplinary Optimization 65(12) (2022) 340.
[23] A. Ziabari, S.V. Venkatakrishnan, Z. Snow, A. Lisovich, M. Sprayberry, P. Brackman, C. Frederick, P. Bhattad, S. Graham, P. Bingham, Enabling rapid X-ray CT characterisation for additive manufacturing using CAD models and deep learning-based reconstruction, npj Computational Materials 9(1) (2023) 91.
[24] X. Zhang, W. Cui, F. Liou, Voxel-based geometry reconstruction for repairing and remanufacturing of metallic components via additive manufacturing, International Journal of Precision Engineering and Manufacturing-Green Technology 8(6) (2021) 1663-1686.
[25] J. Mazur, P. Sobczak, M. Panasiewicz, P. Łusiak, M. Krajewska, P. Findura, S. Obidziński, W. Żukiewicz-Sobczak, Mechanical properties and biodegradability of samples obtained by 3D printing using FDM technology from PLA filament with by-products, Scientific Reports 15(1) (2025) 5847.
[26] A.P. CK, T. M, R. G, 3D fused deposition modelling of PLA/PBAT nanocomposites reinforced with GnP: Mechanical and thermal characterizations, Journal of Elastomers & Plastics (2025) 00952443251339798.

Chapitre 9: Conclusions et Perspectives

9.1 Conclusions

Cette thèse a établi une chaîne intégrée pour observer, prédire et agir en FDM en utilisant le PLA comme matériau, reliant de manière opérationnelle les paramètres du procédé, l'état de la matière et les performances finales. Le socle hors ligne s'appuie sur des jeux d'essais économes et des modèles d'apprentissage capables de prédire UTS, E et ε à partir des paramètres d'impression. La micro-tomographie a servi d'oracle métrologique pour caractériser la porosité. Un plan Taguchi L9, une ANCOVA pondérée et un rapport signal-bruit ont permis d'identifier la hiérarchie des influences des paramètres, de proposer des réglages justifiés et de formuler un planning d'ajustements couche par couche réduisant significativement la surface moyenne des vides. Ce résultat fournit des plages opératoires et clarifie les compromis procédé–structure–propriétés, prêts à être mobilisés en production.

Notons également que, dans un contexte industriel réel, les critères de qualité ne visent pas à être maximisés ou minimisés de manière absolue mais à atteindre des valeurs cibles compatibles avec la fonction de la pièce et ses tolérances. Dans cette thèse, les stratégies d'optimisation, qu'elles soient hors ligne, en ligne mono-objectif ou en ligne multicritère, ont utilisé des formulations en maximisation/minimisation afin d'identifier clairement les sensibilités, de dégager des tendances robustes et de structurer un cadre d'apprentissage cohérent pour l'ensemble du jumeau numérique. Ces formulations extrêmes ont servi à comprendre les leviers dominants du procédé et à stabiliser les modèles prédictifs dans un contexte expérimental contrôlé. Dans une perspective industrielle, ces approches pourront être naturellement étendues vers des formulations centrées sur l'écart à une valeur cible, plus représentatives d'un contrôleur de procédé classique. Cette distinction entre optimisation analytique et commande à valeur cible est désormais explicitée afin de situer précisément la portée et le rôle des résultats obtenus.

Le pilotage en ligne, orchestré par un jumeau numérique et alimenté par une métrologie couche par couche, se décline en deux axes complémentaires. Le premier axe s'attache à la réduction de la rugosité de surface par mise à jour automatique des paramètres à chaque couche à partir de prédicteurs rapides et d'une optimisation en ligne. Le second axe étend la boucle vers un pilotage multicritère qui coordonne simultanément rugosité, précision dimensionnelle et propriétés mécaniques, en s'appuyant sur des prédicteurs spatio-temporels, un tranchage adaptatif pour ajuster l'épaisseur de couche et une optimisation multi-objectifs pour sélectionner, couche après couche, un compromis imprimable. Des interfaces de suivi soutiennent la décision et la

traçabilité en affichant, pour chaque couche, le nuage de points et ses caractéristiques et en visualisant en temps réel l'évolution des paramètres et des consignes appliquées.

Au-delà de la surface, une observabilité volumique prédictive a été introduite. Un cGAN 3D conditionnel reconstruit l'état interne à partir des données de procédé et des acquisitions de surface. Les cartes volumiques prédites permettent d'assurer la qualité, orienter le post-traitement et choisir les prochains réglages, de sorte que la décision s'appuie à la fois sur des mesures externes et sur une lecture interne anticipative.

L'ensemble démontre la faisabilité d'un pilotage multicritère, du hors-ligne vers le temps réel, avec gains de qualité en surface, en géométrie et en santé interne, et une traçabilité renforcée à l'échelle de la couche.

9.2 Perspectives

Ce projet de recherche ouvre des perspectives prometteuses pour renforcer la précision et la rapidité du pilotage intelligent en fabrication additive tout en facilitant un déploiement in-dustriel fiable et traçable.

- Robustesse et généralisation à d'autres matériaux et géométries

L'extension des données à de nouveaux polymères et composites ainsi qu'à des géométries plus complexes et à plusieurs machines permet de garantir des performances stables en de-hors du domaine d'entraînement. Les modèles et les réglages gagnent en transférabilité et résistent mieux aux variations réelles de production. Au-delà de l'élargissement du domaine de données, la méthodologie développée possède un fort potentiel de transposabilité vers d'autres classes de matériaux et d'architectures machine. L'adaptation à des polymères techniques tels que l'ABS, le PC, ou encore les composites haute température (PEEK, PEI) repose principalement sur la réidentification des lois thermo-rhéologiques et des paramètres de solidification, sans modification profonde de la structure du jumeau numérique. De même, le transfert vers des plateformes industrielles multi-matériaux, des têtes indépendantes ou des cellules robotisées 5 à 6 axes ne nécessite qu'une adaptation de la dynamique machine (réponse thermique, précision du dépôt, cinématique non plane). Cette généricité ouvre la voie à une utilisation du cadre proposé dans des environnements d'impression plus complexes et orientés production, incluant l'impression hors-plan et les trajectoires non linéaires.

- Intégration de données multimodales

L'intégration de données thermiques, visuelles et acoustiques permet de détecter plus tôt les dérives que la seule géométrie de surface ne révèle pas. La synchronisation de ces flux avec les nuages de points couche par couche enrichit l'observabilité et éclaire les causes phy-siques des

écarts de qualité. Une fusion cohérente de ces modalités conduit à des actions correctives plus ciblées et diminue les besoins de post traitement.

- Limites actuelles de la chaîne de mesure et robustesse en conditions réelles

Malgré la précision démontrée dans les conditions contrôlées du laboratoire, la chaîne de mesure et les modèles présentent des limites lorsqu'ils sont exposés à des dérives matérielles ou à des perturbations non modélisées. L'usure progressive de la buse, les fluctuations de température ambiante, les variations de débit, ou encore les micro-instabilités mécaniques peuvent modifier la forme du cordon extrudé et détériorer la qualité des mesures géométriques. De plus, certains phénomènes complexes (fluctuations stochastiques du refroidissement, charges thermiques non uniformes, vibrations machine) restent partiellement capturés par les modèles actuels. Ces éléments soulignent la nécessité, pour un déploiement industriel, de mettre en place des mécanismes avancés de détection de dérives, de recalibration automatique, ou encore des modèles adaptatifs capables de maintenir la performance prédictive malgré l'évolution naturelle du procédé.

- Compromis entre complexité des modèles et contraintes de temps réel

La mise en œuvre d'un pilotage intelligent en temps réel impose un compromis entre la complexité des modèles d'apprentissage utilisés et les contraintes computationnelles du procédé. L'architecture hybride CNN–LSTM développée pour la prédiction couche par couche, ainsi que le modèle cGAN employé pour la reconstruction 3D, présentent une charge de calcul non négligeable qui peut limiter leur utilisation en ligne dans un environnement industriel. Plusieurs marges de simplification peuvent toutefois être envisagées : réduction du nombre de filtres et de couches, quantification et compression des réseaux, distillation vers des modèles plus légers, ou optimisation de l'inférence via un pipeline partiellement asynchrone. Ces stratégies permettent de conserver la précision prédictive tout en améliorant la vitesse d'exécution, condition essentielle à l'intégration du jumeau numérique dans un système de pilotage adaptatif.

- Boucle d'auto correction intelligente.

L'intégration d'une boucle d'auto correction qui ajuste progressivement les modèles et les priorités d'optimisation à partir des retours d'usage permet de rendre le contrôle plus résili-ent face aux changements de contexte. La performance s'améliore au fil du temps sans requalification lourde et la dépendance à l'expertise manuelle diminue.

- Intégration dans une cellule de fabrication additive robotisée

À plus long terme, l'approche développée pourrait être intégrée dans une cellule de fabrication additive robotisée où plusieurs machines sont coordonnées au sein d'un même environnement de production. Le jumeau numérique deviendrait alors un module décisionnel capable de gérer

simultanément plusieurs imprimantes, d'optimiser l'ordonnancement des tâches en fonction de la charge, du matériau ou de l'urgence de production, et d'anticiper les dérives grâce à des mécanismes de maintenance prédictive basés sur l'analyse continue des données de procédé. Une telle architecture permettrait de superviser automatiquement la qualité, la disponibilité machine, la planification et la traçabilité, ouvrant la voie à des lignes de production autonomes en fabrication additive. Cette perspective positionne le travail réalisé comme une brique essentielle vers des cellules plus intelligentes, distribuées et interconnectées.

- Ouverture applicative au delà du FDM

Le transfert de la méthodologie vers d'autres procédés d'impression permet d'accroître l'impact scientifique et industriel. La chaîne observer prédire agir se montre portable avec des capteurs et des contraintes différentes et prépare des plateformes hybrides capables de couvrir des besoins plus larges.

ANNEXE 1

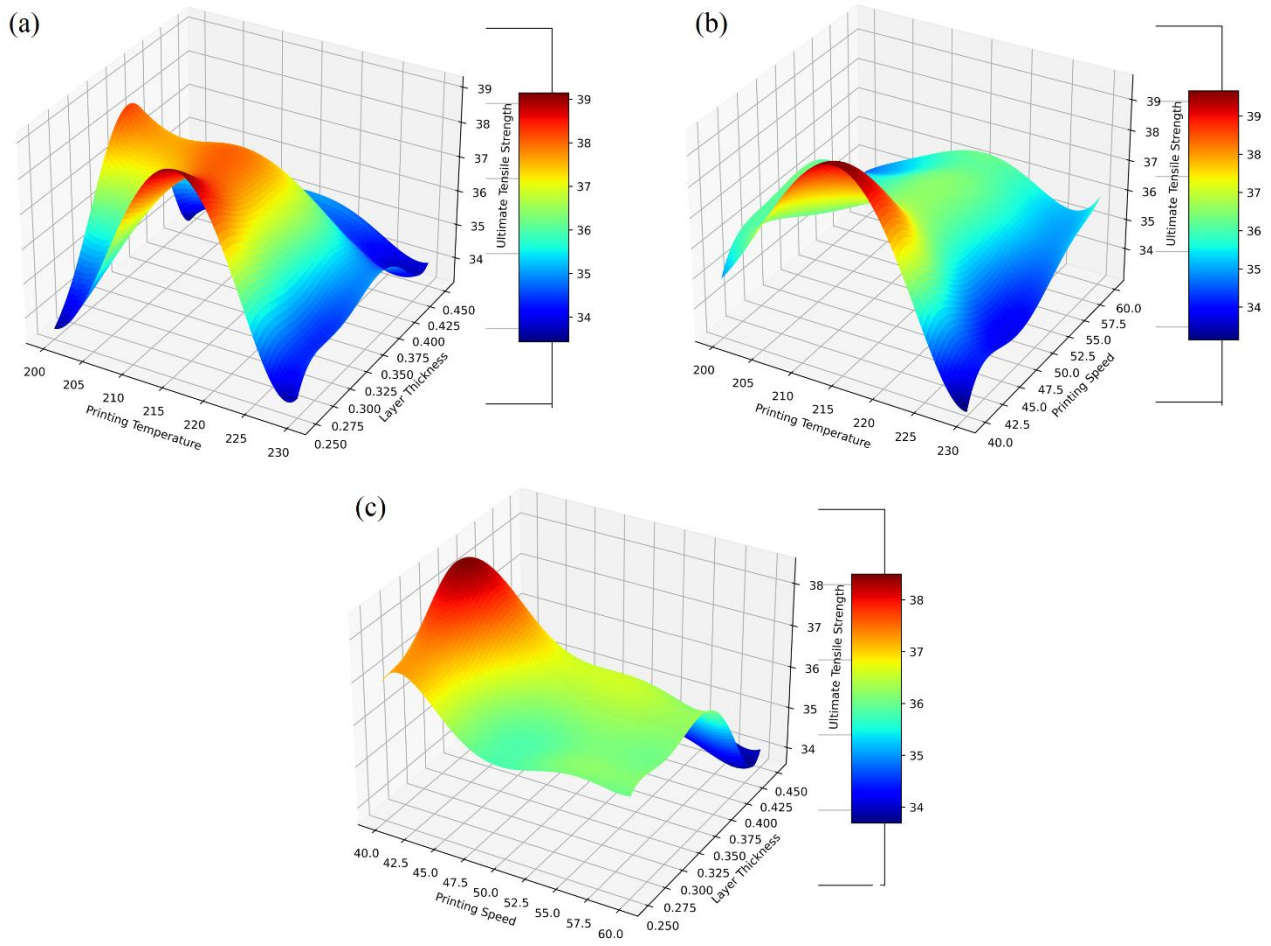

Figure 72. Response surface 3D plots of the predicted ultimate tensile strength of PLA- CF:(a) Printing Temperature vs Layer Thickness, (b) Printing Temperature vs Printing Speed, (c) Printing Speed vs Layer Thickness

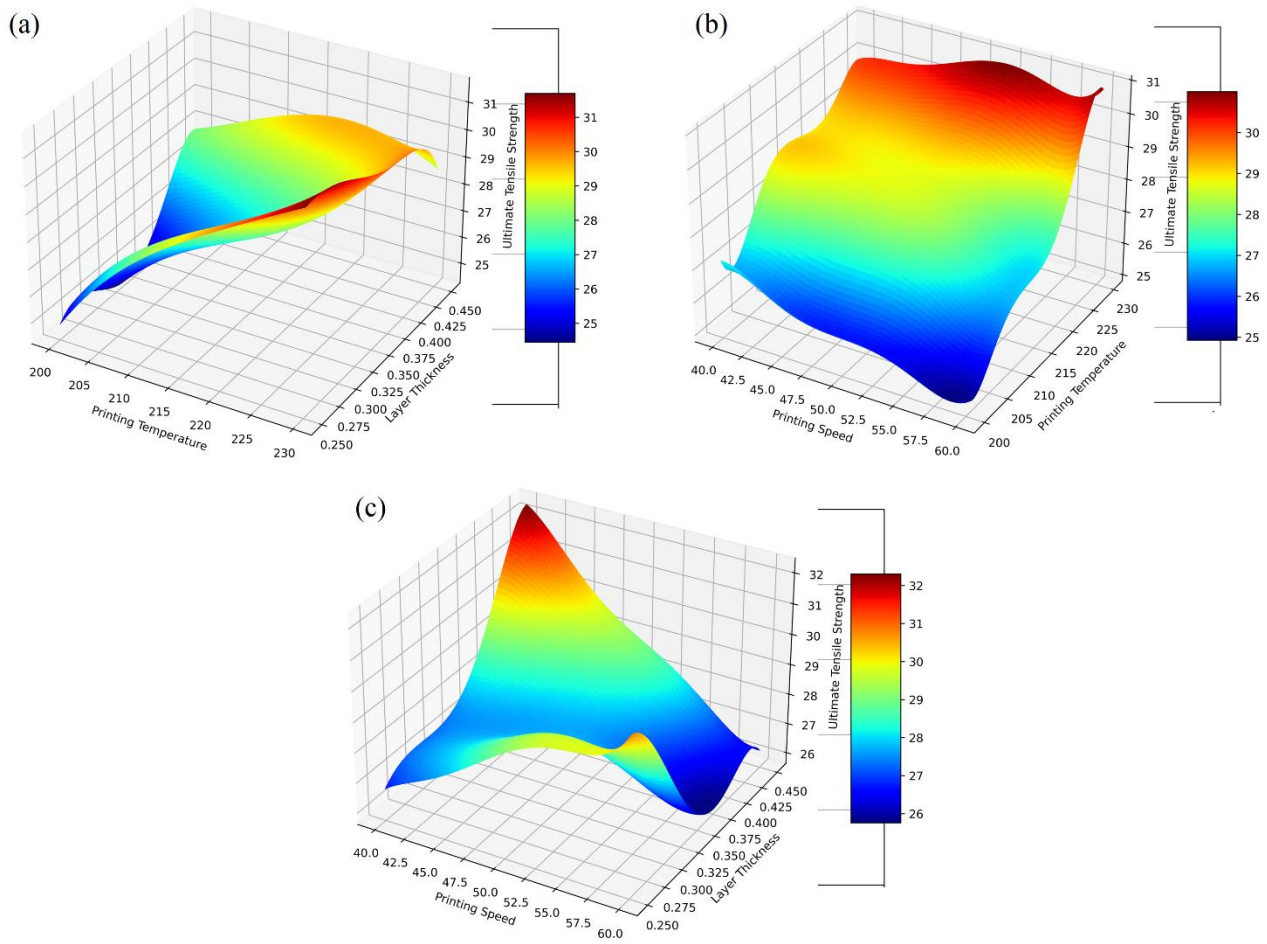

Figure 73. Response surface 3D plots of the predicted ultimate tensile strength of PLA:(a) Printing Temperature vs Layer Thickness, (b) Printing Speed vs Printing Temperature, (c) Printing Speed vs Layer Thickness

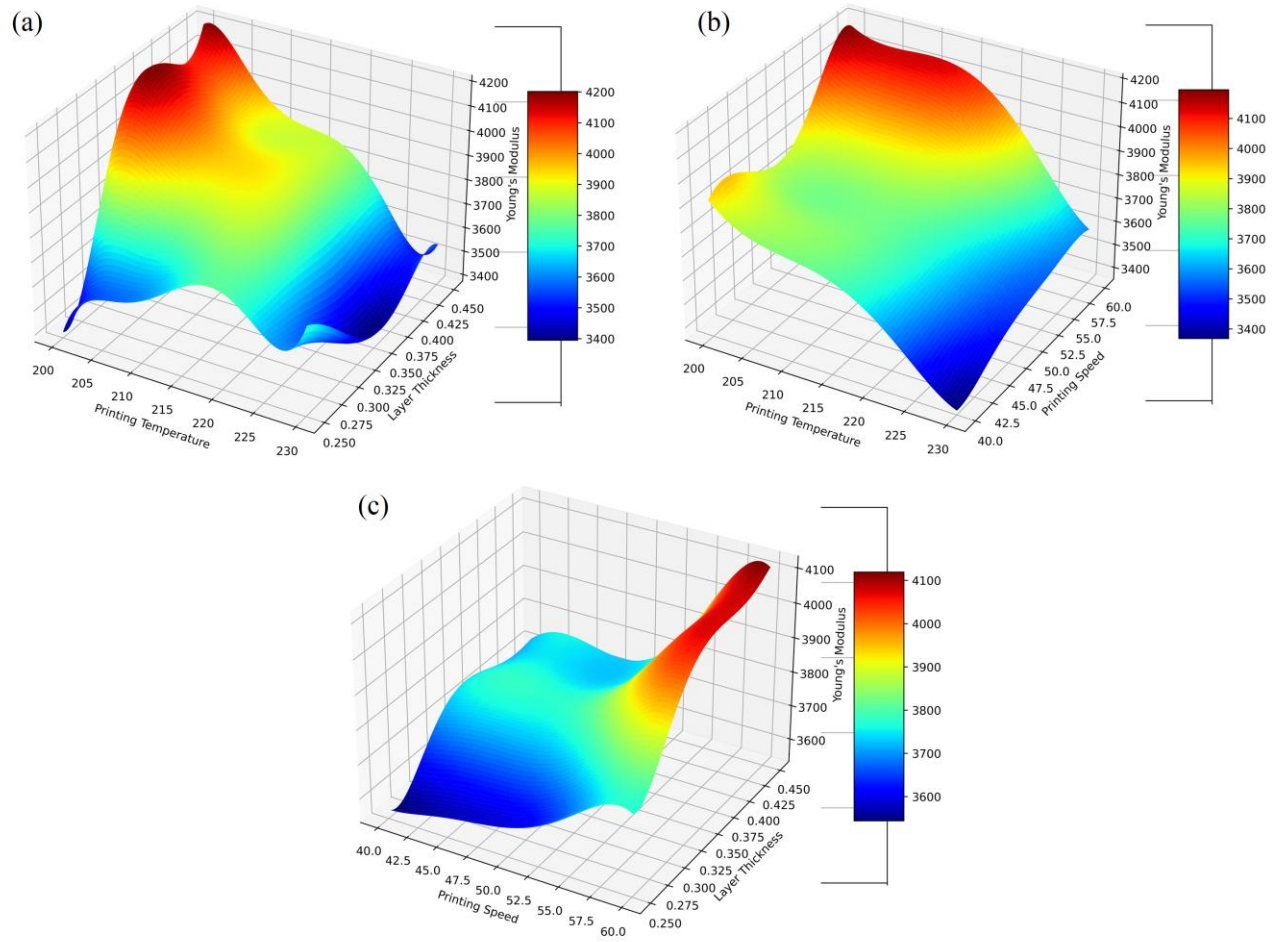

Figure 74. Response surface 3D plots of the predicted Young's modulus of PLA- CF:(a) Printing Temperature vs Layer Thickness, (b) Printing Temperature vs Printing Speed, (c) Printing Speed vs Layer Thickness

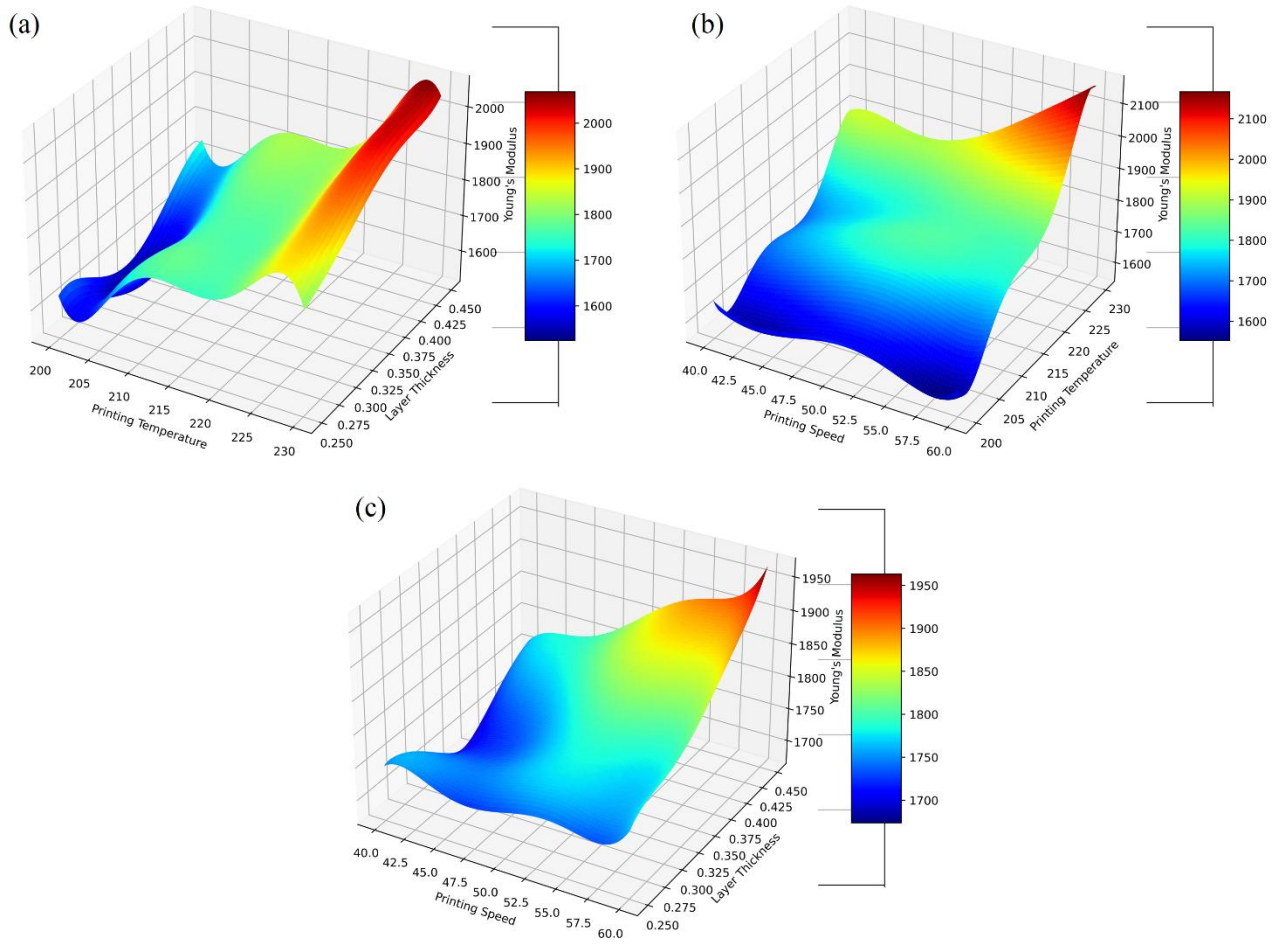

Figure 75. Response surface 3D plots of the predicted Young's modulus of PLA:(a) Printing Temperature vs Layer Thickness, (b) Printing Speed vs Printing Temperature, (c) Printing Speed vs Layer Thickness

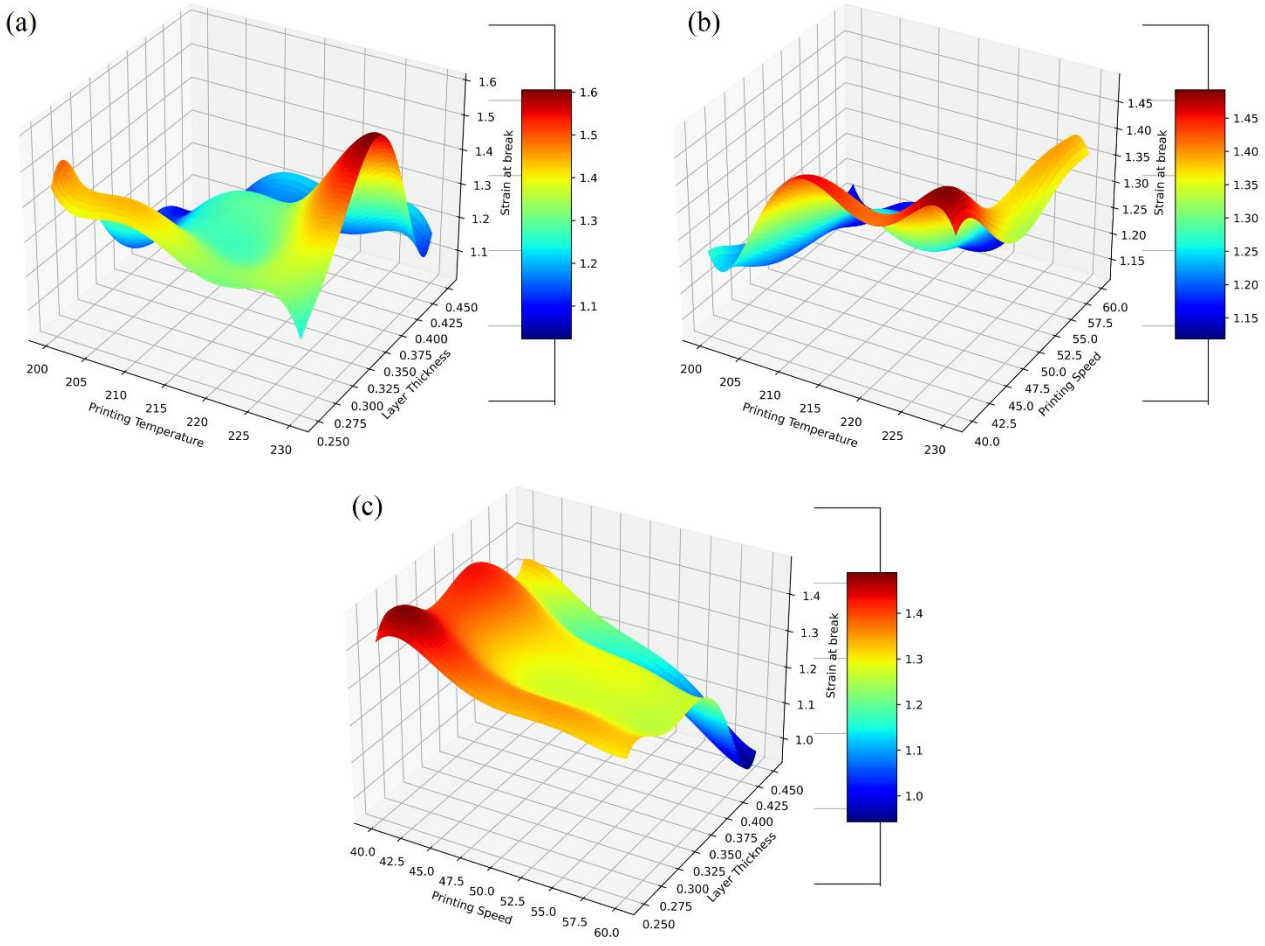

Figure 76. Response surface 3D plots of the predicted Strain at break of PLA-CF:(a) Printing Temperature vs Layer Thickness, (b) Printing Temperature vs Printing Speed, (c) Printing Speed vs Layer Thickness

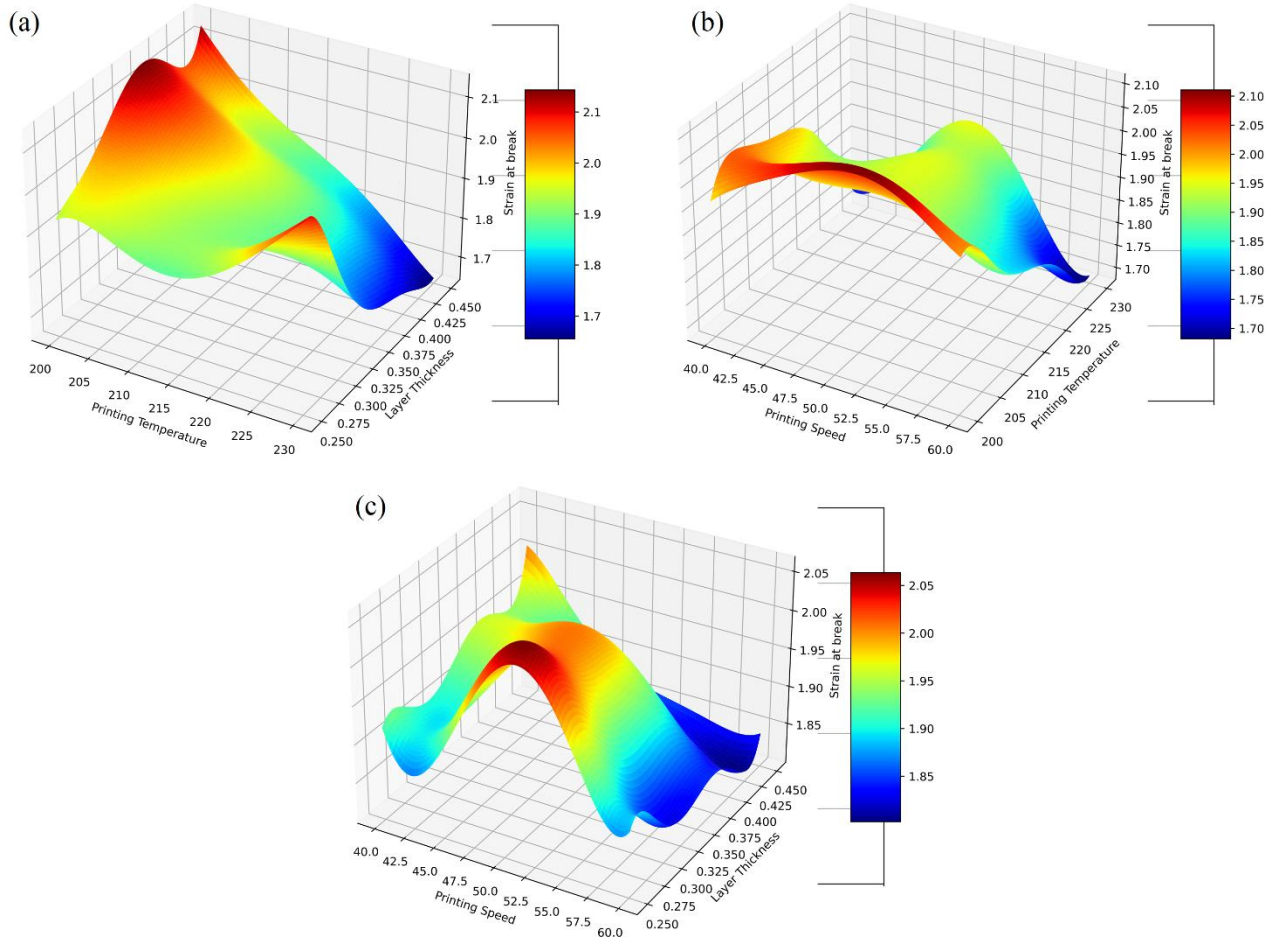

Figure 77. Response surface 3D plots of the predicted Strain at break of PLA:(a) Printing Temperature vs Layer Thickness, (b) Printing Speed vs Printing Temperature, (c) Printing Speed vs Layer Thickness

ANNEXE 2

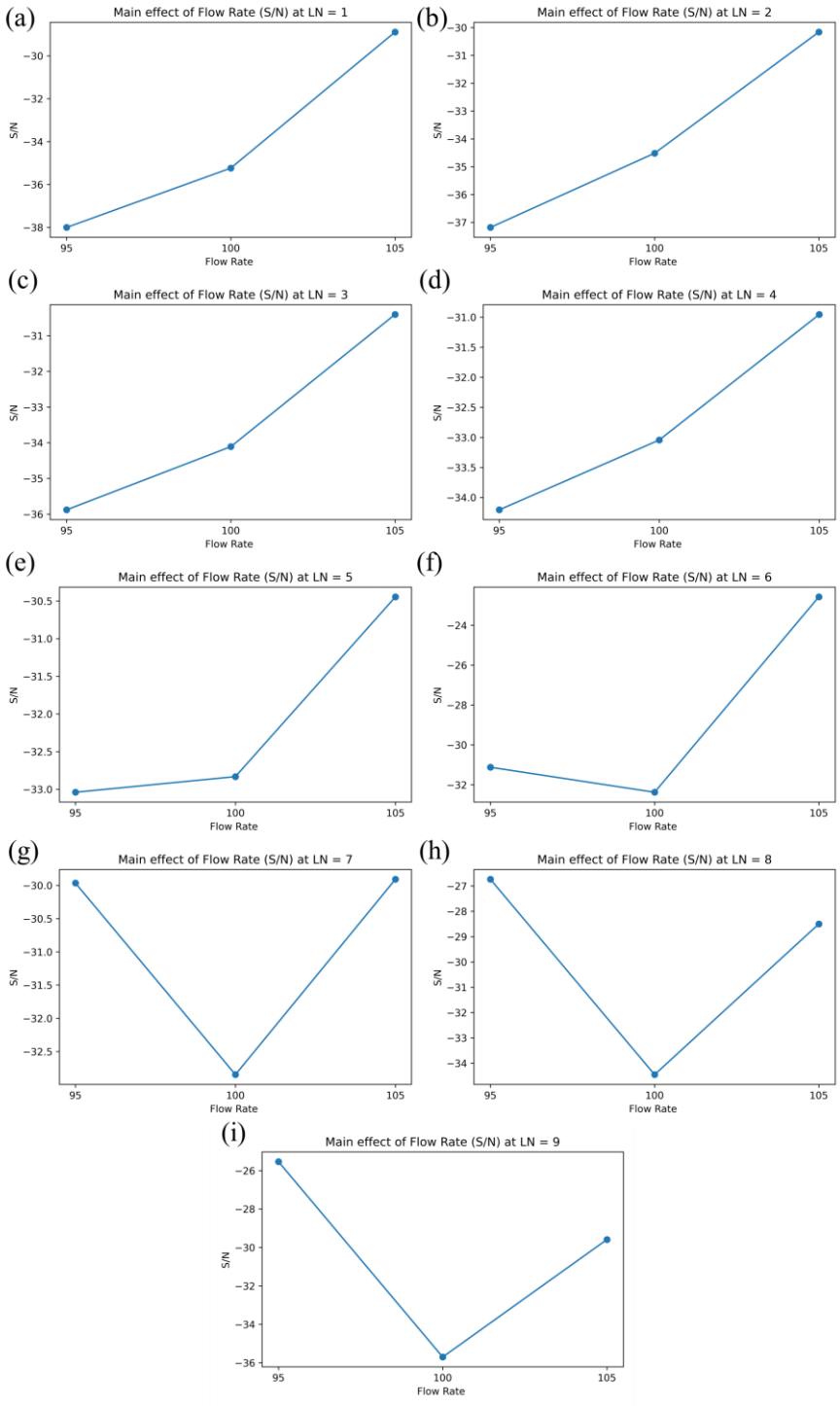

Figure 78. Layer-specific main effect of flow rate for the Smaller-the-Better (S/N).

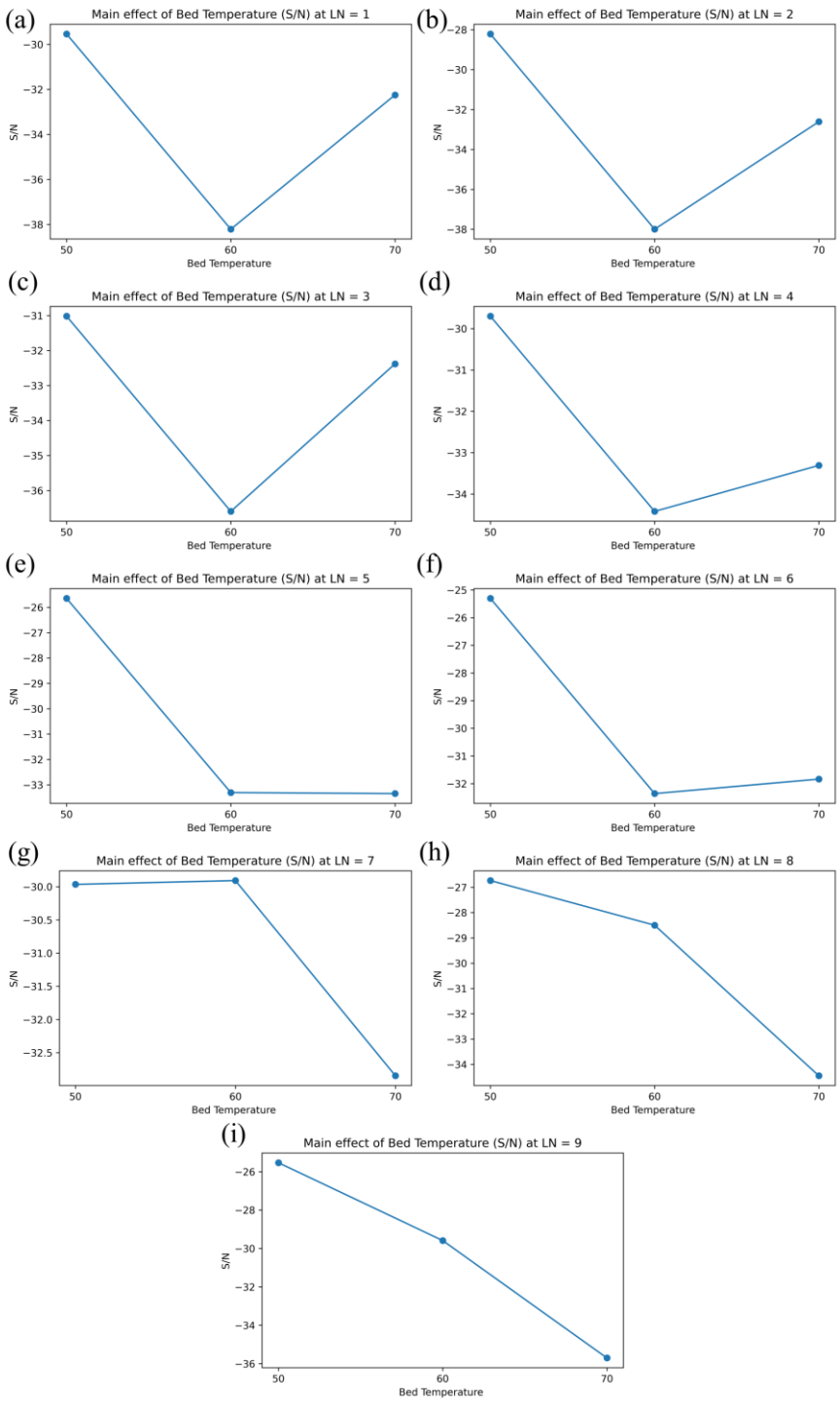

Figure 79. Layer-specific main effect of bed temperature for the Smaller-the-Better (S/N).

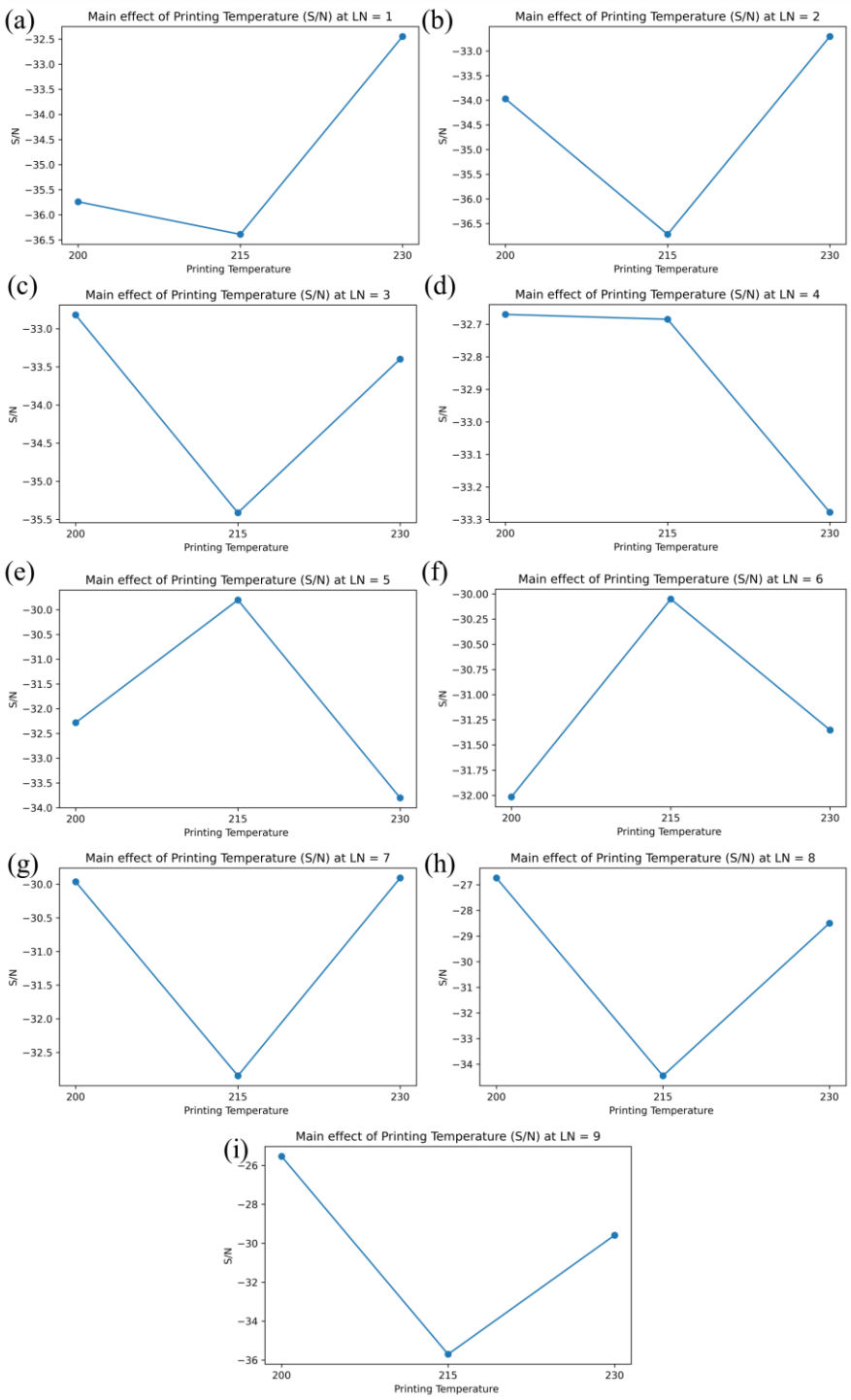

Figure 80. Layer-specific main effect of printing temperature for the Smaller-the-Better (S/N).

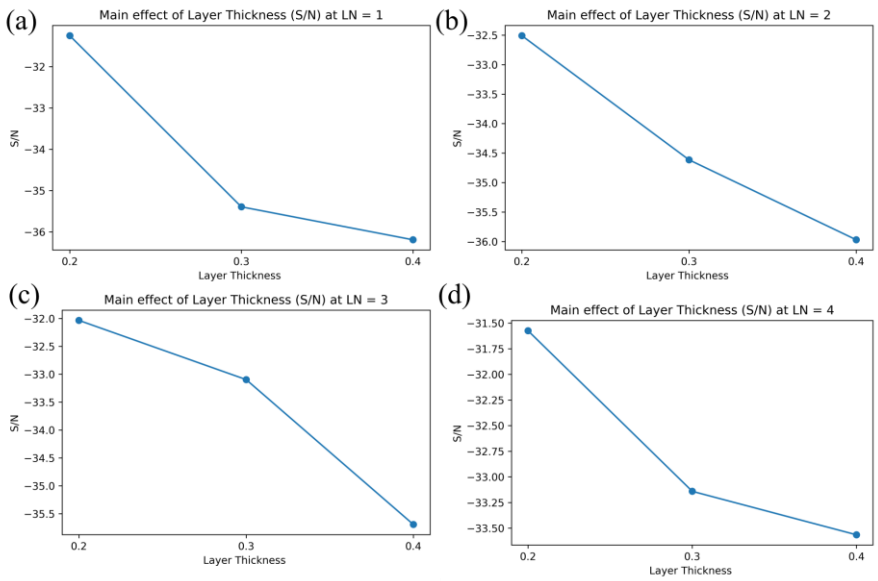

Figure 81. Layer-specific main effect of layer thickness for the Smaller-the-Better (S/N).